RELIABILITY ASSESSMENT OF HULL FORMS SUSCEPTIBLE TO PARAMETRIC ROLL IN IRREGULAR SEAS

A Dissertation

by

ABHILASH SHARMA SOMAYAJULA

Submitted to the Office of Graduate and Professional Studies of
Texas A&M University
in partial fulfillment of the requirements for the degree of

DOCTOR OF PHILOSOPHY

Chair of Committee,	Jeffrey M. Falzarano
Committee Members,	Moo-Hyun Kim
	Richard S. Mercier
	Alan B. Palazzolo
	Loren D. Lutes
Head of Department,	Sharath Girimaji

May 2017

Major Subject: Ocean Engineering

ABSTRACT

Traditionally ships are designed to be symmetric about their centerline which makes head seas a very safe heading for roll motion stability. However, in the recent years several incidents of large amplitude roll motion in head seas have been reported which have later been attributed to parametric roll. Parametric roll motion is a phenomenon in which a ship exhibits a large amplitude of roll motion even when it is moving into head seas with no direct excitation. This phenomenon is particularly an issue for modern high-speed fine form container ships and has gained attention relatively recently.

This instability is dangerous because of its manifestation in counter-intuitive headings. Also the roll amplitude during parametric roll rises exponentially with time which gives ship captains and masters very less time to react. While this instability has been studied extensively in regular waves, its manifestation in irregular seas has not received sufficient attention. This dissertation aims at the development of design criteria based on analytical techniques which can help a designer quickly quantify the stability of a vessel to parametric excitation.

For accurate simulation of parametric response of a vessel/platform in irregular seas, an in-house time domain simulation program has been developed and validated against available experiments. The roll equation of motion is then simplified into a single degree of freedom model for analytical assessment. The existing single degree of freedom models in the literature are compared against the time domain simulation tool to gain an understanding of the extent to which the simplified models capture the dynamics of the phenomenon. In order to improve the roll modeling, a new approach is suggested to overcome some of the limitations of the existing models.

This new model is then investigated using two analytical approaches, one from the theory of nonlinear dynamical systems and the other from stochastic dynamics to come up with two independent measures of stability. Both of these measures are used to demonstrate their potential as a design criteria which can be used by a ship designer. A comparison of the two methods for a variety of cases is undertaken to demonstrate the similar trends they exhibit.

DEDICATION

To my loving parents

ACKNOWLEDGMENTS

I could not have asked for a better Ph.D. advisor than Dr. Jeffrey Falzarano. I am very grateful for his advise, both academic and otherwise, over the years which has been immensely helpful. His patience and continued confidence in me have been a constant source of motivation for me.

I would like to thank my committee members Dr. Richard Mercier, Dr. Alan Palazzolo, Dr. Moo-Hyun Kim and Dr. Loren Lutes for their guidance and teachings. My learning from their courses and discussions with them has had a significant influence in the development of this research work. Particularly, I would like to thank Dr. Lutes who has been kind enough to spend time with me even in his retirement to discuss my research and also helped me out with crucial theoretical derivations. I also thank Dr. Mercier and Dr. Palazzolo for the immensely useful technical discussions on my research.

I am very thankful to Dr. Edmund Muehlner and Dr. Xiaozhi (Christina) Wang for mentoring me during my two summer internships. The practical knowledge gained during these internships has given me a unique perspective which has been a crucial element in the development of this dissertation work.

I am very grateful to the university staff who have helped me through the various administrative processes. In particular I would like to thank Ms. Lisa Baker, Ms. Laura Byrd and Ms. Alberta Ortiz-Ganem who have been very kind and helped me many times. The university library staff deserve a special mention for helping me access various international articles and books from around the world.

Last but not the least, I would like to thank my parents for their constant love and support without which this work would not have been possible.

CONTRIBUTORS AND FUNDING SOURCES

Contributors

This work was supervised by a dissertation committee consisting of Professors Jeffrey Falzarano (PhD advisor) and Moo-Hyun Kim of the Department of Ocean Engineering, Professors Loren Lutes (Emeritus) and Richard Mercier of the Department of Civil Engineering and Professor Alan Palazzolo of the Department of Mechanical Engineering.

The hull form of the Pram hull analyzed in this dissertation was made available by Dr. Frans vanWalree of MARIN. The experimental data for validation of the developed numerical program described in chapter 2 was obtained from the HYDROLAB III project and was made available by Professor Sérgio Bruno Nogueira Ribeiro e Silva of IST Portugal. All other work for the dissertation was completed by the student, under the advisement of Professors Jeffrey Falzarano and Loren Lutes.

Funding Sources

This work was made possible in part by Office of Naval Research under Grant Numbers N00014-07-1-1067, N00014-13-1-0756 and N00014-16-1-2281. This work was also partially supported by National Research Foundation of Korea (NRF) under Grant Number GCRC-SOP (No. 2011-0030013), Chevron Energy Technology Company (ETC) and Society of Naval Architects and Marine Engineers (SNAME).

TABLE OF CONTENTS

Page

ABSTRACT ii

DEDICATION iv

ACKNOWLEDGMENTS v

CONTRIBUTORS AND FUNDING SOURCES vi

TABLE OF CONTENTS vii

LIST OF FIGURES xi

LIST OF TABLES xvii

1. INTRODUCTION 1

    1.1 Overview of Dissertation 5

2. NONLINEAR TIME DOMAIN SIMULATION 9

    2.1 Coordinate System 13
    2.2 Equations of Motion 18
    2.3 Nonlinear Force Vector Evaluation 21
        2.3.1 Diffraction Forces and Moments 23
        2.3.2 Radiation Forces and Moments: 26
        2.3.3 Restoring Forces and Moments 31
        2.3.4 Viscous Forces and Moments 32
            2.3.4.1 Wave Damping 35
            2.3.4.2 Skin Friction Damping 36
            2.3.4.3 Lift Damping 40
            2.3.4.4 Eddy Damping 40
            2.3.4.5 Bilge Keel Damping 44
            2.3.4.6 Effective Linear Damping 48
    2.4 Integration Scheme 51
    2.5 Simulation of Parametric Roll 52
        2.5.1 Comparison with Linear Theory 56
        2.5.2 Ramp Time 57

2.5.3 Roll Motion . . . 57
2.6 Comparison with Experiments . . . 59
2.6.1 Experimental and Numerical Simulation Setup . . . 59
2.6.2 Comparison with Experiments . . . 60
2.6.3 Discussion . . . 64
2.7 The Stochastic Nature of Parametric Roll . . . 65
2.7.1 Ergodicity of Wave Elevation and Motions . . . 67
2.7.2 Probability Distribution . . . 68
2.8 Parametric Excitation of Classic Spar . . . 72
2.8.1 Problem Description . . . 73
2.8.2 Comparison with Experiments . . . 74
2.9 Conclusion . . . 76

3. APPROXIMATE SINGLE DEGREE OF FREEDOM (SDOF) MODELS . 78

3.1 Literature Review . . . 80
3.2 Roll Equation of Motion . . . 83
3.2.1 Roll Restoring Moment . . . 83
3.3 Exact GZ Variation . . . 86
3.4 Volterra Series Method for GM Variation . . . 89
3.5 Grim's Effective Wave Approach . . . 97
3.5.1 No Effect of Dynamic Heave and Pitch . . . 100
3.5.2 Including the Effect of Dynamic Heave and Pitch . . . 102
3.6 Volterra Series Method for GZ Variation . . . 104
3.7 Comparison of Single Degree of Freedom Models . . . 111

4. MELNIKOV PROCESS AND PHASE SPACE FLUX EVALUATION . . . 113

4.1 State Space Formulation . . . 116
4.2 Phase Plane and the Concept of Safe Basin . . . 118
4.3 Melnikov Function . . . 125
4.4 Phase Space Flux . . . 132

5. STOCHASTIC AVERAGING OF ENERGY ENVELOPE . . . 140

5.1 Energy-Phase Transformation . . . 142
5.2 Approximation of a Real Process by Markov Process . . . 148
5.3 Stationary Probability Density Function . . . 159
5.4 First Passage Failure Analysis . . . 160
5.5 Boundary Condition at $E = 0$ . . . 165
5.6 Comparison with Monte Carlo Simulations . . . 166

6. COMPARISON OF THE MARKOV AND THE MELNIKOV APPROACHES 171

6.1 Lyapunov Exponent . . . 171
6.2 Sensitivity Analysis . . . 174
6.2.1 Sensitivity to Significant Wave Height . . . 175
6.2.2 Sensitivity to Peak Period . . . 178
6.2.3 Sensitivity to Damping . . . 178
6.2.4 Sensitivity to Calm Water Metacentric Height . . . 184

7. CONCLUSION AND FUTURE DIRECTIONS . . . 188

7.1 Reliability Analysis . . . 191

REFERENCES . . . 195

APPENDIX A. RELATION BETWEEN TIME AND FREQUENCY DOMAIN DESCRIPTION . . . 215

APPENDIX B. RECASTING EQUATIONS OF MOTION FOR NUMERICAL INTEGRATION . . . 218

APPENDIX C. CALCULATION OF $\overline{GZ}^{2D}$ FOR EXACT $\overline{GZ}$ CALCULATION IN IRREGULAR WAVE . . . 223

APPENDIX D. SUBHARMONIC PARAMETRIC RESPONSE . . . 228

APPENDIX E. INTRODUCTION TO STOCHASTIC DYNAMICS . . . 236

E.1 Markov Process and Chapman-Kolmogorov Equation . . . 236
E.2 Fokker Planck Kolmogorov (FPK) Equation . . . 238
E.3 Kolmogorov Backward Equation . . . 242
E.4 Brownian Motion . . . 245
E.5 Stochastic Differential Equations . . . 246
E.6 Itô's Formula . . . 250
E.7 White Noise . . . 250

APPENDIX F. DRIFT AND DIFFUSION COEFFICIENT EXPRESSIONS . 252

F.1 Drift Coefficient Calculation . . . 252
F.1.1 Energy Drift Coefficient . . . 252
F.1.1.1 Evaluation of 1^{st} Term in (F.3) . . . 253
F.1.1.2 Evaluation of 2^{nd} Term in (F.3) . . . 254
F.1.1.3 Fourier Expansions for Energy Drift Calculation . . . 257
F.1.2 Phase Drift Coefficient . . . 258
F.1.2.1 Evaluation of 1^{st} Term in (F.30) . . . 258
F.1.2.2 Evaluation of 2^{nd} Term in (F.30) . . . 259

F.1.2.3 Fourier Expansions for Phase Drift Calculation . . . 261
F.2 Diffusion Coefficient Calculation 262

APPENDIX G. DERIVATION OF THE SINGULAR BOUNDARY CONDITION OF PONTRYAGIN EQUATION AT $E = 0$ 265

APPENDIX H. SUPPLEMENTARY FILES 272

LIST OF FIGURES

FIGURE Page

2.1 Body plan of the Pram hull form 12

2.2 Description of coordinate systems 13

2.3 Transformation from SMCS to BCS using Euler angles 15

2.4 Roll radiation damping (in $\frac{Nms}{rad}$) for Pram hull at 8 knots forward speed 28

2.5 Roll retardation function (in $\frac{Nm}{rad}$) for Pram hull at 8 knots forward speed with waves incident at 180^0 30

2.6 Roll radiation damping (in $\frac{Nms}{rad}$) for Pram hull at 8 knots forward speed with waves incident at 180^0 31

2.7 Wave damping of Pram hull from potential theory for different values of $F_n = \frac{U}{\sqrt{gL}}$ 36

2.8 Wave damping of Pram hull from potential theory for different values of $\hat{\omega} = \omega\sqrt{\frac{B}{2g}}$ 37

2.9 Skin friction damping of Pram hull for different values of $F_n = \frac{U}{\sqrt{gL}}$. 39

2.10 Skin friction damping of Pram hull for different values of $\hat{\omega} = \omega\sqrt{\frac{B}{2g}}$. 39

2.11 Lift damping of Pram hull for different values of $F_n = \frac{U}{\sqrt{gL}}$ 41

2.12 Eddy damping of Pram hull for different values of $F_n = \frac{U}{\sqrt{gL}}$ 45

2.13 Eddy damping of Pram hull for different values of $\hat{\omega} = \omega\sqrt{\frac{B}{2g}}$ 45

2.14 Bilge keel damping of Pram hull for different values of $\hat{\omega}$ 49

2.15 Effective linear damping and its components for Pram hull ($\hat{\omega} = 0.5$) 50

2.16 Effective linear damping for Pram hull moving with zero speed ($F_n = 0$) 50

2.17 Effective linear damping for Pram hull moving with forward speed ($F_n = 0.1015$) 51

2.18 Bretschneider spectrum of wave elevation 53

2.19 Wave realization from a Bretschneider spectrum with $H_s = 10\ m$, $T_p = 13\ s$ and $\beta = 180^0$ 56

2.20 Parametric roll of Pram hull subjected to a Bretschneider spectrum with $H_s = 10\ m$, $T_p = 13\ s$ and $\beta = 180^0$ 57

2.21 Comparison between time domain simulation tool SIMDYN and frequency domain tool MDLHYDROD 58

2.22 Magnification curves for regular wave excitation 62

2.23 Comparison of roll motion between experimental data and SIMDYN simulation (with input of experimental wave elevation) for Test 5 listed in Table 2.3 63

2.24 Comparison of roll motion between experimental data and SIMDYN simulation (with input of experimental wave elevation) for Test 6 listed in Table 2.3 63

2.25 Comparison of roll motion between experimental data and SIMDYN simulation for incident irregular waves 64

2.26 Plot of 30 time series each obtained from a different wave realization of Bretschneider Spectrum with $H_s = 10\ m$ and $T_p = 13\ s$ 69

2.27 Comparison of heave motion against normal distribution 70

2.28 Comparison of pitch motion against normal distribution 70

2.29 Comparison of roll motion against normal distribution 71

2.30 Heave motion (about the center of gravity) comparison between SIMDYN and Haslum [1] for incident head on ($\beta = 180^0$) regular waves of height $H = 16.0\ m$ and period $T = 22.5\ s$ 75

2.31 Pitch motion (about the center of gravity) comparison between SIMDYN and Haslum [1] for incident head on ($\beta = 180^0$) regular waves of height $H = 16.0\ m$ and period $T = 22.5\ s$ 75

3.1 Roll restoring moment 84

3.2 Separation of Pram hull form into 200 2-D strips; The red shade shows the instantaneous wetted part of each section at $t = 4417s$ from a 3 hour wave realized from Bretschneider spectrum with $H_s = 5\ m$ and $T_p = 13\ s$ 86

3.3 Comparison of roll motion between "SIMDYN" and "exact $\overline{GZ}$ model" of Pram hull form in a 3-hour realization of Bretschneider spectrum with $H_s = 5\ m$ and $T_p = 13\ s$ 88

3.4 Variation of $G_1(x)$ and $G_2(x)$ for Pram hull form 92

3.5 First order $\overline{GM}$ variation transfer function 93

3.6 Second order $\overline{GM}$ variation transfer functions 95

3.7 Comparison of roll motion between "SIMDYN" and "Volterra $\overline{GM}$ model" of Pram hull form in a 3-hour realization of Bretschneider spectrum with $H_s = 5\ m$ and $T_p = 13\ s$ 97

3.8 Square of IGEW transfer functions 99

3.9 Comparison of IGEW and Grim effective wave with actual wave elevation from Bretschneider spectrum with $H_s = 5m$ and $T_p = 13s$ . . . 100

3.10 GZ variation calculation using IGEW 102

3.11 Comparison of quasi-static trim with dynamic pitch for Pram hull form in 5 knots forward speed subjected to an input wave realized from Bretschneider spectrum with significant wave height $H_s = 3m$ and modal period $T_p = 14.1s$ 103

3.12 Comparison of roll motion between "SIMDYN" and "IGEW model" (including dynamic heave and pitch effect) of Pram hull form in a 3-hour realization of Bretschneider spectrum with $H_s = 5\ m$ and $T_p = 13\ s$ 103

3.13 First Order Transfer Functions $f_i(\omega_e)$ 107

3.14 Second order transfer functions $u_i(\omega_e, \omega_e)$ and $v_i(\omega_e, \omega_e)$ for Linear $(i = 1)$, Cubic $(i = 3)$ and Quintic $(i = 5)$ Stiffness Coefficients 108

3.15 Comparison of $\overline{GZ}$ curve prediction in irregular waves from Volterra $\overline{GZ}$ and exact $\overline{GZ}$ methods at time $t = 350\ s$ for a wave elevation from Bretschneider spectrum with $H_s = 5.0\ m$ and $T_p = 13.0\ s$ 110

3.16 Comparison of roll motion between "SIMDYN" and "Volterra $\overline{GZ}$ model" of Pram hull form in a 3-hour realization of Bretschneider spectrum with $H_s = 5.0$ meters and $T_p = 13.0$ seconds 110

3.17 Comparison of roll spectra using different modeling techniques 111

4.1 Phase portrait for $\ddot{x} + x - x^3 = 0$ 118

4.2 Phase portrait for $\ddot{x} + 0.1\dot{x} + 0.05\dot{x}|\dot{x}| + x - x^3 = 0$ 122

4.3 Numerically computed Poincaré manifolds for $\ddot{x} + 0.1\dot{x} + 0.05\dot{x}|\dot{x}| + (1 + 0.1\sin(2t))x - x^3 = 0$ 123

4.4 Numerically computed Poincaré manifolds for $\ddot{x} + 0.1\dot{x} + 0.05\dot{x}|\dot{x}| + (1 + 0.5\sin(2t))x - x^3 = 0$ 124

4.5 $\overline{GZ}$ curve of Pram hull in case of wave crest at midship 129

4.6 $\overline{GZ}$ curve variation in waves 129

4.7 Comparison of first and second order of $\overline{GM}$ variation from Volterra $\overline{GZ}$ model for $H_s = 4\ m$ and $T_p = 13\ s$ 130

4.8 Variation of the rate of phase space flux with significant wave height H_s for various peak periods T_p 135

4.9 Variation of the rate of phase space flux with peak periods T_p for various significant wave heights H_s 135

4.10 Variation of critical significant wave height with the peak period of the spectrum 137

4.11 Variation of critical significant wave height with the peak period of the spectrum 138

5.1 Drift coefficient $m_1(E)$ for $H_s = 6.0\ m$ and $T_p = 13.0\ s$ 154

5.2 Diffusion coefficients $D_{11}(E)$ and $D_{12}(E)$ for $H_s = 6.0\ m$ and $T_p = 13.0\ s$ 154

5.3 Plot of $a_n^{(1j)}(E)$ and $b_n^{(1j)}(E)$ for $n = 1, 2$ and 3 for $H_s = 5.0\ m$ and $T_p = 13.0\ s$ 155

5.4 Plot of $a_n^{(1j)}(E)$ and $b_n^{(1j)}(E)$ for $n = 4$ and 5 for $H_s = 5.0\ m$ and $T_p = 13.0\ s$ 156

5.5 Energy drift coefficient for various H_s and a fixed chosen $T_p = 13.0\ s$ 157

5.6 Energy diffusion coefficient for various H_s and a fixed chosen $T_p = 13.0\ s$ 158

5.7 Energy drift coefficient for various T_p and a fixed chosen $H_s = 8.0\ m$ 158

5.8 Energy diffusion coefficient for various T_p and a fixed chosen $H_s = 8.0\ m$ 159

5.9 Stationary probability density function of energy E for $H_s = 6.0\ m$ and $T_p = 13.0\ s$ 161

5.10 Stationary cumulative distribution function of energy E for $H_s = 6.0\ m$ and $T_p = 13.0\ s$ 161

5.11 Comparison of mean first passage times calculated from stochastic averaging and Monte Carlo simulations for different significant wave heights and fixed peak period $T_p = 13.0\ s$ 167

5.12 Comparison of mean first passage time calculated from stochastic averaging and Monte Carlo simulations of both original and the averaged system for the case with $H_s = 8.0\ m$ and $T_p = 13.0\ s$ 169

6.1 Sensitivity of mean first passage time to significant wave height ($T_p = 13.0\ s$) 175

6.2 Sensitivity of mean first escape rate to significant wave height ($T_p = 13.0\ s$) 176

6.3 Relationship between mean first escape rate and rate of phase space flux for increasing significant wave heights ($T_p = 13.0\ s$) 177

6.4 Variation of the Lyapunov exponent with significant wave height ($T_p = 13.0\ s$) 177

6.5 Sensitivity of mean first passage time to peak period ($H_s = 6.0\ m$) . . 179

6.6 Sensitivity of mean first escape rate to peak period ($H_s = 6.0\ m$) . . 179

6.7 Relationship between mean first escape rate and rate of phase space flux for increasing peak period ($H_s = 6.0\ m$) 180

6.8 Variation of the Lyapunov exponent with peak period ($H_s = 6.0\ m$) . 180

6.9 Wave elevation and roll motion time history ($H_s = 6.0\ m, T_p = 9.0\ s$) 181

6.10 Sensitivity of mean first passage time to bilge keel width ($H_s = 6.0\ m,\ T_p = 13.0\ s$) 182

6.11 Sensitivity of drift coefficient to bilge keel width ($H_s = 6.0\ m,\ T_p = 13.0\ s$) 182

6.12 Sensitivity of diffusion coefficient to bilge keel width ($H_s = 6.0\,m,\ T_p = 13.0\ s$) 183

6.13 Sensitivity of mean first escape rate to bilge keel width ($H_s = 6.0\,m,\ T_p = 13.0\ s$) 183

6.14 Variation of the Lyapunov exponent with bilge keel width ($H_s = 6.0\ m,\ T_p = 13.0\ s$) 184

6.15 Wave elevation and roll motion time history ($H_s = 6.0\ m,\ T_p = 13.0\ s$) for bilge keel width of $0.4\ m$ 185

6.16 Sensitivity of mean first passage time to calm water $\overline{GM}_0$ ($H_s = 6.0\ m$)186

6.17 Sensitivity of mean first escape rate to calm water $\overline{GM}_0$ ($H_s = 6.0\ m$) 186

6.18 Variation of the Lyapunov exponent with calm water $\overline{GM}_0$ ($H_s = 6.0\,m$)187

C.1 Wave elevation and motions in a 3-hour irregular sea 224

C.2 Instantaneous position of hull form with respect to relative water line at $t = 4417s$ 225

D.1 Mathieu instability chart 232

D.2 Behavior of different positions on Mathieu instability chart 233

D.3 Unstable solutions at points A, B and C simulated with no quadratic damping 233

D.4 Stable solutions at points D, E and F simulated with no quadratic damping 234

D.5 Unstable solutions at points A, B and C simulated with quadratic damping 234

LIST OF TABLES

TABLE Page

2.1 Details of the Pram hull form 12

2.2 Details of the Pram hull bilge keels 48

2.3 Comparison of regular wave parametric roll tests 60

2.4 Combined statistics of 30 3-hour time histories 72

2.5 Particulars of the classic spar 74

4.1 Type of equilibrium point and its stability 120

1. INTRODUCTION

Over the past two decades, a large number of container ships and Ro-Ro vessels are being designed for higher service speeds to allow for faster transport and consequently more trade. This has led to the design of finer form hulls to minimize the calm water resistance. However, it has also made them susceptible to other forms of instability which are coming to light from the several reported incidents of large amplitude roll motion of these vessels at sea. Particularly, one such incident involving the container ship APL China in 1998 is regarded as the single worst incident of its kind. APL China was en route to Seattle from Taiwan when it encountered a typhoon in the Pacific Ocean. In order to mitigate the roll motion of the vessel, the captain ordered the vessel to turn into the waves. However, the vessel roll was amplified which led to severe hull damage and significant loss of cargo. Later it was ascertained that 406 containers were lost at sea during this incident. Later investigations [2] revealed that the severe roll motion was caused due to an instability known as the parametric roll. Over the years several instances have been reported where a variety of ship types including cruise ships, Ro-Ro vessels and container ships have experienced severe roll motion which have later been ascertained to be due to parametric instability.

The fine form ships designed to reduce the calm water resistance have a complex underwater geometry which makes them very susceptible to parametric excitation. These hulls are characterized by a large flare at the bow and a broad transom stern. When such a hull form is subjected to head on waves, the waterplane area and the instantaneous underwater volume vary considerably depending on the longitudinal location of the wave crest with respect to the hull. The time varying underwater

volume leads to a time varying roll stiffness resulting in a large amplitude parametric response.

To date, ship stability is still determined using the calm water restoring arm curve. Although this is enough for designing traditional vessels, it certainly is not for the newer generation of fine form ships. Dynamic stability plays a significant role in the design of these vessels. Therefore there is a need to augment the current intact stability rules to include dynamic stability. While many of the classification societies such as American Bureau of Shipping (ABS) and Det Norke Veritas (DNV) have come up with empirical assessment formulations for parametric resonance of ships and offshore structures in regular waves, they still recommend simulating motions in a large number of irregular wave realizations to determine the stability of a ship due to parametric excitation in a realistic ocean environment.

While the method of simulations is suitable for checking how susceptible the final design is to parametric excitation, it is not an effective way to analyze and assess design alternatives. This means that with current standards it is not possible to effectively design a vessel against parametric excitation during the iterative design process. Often by the time the final design is obtained, it is too late to change the hull form even if it is found to be susceptible to parametric roll [3, 4].

Regulatory authorities such as IMO (International Maritime Organization) and several classification societies [5] have proposed to include parametric roll as a more dangerous phenomenon than the traditional resonant roll motion in beam seas. The IMO sub-committee on Stability and Load Lines and Fishing Vessel Safety (SLF) as a part its recent meetings (SLF 55/3) has been discussing revamping the intact stability code, which is mostly limited to prescriptive static stability (based on the calm water righting arm $\overline{GZ}$ curve), to make way for the next generation of stability rules which include the assessment of dynamic failure modes including parametric

roll [6].

One of the easiest approaches to develop a stability criterion for a regulatory framework is to use analytical techniques as they can quickly provide a global picture of the phenomenon. However, the industry currently still relies heavily on prescriptive formulations or performing time domain simulations and physical model tests.

Analytical techniques have the advantage of being less time consuming than simulations and can easily be developed into a criterion for incorporation into dynamic stability rules. However, time domain simulations, besides being significantly time consuming, do not always guarantee the capture of all the critical dynamics of the system. Especially when a system is nonlinear and exhibits multiple steady state solutions, without knowing the correct initial conditions, some characteristics of the system might be completely missed if only time domain simulations are relied upon. However, the time domain simulation models do have the advantage that they can incorporate various nonlinearities and provide a more accurate prediction of the response and are not limited by simplifying assumptions which maybe a drawback of the analytical approaches.

This dissertation aims at developing simplified analytical methods for the analysis of parametric roll in irregular seas while ensuring that the simplified models are reasonably close to reality and capture the relevant dynamics. However, in order to ascertain whether a simplified model performs well or not, it must be compared against either physical model test data or numerical simulations. Available model test data, in general is limited by either the cost or the number of runs available. However, more cases can be studied using numerical simulations. Therefore, a numerical simulation tool is first developed and validated against the limited model test data. This tool is then used as a benchmark to assess the performance of the

various simplified analytical models.

While the analytical models for roll motion of a ship being subjected to beam seas have been studied extensively in the past, limited attention has been devoted to the modeling of parametric roll in irregular seas. The nonlinear modeling of time varying restoring moment in irregular waves has received very little attention and continues to be a major challenge. Although some models have been proposed for parametric roll, these are mostly limited to regular wave scenarios and are insufficient to model the phenomenon accurately in irregular waves. Using these existing models for continued analysis leads to significant differences from reality and makes the approach unreliable. In order to address this issue, a new simplified analytical model for parametric roll in irregular seas is proposed and validated. The improvements of this model over the existing models include the capturing of the actual wave elevation and dynamic heave and pitch motions in the calculation of the nonlinear restoring arm which to the author's knowledge has not been investigated before. The new proposed model is compared against the existing models and the nonlinear numerical simulation tool to show that it better represents reality than the existing models.

Using this new analytical model for parametric roll, further techniques are applied to quantitatively determine the stability of the system due to parametric excitation. Two independent stability assessment techniques are investigated. The first method is based on the nonlinear dynamical systems approach and employs the use of the Melnikov function to assess the rate at which the originally stable set of initial conditions become unstable (unbounded) when excited by parametric random excitation. The second approach is based on the stochastic dynamics approach and uses diffusion theory to analyze the probabilistic characteristics of the system when excited by random parametric excitation. Both these methods, although having a detailed

and documented theory, have mostly only been applied to the problem of direct excitation (roll motion of ships subjected to incident beam seas). Their application to the parametrically excited systems in random waves (roll motion in longitudinal seas) is a relatively new area of research and is significantly more challenging than the conventional direct excitation case.

While the above discussion has been limited to the unstable roll motion of fine form ships, a similar type of parametric instability has also been observed for spar platforms [7, 1, 8, 4]. For the spar hull forms, the instability results in large coupled heave and pitch motions and is attributed to the natural period in pitch mode coinciding with the period associated with envelope of the heave motion. This dissertation also briefly investigates this phenomenon using the time domain simulation described in chapter 2. This example also demonstrates the generic nature of the developed time domain simulation tool in terms of its applicability to analyze the dynamics of both ship shaped and non-ship shaped structures.

1.1 Overview of Dissertation

This dissertation is structured into seven chapters including the current one. Chapter 2 describes in detail the development of a nonlinear time domain simulation program [9] and describes its various aspects including:

- Large amplitudes of rotation using the Euler angles approach
- Calculating nonlinear Froude Krylov and hydrostatic forces to "exact" incident wetted surface
- Prediction of viscous roll damping for ship shaped structures
- Formulating and solving the nonlinear equation of motion in the time domain

It is well known that the added mass and radiation damping due to their dependence on frequency when transformed into the time domain result in a convolution integral involving an impulse response function (IRF). The derivation and numerical implementation of the IRF from the frequency domain hydrodynamic data is described in detail. In addition, chapter 2 also details the current industry standard approach to predict the roll damping for ship shaped structures [10]. It also details the application of the developed time domain simulation tool to simulate the phenomenon of parametric roll. These simulations are then validated against available experimental data to gain confidence that the numerical simulations are able to capture the relevant nonlinearities. After validation, the developed simulation tool is then used to analyze the statistical characteristics of parametric roll in irregular seas to demonstrate its non-Gaussian nature. It is also shown that parametric roll motion does not affect the other seakeeping modes which allows for the possibility of its analysis using a single degree of freedom model which forms the central idea of chapter 3. Finally, chapter 2 also discusses the application of the developed tool to analyze offshore structure dynamics. Particular attention is given to the problem of parametric excitation for a classic spar platform. The simulated motions of the classic spar are compared against the experimental data provided by Haslum [1] for validation.

Chapter 3 focuses on the development of a single degree of freedom analytical model for parametric roll. The existing approaches for modeling parametric roll are surveyed and critically assessed [11]. Two of the more accepted approaches - Volterra $\overline{GM}$ method and the Grim's effective wave approach are discussed in detail. Within these two methods, the Grim's effective wave approach has been more popular among researchers due to its approximation resulting in the simplification of the problem in irregular sea to that in an equivalent regular wave obtained by a least

squared fit. Although the Volterra $\overline{GM}$ method models the $\overline{GM}$ variation in "exact" irregular waves, it has received much lesser attention due to its inability to capture the time varying higher order stiffness terms (e.g. the cubic and quintic terms). A new approach for modeling the restoring arm in waves is suggested based on an extension of the Volterra $\overline{GM}$ method to overcome the limitations of the existing models. This extended approach is called the Volterra $\overline{GZ}$ method. The existing and the new methods are compared against the nonlinear time domain simulation tool developed in chapter 2 to ascertain which model represents reality most accurately. The improved Volterra $\overline{GZ}$ method is found to have the best agreement among the three models and is chosen as the candidate for further stability analysis.

Chapter 4 discusses the application of global geometric methods developed in the field of nonlinear dynamical systems [12, 13] to analyze the response of the Volterra $\overline{GZ}$ model developed in chapter 3. Even within the field of nonlinear dynamical systems, only a few methods are available where the response characteristics can be quantified without resorting to simulation. With this in mind, the Melnikov method is chosen as the approach to analyze the response characteristics. Although there are many research papers [14, 15, 16, 17] describing the application of this approach to the directly excited roll motion, little literature is available describing its application to the problem of parametric roll in irregular seas. Chapter 4 details the extension of the Melnikov approach to the problem of parametric excitation and the development of a stability measure quantifying the susceptibility of a hull form to this instability.

Chapter 5 details a semi-analytical approach from the field of stochastic dynamics to assess the stability of a system excited by parametric excitation. This technique begins by averaging the roll equation of motion which leads to approximating the energy of the system as a Markov process [18]. This opens the door to a variety of analysis techniques applicable to Markov process to be extended to the roll motion

system of equations. Similar to the Melnikov approach discussed in chapter 4, this technique too has been applied extensively to study directly excited roll motion [19, 20, 21, 17]. However, the parametrically excited roll motion analysis using this technique is more complicated than the directly excited system analysis. The intricacies of application to parametrically excited systems is discussed in detail in chapter 5. Particularly attention is given to the estimation of mean first passage time calculation which is used as a measure to quantify the stability of the system.

Chapter 6 compares the two independent methods developed in chapter 4 and chapter 5 to demonstrate the similarity between them. This comparison also demonstrates a cross check of the two methods and may give more confidence to a designer. Chapter 6 also details the results of a sensitivity analysis performed to compare the trends of the two methods as various parameters of the system are changed. This study not only allows comparison of the two methods but also demonstrates that the stability trends observed due to the variation of parameters of the system by the two methods are in agreement.

Finally chapter 7 summarizes the contributions of the dissertation and briefly discusses the future directions which can be pursued in this area. It also provides an overview and a global picture of how the developments of this dissertation are in line with the current efforts by the International Maritime Organization (IMO) towards a new generation of stability assessment rules.

2. NONLINEAR TIME DOMAIN SIMULATION* †

The motion of a ship or offshore structure in waves has always been a fascinating problem for the naval architect. In the past, before the advent of computers, the study of motions of a ship were primarily restricted to model scale experiments [22]. With the advent of computers and high computational power it became possible to simulate the motions of a ship/offshore platform. The advantages of a simulation over the experiments include not only the lesser physical effort but also the quicker estimation of stability and the possibility of testing many more loading conditions. However, the simulations do have a drawback of including simplifying assumptions to make the problem tenable. These assumptions in some cases may render the model incapable of simulating certain dynamic phenomena which are otherwise observed in reality. A classic example of this is the inability of the linear hydrodynamic theory to simulate the parametric rolling of ships.

One of the first approaches used in the study of seakeeping was to divide the ship into a number of strips along the length and study the dynamics of each strip independently and then combine the effect of all strips to predict the dynamics of the 3-dimensional (3D) ship/platform. This idea known as the strip theory reduces the issue of motion prediction from a 3D problem to a 2D one. A number of approaches were developed based on this idea by various researchers including Salvesen et al. [23], Newman [24], Ogilvie and Tuck [25], Journee [26], Beck and Troesch [27] etc. However, the approach adopted by Salvesen et al. [23] has by far been the most

*Part of this chapter is reprinted with permission from "Large-amplitude time-domain simulation tool for marine and offshore motion prediction", 2015. Marine Systems and Ocean Technology, 10(1), pp 1-17, Copyright 2015 by Sociedade Brasileira de Engenharia Naval

†Part of this chapter is reprinted with permission from "An overview of the prediction methods for roll damping of ships", 2015. Ocean Systems Engineering, 5(2), pp 55-76, Copyright 2015 by Techno-Press, Ltd.

successful and is still widely used by the industry.

The primary drawback of the strip theory method is its inapplicability to full-form ships (e.g. tankers) which violate the slender body assumption. Other issues include poor predictions in high Froude numbers and in following sea cases. These drawbacks paved way for the 3D ship motion prediction theory which did not suffer from the slender body approximation.

With the advancement of computational power in the 1980s it became possible to solve the 3D ship motion problem by the use of 3D panel methods. The 3D panel methods do not suffer from the slender body approximation and are applicable to a wider range of vessel types and loading conditions. The earlier methods attempted to solve the problem in the frequency domain. The broad family of 3D panel methods can further be classified into two categories. The first is the Rankine source approach which requires discretization of both the body and the free surface (e.g. Nakos and Sclavounos [28]) and the other is the Green function method which requires discretization of only the underwater hull form (e.g. Lee and Newman [29]).

The Green function method has the advantage of requiring panels only on the body surface and hence has become more popular. This method for the zero speed case uses the zero speed 3D Green function and has become the industry standard in the design of offshore structures (e.g. Faltinsen [30]). The forward speed case requires the calculation of the forward speed Green function which is significantly difficult to evaluate numerically. However, based on the theory developed by Salvesen et al. [23] it is possible to use the zero speed Green function to predict the vessel motions in slow and moderate forward speeds with reasonable accuracy [31]. Eventually the complexity of the frequency domain problem in forward speed case led researchers to explore the possibility of solving the ship motions problem using a transient time domain Green function. The notable contributors to this approach include Liapis

[32], King [33], Lin and Yue [34], Magee [35], Bingham [36], Beck [37] and Sen [38].

Although much research has been performed in the area of ship motion prediction, there is still no standard time domain simulation tool, which is available to all the researchers. This chapter aims to document the complete development of such a tool which can then be used as a starting point to investigate other research problems in the area of ship motions (e.g. parametric rolling of ships in irregular waves [39]).

In this work, instead of developing a time domain Green function based simulation tool [40], the radiation and scattering force results are obtained from a frequency domain computer program - "MDLHYDROD" - developed by Guha and Falzarano [41] (later extended by Somayajula et al. [42] and Guha and Falzarano [31]). Using these results as inputs, a nonlinear time domain simulation tool has been developed [9]. This tool includes the capability of solving the nonlinear Euler equations of motion valid for large amplitudes of translation and rotation. While the linear radiation and scattering forces are retained from the frequency domain program, the nonlinearities are included in the incident (Froude-Krylov forces), restoring (hydrostatic) and inertial forces.

For the purpose of simulation, a standard hull form i.e. the APL China with minor modifications (Pram hull form) is chosen. The APL China is known to exhibit parametric rolling [2] and is chosen specifically to demonstrate the capability of the developed tool to simulate the complex nonlinear phenomenon of parametric rolling. The particulars of the ship used are shown in Table 2.1 and its body plan is shown in Figure 2.1. The geometry file for Pram hull is provided as a supplementary file and is detailed in appendix H.

Table 2.1: Details of the Pram hull form

Particulars	**Value**
Length between perpendiculars L_{pp} (m)	262.00
Breadth B (m)	40.00
Depth D (m)	24.45
Mean Draft T (m)	12.32
Displacement $\Delta = \rho\nabla$ (tonnes)	76056.00
Vertical Center of Gravity $\overline{KG}$ (m)	18.32
Metacentric Height $\overline{GM}$ (m)	1.973
Roll Natural Period T_n (sec)	22.78

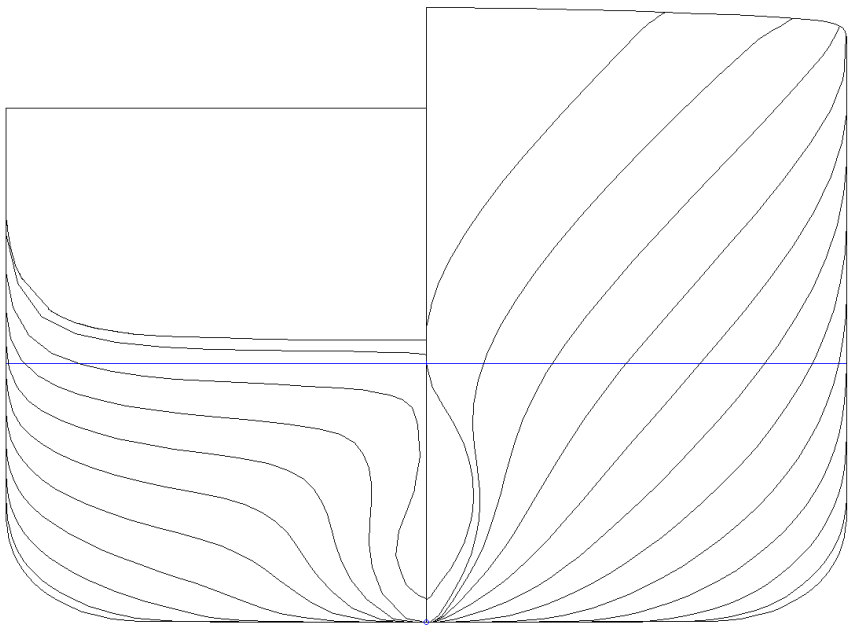

Figure 2.1: Body plan of the Pram hull form

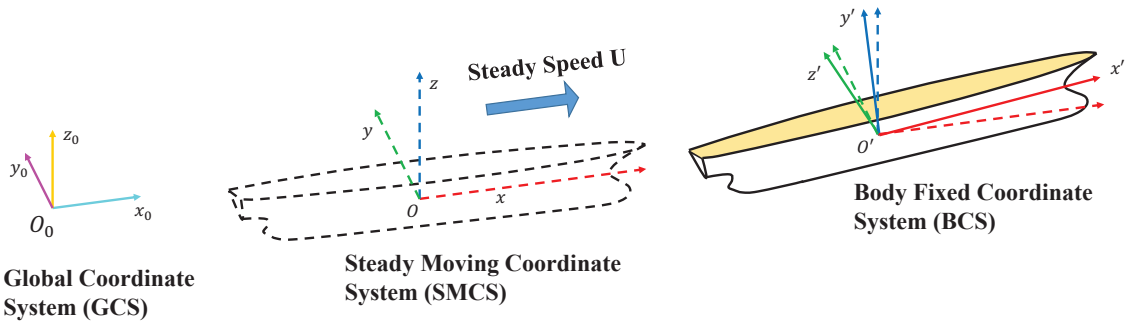

Figure 2.2: Description of coordinate systems

2.1 Coordinate System

Formulating the equations of motion of bodies undergoing large angles of rotation requires defining the right set of coordinate systems and understanding how a vector in one is expressed in the other. The nonlinear equations of motion for a general body have been defined in a number of references like Vugts [43], Abkowitz [44] and Lewandowski [45]. In this work we follow an approach based on the method adopted by Ogilvie [46]. Three coordinate systems are defined and are shown in Figure 2.2.

Global Earth Fixed Coordinate System (GCS) $O_0x_0y_0z_0$ is the global coordinate system and is fixed to the earth. The coordinates of any general point in GCS are specified by the vector $\boldsymbol{x_0} = (x_0, y_0, z_0)$.

Steady Moving Coordinate System (SMCS) $Oxyz$ moves with a constant velocity $\boldsymbol{U} = U\hat{i} + 0\hat{j} + 0\hat{k}$ with respect to GCS. The coordinates of a point in SMCS are given by the vector $\boldsymbol{x} = (x, y, z)$.

Body Fixed Coordinate System (BCS) $O'x'y'z'$ is fixed with the body and changes orientation as the body undergoes translation and rotation. When the ship is moving steadily with velocity $\boldsymbol{U}$, the BCS coincides with the SMCS. The coordinates of a point in BCS are given by the vector $\boldsymbol{x'} = (x', y', z')$.

While GCS and SMCS are inertial frames of reference, BCS is a non-inertial frame of reference. At any time instant, the translation of the body is defined by the vector from the origin of SMCS to the origin of BCS and the rotation of the body is defined by the difference in orientation of the two coordinate systems. For a body moving steadily with forward speed without any external excitation (waves and current) the origin of BCS and SMCS are coincident.

Let $\boldsymbol{x}$ and $\boldsymbol{x'}$ denote the position vectors of an arbitrary point in SMCS and BCS respectively. When the body is at rest or moving steadily with forward speed, $\boldsymbol{x}$ and $\boldsymbol{x'}$ are the same vector (assuming that the sinkage and trim in case of the steady forward speed are negligibly small). However, when subjected to dynamic excitation (waves and current), the BCS due to its translation and rotation with the body is no more coincident with SMCS. Let the position of BCS origin with respect to SMCS origin be given by $\boldsymbol{\xi} = (\xi_1, \xi_2, \xi_3) = \xi_1\hat{\imath} + \xi_2\hat{\jmath} + \xi_3\hat{k}$. Then the position vectors of an arbitrary point in the two coordinate systems can be related by a linear transformation as shown in (2.1)

$$\boldsymbol{x'} = R(\boldsymbol{x} - \boldsymbol{\xi}) \tag{2.1}$$

where R is the rotation matrix to rotate the vector in SMCS coordinate system into BCS orientation. Although the infinitesimal rotations commute, finite rotations do not and require a specification of the order of rotations. In this work we follow the convention of roll, pitch and yaw as specified by Ogilvie [46].

For convenience of understanding let us consider a case where the origins of the SMCS and BCS are coincident (no translation). Define a new coordinate system $O\bar{x}\bar{y}\bar{z}$ that is identical to SMCS except for a rotation of ξ_4 radians about x-axis of SMCS (see Figure 2.3a). In this new coordinate system $O\bar{x}\bar{y}\bar{z}$, the vector $\boldsymbol{x}$ in SMCS

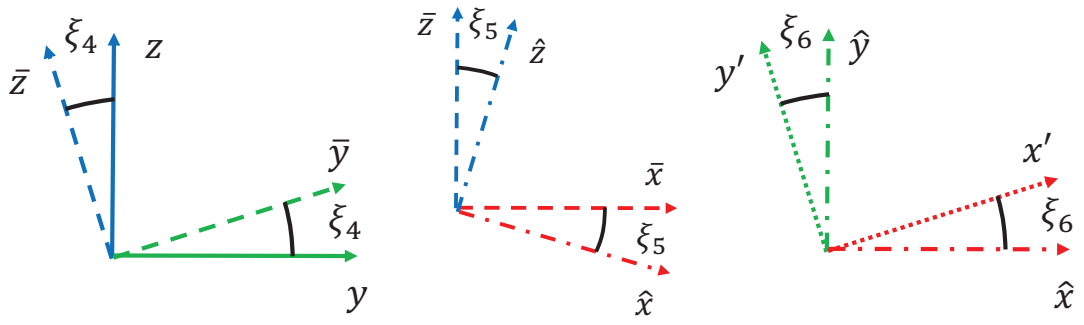

(a) Roll (b) Pitch (c) Yaw

Figure 2.3: Transformation from SMCS to BCS using Euler angles

is given by

$$\bar{\boldsymbol{x}} = R_1 \boldsymbol{x} \tag{2.2}$$

where

$$R_1 = \begin{bmatrix} 1 & 0 & 0 \\ 0 & \cos(\xi_4) & \sin(\xi_4) \\ 0 & -\sin(\xi_4) & \cos(\xi_4) \end{bmatrix} \tag{2.3}$$

Now we consider a second coordinate system $O\hat{x}\hat{y}\hat{z}$ obtained by rotation of $O\bar{x}\bar{y}\bar{z}$ by ξ_5 radians about the $\bar{y}$-axis (see Figure 2.3b). The vector $\boldsymbol{x}$ in this new system is given by

$$\hat{\boldsymbol{x}} = R_2 \bar{\boldsymbol{x}} = R_2 R_1 \boldsymbol{x} \tag{2.4}$$

where

$$R_2 = \begin{bmatrix} \cos(\xi_5) & 0 & -\sin(\xi_5) \\ 0 & 1 & 0 \\ \sin(\xi_5) & 0 & \cos(\xi_5) \end{bmatrix} \tag{2.5}$$

Finally rotating the coordinate system $O\hat{x}\hat{y}\hat{z}$ by ξ_6 radians about the $\hat{z}$-axis (see Figure 2.3c), brings the resulting system into BCS orientation. Thus the position vector in BCS is given by

$$\boldsymbol{x}' = R_3\hat{\boldsymbol{x}} = R_3R_2R_1\boldsymbol{x} = R\boldsymbol{x} \tag{2.6}$$

where

$$R_3 = \begin{bmatrix} \cos(\xi_6) & \sin(\xi_6) & 0 \\ -\sin(\xi_6) & \cos(\xi_6) & 0 \\ 0 & 0 & 1 \end{bmatrix} \tag{2.7}$$

$$R = R_3R_2R_1 = \begin{bmatrix} c_5c_6 & (c_4s_6 + s_4s_5c_6) & (s_4s_6 - c_4s_5c_6) \\ -c_5s_6 & (c_4c_6 - s_4s_5s_6) & (s_4c_6 + c_4s_5s_6) \\ s_5 & -s_4c_5 & c_4c_5 \end{bmatrix} \tag{2.8}$$

where the short hand notation $c_i = \cos(\xi_i)$ and $s_i = \sin(\xi_i)$ for $i = 4, 5, 6$ has been used. Each of the rotation matrices R_1, R_2, R_3 and R are orthogonal. This means that the inverse of the rotation matrix R is given by its transpose R^T. If the origins of SMCS and BCS are not coincident (finite translation $\boldsymbol{\xi}$) then the position vector $\boldsymbol{x}$ in SMCS may be related to the corresponding position vector $\boldsymbol{x}'$ in BCS as

shown in (2.1). However, the rotation matrix is still given by (2.8).

The angular velocity $\boldsymbol{\omega}'$ of the body in the BCS can also be derived in terms of the Euler angles (ξ_4, ξ_5, ξ_6) and their derivatives $(\dot{\xi_4}, \dot{\xi_5}, \dot{\xi_6})$ as shown below.

$$\boldsymbol{\omega}'_{roll} = R_3 R_2 R_1 \begin{Bmatrix} \dot{\xi_4} \\ 0 \\ 0 \end{Bmatrix} = \begin{Bmatrix} c_5 c_6 \dot{\xi_4} \\ -c_5 s_6 \dot{\xi_4} \\ s_5 \dot{\xi_4} \end{Bmatrix} \tag{2.9}$$

$$\boldsymbol{\omega}'_{pitch} = R_3 R_2 \begin{Bmatrix} 0 \\ \dot{\xi_5} \\ 0 \end{Bmatrix} = \begin{Bmatrix} s_6 \dot{\xi_5} \\ c_6 \dot{\xi_5} \\ 0 \end{Bmatrix} \tag{2.10}$$

$$\boldsymbol{\omega}'_{yaw} = R_3 \begin{Bmatrix} 0 \\ 0 \\ \dot{\xi_6} \end{Bmatrix} = \begin{Bmatrix} 0 \\ 0 \\ \dot{\xi_6} \end{Bmatrix} \tag{2.11}$$

$$\boldsymbol{\omega'} = \boldsymbol{\omega}'_{roll} + \boldsymbol{\omega}'_{pitch} + \boldsymbol{\omega}'_{yaw} = \begin{Bmatrix} c_5 c_6 \dot{\xi_4} + s_6 \dot{\xi_5} \\ -c_5 s_6 \dot{\xi_4} + c_6 \dot{\xi_5} \\ s_5 \dot{\xi_4} + \dot{\xi_6} \end{Bmatrix} \tag{2.12}$$

Similar to the position vectors, the angular velocity $\boldsymbol{\omega}$ in the SMCS is also related

to the BCS angular velocity $\boldsymbol{\omega'}$ by the rotation matrix R.

$$\begin{aligned}\boldsymbol{\omega} &= R^T\boldsymbol{\omega'} \\ &= \begin{bmatrix} c_5c_6 & (c_4s_6 + s_4s_5c_6) & (s_4s_6 - c_4s_5c_6) \\ -c_5s_6 & (c_4c_6 - s_4s_5s_6) & (s_4c_6 + c_4s_5s_6) \\ s_5 & -s_4c_5 & c_4c_5 \end{bmatrix}^T \begin{Bmatrix} c_5c_6\dot{\xi_4} + s_6\dot{\xi_5} \\ -c_5s_6\dot{\xi_4} + c_6\dot{\xi_5} \\ s_5\dot{\xi_4} + \dot{\xi_6} \end{Bmatrix}\end{aligned} \tag{2.13}$$

$$\boldsymbol{\omega} = \begin{Bmatrix} \dot{\xi_4} + \dot{\xi_6}s_5 \\ \dot{\xi_5}c_4 - \dot{\xi_6}s_4c_5 \\ \dot{\xi_5}s_4 + \dot{\xi_6}c_4c_5 \end{Bmatrix} \tag{2.14}$$

2.2 Equations of Motion

Motion of any general rigid body is governed by the Newton's 2^{nd} law of motion (conservation of linear and angular momentum). The analysis of rigid motions is performed by dividing it into two parts:

1. The entire mass of the body is assumed to be concentrated at the center of gravity, G. The application of Newton's 2^{nd} law gives equations describing the translational motion of G as if the body were just a point mass.

2. Application of Newton's 2^{nd} law to the angular momentum of the body gives the equations describing the rotational motion of the body.

Let $\boldsymbol{x_G}$ denote the instantaneous location of the center of gravity of the vessel in SMCS. It may be related to the location of center of gravity in BCS by

$$\boldsymbol{x_G} = \boldsymbol{\xi} + R^T\boldsymbol{x_G}' \tag{2.15}$$

Differentiating (2.15) and using the identity that $\dot{R}^T R(\boldsymbol{x_G} - \boldsymbol{\xi}) = \boldsymbol{\omega} \times (\boldsymbol{x_G} - \boldsymbol{\xi})$, the translation equation of motion may be expressed in vector form as (2.18) where m represents the mass of the vessel and $\boldsymbol{F}$ represents the external force on the body in SMCS.

$$\dot{\boldsymbol{x}}_G = \dot{\boldsymbol{\xi}} + \boldsymbol{\omega} \times (\boldsymbol{x_G} - \boldsymbol{\xi})] \tag{2.16}$$

$$\ddot{\boldsymbol{x}}_G = \ddot{\boldsymbol{\xi}} + \dot{\boldsymbol{\omega}} \times (\boldsymbol{x_G} - \boldsymbol{\xi}) + \boldsymbol{\omega} \times [\boldsymbol{\omega} \times (\boldsymbol{x_G} - \boldsymbol{\xi})] \tag{2.17}$$

$$m\ddot{\boldsymbol{x}}_G = m[\ddot{\boldsymbol{\xi}} + \dot{\boldsymbol{\omega}} \times (\boldsymbol{x_G} - \boldsymbol{\xi}) + \boldsymbol{\omega} \times [\boldsymbol{\omega} \times (\boldsymbol{x_G} - \boldsymbol{\xi})]] = \boldsymbol{F} \tag{2.18}$$

The conservation of angular momentum ($\boldsymbol{L}$) about the SMCS may be expressed as

$$\frac{d\boldsymbol{L}}{dt} = \boldsymbol{M_G} \tag{2.19}$$

where $\boldsymbol{M_G}$ is the external applied moment about the center of gravity G and can be expressed in terms of the external applied force and moment about SMCS origin as shown in (2.20).

$$\boldsymbol{M_G} = \boldsymbol{M} - \boldsymbol{x_G} \times \boldsymbol{F} \tag{2.20}$$

Let $\boldsymbol{L}'$ denote the angular momentum of the body about the BCS. Note that $\boldsymbol{L}'$ and $\boldsymbol{L}$ represent the same vector in different coordinate systems and are related by

$\boldsymbol{L}' = R\boldsymbol{L}$. Using the above, (2.19) can be recast as (2.21).

$$\begin{aligned}
\boldsymbol{M} - \boldsymbol{x_G} \times \boldsymbol{F} = \frac{d\boldsymbol{L}}{dt} &= \frac{d}{dt}\left(R^T \boldsymbol{L}'\right) \\
&= R^T \dot{\boldsymbol{L}}' + \dot{R}^T \boldsymbol{L}' \\
&= R^T \dot{\boldsymbol{L}}' + \dot{R}^T R\boldsymbol{L} \\
&= R^T \dot{\boldsymbol{L}}' + \boldsymbol{\omega} \times \boldsymbol{L} \\
&= R^T \dot{\boldsymbol{L}}' + R^T(\boldsymbol{\omega}' \times \boldsymbol{L}') \qquad (2.21)
\end{aligned}$$

It is well known from rigid body mechanics that the angular momentum of a body in the BCS orientation may be expressed as $\boldsymbol{L}' = I\boldsymbol{\omega}'$ where I is the 3x3 inertia tensor given by (2.22)

$$I = \begin{bmatrix} I_x & -I_{yx} & -I_{zx} \\ -I_{xy} & I_y & -I_{zy} \\ -I_{xz} & -I_{yz} & I_z \end{bmatrix} \qquad (2.22)$$

where I_x, I_y, I_z are the second mass moments of inertia about the x,y and z axes of the BCS respectively and $I_{xy}, I_{yx}, I_{yz}, I_{zy}, I_{zx}, I_{xz}$ are the cross mass moments of inertia about the x,y and z axes of the BCS. The mathematical formulation for evaluating I_x and I_{xy} are shown in (2.23) and (2.24) respectively where μ represents the mass density.

$$I_x = I_{yy} + I_{zz} = \iiint \mu \left[(y' - y'_G)^2 + (z' - z'_G)^2\right] dV' \qquad (2.23)$$

$$I_{xy} = \iiint \mu(x' - x'_G)(y' - y'_G) dV' \qquad (2.24)$$

The others terms of the inertia tensor may be derived in a similar fashion. Note

that the inertia tensor is defined about the body fixed coordinate system and is time-invariant. Using the above and $\boldsymbol{L}' = I\boldsymbol{\omega}'$, (2.21) can be recast as

$$I\dot{\boldsymbol{\omega}}' + \boldsymbol{\omega}' \times I\boldsymbol{\omega}' = R\left[\boldsymbol{M} - \boldsymbol{x_G} \times \boldsymbol{F}\right] \tag{2.25}$$

Thus the exact Euler equations of motion for a rigid body motion in 6 degrees of freedom are given by (2.26) and (2.27).

$$m[\ddot{\boldsymbol{\xi}} + \dot{\boldsymbol{\omega}} \times (\boldsymbol{x_G} - \boldsymbol{\xi}) + \boldsymbol{\omega} \times [\boldsymbol{\omega} \times (\boldsymbol{x_G} - \boldsymbol{\xi})]] = \boldsymbol{F} \tag{2.26}$$

$$I\dot{\boldsymbol{\omega}}' + \boldsymbol{\omega}' \times I\boldsymbol{\omega}' = R\left[\boldsymbol{M} - \boldsymbol{x_G} \times \boldsymbol{F}\right] \tag{2.27}$$

These expressions are exact and are valid for arbitrary translations and large angles of rotation. These nonlinear equations of motion can be solved if the expressions for the nonlinear force $\boldsymbol{F}$ and nonlinear moment $\boldsymbol{M}$ are known. The calculation of the external forces and moments are discussed in section 2.3.

2.3 Nonlinear Force Vector Evaluation

The nonlinear force and moment vector may be combined into a single 6×1 vector and can expressed as

$$\{F\} = \begin{Bmatrix} \boldsymbol{F} \\ \boldsymbol{M} \end{Bmatrix} = \{F_D\} + \{F_{Rad}\} + \{F_V\} + \{F_{Res}\} \tag{2.28}$$

where $\boldsymbol{F}$ and $\boldsymbol{M}$ represent the force and the moment vector in SMCS respectively. The force vector can in turn be decomposed into its components - diffraction forces $\{F_D\}$, radiation forces $\{F_{Rad}\}$, viscous forces $\{F_V\}$ and restoring forces $\{F_{Res}\}$ - as shown in (2.28). The diffraction force is further composed of the incident Froude

Krylov force and the scattering force.

Traditionally, deep water waves for offshore application have always been represented using Airy's wave theory which relies on perturbation theory and is based on small wave slope approximation [47]. Thus theoretically up to the first order of perturbation, one can calculate the pressure under a wave only up to the mean water line. However, in many of the dynamic phenomenon observed in reality, the forces on the structure due to the pressures in the crest play a significant role.

It was Paulling [48] who was among the first to come up with an approximation to consider the Froude Krylov pressure up to the incident waterline instead of the mean waterline. The Froude Krylov pressure is calculated in the displaced body position and integrated over the instantaneous wetted surface under the incident wave while scattering forces and radiation forces are computed in the undisplaced position using linear hydrodynamic method. Note however that in this approach Paulling [48] still calculates the scattering forces and radiation forces using a linear frequency domain approach. Thus this method of force and moment calculation is not consistent with the perturbation approach. Although inconsistent with perturbation approach, such methods have been utilized extensively by the industry for including nonlinearity in the design and analysis of marine and offshore structures [49, 38, 50, 51].

The nonlinear Froude Krylov forces in this present work are computed using an approach similar to that adopted by Paulling [48]. The linear scattering forces and radiation forces in the present work are obtained from a Green function based frequency domain program developed by Guha [52] and later extended by Somayajula et al. [42].

2.3.1 Diffraction Forces and Moments

The diffraction force is composed of the incident Froude-Krylov component and the scattering component. Each component of the 6×1 diffraction force vector $\{F_D\}$ can be expressed as the corresponding sum of components of incident force vector $\{F_I\}$ and scattering force vector $\{F_S\}$ as shown in (2.29).

$$F_{D_j} = F_{I_j} + F_{S_j} \quad \text{for } j = 1, 2, ..., 6 \tag{2.29}$$

Incident Forces and Moments: In linear theory, the Froude-Krylov forces are obtained by integrating the linear dynamic pressure p over the linearized wetted surface area up to the calm water level $z = 0$ denoted by S_{B_0}. In this work our aim is to develop a time domain simulation tool for the analysis of parametric roll of container ships in long crested irregular seas. With that in focus, we consider only long crested unidirectional waves. The irregular wave elevation η incident at a counter clockwise angle β to the positive x-axis of the SMCS may be expressed as a superposition of regular waves as shown in

$$\eta(t, x, y) = \sum_{i=1}^{N} a_i \cos(k_i(x \cos(\beta) + y \sin(\beta)) - \omega_i t + \epsilon_i) \tag{2.30}$$

where

a_i is the amplitude of the i-th wave component

ω_i is the encounter frequency of the i-th wave component

k_i is the wave number of the i-th wave component

The linear incident Froude Krylov pressure for the wave elevation $\eta(t, x, y)$ is

given by (2.31) where the incident wave potential $\phi_I(t, x, y, z)$ is given by (2.32).

$$p(t, x, y, z) = -\rho \frac{\partial \phi_I}{\partial t}(t, x, y, z) \text{ for } z \leq 0 \tag{2.31}$$

$$\phi_I(t, x, y) = \sum_{i=1}^{N} \frac{a_i g}{\omega_i} e^{k_i z} \sin(k_i(x \cos(\beta) + y \sin(\beta)) - \omega_i t + \epsilon_i) \tag{2.32}$$

The corresponding linear Froude Krylov force and moment are given by (2.33) and (2.34) respectively.

$$\boldsymbol{F}_I = \int_{S_{B_0}} p.\boldsymbol{n} dS \tag{2.33}$$

$$\boldsymbol{M}_I = \int_{S_{B_0}} p.(\boldsymbol{x} \times \boldsymbol{n}) dS \tag{2.34}$$

where $\boldsymbol{n}$ is the normal vector pointing out of the fluid domain and $\boldsymbol{x}$ is the position vector of a point on S_{B_0} in SMCS and at any instantaneous time is given by rearranging (2.1).

In a time domain simulation, the instantaneous position and orientation of the vessel is known and hence the integrals in (2.33) and (2.34) can be performed over the instantaneous wetted surface area under the incident wave S_B instead of the mean wetted surface area S_{B_0}. Since linear theory does not provide an expression for pressure on the first order wetted surface area $S_B - S_{B_0}$, Wheeler stretching [53] is used to scale the dynamic pressure at calm water level $z = 0$ to the instantaneous

waterline $z = \eta(t, x, y)$.

$$p(t, x, y, z) = -\rho \frac{\partial \phi_I}{\partial t}(t, x, y, z - \eta) \text{ for } z \leq \eta(t, x, y) \tag{2.35}$$

$$= -\sum_{i=1}^{N} a_i g e^{k_i(z-\eta)} \sin(k_i(x\cos(\beta) + y\sin(\beta)) - \omega_i t + \epsilon_i) \tag{2.36}$$

The nonlinear Froude Krylov force is evaluated by substituting (2.35) into (2.37) and (2.38) where the integration is now performed over the instantaneous wetted surface area under the incident waterline S_B.

$$\boldsymbol{F}_I(t) = \int_{S_B} p(t, x, y, z).\boldsymbol{n} dS \tag{2.37}$$

$$\boldsymbol{M}_I(t) = \int_{S_B} p(t, x, y, z).(\boldsymbol{x} \times \boldsymbol{n}) dS \tag{2.38}$$

Scattering Forces and Moments: The scattering component is evaluated from the linear frequency domain results as shown below.

$$F_{S_j}(t) = \mathscr{F}^{-1}\left[F_{S_j}(\omega) \times \mathscr{F}\left[\eta(t)\right]\right] \tag{2.39}$$

where $\mathscr{F}[\ ]$ and $\mathscr{F}^{-1}[\ ]$ represent the Fourier and inverse Fourier transforms of arguments and $F_{S_j}(\omega)$ represents the wave force RAO for j^{th} mode of motion obtained from a standard frequency domain program [31].

Numerically, the complex discrete wave amplitudes generated from spectrum specified as input (or from a Fast Fourier Transform of wave profile in case of an user specified wave profile) are multiplied with the corresponding scattering wave force RAO from the frequency domain and an inverse Fourier transform of the resulting vector gives the scattering force/moment in the time domain.

2.3.2 Radiation Forces and Moments:

Similar to the scattering force, the radiation force vector is also computed from the frequency domain results. For a single wave excitation frequency ω, the radiation force can be expressed as shown in (2.40).

$$\{F_{Rad}\} = -[A(\omega)]\{\ddot{\xi}\} - [B(\omega)]\{\dot{\xi}\} \tag{2.40}$$

where $[A(\omega)]$ and $[B(\omega)]$ are the 6×6 frequency dependent added mass and radiation damping matrices and $\{\xi\} = [\xi_1\ \xi_2\ \xi_3\ \xi_4\ \xi_5\ \xi_6]^T$ is a 6×1 vector containing 3 translational and 3 rotational components as defined in section 2.2. However, when the excitation consists of multiple frequency components (irregular waves), the radiation force is expressed in terms of a convolution integral [54, 55] as shown below.

$$\{F_{Rad}\} = -[A(\infty)]\{\ddot{\xi}\} - [B(\infty)]\{\dot{\xi}\} - \int_{-\infty}^{t} [K(t-\tau)]\{\dot{\xi}(\tau)\}d\tau \tag{2.41}$$

$$= -[A(\infty)]\{\ddot{\xi}\} - [B(\infty)]\{\dot{\xi}\} - \int_{0}^{\infty} [K(\tau)]\{\dot{\xi}(t-\tau)\}d\tau \tag{2.42}$$

where

$[A(\infty)]$ and $[B(\infty)]$ are the 6×6 infinite frequency added mass and radiation damping matrices

$[K(\tau)]$ is the 6×6 matrix of retardation functions which are related to the frequency dependent radiation damping as shown in (2.43).

$$[K(\tau)] = \frac{2}{\pi}\int_{0}^{\infty} [B(\omega) - B(\infty)]\cos(\omega\tau)d\omega \tag{2.43}$$

The corresponding inverse relations are given by (2.44) and (2.45).

$$[B(\omega)] = [B(\infty)] + \int_0^\infty [K(\tau)] \cos(\omega\tau) d\tau \tag{2.44}$$

$$[A(\omega)] = [A(\infty)] - \frac{1}{\omega} \int_0^\infty [K(\tau)] \sin(\omega\tau) d\tau \tag{2.45}$$

These expressions are well established in theory and details of the derivation can be found in appendix A. For more in-depth discussion the reader is referred to the works of Cummins [54] and Ogilvie [55]. In zero speed case, the infinite frequency damping $B(\infty) \to 0$ and the relations between the damping and retardation function reduce to

$$[K(\tau)] = \frac{2}{\pi} \int_0^\infty [B(\omega)] \cos(\omega\tau) d\omega \tag{2.46}$$

$$[B(\omega)] = \int_0^\infty [K(\tau)] \cos(\omega\tau) d\tau \tag{2.47}$$

In case of non-zero forward speed, (2.43) is replaced by (2.48)

$$[K(\tau)] = \frac{2}{\pi} \int_0^\infty [B(\omega_e) - B(\infty)] \cos(\omega_e\tau) d\omega_e \tag{2.48}$$

where ω_e is the encounter frequency corresponding to the wave frequency ω and is given by

$$\omega_e = \omega - \frac{\omega^2 U}{g} \cos(\beta) \tag{2.49}$$

The added mass and radiation damping denote the forces and moments acting on a body on account of forced harmonic motion in calm water. Therefore in zero speed case, these quantities are independent of wave direction. However for non-zero

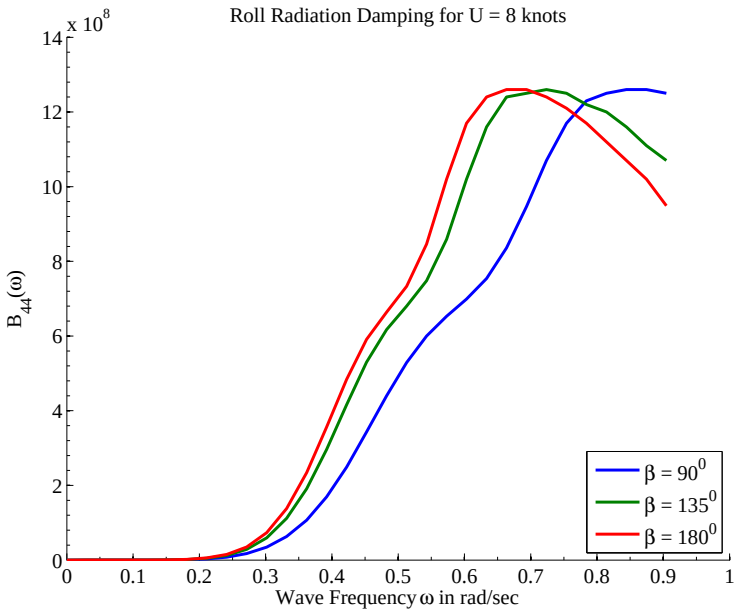

Figure 2.4: Roll radiation damping (in $\frac{Nms}{rad}$) for Pram hull at 8 knots forward speed

forward speed, due to dependence of encounter frequency on wave direction, the added mass and radiation damping are also functions of wave direction. The roll radiation damping of Pram hull at different wave headings for 8 knots forward speed is shown in Figure 2.4.

Tail Extension Although the theoretical upper limit for the integral in (2.48) is ∞, in practice the radiation damping is calculated only at a few discreetly spaced frequencies. The integral can be numerically computed only up to the maximum finite frequency for which the radiation damping is calculated using the frequency domain panel method code. This introduces a significant error in the computed impulse response function. In order to improve the accuracy, Greenhow [56] suggested that a tail approximation with two decay rates ($A\omega_e^{-2} + B\omega_e^{-4}$) be used while computing the impulse response functions. However a later study by Perez and Fossen [57] concluded that a tail proportional to ω_e^{-2} was sufficiently accurate and has been

followed in this work.

Assuming that the maximum encounter frequency at which the radiation damping has been calculated by potential theory to be $\omega_{e,max}$, the impulse response function can be expressed as a sum of two integrals as shown below.

$$[K(\tau)] = \frac{2}{\pi}\int_0^{\omega_{e,max}} [B(\omega_e) - B(\infty)]\cos(\omega_e\tau)d\omega_e + \frac{2}{\pi}\int_{\omega_{e,max}}^{\infty} [B(\omega_e) - B(\infty)]\cos(\omega_e\tau)d\omega_e \tag{2.50}$$

Now for ω_e in the range $[\omega_{e,max}, \infty)$ $[B(\omega_e) - B(\infty)]$ can be approximated by a geometrically decaying tail given by

$$[B(\omega_e) - B(\infty)] = P\omega_e^{-2} \quad \text{for} \quad \omega_e \in [\omega_{e,max}, \infty) \tag{2.51}$$

The coefficient P is obtained by ensuring the continuity at $\omega_e = \omega_{e,max}$ and is given by $P = \omega_{e,max}^2[B(\omega_{e,max}) - B(\infty)]$. Thus the integrand in the second integral in (2.50) can be replaced by (2.51). The integration over the tail is given by (2.52) where Si( ) denotes the sine integral function.

$$\begin{aligned}\frac{2}{\pi}\int_{\omega_{e,max}}^{\infty} [B(\omega_e) - B(\infty)]\cos(\omega_e\tau)d\omega_e &= \frac{2}{\pi}\int_{\omega_{e,max}}^{\infty} P\omega_e^{-2}\cos(\omega_e\tau)d\omega_e \\ &= -\frac{2P}{\pi}\left[\tau\mathrm{Si}\left(\omega_e\tau\right) + \frac{\cos(\omega_e\tau)}{\omega_e}\right]_{\omega_{e,max}}^{\infty} \\ &= \frac{2P}{\pi}\left[\tau\left(\mathrm{Si}\left(\omega_{e,max}\tau\right) - \frac{\pi}{2}\right) + \frac{\cos(\omega_{e,max}\tau)}{\omega_{e,max}}\right]\end{aligned} \tag{2.52}$$

The expression for evaluating the impulse response function when the radiation damping is calculated up to maximum discreet encounter frequency $\omega_{e,max}$ is given

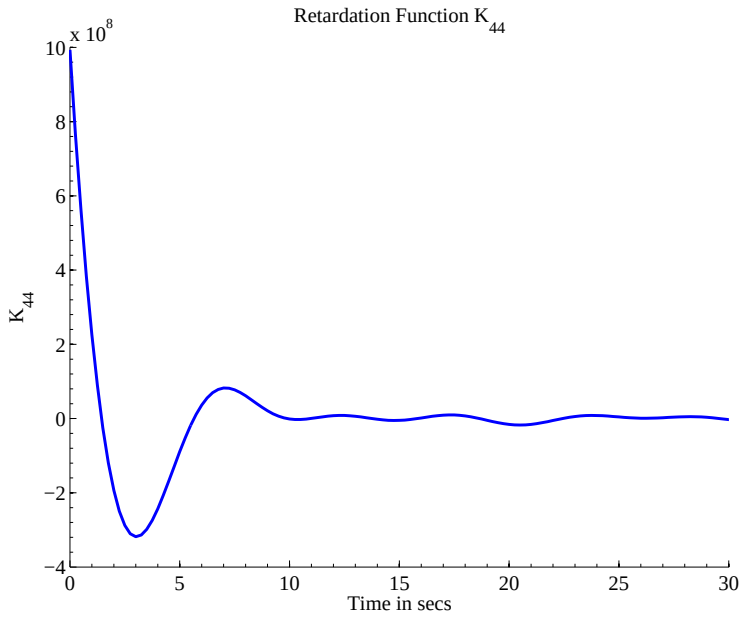

Figure 2.5: Roll retardation function (in $\frac{Nm}{rad}$) for Pram hull at 8 knots forward speed with waves incident at 180^0

by (2.53).

$$[K(\tau)] = \frac{2}{\pi}\int_0^{\omega_{e,max}} [B(\omega_e) - B(\infty)]\cos(\omega_e\tau)d\omega_e + \frac{2}{\pi}\omega_{e,max}^2[B(\omega_{e,max}) - B(\infty)] \times \left[\tau\left(\mathrm{Si}\left(\omega_{e,max}\tau\right) - \frac{\pi}{2}\right) + \frac{\cos(\omega_{e,max}\tau)}{\omega_{e,max}}\right] \tag{2.53}$$

Figure 2.5 shows the retardation function $K_{44}(\tau)$ for the Pram hull form for a forward speed case of 8 knots and incident wave direction of 180^0. As seen from (2.44), it is possible to back calculate the frequency dependent radiation damping from the retardation function to verify the validity of the transform. Figure 2.6 shows the comparison of the frequency domain roll radiation damping B_{44} with that calculated from the retardation function using (2.44). Figure 2.5 and Figure 2.6 demonstrate the equality of the radiation damping in the frequency domain to the retardation function in the time domain.

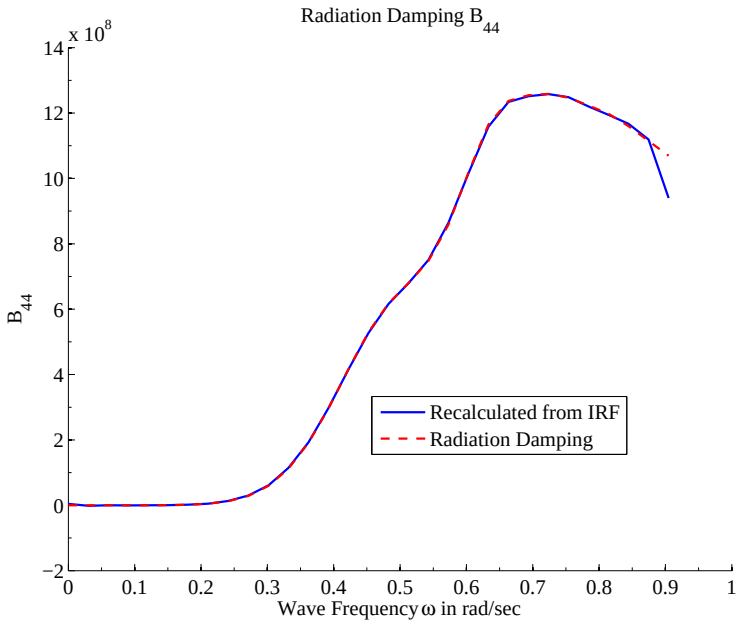

Figure 2.6: Roll radiation damping (in $\frac{Nms}{rad}$) for Pram hull at 8 knots forward speed with waves incident at 180^0

2.3.3 Restoring Forces and Moments

Similar to the Froude Krylov forces, the hydrostatic restoring forces and moments on the body are calculated over the exact instantaneous wetted surface area under the incident waterline and follow the same procedure as discussed in subsection 2.3.1. Note that the static forces which include the hydrostatic and gravitational forces on the body are considered in calculation of the restoring forces and moments. The expression for the hydrostatic pressure in calm water is given by

$$p = -\rho g z \text{ for } z \leq 0 \tag{2.54}$$

However, when computing dynamic pressure in waves up to the incident waterline, it is also important to consider the static pressure up to the same waterline. This

means that the hydrostatic pressure is given by

$$p = -\rho g z \text{ for } z \leq \eta(t, x, y) \tag{2.55}$$

This means that the hydrostatic pressure inside the crest of a wave is negative. However, this condition is required to satisfy the dynamic free surface boundary condition that the pressure on the wave crest $z = \eta(t, x, y)$ is equal to the atmospheric pressure. The corresponding nonlinear hydrostatic force and moment are given by

$$\boldsymbol{F} = \int_{S_B} -\rho g z . \boldsymbol{n} dS + \boldsymbol{W} \tag{2.56}$$

$$\boldsymbol{M} = \int_{S_B} -\rho g z . (\boldsymbol{x} \times \boldsymbol{n}) dS + \boldsymbol{x_G} \times \boldsymbol{W} \tag{2.57}$$

where $\boldsymbol{W} = -mg\hat{k}$ represents weight vector of the rigid body. Note that the integral is specified over S_B which represents the instantaneous surface area under incident waterline.

2.3.4 Viscous Forces and Moments

The importance of viscous forces in any physical phenomenon is assessed by value of the Reynolds number $R_n = \frac{UL}{\nu}$ which is the ratio of inertial to viscous forces. In the case of fluid structure interaction of ships and large offshore structures, the Reynolds number is very large $O(10^8 - 10^9)$ owing to the large characteristic length $L \approx 100 - 200\ m$ and low kinematic viscosity of water $\nu \approx 10^{-6}\ m^2/s$. This indicates that the contribution of the viscous forces and moments is insignificant to the seakeeping behavior.

Historically it has been observed from both simulations and experiments that for common ship shaped structures the roll mode of motion has very low radiation

damping at the roll natural frequency. For example consider the Pram hull form described in Table 2.1 and shown in Figure 2.1. This hull has a natural period of $T = 22.78\ s$ which corresponds to a natural frequency of $\omega_n = \frac{2\pi}{T} \approx 0.276\ rad/s$. It can be seen from Figure 2.6 that the radiation damping is extremely low at the natural frequency. This implies that the significant damping in the roll mode of motion at the resonant frequency is due to viscous effects. Thus, in order to predict the amplitude of motion at the resonance frequency it is important to include the effect of viscous damping.

Although many researchers have investigated the topic of ship roll damping since Froude's investigations [22], it was the Japanese as far back as the 1950s and even before that investigated the various aspects of ship roll damping in a systematic and detailed manner [58, 59, 60, 61]. For a more complete literature review on the subject of roll damping please refer to Falzarano et al. [10]. The empirical damping model suggested by Japanese researchers [62, 63] has become the de facto industry standard for estimating the roll damping of a ship shaped structure and is detailed below.

It is accepted that the roll damping is in general nonlinear and involves both linear and nonlinear quadratic and possibly cubic terms [64]. However for practical estimation either from experiments or empirical methods, the damping may be characterized by an effective linear damping which involves equivalent linearization.

For a regular wave case, the equivalent linearized damping is calculated by equating the energy dissipated due to the nonlinear damping. For a ship subjected to regular beam waves of frequency ω and experiencing a roll amplitude of R_0 the equivalent linearized damping B_{eq} can be related to the actual linear (B_1) and non-

linear (quadratic coefficient B_2 and cubic coefficient B_3) coefficients as shown below

$$B_{eq} = B_1 + \frac{8}{3\pi}\omega R_0 B_2 + \frac{3}{4}\omega^2 R_0^2 B_3 \tag{2.58}$$

In case of random excitation, a stochastic linearization procedure originally described by Kaplan [65] is employed. The resulting equivalent linearized damping is obtained by minimizing the error between the actual and the linearized system where both the input and output processes are assumed to be Gaussian processes. The stochastic linearization for a linear and quadratic model results in the following relation

$$B_{eq} = B_1 + \frac{8}{\pi}\sigma_{\dot{\phi}} B_2 \tag{2.59}$$

where $\sigma_{\dot{\phi}}$ is the standard deviation of the angular roll velocity. The stochastic linearization method has also been implemented in the University of Michigan SHIPMO program [27]. However, in case of parametrically excited roll motion, it is not possible to predict the standard deviation of the angular roll velocity a priori. Also it is observed that the parametric roll motion always occurs at the roll natural frequency which allows for the approximation to use the regular wave linearization at the roll natural frequency.

In the method described by Ikeda et al. [63] the equivalent linear damping B_{eq} is assumed to be composed of 5 components: wave damping B_W, skin friction damping B_F, eddy damping B_E, lift damping B_L and bilge keel damping B_{BK} as shown in (2.60). Although physically these components affect each other, their effect is

assumed to be negligible in this method [66].

$$B_{eq} = B_W + B_F + B_E + B_L + B_{BK} \tag{2.60}$$

In general it is difficult to estimate the individual components of the effective damping. However, after performing numerous experiments Ikeda et al. [63] and Himeno [62] came up with empirical relations for separately estimating each of the components. The empirical formulations for each of the components are described below. The same non-dimensionalization procedure as specified by Ikeda et al. [63] has been followed where the non-dimensional damping $\hat{B}$ and non-dimensional frequency $\hat{\omega}$ are given by

$$\hat{B} = \frac{B}{\rho \nabla B^2 \sqrt{\frac{2g}{B}}} \tag{2.61}$$

$$\hat{\omega} = \omega \sqrt{\frac{B}{2g}} \tag{2.62}$$

Note that in zero forward speed case, ω denotes the wave frequency and for non-zero forward speed it denotes the encounter wave frequency.

2.3.4.1 Wave Damping

Ikeda et al. [63] specify a formulation for predicting the forward speed wave damping from the zero speed radiation wave damping. However, the potential flow theory as described by Salvesen et al. [23] provides a theoretically accurate prediction of the forward speed added mass and radiation damping as compared to the empirical formulae specified by Ikeda et al. [63]. The research work detailed here uses the wave

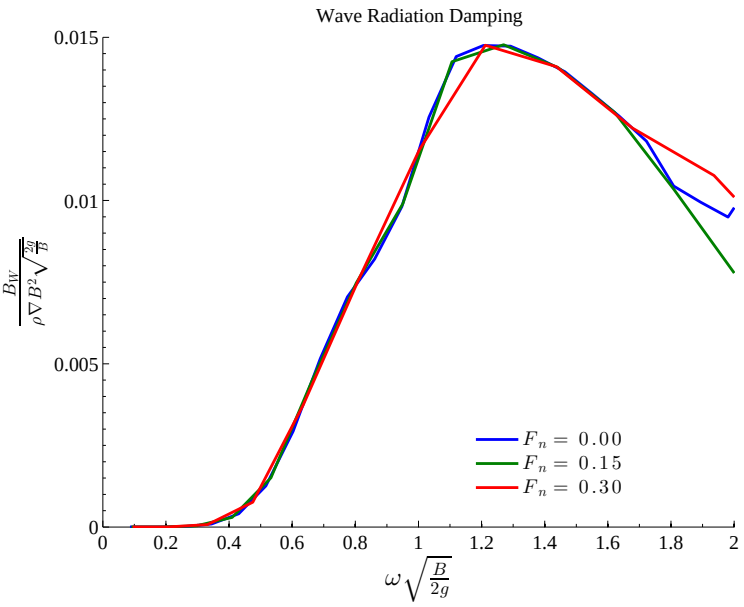

Figure 2.7: Wave damping of Pram hull from potential theory for different values of $F_n = \frac{U}{\sqrt{gL}}$

damping calculated by a panel method code whose details are described by Guha [31].

Figure 2.7 shows that the plot of radiation wave damping versus encounter wave frequency does not change for different Froude numbers. The variation of wave damping with speed is shown in Figure 2.8. Although for different values of $\hat{\omega}$ the radiation damping is different, it's variation is fairly independent of Froude number.

2.3.4.2 Skin Friction Damping

The skin friction drag is caused by the viscous skin friction stress acting on the hull surface. The empirical expression for skin friction damping coefficient for laminar

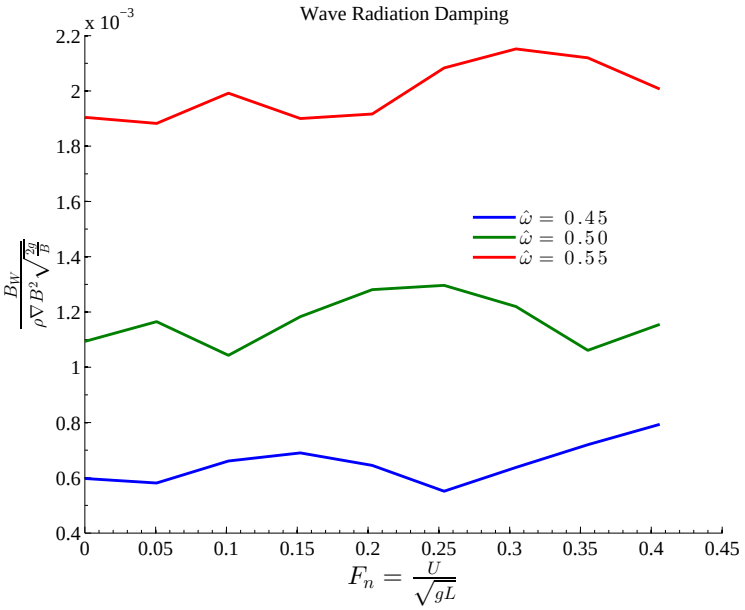

Figure 2.8: Wave damping of Pram hull from potential theory for different values of $\hat{\omega} = \omega\sqrt{\frac{B}{2g}}$

flow was provided by Kato [67] and is shown in (2.63).

$$B_{f0} = \frac{4}{3\pi}\rho S {r_e}^3 R_0 \omega C_f \tag{2.63}$$

$$C_f = 1.328\sqrt{\frac{2\pi\nu}{3.22 {r_e}^2 {R_0}^2 \omega}} \tag{2.64}$$

$$r_e = \frac{1}{\pi}\left[(0.887 + 0.145C_B)\frac{S}{L} - 2\overline{OG}\right] \tag{2.65}$$

$$S = L\left(1.7D + C_B B\right) \tag{2.66}$$

where

ρ is the density of the fluid (sea water for full scale ships and fresh water for models)

S is the wetted surface area which is empirically calculated as given by (2.66)

r_e is the effective bilge radius as given by (2.65)

R_0 is the roll amplitude

ω is the encounter frequency of excitation

C_f is the friction coefficient given by (2.64)

ν is the kinematic viscosity of fluid

C_B is the block coefficient of the ship

L is the length of the ship

B is the breadth of the ship

D is the draft of the ship

$\overline{OG}$ is the distance between the roll center of the ship and the center of gravity

Although the model is subjected to laminar flow owing to its scale, the full scale ship experiences a turbulent flow and hence (2.63) requires a correction for turbulent flow which is given by (2.67). The second term is the correction factor to account for the turbulent flow.

$$B_{f0} = 0.787\rho S {r_e}^2 \sqrt{\omega\nu} \left\{ 1 + 0.00814 \left(\frac{{r_e}^2 {R_0}^2 \omega}{\nu} \right)^{0.386} \right\} \tag{2.67}$$

For the case of roll motion of a ship moving with forward speed U, Schmitke [68] provided a modification factor as shown in (2.68).

$$B_F = B_{f0} \left(1 + 4.1 \frac{U}{\omega L} \right) \tag{2.68}$$

The variation of skin friction damping with encounter frequency and forward speed are shown in Figure 2.9 and Figure 2.10 respectively. It is worth noting that

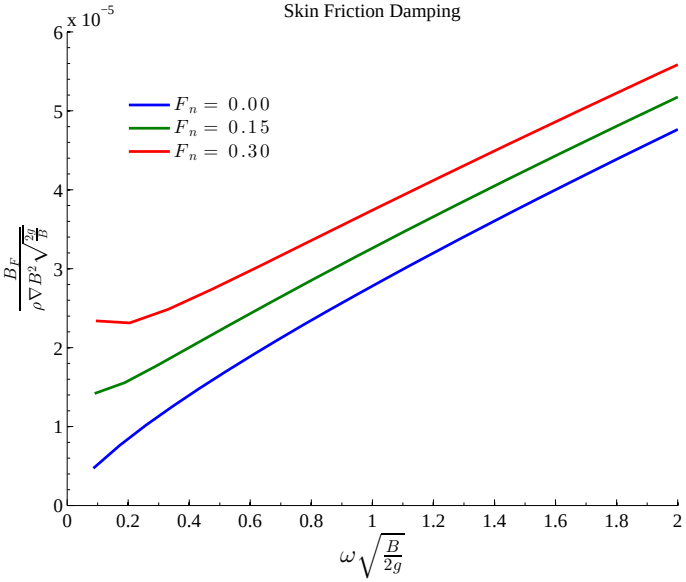

Figure 2.9: Skin friction damping of Pram hull for different values of $F_n = \frac{U}{\sqrt{gL}}$

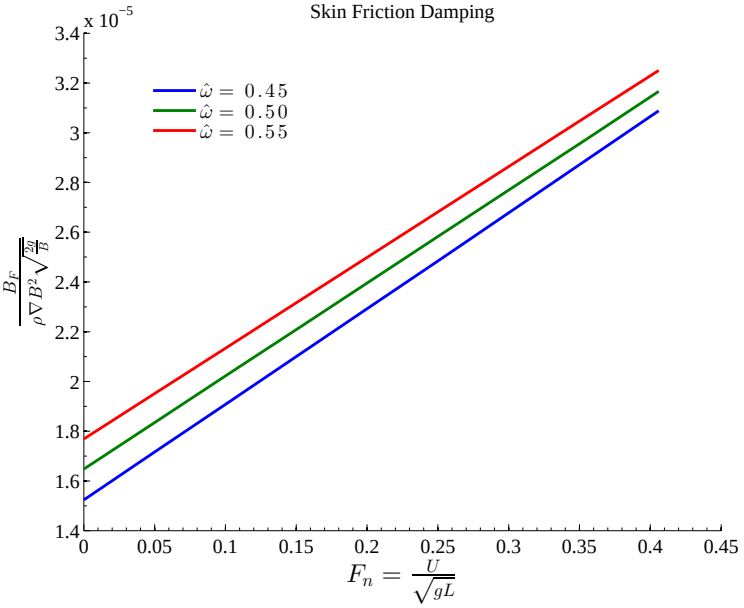

Figure 2.10: Skin friction damping of Pram hull for different values of $\hat{\omega} = \omega\sqrt{\frac{B}{2g}}$

the skin friction damping is orders of magnitude smaller than the radiation damping as is expected due to the large Reynolds number.

2.3.4.3 Lift Damping

When the ship is moving with forward speed $U > 0$, the hull appendages such as the rudder, skeg and the propeller shaft bracket act as lifting surfaces and generate both damping and exciting forces [68]. The damping moment in the roll mode is particularly significant. Ikeda et al. [63] provide a simple empirical formulation for calculating the lift component of the roll damping as shown in (2.69).

$$B_L = 0.075\rho U L D^3 k_N \left[1 - 2.8\frac{\overline{OG}}{D} + 4.667\left(\frac{\overline{OG}}{D}\right)^2\right] \tag{2.69}$$

$$k_N = 2\pi\frac{D}{L} + \kappa\left(4.1\frac{B}{L} - 0.045\right) \tag{2.70}$$

$$\begin{aligned} &\kappa = 0.0 \text{ for } C_M \leq 0.92 \\ &\kappa = 0.1 \text{ for } 0.92 \leq C_M \leq 0.97 \\ &\kappa = 0.3 \text{ for } 0.97 \leq C_M \leq 0.99 \end{aligned} \tag{2.71}$$

It may be noted from the expression in (2.69) that the lift damping coefficient varies linearly with the speed and is independent of the frequency of roll motion. This is also demonstrated by the plot of the lift damping in Figure 2.11.

2.3.4.4 Eddy Damping

The eddy damping is caused by the separation of flow and the shedding of vortices around the bottom of the ship. For slender ships, the vortices are shed from the forward and the aft regions while for a vessel with fuller shape the mid ship re-

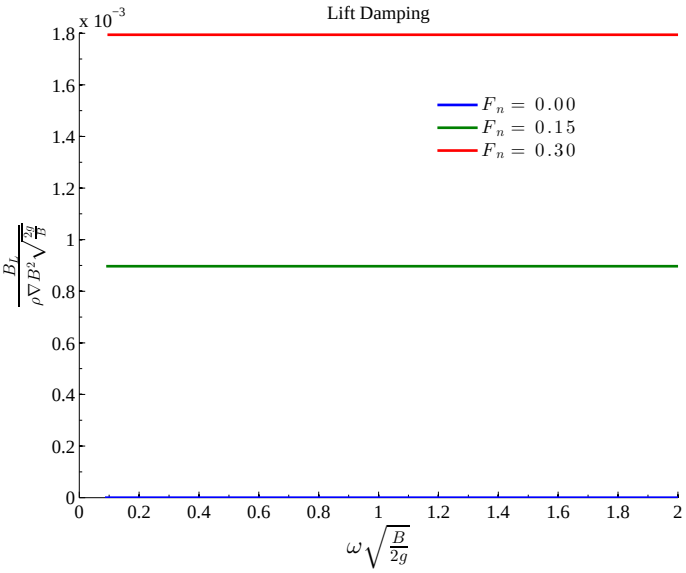

Figure 2.11: Lift damping of Pram hull for different values of $F_n = \frac{U}{\sqrt{gL}}$

gion contributes significantly to the phenomenon. There are two primary schools of thought for estimating the eddy damping. The first approach suggested by Ikeda et al. [69] is based on empirical formulae. The second approach is the vortex tracking method suggested by Standing [70], Patel and Brown [71] and Braathen and Faltinsen [72]. Although the vortex tracking method has a strong theoretical background, its application is limited to vessels with sharp bilge corner. The relatively good results achievable for square bilges is not generally achievable for rounded bilges as the separation point is no longer well defined.

In this work the first method of estimation of eddy damping is utilized. The empirical formula for estimating the eddy damping is similar to the estimation of drag force on a cylinder using a drag coefficient. The eddy damping per unit length for a cross-section is given by (2.72).

$$\frac{B_{E0}}{L} = \frac{4}{3\pi} D^4 \omega R_0 C_R \tag{2.72}$$

The 3D eddy damping coefficient is obtained by integrating $\frac{B_{E0}}{L}$ over cross-sections along the length of the ship. C_R is defined as shown in (2.73) where M_{RE} represents the eddy damping moment.

$$C_R = \frac{M_{RE}}{\frac{1}{2}\rho D^4 L\dot{\theta}|\dot{\theta}|} \tag{2.73}$$

Let H_0 and σ represent the half the beam-draft ratio and area coefficient at the underwater cross-section under consideration.

$$H_0 = \frac{B}{2D} \tag{2.74}$$

$$\sigma = \frac{A_{\text{sec}}}{BD} \tag{2.75}$$

The eddy damping moment M_{RE} is empirically estimated by

$$\begin{aligned} M_{RE} = {} & \frac{1}{2}\rho L {r_{\max}}^2 D^2 \dot{\theta}|\dot{\theta}| C_P \\ & \times \left\{ \left(1 - f_1 \frac{R_b}{D}\right)\left(1 - \frac{\overline{OG}}{D} - f_1\frac{R_b}{D}\right) + f_2\left(H_0 - f_1\frac{R_b}{D}\right)^2 \right\} \end{aligned} \tag{2.76}$$

where R_b is the bilge radius given by (2.77).

$$R_b = \begin{cases} 2D\sqrt{\frac{H_0(\sigma-1)}{\pi-4}} & \text{for } R_b < D, R < \frac{B}{2} \\ D & \text{for } H_0 \geq 1, \frac{R_b}{D} > 1 \\ \frac{B}{2} & \text{for } H_0 \leq 1, \frac{R_b}{D} > H_0 \end{cases} \tag{2.77}$$

$$f_1 = \frac{1}{2}\left[1 + \tanh\left\{20\left(\sigma - 0.7\right)\right\}\right] \tag{2.78}$$

$$f_2 = \frac{1}{2}\left(1 - \cos\left(\pi\sigma\right)\right) - 1.5\left(1 - e^{-5(1-\sigma)}\right)\sin^2\left(\pi\sigma\right) \tag{2.79}$$

The coefficient C_P is further given by

$$C_P = \frac{1}{2}\left(0.87e^{-\gamma} - 4e^{-0.187\gamma} + 3\right) \tag{2.80}$$

$$\gamma = \frac{\sqrt{\pi} f_3}{2D\left(1 - \frac{\overline{OG}}{D}\right)\sqrt{{H_0}'\sigma'}}\left(r_{\max} + \frac{2M_1}{H_1}\sqrt{{A_1}^2 + {B_1}^2}\right) \tag{2.81}$$

where ${H_0}' = \frac{H_0 D}{D - \overline{OG}}$ and $\sigma' = \frac{\sigma D - \overline{OG}}{D - \overline{OG}}$.

$$f_3 = 1 + 4e^{-1.65\times 10^5 (1-\sigma)^2} \tag{2.82}$$

$$\begin{aligned} A_1 = &-2a_3\cos\left(5\psi\right) + a_1\left(1 - a_3\right)\cos\left(3\psi\right) \\ &+ \left\{\left(6 - 3a_1\right){a_3}^2 + \left({a_1}^2 - 3a_1\right)a_3 + {a_1}^2\right\}\cos\left(\psi\right) \end{aligned} \tag{2.83}$$

$$\begin{aligned} B_1 = &-2a_3\sin\left(5\psi\right) + a_1\left(1 - a_3\right)\sin\left(3\psi\right) \\ &+ \left\{\left(6 + 3a_1\right){a_3}^2 + \left({a_1}^2 + 3a_1\right)a_3 + {a_1}^2\right\}\sin\left(\psi\right) \end{aligned} \tag{2.84}$$

$$H_1 = 1 + {a_1}^2 + 9{a_3}^2 + 2a_1\left(1 - 3a_3\right)\cos\left(2\psi\right) - 6a_3\cos\left(4\psi\right) \tag{2.85}$$

$$M_1 = \frac{B}{2\left(1 + a_1 + a_3\right)} \tag{2.86}$$

$$r_{\max} = M_1 \sqrt{\left\{(1 + a_1)\sin(\psi) - a_3 \sin(3\psi)\right\}^2 + \left\{(1 - a_1)\cos(\psi) + a_3 \cos(3\psi)\right\}^2} \tag{2.87}$$

where the coefficients a_1 and a_3 are the Lewis form parameters [73, 74] corresponding to the shape of the modified cylinder below the roll axis and ψ is given by

$$\psi = \begin{cases} \psi_1 = 0 & \text{for } r_{\max}(\psi_1) \geq r_{\max}(\psi_2) \\ \psi_2 = \frac{1}{2}\cos^{-1}\left(\frac{a_1(1+a_3)}{4a_3}\right) & \text{for } r_{\max}(\psi_1) < r_{\max}(\psi_2) \end{cases} \tag{2.88}$$

In the presence of forward speed, the eddy damping rapidly decreases according to the empirical formula (2.89).

$$B_E = B_{E0}\left[\frac{(0.04\omega L/U)^2}{1 + (0.04\omega L/U)^2}\right] \tag{2.89}$$

Figure 2.12 and Figure 2.13 show the variation of eddy damping with encounter frequency and forward speed. It is clear from these plots that the eddy damping plays an important role in the design and analysis of ship shaped offshore structures like FPSOs.

2.3.4.5 Bilge Keel Damping

The most common method to introduce more damping in the roll mode is to attach bilge keels to the hull. The damping due to bilge keels may be separated into

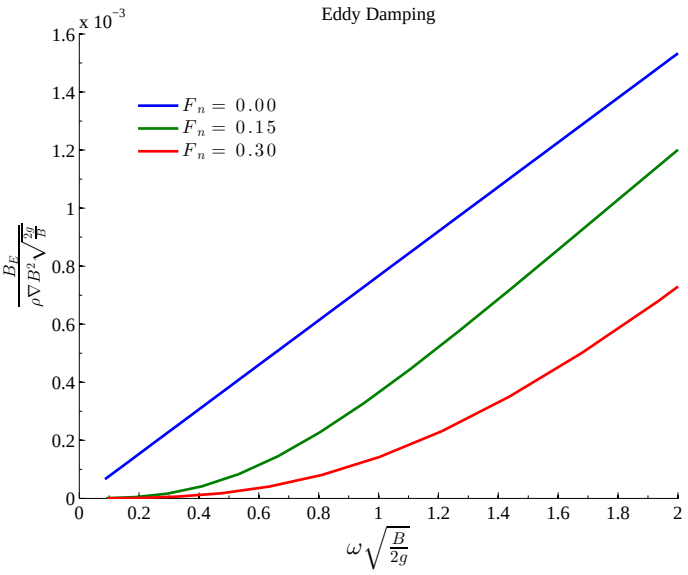

Figure 2.12: Eddy damping of Pram hull for different values of $F_n = \frac{U}{\sqrt{gL}}$

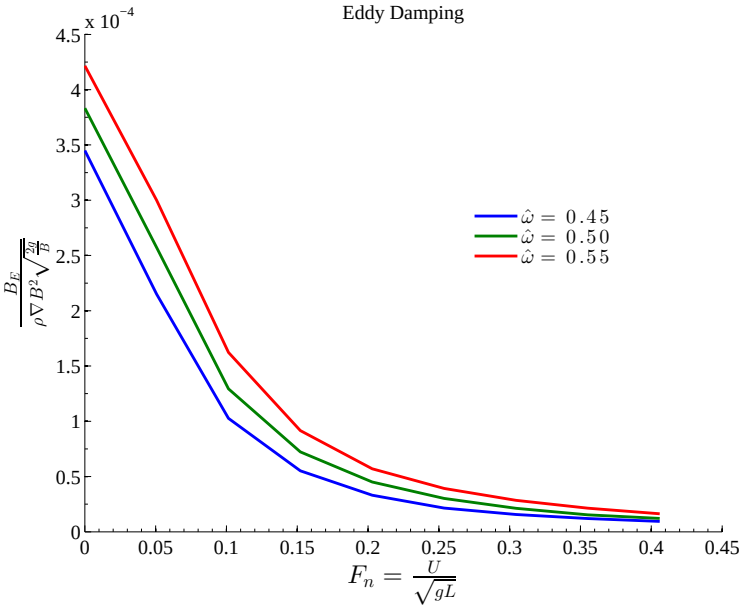

Figure 2.13: Eddy damping of Pram hull for different values of $\hat{\omega} = \omega\sqrt{\frac{B}{2g}}$

two components: normal pressure damping and hull damping.

$$B_{BK} = B_{BKN} + B_{BKH} \tag{2.90}$$

The normal component of the damping per unit length is given by

$$\frac{B_{BKN}}{L} = \frac{8}{3\pi}\rho {r_{cb}}^3 b_{BK}\omega R_0 f^2 C_D \tag{2.91}$$

where b_{BK} is the breadth of the bilge keel and r_{cb} is the mean distance from the roll axis to the bilge keel and is given by

$$r_{cb} = D\sqrt{\left\{H_0 - 0.293\frac{R_b}{D}\right\}^2 + \left\{1 - \frac{\overline{OG}}{D} - 0.293\frac{R_b}{D}\right\}^2} \tag{2.92}$$

$$f = 1 + 0.3e^{-160(1-\sigma)} \tag{2.93}$$

$$C_D = 22.5\frac{b_{BK}}{\pi r_{cb} R_0 f} + 2.4 \tag{2.94}$$

The pressure component of damping per unit length is given by

$$\frac{B_{BKH}}{L} = \frac{4}{3\pi}\rho {r_{cb}}^2 D^2 \omega R_0 f^2 \left\{-\left(-22.5\frac{b_{BK}}{\pi r_{cb} f R_0} - 1.2\right) A_2 + 1.2B_2\right\} \tag{2.95}$$

where

$$A_2 = (m_3 + m_4)\, m_8 - {m_7}^2 \tag{2.96}$$

$$B_2 = \frac{{m_3}^2}{3\,(H_0 - 0.215m_1)} + \frac{(1 - m_1)^2\,(2m_3 - m_2)}{6\,(1 - 0.215m_1)} + (m_3 m_5 + m_4 m_6)\, m_1 \tag{2.97}$$

$$m_1 = \frac{R_b}{D} \tag{2.98}$$

$$m_2 = \frac{\overline{OG}}{D} \tag{2.99}$$

$$m_3 = 1 - m_1 - m_2 \tag{2.100}$$

$$m_4 = H_0 - m_1 \tag{2.101}$$

$$m_5 = \frac{0.414H_0 + 0.0651{m_1}^2 - (0.382H_0 + 0.0106)\, m_1}{(H_0 - 0.215m_1)\,(1 - 0.215m_1)} \tag{2.102}$$

$$m_6 = \frac{0.414H_0 + 0.0651{m_1}^2 - (0.382 + 0.0106H_0)\, m_1}{(H_0 - 0.215m_1)\,(1 - 0.215m_1)} \tag{2.103}$$

$$m_7 = \begin{cases} \frac{S_0}{D} - 0.25\pi m_1 & \text{for } S_0 > 0.25\pi R_b \\ 0 & \text{for } S_0 \leq 0.25\pi R_b \end{cases} \tag{2.104}$$

$$m_8 = \begin{cases} m_7 + 0.414m_1 & \text{for } S_0 > 0.25\pi R_b \\ m_7 + m_1\sqrt{2}\left(1 - \cos\left(\frac{S_0}{R_b}\right)\right) & \text{for } S_0 \leq 0.25\pi R_b \end{cases} \tag{2.105}$$

where S_0 is the constant pressure distribution length given by

$$S_0 = 0.3\pi f r_{cb} R_0 + 1.95 b_{BK} \tag{2.106}$$

The three dimensional bilge keel damping is obtained by integrating the normal and hull components of damping over the length of the bilge keel. The details of the bilge keel of the Pram hull are listed in Table 2.2.

Table 2.2: Details of the Pram hull bilge keels

Particulars	**Value**
Length (m)	76.53
Breadth (m)	0.40
Aft end from Midship (m)	-37.265
Forward end from Midship (m)	39.265

It is observed from (2.91) and (2.95) that the bilge keel damping does not depend on the speed U and hence is invariant to changes in speed as shown in Figure 2.14. However, it does depend on the encounter frequency of oscillation ω. Higher frequency oscillations results in a larger relative velocity of water across the bilge keels which increases the damping. This effect is also illustrated in Figure 2.14.

2.3.4.6 Effective Linear Damping

Summing each of the components of roll damping results in the effective linear damping as shown in (2.60). The components and effective linear damping for $\hat{\omega} = 0.5$ are shown in Figure 2.15. It can be seen that in the case of a ship moving with moderate forward speed, the contribution due to eddy and skin friction damping is negligible. The main contribution to roll damping is due to lift forces followed by

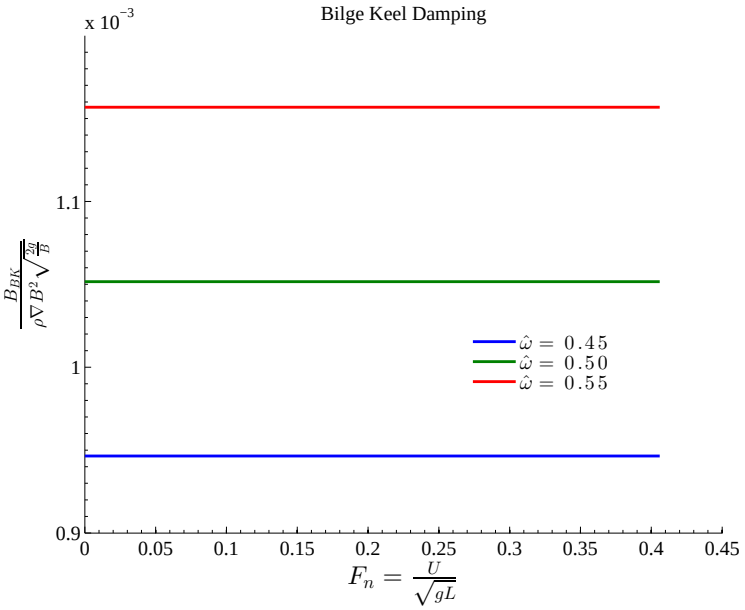

Figure 2.14: Bilge keel damping of Pram hull for different values of $\hat{\omega}$

wave and bilge keel damping.

The variation of effective damping with frequency for both zero and forward speed are illustrated in Figure 2.16 and Figure 2.17 respectively. The non-dimensional roll natural frequency $\hat{\omega}_n$ is given by (2.107).

$$\hat{\omega}_n = \frac{2\pi}{T_n}\sqrt{\frac{B}{2g}} = 0.3939 \approx 0.4 \qquad \text{for} \quad T_n = 22.78\ s \tag{2.107}$$

From Figure 2.16 and Figure 2.17 it can be seen that the damping at natural frequency ($\hat{\omega}_n \approx 0.4$) even after including the viscous effects is very small. Although the empirical method described above provides a frequency dependent damping, it is accepted practice to evaluate the viscous components at only the natural frequency. This is a reasonable assumption since the roll motion is mostly concentrated around the natural frequency.

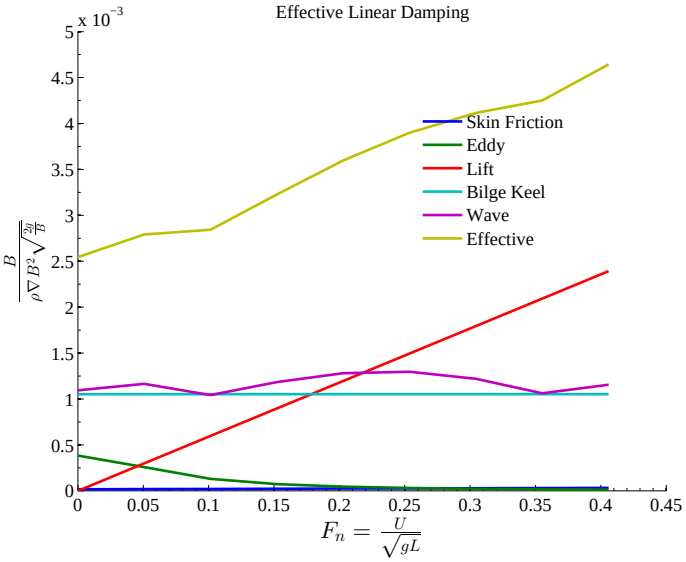

Figure 2.15: Effective linear damping and its components for Pram hull ($\hat{\omega} = 0.5$)

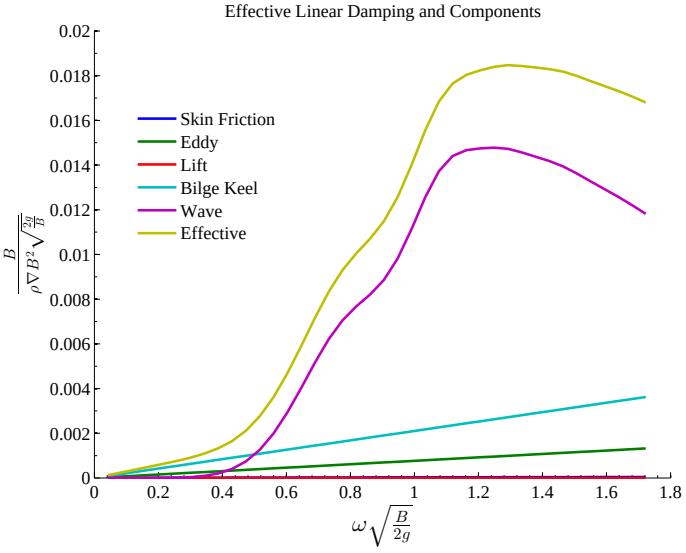

Figure 2.16: Effective linear damping for Pram hull moving with zero speed ($F_n = 0$)

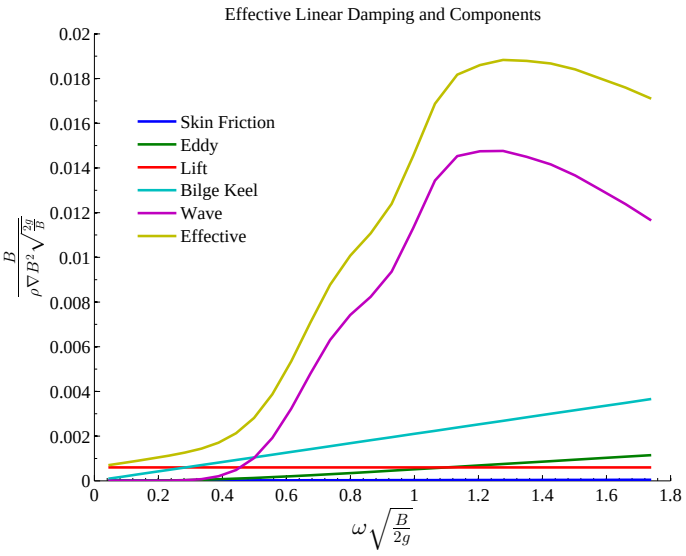

Figure 2.17: Effective linear damping for Pram hull moving with forward speed ($F_n = 0.1015$)

2.4 Integration Scheme

The equations of motion derived in (2.26) and (2.27) can be recast into the form

$$[\boldsymbol{M_a}]\{\dot{\boldsymbol{v}}\} = \{\boldsymbol{f}\} \tag{2.108}$$

where $\boldsymbol{v} = \begin{Bmatrix} \dot{\boldsymbol{\xi}} \\ \dot{\boldsymbol{\alpha}} \end{Bmatrix} = \{\dot{\xi}_1 \ \dot{\xi}_2 \ \dot{\xi}_3 \ \dot{\xi}_4 \ \dot{\xi}_5 \ \dot{\xi}_6\}^T$ is the generalized velocity vector and $\{\boldsymbol{f}\}$ is the vector formed by moving the terms of left hand side of (2.26) and (2.27) independent of acceleration to the right hand side in (2.108). The complete expressions for $\boldsymbol{M_a}$ and $\boldsymbol{f}$ have been derived in appendix B. Eqn. (2.108) is solved for the generalized velocities and displacements as follows.

$$\boldsymbol{w}_{12\times1} = \int_t \boldsymbol{h}_{12\times1}(t, \boldsymbol{w})dt \tag{2.109}$$

where $\boldsymbol{w} = \{\boldsymbol{v}^T\ \xi_1\ \xi_2\ \xi_3\ \xi_4\ \xi_5\ \xi_6\}^T$ and $\boldsymbol{h}_{12\times1}(t, \boldsymbol{w})$ is given by

$$\boldsymbol{h} = \begin{bmatrix} \boldsymbol{M_a}_{6\times6} & \boldsymbol{0}_{6\times6} \\ \boldsymbol{0}_{6\times6} & \boldsymbol{I}_{6\times6} \end{bmatrix}^{-1} \times \begin{Bmatrix} \boldsymbol{f}_{6\times1} \\ \boldsymbol{v}_{6\times1} \end{Bmatrix} \tag{2.110}$$

It is important to note that the matrix $[\boldsymbol{M_a}]$ varies with time as is shown in appendix B. Thus the matrix inversion in (2.110) needs to be computed every time step. Eqn. (2.109) can be solved by any standard numerical integration technique. Some of the popular integration schemes are Adam-Bashforth predictor corrector scheme [38] and the Runge Kutta Methods [34]. In this work the 4th order Runge-Kutta method has been employed to integrate (2.109) as shown in (2.111).

$$\boldsymbol{w}(t_{n+1}) = \boldsymbol{w}(t_n) + \frac{h}{6}(\boldsymbol{k_1} + 2\boldsymbol{k_2} + 2\boldsymbol{k_3} + \boldsymbol{k_4}) \tag{2.111}$$

$$t_{n+1} = t_n + h \tag{2.112}$$

where h denotes the time step and $\boldsymbol{k_1}$, $\boldsymbol{k_2}$, $\boldsymbol{k_3}$ and $\boldsymbol{k_4}$ are given by

$$\boldsymbol{k_1} = \boldsymbol{h}\left(t_n, \boldsymbol{w}(t_n)\right) \tag{2.113}$$

$$\boldsymbol{k_2} = \boldsymbol{h}\left(t_n + \frac{h}{2}, \boldsymbol{w}(t_n) + \frac{h\boldsymbol{k_1}}{2}\right) \tag{2.114}$$

$$\boldsymbol{k_3} = \boldsymbol{h}\left(t_n + \frac{h}{2}, \boldsymbol{w}(t_n) + \frac{h\boldsymbol{k_2}}{2}\right) \tag{2.115}$$

$$\boldsymbol{k_4} = \boldsymbol{h}\left(t_n + h, \boldsymbol{w}(t_n) + h\boldsymbol{k_3}\right) \tag{2.116}$$

2.5 Simulation of Parametric Roll

In this section, the numerical tool described in the above sections is utilized to simulate the parametric roll of APL China (Figure 2.1) in irregular head seas. For this purpose, a Bretschneider wave elevation spectrum has been chosen. The

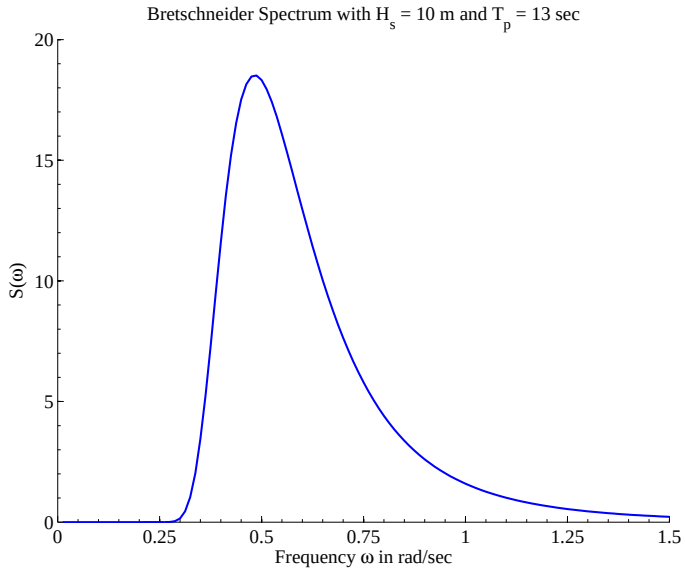

Figure 2.18: Bretschneider spectrum of wave elevation

mathematical form of the spectrum is shown in (2.117). Figure 2.18 shows the plot of Bretschneider spectrum for parameters $H_s = 10\ m$ and $T_p = 13\ s$.

$$S(\omega) = \frac{5T_p H_s^2}{32\pi}\left(\frac{2\pi}{\omega T_p}\right)^5 e^{-\frac{5}{4}\left(\frac{2\pi}{\omega T_p}\right)^4} \tag{2.117}$$

For a ship moving with forward speed U, the apparent frequency of encounter of waves ω_e as perceived by an observer aboard the ship is different from the actual frequency of the waves ω. The two frequencies can be related to each other by Doppler's theory and is shown in (2.118) where β is the wave direction measured anti-clockwise from the positive x-axis of GCS.

$$\omega_e = \omega - kU\cos\beta \tag{2.118}$$

As the problem of parametric roll mostly occurs in deep water, the wave number k can be expressed in terms of the wave frequency ω by using the deep water dispersion

relation ($\omega^2 = gk$).

$$\omega_e = \omega - \frac{\omega^2}{g} U \cos\beta \tag{2.119}$$

The effect of encounter frequency also changes the observed spectrum of the sea. However, the energy under both the original wave spectrum and the encounter wave spectrum must be the same which leads to the following expression for encounter spectrum.

$$S_e(\omega_e)|d\omega_e| = S(\omega)|d\omega| \tag{2.120}$$

$$S_e(\omega_e) = S(\omega)\left|\frac{d\omega}{d\omega_e}\right| = \frac{S(\omega)}{\left|1 - \frac{2U\cos\beta}{g}\omega\right|} \tag{2.121}$$

For obtaining a wave realization the encounter spectrum $S_e(\omega_e)$ is discretized into $N = \frac{T_{max}}{2dt}$ points where T_{max} is the simulation time and dt is the discrete time step. The discrete frequency step is given by $\Delta\omega_n = \frac{2\pi}{T_{max}}$. The irregular sea is obtained by linear superposition of N harmonic components as shown below.

$$\eta(t) = \sum_{n=1}^{N} a_n \cos(k_n(x\cos\beta + y\sin\beta) + \omega_{e,n}t + \epsilon_n) \tag{2.122}$$

where

$a_n = \sqrt{2S(\omega_n)\Delta\omega_n}$ is the amplitude of the n^{th} harmonic component

$\omega_{e,n}$ and k_n are the encounter frequency and the wave number of the n^{th} harmonic component respectively

ϵ_n is the phase of the n^{th} harmonic component and is realized from a uniform random variable varying in the range [0 2π]

This method of obtaining the wave elevation is known as the random phase method. The wave elevation described by (2.122) is only approximately Gaussian for a finite N and approaches a Gaussian process only in the limit $N \to \infty$ [75]. Based on this asymptotic convergence, Tucker et. al. [76] have argued that simulating wave elevation time series of finite length (finite N) either for the purpose of model testing or numerical simulations using the random phase method is inaccurate. In particular, Tucker et. al. [76] argued that the wave group statistics estimated from time histories generated by random phase method are not representative of a true zero mean Gaussian wave elevation process. In order to correct this inaccuracy Tucker et. al. suggested an alternate method known as the random Fourier coefficient method where the amplitude of harmonic components a_n are obtained from a Rayleigh distribution instead of the deterministic approach adopted by the random phase method. While there were disagreements about the idea that the random phase method results in large errors [77], a later numerical investigation by Elgar et. al. [78] demonstrated that when sufficiently large number of Fourier components are used to discretize the spectrum there is no statistically significant difference between the two methods. While the random Fourier coefficient method is the theoretically accurate approach to simulate a Gaussian process, the random phase method with enough number of components is statistically indistinguishable with the random Fourier coefficient method. Further, with the random phase method, certain characteristics such as the peak period of the spectrum are fixed deterministically while in the random Fourier coefficient technique these are liable to change with different realizations. In this work the random phase method is chosen to simulate the wave time histories in irregular seas. However adequate caution is taken to ensure that the number of spectral components used to simulate the wave elevation is sufficiently large ($N \approx 20000$ components for a 3-hour realization).

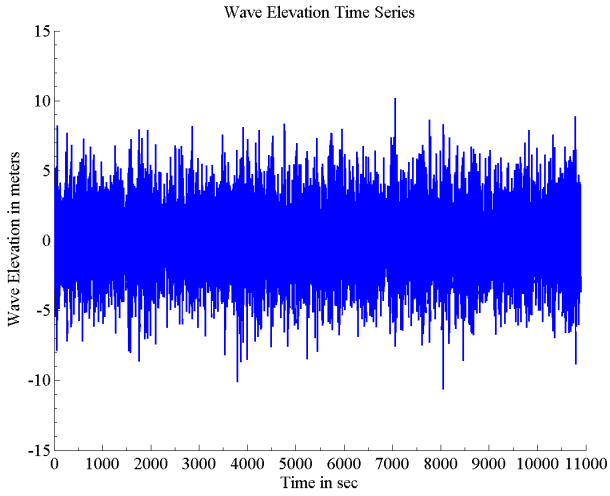

Figure 2.19: Wave realization from a Bretschneider spectrum with $H_s = 10\ m$, $T_p = 13\ s$ and $\beta = 180^0$

A 3-hour sample realization from a Bretschneider spectrum shown in Figure 2.18 using the method described above is shown in Figure 2.19. The corresponding roll motion time series calculated by nonlinear time domain simulation is shown in Figure 2.20.

2.5.1 Comparison with Linear Theory

The results from the time domain simulation are compared against the linear theory results obtained by a frequency domain program. The wave elevation comparison is shown in Figure 2.21a to demonstrate that the two programs use the same input wave elevation. The comparisons of heave, roll and pitch motions are shown in Figure 2.21b, Figure 2.21c and Figure 2.21d respectively. In all of the comparison plots, the legend "SIMDYN" corresponds to the nonlinear time domain simulation while the legend "MDLHYDROD" corresponds to the linear frequency domain results. Note that although the simulation has been performed for the entire 3-hour simulation time, only the first 500 seconds are shown in the comparisons to

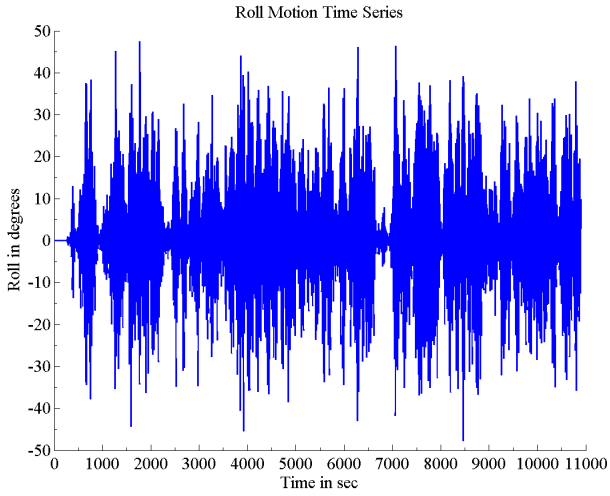

Figure 2.20: Parametric roll of Pram hull subjected to a Bretschneider spectrum with $H_s = 10\ m$, $T_p = 13\ s$ and $\beta = 180^0$

help visualize the decay of transient motion and the approach to the steady state solution.

2.5.2 Ramp Time

The time domain simulation, in general, requires a smooth ramp up of the excitation forces to avoid large transient behavior. In the current simulation a ramp time of 100 seconds has been utilized. Thus the heave and pitch motions in Figure 2.21b and Figure 2.21d are not in agreement in the ramp zone (100 seconds) but approach the steady state solution beyond the ramp time.

2.5.3 Roll Motion

It can be seen that the nonlinear heave and the pitch motions do not significantly deviate from the linear theory even when the ship is undergoing severe parametric roll. This demonstrates that the parametric roll motion has negligible effect on the heave and pitch motions. This is consistent with the conclusions of Belenky et al.

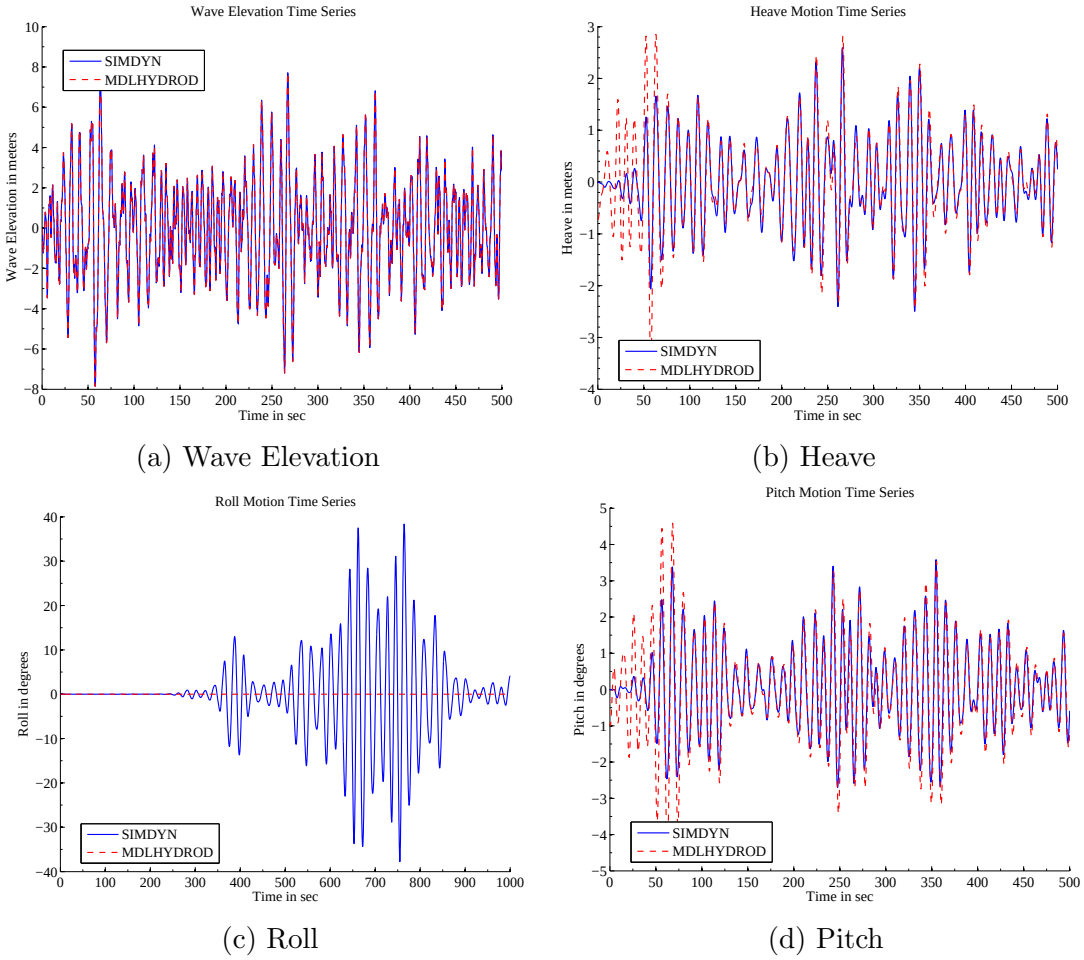

(a) Wave Elevation

(b) Heave

(c) Roll

(d) Pitch

Figure 2.21: Comparison between time domain simulation tool SIMDYN and frequency domain tool MDLHYDROD

[79] who performed multiple time domain simulations to assess the ergodicity of seakeeping motions while undergoing severe parametric resonance.

Notice however that this does not imply that the roll motion is independent of heave and pitch motions. The heave and pitch motions change the underwater hull form considerably and have a strong influence on parametric roll amplitude. More details on this are discussed in chapter 3.

2.6 Comparison with Experiments

In addition to simulating parametric roll, it is important to know that the simulations are accurate. The best method to ascertain accuracy is to compare the simulations against experimental data. In this section the numerical simulation tool is compared against the experimental data published by Silva et al. [80]. Silva et al. [80] performed experiments on Pram hull in both regular and irregular head seas.

2.6.1 Experimental and Numerical Simulation Setup

These experiments were performed in Canal de Experiências Hidrodinâmicas de El Pardo (CEHIPAR), Spain as a part of HYDROLAB III project [80]. The towing tank has a length of 150 meters, width of 30 meters, and a depth of 5 m. It is equipped with a flap type wave maker and an overhead wing carriage. A 1:65 scaled Pram hull model was used for performing parametric rolling tests. The model was held fixed in its longitudinal and transverse position by means of two actuators (combination of dynamometer and a heaving rod). The aft actuator was clamped to the carriage so that it remained vertical at all times. The forward heaving rod was attached to the carriage through a hinge connection. This allowed the model to heave, roll and pitch freely about its natural position while restricting it in surge, sway and yaw modes of motion. All the motions are output about the origin located at the midship, waterline and centerline of the ship. For all tests the model was towed at a full scale speed of 8 knots.

The displacement and the metacentric height in the full scale were specified as $\Delta = \rho\nabla = 76056$ tonnes and $\overline{GM} = 1.973$ meters respectively. The natural period has been mentioned as $T_n = 22.78$ seconds. Based on these values the roll radius of

Table 2.3: Comparison of regular wave parametric roll tests

Test	λ/L	**Height**	**Period**	**Speed**	**Roll Angle**		
		H	T	U	Expt. [80]	SIMDYN	
						Expt. Waves	Regular Waves
(-)	(-)	(m)	(sec)	(knots)	(deg)	(deg)	(deg)
5	0.8	6.0	11.59	8.0	31.0	31.2	30.2
6	1.0	6.0	12.95	8.0	23.2	24.8	23.9
7	1.2	6.0	14.19	8.0	2.0	0.1	0.2
8	1.4	6.0	15.33	8.0	0.5	0.1	0.3
9	0.8	8.0	11.59	8.0	32.8	37.1	39.5
10	1.0	8.0	12.95	8.0	25.0	33.9	24.5
11	1.2	8.0	14.19	8.0	1.7	10.6	5.8
12	1.4	8.0	15.33	8.0	0.8	0.2	0.1
13	0.8	10.0	11.59	8.0	35.7	-	41.3
14	1.0	10.0	12.95	8.0	27.3	-	24.0
15	1.2	10.0	14.19	8.0	1.3	-	0.1
16	1.4	10.0	15.33	8.0	0.6	-	0.4

gyration has been evaluated using (2.123).

$$k_{xx} = \sqrt{\frac{\left[\frac{\Delta g T_n^2 \overline{GM}}{4\pi^2}\right] - A_{44}(\omega_n)}{\Delta}} = 13.61\ m \tag{2.123}$$

where $A_{44}(\omega_n)$ is the forward speed roll added moment of inertia about the longitudinal axis through the origin (midship, waterline and centerline) and is calculated at the encounter frequency of $\omega_n = \frac{2\pi}{T_n}$ using the frequency domain program MDL-HYDROD.

2.6.2 Comparison with Experiments

The data of 12 regular wave tests and one irregular wave test in head seas ($\beta = 180^0$) were available from Silva et al. [80] and were analyzed. The regular wave test

cases spanned three different wave heights, four different wave periods and one speed as shown in Table 2.3. For each case two cases of the nonlinear time domain code (SIMDYN) have been run:

1. SIMDYN simulation has the same input wave elevation as the experimental test

2. SIMDYN simulation has a regular wave input corresponding to the case

Note that for the case of wave height $H = 10\ m$ the experimental wave time histories were unavailable and only the mean roll amplitude was available. Hence for the last four cases in Table 2.3, only the regular wave simulation results are available.

The resulting mean of the fully developed roll motion peaks from SIMDYN are listed in the last two columns of Table 2.3. Figure 2.22 shows the comparison of the mean amplitudes of parametric roll from regular wave simulations and experiments. The comparison of the roll time series from experiments and SIMDYN runs (with input of experimental wave elevation) for "Test 5" and "Test 6" are shown in Figure 2.23 and Figure 2.24 respectively.

The comparison between SIMDYN simulations and experiments for 6 meter wave height are very accurate both in terms of the roll amplitude prediction as well as the detuning effect at higher periods. However, the error in roll amplitude predictions from SIMDYN and the experiments for 8 meter and 10 meter wave heights are slightly higher. Also in the 8 meter wave height case for 14.19 second period (Test 11), SIMDYN simulations show a small parametric resonance (tuned response), while the experiments are fully detuned. This suggests that the damping model is fairly accurate for the 6 meter wave height case but is slightly incorrect for the 8 meter wave height scenario. The comparison between SIMDYN simulations and experiments for the same incident irregular wave are shown in Figure 2.25.

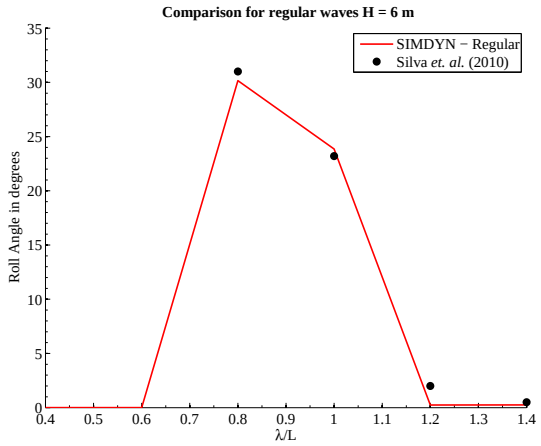

(a) 6 m wave height

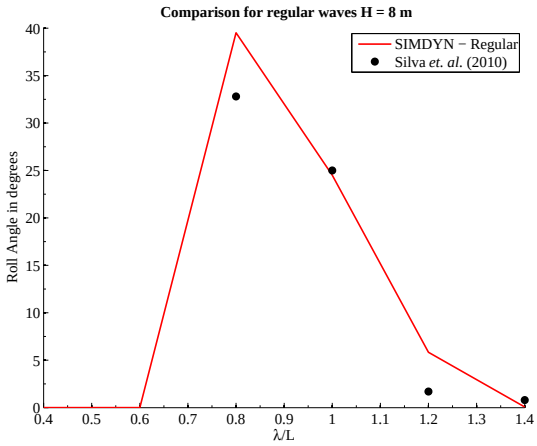

(b) 8 m wave height

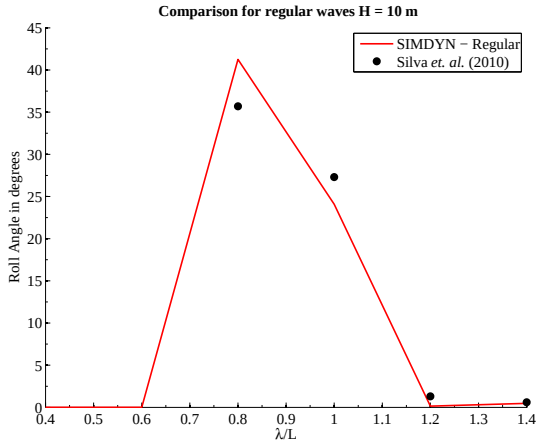

(c) 10 m wave height

Figure 2.22: Magnification curves for regular wave excitation

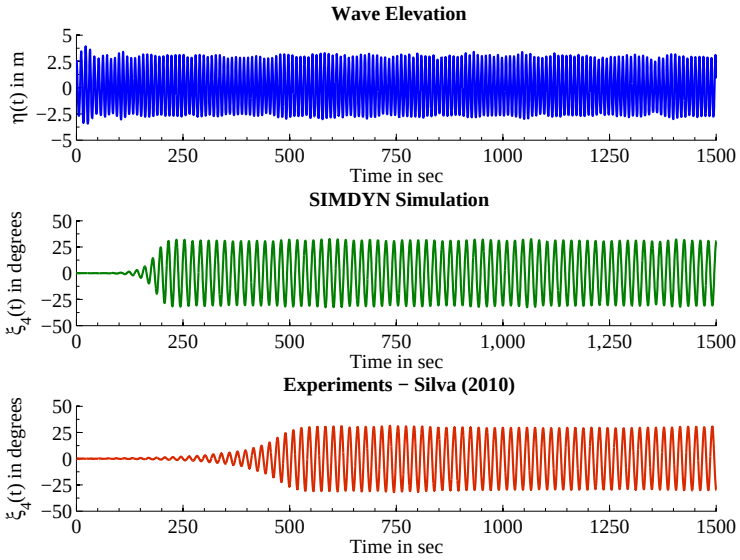

Figure 2.23: Comparison of roll motion between experimental data and SIMDYN simulation (with input of experimental wave elevation) for Test 5 listed in Table 2.3

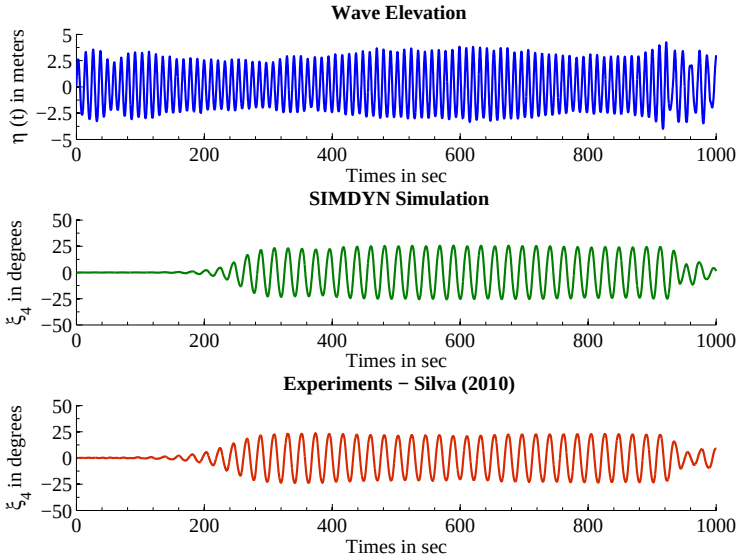

Figure 2.24: Comparison of roll motion between experimental data and SIMDYN simulation (with input of experimental wave elevation) for Test 6 listed in Table 2.3

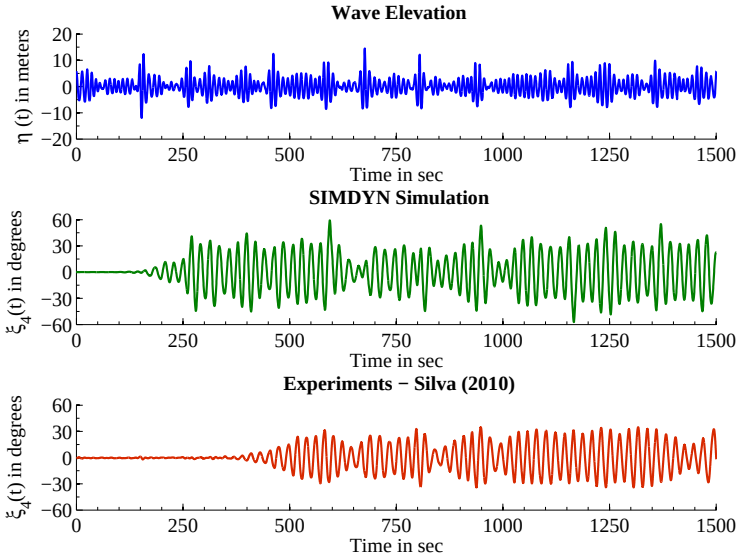

Figure 2.25: Comparison of roll motion between experimental data and SIMDYN simulation for incident irregular waves

2.6.3 Discussion

The parametric roll is caused by an instability mechanism which for the linear system results in an unbounded growth in the amplitude of roll motion. It is the nonlinear damping which bounds the amplitude by dissipating the energy of the system. This means that the final amplitude of motion is highly sensitive to both the damping model and the damping coefficients used.

The comparisons for the 6 meter wave height indicate that the empirical damping model proposed by Ikeda et al. [63] is a sufficiently accurate match to the experiments performed by Silva et al [80]. As the wave height is increased, the damping predicted by the empirical model remains the same. However, the experiments indicate that the roll amplitude is somewhat less than predicted by simulations. This indicates that in case of higher incident waves, the damping is slightly increased in experiments and results in a small divergence from the predicted roll motions. This

is also demonstrated by the random wave case represented in Figure 2.25 where the simulations show a higher response than experiments.

The current state of the art methods to predict viscous roll damping include analyzing free decay tests or the use of the Ikeda et al. [63] method when free decay tests are unavailable. These observations suggest that the aforementioned methods might not always be sufficient to represent the reality and there is a need for a new approach for extracting the damping information from experimental forced motion time series. A possible avenue would be to investigate the advanced system identification tools for this problem [81, 82]. Due to the lack of free decay test for the specified load case and the lack of a new method to estimate viscous damping in random waves, the research discussed herein continues using the empirical damping model proposed by Ikeda et al. [63].

2.7 The Stochastic Nature of Parametric Roll

The wave elevation shown in Figure 2.19 is only one of the many possible realizations obtained from the spectrum represented in Figure 2.18. Generating a new set of ϵ_n for $n = 1, 2, ..., N$ in (2.122) results in a different realization of wave elevation with the same energy distribution as depicted by the spectrum in Figure 2.18. The wave elevation $\eta_t = \eta(t)$ at any given time t can be considered to be a random quantity which depends on the realization chosen. In statistical terms, the wave elevation at time t is expressed by a random variable η_t. Expanding from this definition, the wave elevation process can be represented as a combination of such random variables $\{\eta_{t_1}, \eta_{t_2}, \eta_{t_3}, ...\}$ where η_{t_n} is a random variable denoting the wave elevation at time $t = t_n$. This combination of discreet number of random variables is known as a stochastic process and can be expressed in a compact notation as $\{\eta_t\}$ where $t \in [0, \infty)$.

Any stationary stochastic process is said to be *ergodic* if its statistical properties can be accurately obtained from a single time series [83, 84]. This means that the time average of a process or a function of the process over long periods of time converges to the corresponding ensemble averages. Thus the ensemble averages of a process (such as mean or auto-covariance function) can be approximated by the corresponding temporal averages. If $\{X_t\}$ represents a stochastic process, then its mean and auto-covariance functions may be expressed as shown in (2.124) and (2.125).

$$E[X_t] = \int_{-\infty}^{\infty} x f_1(x) dx \tag{2.124}$$

$$R(t,s) = E[X_t X_s] = \int_{-\infty}^{\infty} \int_{-\infty}^{\infty} x_1 x_2 f_2(x_1, x_2) dx_1 dx_2 \tag{2.125}$$

where $f_1(x)$ and $f_2(x_1, x_2)$ represent the probability density function and the joint probability density function of the stochastic process $\{X_t\}$. If $\{X_t\}$ is ergodic then the mean and auto-covariance functions can be expressed in terms of their temporal averages as shown in (2.126) and (2.127).

$$\lim_{T\to\infty} \frac{1}{2T} \int_{-T}^{T} x(t) dt = E[X_t] \tag{2.126}$$

$$\lim_{T\to\infty} \frac{1}{2T} \int_{-T}^{T} x(u) x(u+\tau) du = R(\tau) \tag{2.127}$$

where $x(t)$ represents a single realization of $\{X_t\}$ for $t \in [0, \infty)$. It is well known from linear theory that the linear motions of ship are ergodic since the input wave elevation is an ergodic process. However, this relation is not true in case of phe-

nomenon such as parametric roll which strongly depend on nonlinear damping and nonlinear stiffness.

Theoretically to prove or to disprove that a process is ergodic, one needs infinite number of realizations each of which are infinitely long. Since getting one or multiple infinitely long realizations is practically not possible, practical investigations are usually limited to a finite number of finitely long realizations. Thus the study of ergodic nature from finitely long time histories only provides us a measure of the *practical ergodicity* [83, 79].

2.7.1 Ergodicity of Wave Elevation and Motions

In order to analyze the stochastic characteristics of the simulated data, 30 3-hour simulations have been performed with each simulation using a different realization of the wave elevation from a Bretschneider spectrum with $H_s = 10\ m$ and $T_p = 13\ s$ as shown in Figure 2.18.

Figure 2.26a shows a plot of the auto-covariance of 30 different wave elevations from the Bretschneider spectrum on the same plot. The auto-covariance is computed using the temporal average as shown in (2.127). Note that all of the 30 plots coincide which demonstrates the ergodicity (or stationarity) of the wave elevation. Similar behavior is also shown by heave and pitch motions as shown in Figure 2.26b and Figure 2.26c respectively.

Note that the distance between the successive peaks of the auto-covariance function in Figure 2.26a is around 11 seconds corresponding to the encounter period associated with the modal period ($T_p = 13\ s$) of the spectrum. The highest energy in the spectrum is associated with the modal period and is reflected in the auto-covariance function. However, the heave and pitch auto-covariances as shown in Figure 2.26b and Figure 2.26c show a periodicity based on the response spectrum

of the respective modes which in turn depends both on input spectrum and the corresponding RAO. On the contrary, due to no direct excitation, the observed roll motion is entirely due to parametric roll and we would expect oscillation close to the roll natural frequency of $T_n \approx 23$ seconds (see Figure 2.26d).

The roll motion does not exhibit the ergodicity as shown by the heave and pitch motions. Figure 2.26d shows the plot of auto-covariance of 30 roll time series on the same plot. It can be seen that the variance in roll motion (indicated by $R_{\xi_4\xi_4}(0)$) varies significantly for various input realizations from the same spectrum. However, a plot of the auto-correlation (normalized auto-covariance) function in Figure 2.26e shows that the 30 simulations display a correlation-ergodicity. Another important feature to note is that the roll auto-covariance function decays much more slowly than the corresponding heave and pitch auto-covariance functions due to the lower damping (and hence longer memory) in the roll mode.

2.7.2 Probability Distribution

In order to display the degree of non-Gaussian nature of the response, the data from all the 30 simulations are collected together to generate a normalized histogram plot which is indicative of the empirical distribution function. Comparison of the empirical probability density function (pdf) with the normal PDF shows the non-Gaussian nature of the response. Figure 2.27 and Figure 2.28 show that the heave and pitch motion continue to follow a Gaussian distribution even in the event of large parametric roll of up to 35 degrees. However, the roll motion distribution is far from the Gaussian distribution as shown in Figure 2.29.

Another way to describe a random process is to compute the moments of the random process. It is well known in theory that the Gaussian distribution only requires the first two moments (mean and variance) to provide a complete probabilistic

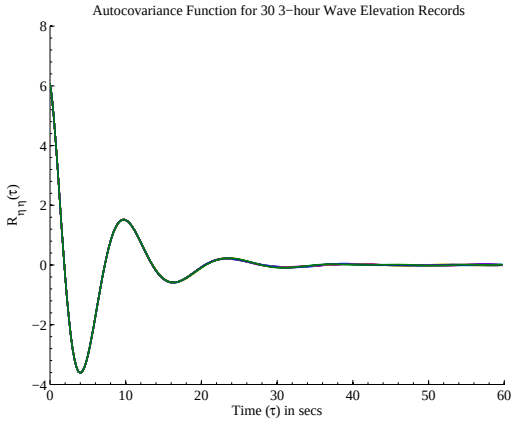

(a) Wave Elevation Auto-covariance

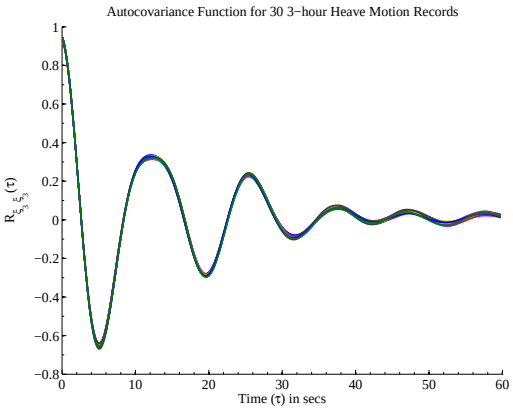

(b) Heave Auto-covariance

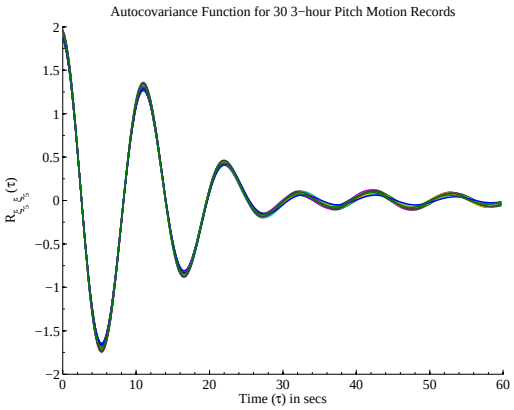

(c) Pitch Auto-covariance

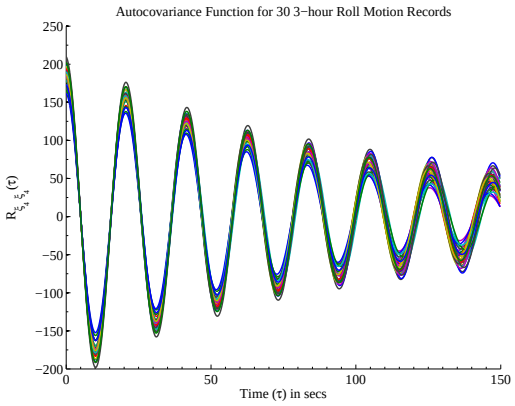

(d) Roll Auto-covariance

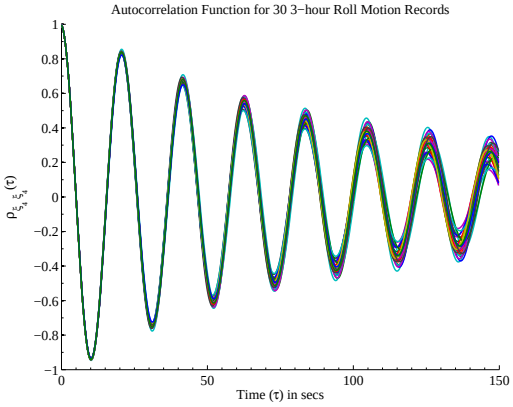

(e) Roll Auto-correlation

Figure 2.26: Plot of 30 time series each obtained from a different wave realization of Bretschneider Spectrum with $H_s = 10\ m$ and $T_p = 13\ s$

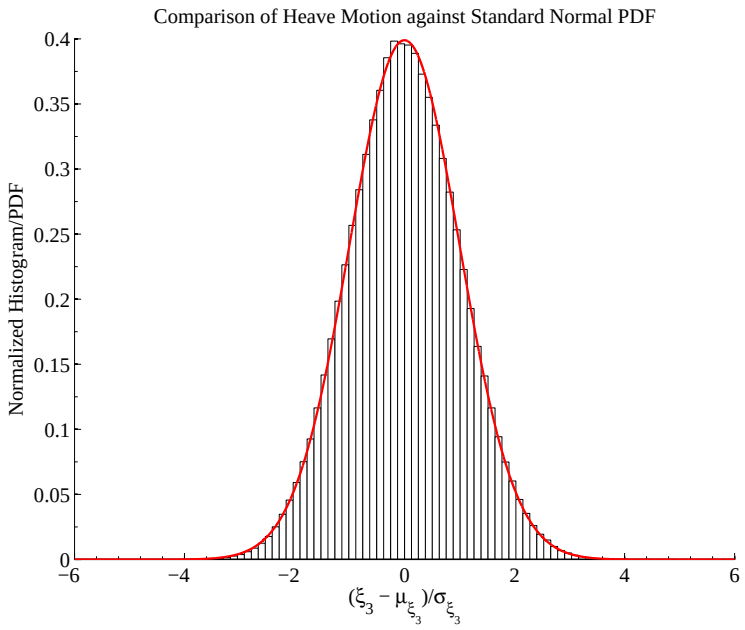

Figure 2.27: Comparison of heave motion against normal distribution

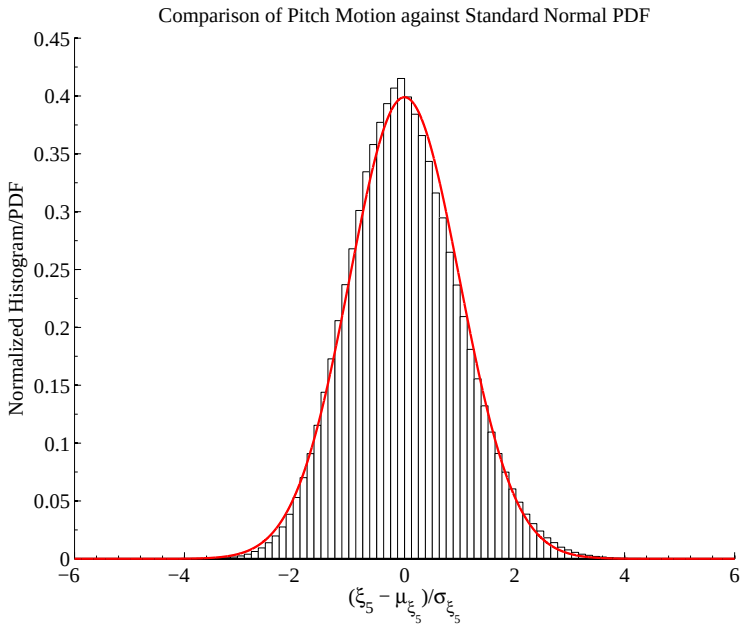

Figure 2.28: Comparison of pitch motion against normal distribution

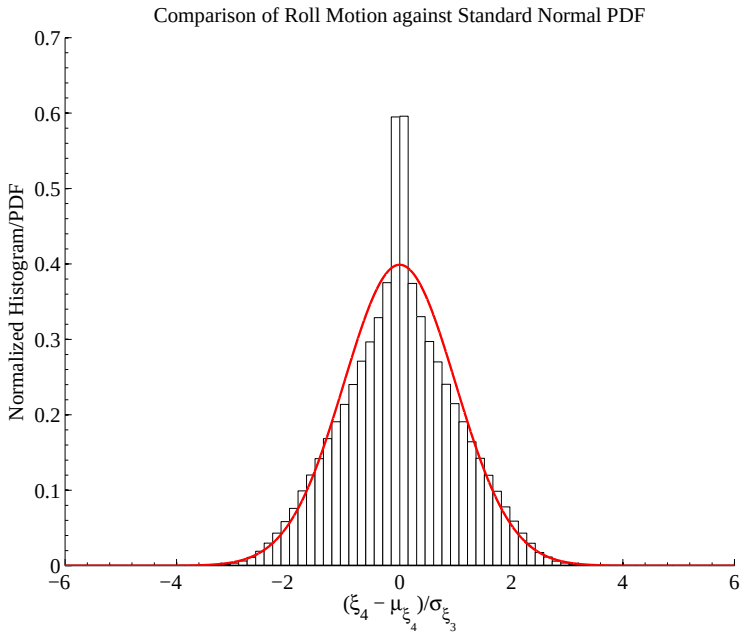

Figure 2.29: Comparison of roll motion against normal distribution

description of the process. Thus if the data of a time series is ergodic and Gaussian distributed, the sample mean and sample variance of the time series provide an accurate probabilistic description of the empirical distribution. However, in case of a non-Gaussian distribution it is much more difficult to get the probabilistic characteristics of response. One approaches is to fit a known distribution to the data [85, 86] and then use the fitted distribution to obtain the statistical properties. However, the theoretically accurate method requires the higher moments up to infinite powers to be computed. For practical applications, the higher moments are closed using specific approximations to achieve the probabilistic description of the non-Gaussian data and is discussed extensively by Su and Falzarano [87].

However, a preliminary check against the normal distribution can be performed by comparing the 4th central moment - *kurtosis*. For a normally distributed data kurtosis, given by (2.128), is always equal to 3. In (2.128) μ is the mean and σ is

Table 2.4: Combined statistics of 30 3-hour time histories

Time Series	**Standard Deviation**		**Variance**		**Kurtosis**	
	Value	Unit	Value	Unit	Value	Unit
Wave Elevation	2.500	m	6.249	m^2	2.995	-
Heave Motion	0.977	m	0.954	m^2	2.941	-
Roll Motion	13.672	deg	186.915	deg^2	2.975	-
Pitch Motion	1.388	deg	1.925	deg^2	3.117	-

the standard deviation of the process X.

$$Kurt[X] = E\left[\left(\frac{X-\mu}{\sigma}\right)^4\right] \tag{2.128}$$

The statistics of the various time series are shown in Table 2.4. The kurtosis for wave elevation, heave and pitch motion calculated from the 30 3-hour simulations was found to be 2.9954, 2.9406 and 3.1169 respectively. The kurtosis for the roll motion was found to be 2.9748 indicating that the tail of the distribution falls off similar to normal distribution. The central peak of the distribution as seen in Figure 2.29 has little effect on the kurtosis and hence provides a value similar to normally distributed data.

2.8 Parametric Excitation of Classic Spar

The phenomenon of parametric excitation is not limited to ships and is also observed for certain offshore platforms. One of the well known example is the parametric excitation of the classic spar in regular waves which was extensively studied by Haslum [1]. He suggested that when the system is excited by a critical long period swell the spar can exhibit large heave and pitch motions due to the Mathieu type instability. Later on Koo et al. [8] undertook a numerical investigation of the effect

of damping on the phenomenon by including mooring and riser effects and concluded that although with enough damping the parametric tuning can be avoided, in a realistic scenario there is still significant contribution to the heave and pitch motions due to this instability, especially in the case of long period swell environments (like West Africa). A second school of thought was provided by Liu et al. [88] suggesting that the observed instability was due to second order difference frequency interaction between the surface waves and body motions but was not due to a Mathieu type instability.

In this section, the nonlinear simulation tool developed in this chapter is applied to the classic spar problem and the results are compared against the experimental results provided by Haslum [1]. The detailed investigation of this problem is beyond the scope of this thesis and this comparison is only shown to demonstrate the ability of the developed nonlinear simulation tool to be generic and applicable to both ship shaped and non-ship shaped vessels alike.

2.8.1 Problem Description

Haslum [1] described the instability as a coupled Mathieu phenomenon where the envelope of the heave motion results in an unstable pitch excitation and the resulting pitch instability feeds back into coupled system causing amplified resonant heave motion. The particulars of the classic spar used by Haslum [1] are listed in Table 2.5. Note that the vertical center of gravity (VCG) listed by Haslum [1] is $-97.25\ m$ which results in the $\overline{GM}$ not matching the value listed in Table 2.5. Instead using a value of $-105.25\ m$ for VCG from waterline results in the same $\overline{GM}$ listed by Haslum [1]. This correction is also confirmed by Dahl [89].

Table 2.5: Particulars of the classic spar

Particulars	**Value**
Diameter (m)	37.5
Draft (m)	202.5
Radius of Gyration (m)	80
VCG from waterline (m)	-105.25
$\overline{GM}$ (m)	4.4

2.8.2 Comparison with Experiments

This classic spar listed in Table 2.5 is simulated using the nonlinear simulation tool developed in this chapter. The spar system is subjected to regular waves of height $H = 16.0\ m$ and period $T = 22.5\ s$ incident head on with $\beta = 180^0$. No moon pool is considered to match the Haslum's experimental scenario.

The comparison of heave and pitch motions about the center of gravity are shown in Figure 2.30 and Figure 2.31 respectively which demonstrates the ability of the nonlinear time domain simulation tool developed to qualitatively simulate the spar instability. Haslum [1] provides the experimental simulation of the only first 1500 seconds which still exhibits a transient behavior. An experimental simulation of longer period might have provided a steady state comparison between the simulations and the model tests.

The simulations seems to be in general agreement with the experiment performed by Haslum [1] and support his theory of being parametrically excited responses. Later, Haslum [3] also mentioned that the single column floater (SCF) proposed by ABB [90, 91] was found to experience severe parametric response during the model tests. Similar to the classic spar, the SCF has also been investigated using the above developed time domain program. However, the results of simulation of SCF are not

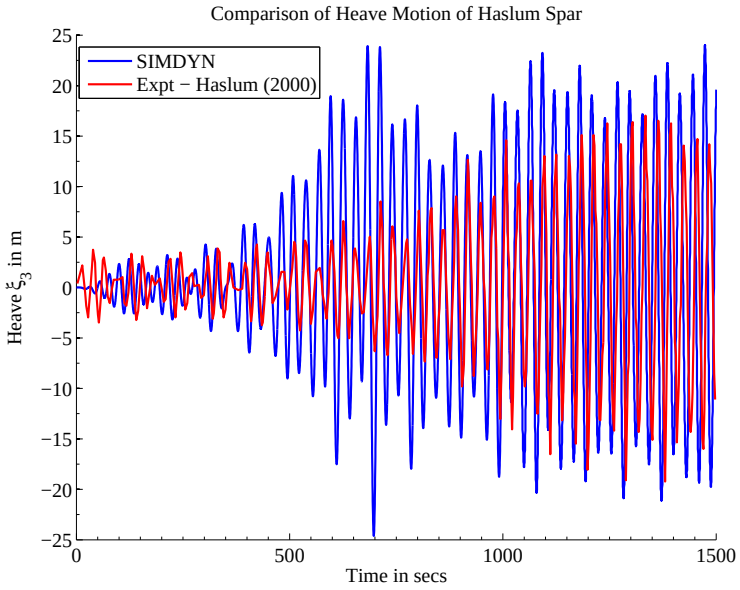

Figure 2.30: Heave motion (about the center of gravity) comparison between SIMDYN and Haslum [1] for incident head on ($\beta = 180^0$) regular waves of height $H = 16.0\ m$ and period $T = 22.5\ s$

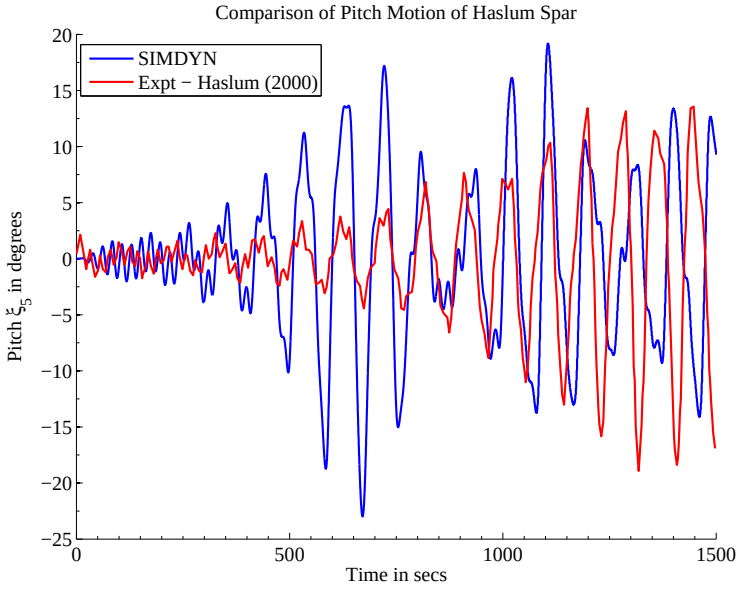

Figure 2.31: Pitch motion (about the center of gravity) comparison between SIMDYN and Haslum [1] for incident head on ($\beta = 180^0$) regular waves of height $H = 16.0\ m$ and period $T = 22.5\ s$

presented here and can be found in [4].

2.9 Conclusion

In this chapter the development of a generic nonlinear time domain simulation tool has been described. The described tool handles large amplitudes of rotation using an Euler angle approach with the order of rotation - roll first, pitch second and yaw third. A nonlinear force vector description has been provided to include various nonlinearities:

1. Nonlinear Froude-Krylov forces and moments
2. Nonlinear hydrostatic forces and moments
3. Viscous roll damping moment using empirical methods

The developed tool has been applied to simulate the parametric roll of a container ship in head waves. The numerical simulation responses in regular and irregular waves have compared with experiments and have been found to be in general agreement. Further ergodicity tests have been performed where the data from 30 different simulations of parametric roll in irregular waves have been analyzed to check the practical ergodicity of the phenomenon. It was found that the parametric roll is a highly tuned response displaying a strong periodicity in its auto-covariance. However, the standard deviation of the roll motion in different realizations of the same sea state are not same demonstrating a non-ergodic behavior. It was further observed that even in case of severe parametric roll, the heave and the pitch motions are ergodic and follow a normal distribution. This provides an insight that parametric roll may be studied as a single degree of freedom as its effect on other motions is significantly low. However, the vice-versa is not true and the heave and pitch have significant effects on roll. This leads to the idea that although roll might

be studied as a single degree of freedom, the coupling effects with other modes must be incorporated into the model. This forms the central idea of chapter 3 where it is explored in more detail.

3. APPROXIMATE SINGLE DEGREE OF FREEDOM (SDOF) MODELS *

The time domain simulation approach as described in chapter 2 is the current state of the art used by the marine and offshore industry to assess the large amplitude nonlinear motions of ships and offshore platforms in random waves. These simulations are capable of including the effect of various nonlinear forces in calculating the motions of marine and offshore structures which otherwise cannot be included in a standard frequency domain analysis (which is limited to linear systems). Although such time domain methods are robust in analyzing linear and weakly nonlinear systems, there are limitations when dealing with a strongly nonlinear system (e.g. roll motion of a ship).

Unlike their linear counterparts, nonlinear systems in general, may exhibit multiple steady state solutions depending on the initial condition chosen [92]. Each of these coexisting steady state solutions (known as Poincaré map fixed points in nonlinear dynamics nomenclature) have an associated domain of attraction which is the set of all initial conditions which when integrated in time converge to that steady state solution. Thus for the same external forcing, depending on which domain of attraction the chosen initial condition lies in, the system would exhibit different responses. Such a characteristic is not observed with linear systems where the system has a unique steady state response for a given external forcing.

A numerical simulation always starts from an initial condition and integrates the differential equations with respect to time to obtain a solution to one particular input (usually the external forcing). For a given input, even after testing out

*Part of this chapter is reprinted with permission from "A comparative assessment of simplified models for simulating parametric roll", 2017. Journal of Offshore Mechanics and Arctic Engineering, 139(2), pp 021103, Copyright 2017 by ASME

multiple initial conditions with a simulation tool, there is no guarantee that all the possible steady state solutions have been found. Especially when unstable steady state solutions exist, it is very tedious to identify them in a time domain simulation as it requires an accurate guess of the initial condition. Yet another disadvantage with numerical simulations is that while analyzing dynamics of a system subjected to random excitation, one needs to simulate motions for multiple input realizations to obtain accurate statistics of the response. This requires significant time and computational resources. In such cases, it becomes impractical to analyze the nonlinear system using time domain simulations.

The alternative is to use an analytical method which can quickly show the existence of multiple solutions of a system without the need to simulate long time histories. The analytical approach allows for the application of stochastic methods which are computationally less expensive than predicting the statistical characteristics by performing multiple time domain simulations. It also has the advantage of not missing certain dynamic characteristics due to the choice of initial condition. The drawback of analytical methods is that the system must be defined using analytical functions. This is in contrast to the numerical simulations where only the numerical value of the function is required even if its analytical form is unknown.

For real world problems, it is hard or even impossible at times to express the system analytically. In general, several assumptions are required before real problems can be approximated as an analytical system with manageable number of parameters. The simplifying assumptions often come at the cost of rendering the model incapable of capturing the complete dynamics of the system. It is imperative that the right choice of assumptions be made to simplify the system while ensuring that it is still qualitatively similar to reality.

This chapter provides a discussion of the various approaches to simplify the prob-

lem of parametric roll of a ship in irregular head seas and cast it into an approximate analytical model. These different methods are compared against one another and the nonlinear simulation tool developed in chapter 2 to demonstrate their relative accuracy and ability to capture the dynamics of the system. The model, most qualitatively similar to the real phenomenon, is then chosen to be the candidate for further analysis in chapters 4, 5 and 6.

3.1 Literature Review

The parametric roll of ships in head seas is a complex nonlinear phenomenon and many researchers have approached this problem with simplified models and numerical simulations. A lot of studies have also adopted a combination of simplified models and simulation techniques to understand the phenomenon. The earlier investigators preferred to study this phenomenon only in regular waves. Paulling [93] was one of the first investigators of this phenomenon who suggested a few simplified approaches. However, these methods were insufficient to study large amplitudes of motion. Neves and Rodriguez [94] proposed a coupled model with third order restoring coefficients and showed that the second order model was insufficient in capturing the dynamics in regular waves. Analytical expressions for the coefficients in regular waves were obtained based on the offset data of the ship. Neves and Rodriguez [95] later extended this method to calculate the new stability boundaries for the Hill's equation. However, as the model is improved from the second to the third order, both the complexity and the number of coefficients to evaluate increases tremendously. There also is a speculation that such detailed geometrical data might not always be available [96]. Spyrou et al. [97] suggested analytical and probabilistic techniques to predict the susceptibility of a hull form to parametric roll in regular waves. However, these methods were based on the assumption of a Mathieu type instability and

were not applicable as the mathematical models became more realistic [98]. Moideen et al. [99] suggested a Hill's equation approach instead of a Mathieu equation for modeling the parametric roll in regular waves and developed 3-D stability charts to predict the roll amplitude in regular waves. The advantage of using Hill's equation was to capture the non-harmonic periodic variation of hydrostatic stiffness in regular waves [100]. More theoretical discussion on the analytical techniques to analyze the problem of parametric roll in regular waves is provided in appendix D.

While the investigations into regular wave parametric roll continued, many researchers also started investigating the problem in irregular seas. One of the first ideas was to extend the regular wave models to the irregular waves using the concept of Grim effective wave (GEW) [101]. In this approach the spatial variation of irregular wave is modeled by an equivalent regular wave obtained by least square fit in space. Umeda et al. [102] developed a simplified model for irregular waves in which the roll restoring stiffness was calculated using the GEW concept. The GEW reduced the problem of calculating roll stiffness over an irregular wave profile to the calculation of roll stiffness in an equivalent regular wave whose crest/trough was fixed at midship. The model was quasi-statically balanced on the regular wave to match the calm water displacement. However, Hashimoto and Umeda [103] found that this approach did not agree well with experiments, suggesting that an improvement was needed. Bulian [96] improved upon Umeda's model by incorporating the Improved Grim Effective Wave (IGEW) into the roll stiffness. The IGEW allowed the equivalent regular wave to have crest/trough at any point along the length of the hull [104] and resulted in a better fit of the irregular wave profile. This model also predicted a better quasi-static equilibrium trim than the original Grim effective wave model. However, even this improved model only showed a some what reasonable agreement with the experiments [96]. The SCAPE committee (setup by Japan Society of Naval

Architects and Ocean Engineers to investigate various methods to estimate the capsizing risk of vessels for incorporation into the new generation stability criteria of IMO) as a part of its investigation also documented the comparison of the GEW and IGEW models against experimental results and suggested the use of a vulnerability criterion and direct assessment for the design against parametric roll [105]. It also concluded that although the simplified 1-degree of freedom (DOF) model could be used as an assessment, a complete nonlinear time domain simulation tool would still be required to quantify the susceptibility in terms of expected roll response.

While the GEW and IGEW were becoming popular, an alternate simplified model was proposed by Hua et al. [106] which modeled the $\overline{GM}$ variation in waves using a Volterra series method. Unlike the earlier approaches, this method included the actual wave elevation instead of an approximate regular wave fit. This method was further investigated by Moideen et al. [107] and Somayajula et al. [42, 11] who progressively included more nonlinearities to the system. The Volterra series method allows the $\overline{GM}$ variation to be obtained through frequency domain transfer functions while including the effect of dynamic heave and pitch of the vessel in waves. Its advantages include using the exact irregular wave profile instead of using an equivalent regular wave, and incorporating the effect of dynamic heave and pitch in the roll restoring moment. However, its drawback is the exclusion of the time varying cubic restoring stiffness. Somayajula and Falzarano [108] further improved upon this model to include a constant cubic restoring stiffness in addition to the time varying linear stiffness to the roll equation. Another key improvement in the later formulations by Somayajula and Falzarano [11] was the correction of adopting a time-invariant $\overline{KG}$ in contrast to the time-varying $\overline{KG}$ adopted by Hua et. al. [106].

In this chapter, the method developed by Somayajula and Falzarano [108, 11]

is extended further. Instead of modeling the $\overline{GM}$ in waves, a $\overline{GZ}$ variation model is developed where stiffness is modeled by a 11^{th} order polynomial each with time varying coefficients.

3.2 Roll Equation of Motion

For a ship subjected to head on waves, the roll mode of motion may be assumed to be decoupled from the other modes [109]. The 1-DOF roll equation of motion can then be expressed as shown in (3.1).

$$[I_{44} + A_{44}(\infty)]\ddot{\phi} + \int_{-\infty}^{t} K_{44}(t-\tau)\dot{\phi}(\tau)d\tau + B_1\dot{\phi} + B_2\dot{\phi}|\dot{\phi}| + C_{44}(t,\phi) = 0 \qquad (3.1)$$

where

I_{44} is the roll mass moment of inertia

$A_{44}(\infty)$ is the infinite frequency roll added moment of inertia

$K_{44}(\tau)$ is the roll impulse response function (IRF) / roll retardation function

B_1 is the linear roll damping coefficient due to viscous effects

B_2 is the quadratic roll damping coefficient due to viscous effects

$C_{44}(t,\phi)$ is the nonlinear instantaneous roll restoring moment including the dynamic effects due to instantaneous wave elevation and the heave and pitch motions

3.2.1 Roll Restoring Moment

From traditional naval architecture, the roll restoring moment of a statically balanced ship can be expressed as the product of weight $W = \rho g \nabla_0$ and the restoring arm $\overline{GZ}$ where ∇_0 is the calm water displacement of the vessel. In case of a static equilibrium, the moment due to the weight and the restoring moment are equal

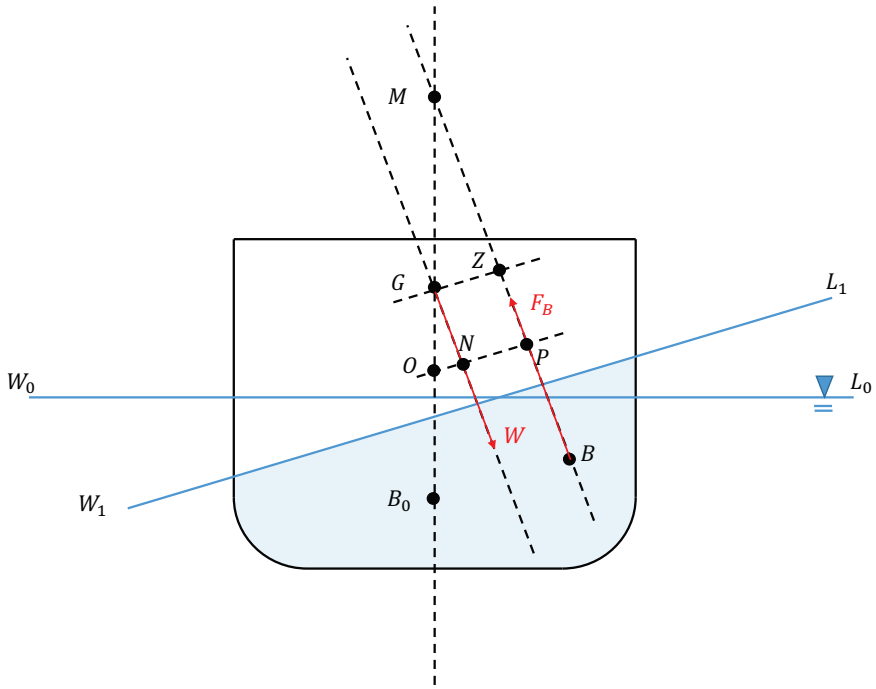

Figure 3.1: Roll restoring moment

and opposite. However, in a dynamic equilibrium as described in (3.1), there are other forces such as inertial, damping and external forces acting on the system. This implies that the buoyancy force are no longer equal in magnitude to the weight.

Consider a transverse section of a ship at a distance x from the origin as shown in Figure 3.1. Let $\overline{W_0L_0}$ be the calm water line and $\overline{W_1L_1}$ be the relative waterline (including the effects of incident wave, heave and pitch motions) for an instantaneous roll angle ϕ. It is assumed that the rotation is considered about the longitudinal axis of the body fixed frame with its origin at O. Due to the change in underwater hull form, the center of buoyancy shifts from B_0 to B. The buoyancy force $F_B = \rho g \nabla(t, \phi)$ now acts along the line $\overline{BM}$. From Figure 3.1 the instantaneous moment about O is

given by (3.2).

$$
\begin{aligned}
C_{44}(t,\phi) &= F_B \times \overline{OP} - W \times \overline{ON} \\
&= \rho g \nabla(t,\phi)\overline{OP} - \rho g \nabla_0 \overline{ON} \\
&= \rho g \nabla_0 \left[\overline{OP}\frac{\nabla(t,\phi)}{\nabla_0} - \overline{ON}\right] \\
&= \rho g \nabla_0 \overline{GZ}_{\text{eff}}(t,\phi) \qquad (3.2) \\
\overline{GZ}_{\text{eff}} &= \left[\overline{OP}\frac{\nabla(t,\phi)}{\nabla_0} - \overline{ON}\right] \qquad (3.3)
\end{aligned}
$$

The dynamic righting arm defined by $\overline{GZ}_{\text{eff}}$ depends on both instantaneous arm lengths as well as instantaneous underwater displacement. For convenience we shall drop the subscript and refer to the dynamic restoring arm as $\overline{GZ}$ instead of $\overline{GZ}_{\text{eff}}$. Substituting (3.2) into (3.1) and dividing by $[I_{44} + A_{44}(\infty)]$ leads to (3.4).

$$
\ddot{\phi} + \int_{-\infty}^{t} k_{44}(t-\tau)\dot{\phi}(\tau)d\tau + b_1\dot{\phi} + b_2\dot{\phi}|\dot{\phi}| + c_{44}\overline{GZ}(t,\phi) = 0 \qquad (3.4)
$$

where

$$
\begin{aligned}
k_{44}(\tau) &= \frac{K_{44}(\tau)}{[I_{44} + A_{44}(\infty)]} \qquad & b_1 &= \frac{B_1}{[I_{44} + A_{44}(\infty)]} \\
b_2 &= \frac{B_2}{[I_{44} + A_{44}(\infty)]} \qquad & c_{44} &= \frac{\rho g \nabla_0}{[I_{44} + A_{44}(\infty)]}
\end{aligned}
$$

In (3.4), the parameters $k_{44}(\tau)$, b_1, b_2 and c_{44} are known values. For a complete analytical description $\overline{GZ}(t,\phi)$ needs to be expressed in terms of parameters which are dependent on the geometry of the hull form.

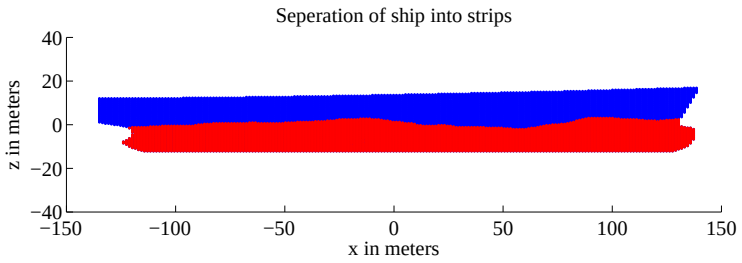

Figure 3.2: Separation of Pram hull form into 200 2-D strips; The red shade shows the instantaneous wetted part of each section at $t = 4417s$ from a 3 hour wave realized from Bretschneider spectrum with $H_s = 5\ m$ and $T_p = 13\ s$

3.3 Exact GZ Variation

Before developing an approximate analytical forms for $\overline{GZ}$ in irregular wave profile, an exact formulation of $\overline{GZ}$ in waves is required to verify that the analytical approximation gives a reasonable estimate. If only regular wave profiles are of interest, $\overline{GZ}$ in waves can be obtained by utilizing many of the commercially available hydrostatic calculation software. However, most commercial softwares do not provide the option to get $\overline{GZ}$ in an irregular wave profile. This section describes the details of evaluating $\overline{GZ}$ in an irregular wave while including the effects of instantaneous heave and pitch motions.

The input hull form is described by a set of offset data (a table listing the values of half breadth for a range of longitudinal and vertical distances along the length and height of the vessel respectively) which is output by most commercially available hydrostatic calculation software. An example of a 200 section model of Pram hull form described in Figure 2.1 is shown in Figure 3.2. The origin in this plot is located at the intersection of midship plane, centerline plane and at the calm waterline. The red shade indicates the part of each section under an irregular wave (generated by Bretschneider spectrum with $H_s = 5\ m$ and $T_p = 13\ s$) at time $t = 4417\ s$.

The wave elevation in irregular head seas ($\beta = 180^0$) can be expressed as a superposition of linear regular components as shown in (3.5) where a_m, k_m, ω_m and ϵ_m represent the amplitude, wave number, encounter frequency and phase of the m^{th} regular wave component.

$$\eta(t,x) = \frac{1}{2}\sum_{m=1}^{N} a_m \left[e^{i(k_m x+\omega_m t+\epsilon_m)} + e^{-i(k_m x+\omega_m t+\epsilon_m)}\right] \tag{3.5}$$

Assuming that $\xi_3(\omega_m)$ and $\xi_5(\omega_m)$ are the heave and pitch response amplitude operators (RAO) at encounter frequency ω_m, the corresponding relative wave elevation incorporating the dynamic heave and pitch of the vessel can be expressed as shown in (3.6).

$$r(t,x) = \frac{1}{2}\sum_{m=1}^{N} a_m \left[\nu(\omega_m,x)e^{i(\omega_m t+\epsilon_m)} + \bar{\nu}(\omega_m,x)e^{-i(\omega_m t+\epsilon_m)}\right] \tag{3.6}$$

where ($\bar{}$) denotes the complex conjugate and $\nu(x,\omega_m)$ and $\bar{\nu}(x,\omega_m)$ are given by

$$\nu(x,\omega_m) = \left[e^{ik_m x} - \xi_3(\omega_m) + x\xi_5(\omega_m)\right] \tag{3.7}$$

$$\bar{\nu}(x,\omega_m) = \left[e^{-ik_m x} - \bar{\xi}_3(\omega_m) + x\bar{\xi}_5(\omega_m)\right] \tag{3.8}$$

The local draft at each section can be obtained by adding the mean draft of the ship to the relative waterline and is shown below

$$T_r(t,x) = T(x) + r(t,x) \tag{3.9}$$

The mean draft $T(x)$ is a constant for a vessel floating at an even keel and varies linearly for a ship with a static trim angle. The local draft at each section under the irregular relative waterline is shown in Figure 3.2. Now the problem of estimating

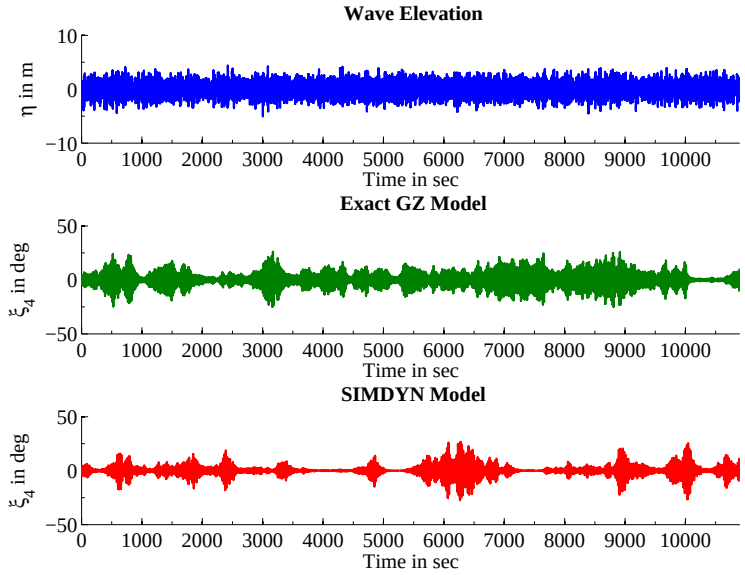

Figure 3.3: Comparison of roll motion between "SIMDYN" and "exact $\overline{GZ}$ model" of Pram hull form in a 3-hour realization of Bretschneider spectrum with $H_s = 5\ m$ and $T_p = 13\ s$

$\overline{GZ}$ of the hull is reduced to finding the $\overline{GZ}^{2D}(x)$ of the each of the 2-D sections. The $\overline{GZ}$ is estimated from $\overline{GZ}^{2D}(x)$ by

$$\overline{GZ} = \frac{1}{\nabla}\int_L \overline{GZ}^{2D}(x)A(x)dx \tag{3.10}$$

where $A(x)$ and ∇ are the sectional area at section x and the displacement under the relative waterline respectively in the upright condition (roll angle $\phi = 0$). $\overline{GZ}^{2D}(x)$ is calculated in a similar fashion as described in (3.3) and is detailed further in appendix C. Substituting the $\overline{GZ}$ in (3.4) at every time step, the resulting differential equation can be solved for roll motion. A comparison of the simulated roll motion using the exact $\overline{GZ}$ model and SIMDYN (developed in chapter 2) is shown in Figure 3.3. While the time history demonstrates a difference between the two models a more detailed comparison is given in section 3.7.

3.4 Volterra Series Method for GM Variation

The effective restoring arm $\overline{GZ}(t,\phi)$ in waves depends on the incident wave profile and the instantaneous position of the body. Due to the symmetry of a ship about the centerline, the restoring arm $\overline{GZ}(t,\phi)$ in waves must be an odd function of the roll angle ϕ. It is assumed that it can be expressed as an odd polynomial function of ϕ with time varying coefficients as shown in (3.11). However, in the method described in this section only K_1 is assumed to be time varying and the rest $(K_3, K_5, K_7, ...)$ are assumed to be time invariant resulting in (3.12).

$$\overline{GZ}(t,\phi) = K_1(t)\phi + K_3(t)\phi^3 + K_5(t)\phi^5 + ... \tag{3.11}$$

$$\overline{GZ}(t,\phi) = K_1(t)\phi + K_3\phi^3 + K_5\phi^5 + ... \tag{3.12}$$

The first term K_1 denotes the slope of the $\overline{GZ}(t,\phi)$ curve at $\phi = 0$ and is also known as the "*metacentric height*" $\overline{GM}$. $\overline{GM}$ represents the vertical distance between the center of gravity of the vessel G and its metacenter M (shown in Figure 3.1). This section describes the method of estimating the $\overline{GM}$ variation from a Volterra series approach which was originally introduced by Hua et al. [106] and later applied by Moideen [110] and Moideen et al. [107]. However, the derivation presented here differs from the above listed works with respect to the phase conventions and other important assumptions used.

The ship is assumed to be composed of multiple slender strips along the length as shown in Figure 3.2. When the ship is encountering irregular head waves, at every time instant the local draft at each of these sections is different due the effects of the wave and instantaneous heave and pitch motions of the ship. The red shaded area in Figure 3.2 shows the variation of local draft of the ship in irregular waves. The

local breadth $B(x, T+z)$ and moment of sectional underwater area about the keel $M(x, T+z)$ at any section x and local draft $T+z$ can be expanded into a Taylor series about the calm water draft T as shown in (3.13) and (3.14) respectively.

$$B(x, T+z) = B(x,T) + c_1 z + c_2 z^2 + ... \tag{3.13}$$

$$M(x, T+z) = M(x,T) + d_1 z + d_2 z^2 + ... \tag{3.14}$$

where the coefficients of higher powers of z are given by

$$c_1 = \frac{\partial B}{\partial z}(x,T),\ c_2 = \frac{1}{2!}\frac{\partial^2 B}{\partial z^2}(x,T),\ ... \tag{3.15}$$

$$d_1 = \frac{\partial M}{\partial z}(x,T),\ d_2 = \frac{1}{2!}\frac{\partial^2 M}{\partial z^2}(x,T),\ ... \tag{3.16}$$

From traditional naval architecture the metacentric height $\overline{GM}$ for any free floating structure is given by (3.17). The instantaneous $\overline{BM}$ and $\overline{KB}$ can be expressed by their usual definitions as shown in (3.18) and (3.19). Unlike in statics, the integrands of the integrals depend on the relative waterline $r(t,x)$ and are hence time varying quantities.

$$\overline{GM} = \overline{BM} + \overline{KB} - \overline{KG} \tag{3.17}$$

$$\overline{BM} = \frac{I_{wp}}{\nabla} = \frac{1}{12\nabla}\int_L B^3(x, T + r(t,x))dx \tag{3.18}$$

$$\overline{KB} = \frac{1}{\nabla}\int_L M(x, T + r(t,x))dx \tag{3.19}$$

Substituting (3.18) and (3.19) into (3.17) gives and expression for time varying

$\overline{GM}$ in waves. Hua et al. [106] and Moideen [110] also suggest including a time varying $\overline{KG}$ across the length of the ship. However, there is no theoretical background to support a time varying $\overline{KG}$ as the location of the center of gravity with respect to the keel is independent of the waves the ship is subjected to. Hence the approach presented here shall adopt a time invariant $\overline{KG}$.

$$GM = \frac{1}{\nabla}\int_L \left[\frac{B^3(x, T + r(t,x))}{12} + M(x, T + r(t,x))\right] dx - \overline{KG} \tag{3.20}$$

Expanding the integrands using (3.13) and (3.14) and collecting coefficients to various powers of $r(t,x)$ gives (3.21).

$$\overline{GM} = \overline{GM}_0 + \delta\overline{GM}_1 + \delta\overline{GM}_2 + ... \tag{3.21}$$

where $\overline{GM}_0$ denotes the calm water metacentric height and $\delta\overline{GM}_1$ and $\delta\overline{GM}_2$ represent the 1^{st} and 2^{nd} order contributions respectively.

$$\overline{GM}_0 = \frac{1}{\nabla}\int_L \left[\frac{B^3(x,T)}{12} + M(x,T)\right] dx - KG \tag{3.22}$$

$$\begin{aligned}\delta\overline{GM}_1 &= \frac{1}{\nabla}\int_L \left[\frac{c_1(x,T)B^2(x,T)}{4} + d_1(x,T)\right] r(t,x)dx \\ &= \frac{1}{\nabla}\int_L G_1(x)r(t,x)dx\end{aligned} \tag{3.23}$$

$$\begin{aligned}\delta\overline{GM}_2 &= \frac{1}{\nabla}\int_L \left[\frac{c_2(x,T)B^2(x,T) + c_1^2(x,T)B(x,T)}{4} + d_2(x,T)\right] r^2(t,x)dx \\ &= \frac{1}{\nabla}\int_L G_2(x)r^2(t,x)dx\end{aligned} \tag{3.24}$$

...

The geometry dependent functions $G_1(x)$ and $G_2(x)$ defined in (3.23) and (3.24) represent the first and second order effect of geometry on the variation in $\overline{GM}$.

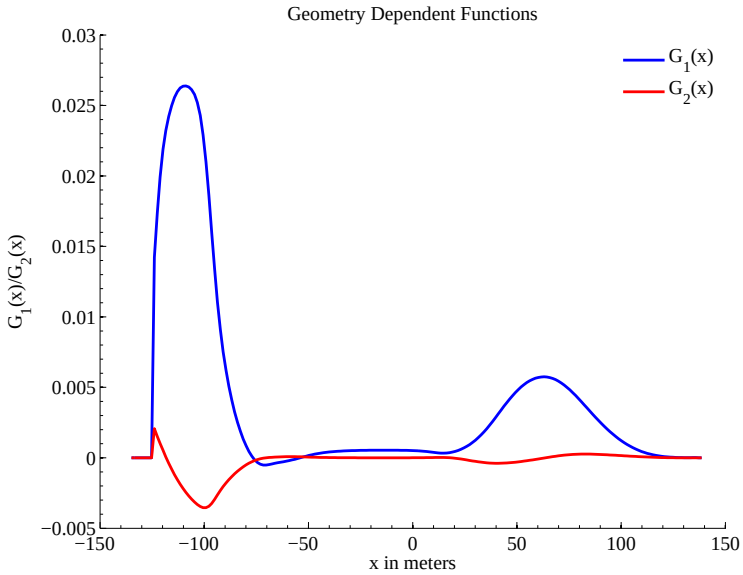

Figure 3.4: Variation of $G_1(x)$ and $G_2(x)$ for Pram hull form

Figure 3.4 shows the plot of $G_1(x)$ and $G_2(x)$ for the Pram hull form. The sharp jump at the aft in both $G_1(x)$ and $G_2(x)$ is due to the effect of transom stern. The point of discontinuity marks the aft most intersection of the waterline and the hull form. It can be seen that the effect of $G_1(x)$ and $G_2(x)$ are prominent only in the aft and forward regions of the ship indicating the strong influence of transom stern and forward flare on $\overline{GM}$ variation in waves. Over the parallel middle body, change in local draft does not cause significant variation in the waterplane area and hence does not contribute much to the $\overline{GM}$ variation.

Now in order to calculate the $\overline{GM}$ variation in waves, the relative wave elevation given by (3.6) is substituted into (3.23) and (3.24). This results in expressions for

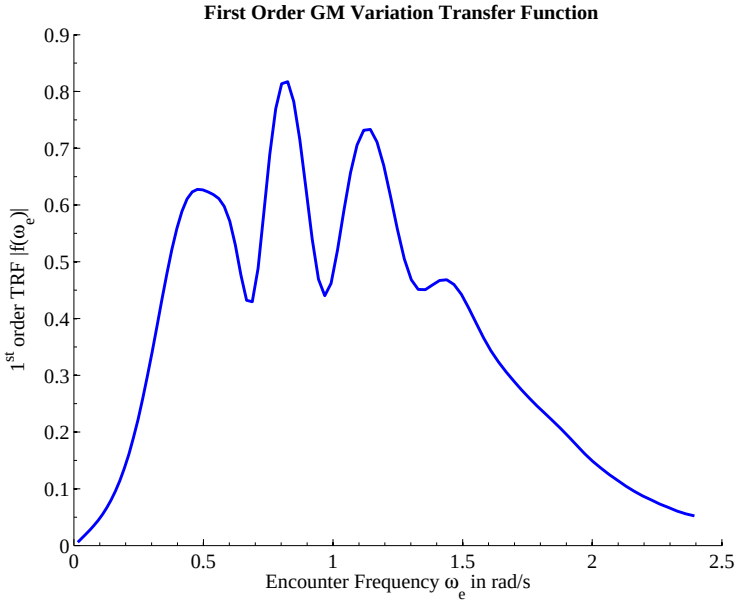

Figure 3.5: First order $\overline{GM}$ variation transfer function

various orders of $\overline{GM}$. The first order $\overline{GM}$ variation is given by (3.25).

$$\begin{aligned}\delta\overline{GM}_1 &= \frac{1}{2}\sum_{m=1}^{N} a_m \left[\left\{\int_L G_1(x)\nu(\omega_m,x)dx\right\} e^{i(\omega_m t+\epsilon_m)}\right. \\ &\qquad \left. + \left\{\int_L G_1(x)\bar{\nu}(\omega_m,x)dx\right\} e^{-i(\omega_m t+\epsilon_m)}\right] \\ &= \frac{1}{2}\sum_{m=1}^{N} a_m \left[f(\omega_m)e^{i(\omega_m t+\epsilon_m)} + \bar{f}(\omega_m)e^{-i(\omega_m t+\epsilon_m)}\right] \end{aligned} \tag{3.25}$$

where $f(\omega_e)$ is the first order transfer function given by

$$f(\omega_e) = \int_L G_1(x)\nu(\omega_e,x)dx \tag{3.26}$$

Figure 3.5 shows the plot of the first order $\overline{GM}$ variation transfer function $|f(\omega_e)|$.

Similarly, the second order GM variation is given by (3.28).

$$\begin{aligned}\delta\overline{GM}_2 = \frac{1}{4}\sum_{m=1}^{N}\sum_{n=1}^{N} a_m a_n \Bigg[&\left\{\int_L G_2(x)\nu(\omega_m,x)\nu(\omega_n,x)dx\right\} e^{i\{(\omega_m+\omega_n)t+\epsilon_m+\epsilon_n\}} \\ &+ \left\{\int_L G_2(x)\nu(\omega_m,x)\bar{\nu}(\omega_n,x)dx\right\} e^{i\{(\omega_m-\omega_n)t+\epsilon_m-\epsilon_n\}} \\ &+ \left\{\int_L G_2(x)\bar{\nu}(\omega_m,x)\nu(\omega_n,x)dx\right\} e^{i\{(-\omega_m+\omega_n)t-\epsilon_m+\epsilon_n\}} \\ &+ \left\{\int_L G_2(x)\bar{\nu}(\omega_m,x)\bar{\nu}(\omega_n,x)dx\right\} e^{i\{(-\omega_m-\omega_n)t-\epsilon_m-\epsilon_n\}}\Bigg] \end{aligned} \tag{3.27}$$

$$\begin{aligned}\delta\overline{GM}_2 = \frac{1}{4}\sum_{m=1}^{N}\sum_{n=1}^{N} a_m a_n \big[&g_1(\omega_m,\omega_n)e^{i\{(\omega_m+\omega_n)t+\epsilon_m+\epsilon_n\}} + \bar{g}_2(\omega_m,\omega_n)e^{i\{(\omega_m-\omega_n)t+\epsilon_m-\epsilon_n\}} \\ &+ g_2(\omega_m,\omega_n)e^{i\{(-\omega_m+\omega_n)t-\epsilon_m+\epsilon_n\}} + \bar{g}_1(\omega_m,\omega_n)e^{i\{(-\omega_m-\omega_n)t-\epsilon_m-\epsilon_n\}}\big] \end{aligned} \tag{3.28}$$

where $g_1(\omega_m,\omega_n)$ and $g_2(\omega_m,\omega_n)$ are the second order transfer functions given by

$$g_1(\omega_m,\omega_n) = \int_L G_2(x)\nu(\omega_m,x)\nu(\omega_n,x)dx \tag{3.29}$$

$$\bar{g}_2(\omega_m,\omega_n) = \int_L G_2(x)\nu(\omega_m,x)\bar{\nu}(\omega_n,x)dx \tag{3.30}$$

$$g_2(\omega_m,\omega_n) = \int_L G_2(x)\bar{\nu}(\omega_m,x)\nu(\omega_n,x)dx \tag{3.31}$$

$$\bar{g}_1(\omega_m,\omega_n) = \int_L G_2(x)\bar{\nu}(\omega_m,x)\bar{\nu}(\omega_n,x)dx \tag{3.32}$$

Figure 3.6 shows the plot of the two transfer functions $g_1(\omega_e,\omega_e)$ and $g_2(\omega_e,\omega_e)$. The sum frequency transfer function $g_1(\omega_e,\omega_e)$ is symmetric while the difference frequency transfer function $g_2(\omega_e,\omega_e)$ is conjugate-symmetric. These properties can

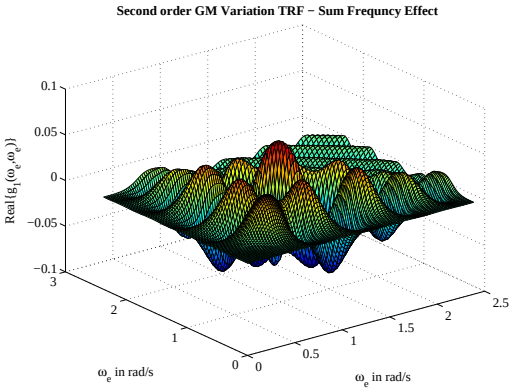

(a) Real part of $g_1(\omega_e, \omega_e)$

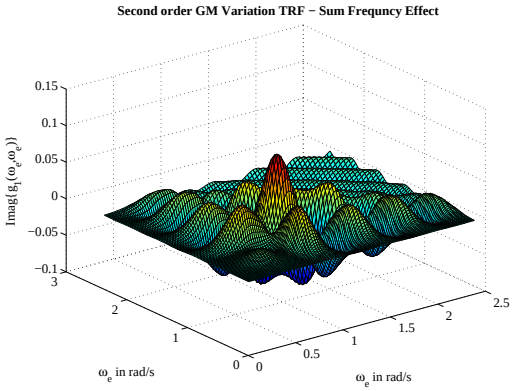

(b) Imaginary part of $g_1(\omega_e, \omega_e)$

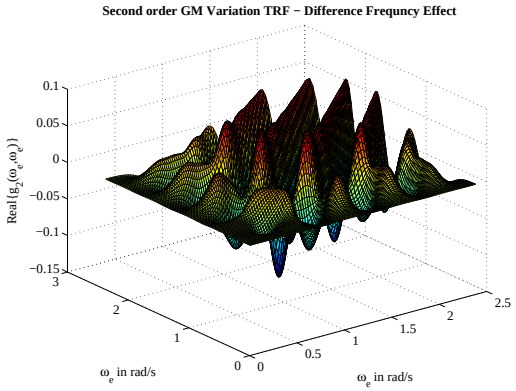

(c) Real part of $g_2(\omega_e, \omega_e)$

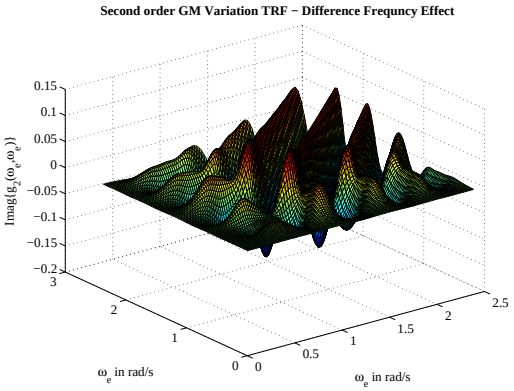

(d) Imaginary part of $g_2(\omega_e, \omega_e)$

Figure 3.6: Second order $\overline{GM}$ variation transfer functions

mathematically be expressed as

$$g_1(\omega_m, \omega_n) = g_1(\omega_n, \omega_m) \tag{3.33}$$

$$g_2(\omega_m, \omega_n) = \bar{g}_2(\omega_n, \omega_m) \tag{3.34}$$

This property can also be checked visually by observing the surface plots of imaginary part of the transfer functions - Figure 3.6b is symmetric about the diagonal while Figure 3.6d is anti-symmetric.

Thus by application of the Volterra series method the time varying effective restoring arm $\overline{GZ}$ can be represented by (3.35) where the coefficients of the higher powers of ϕ are obtained by polynomial fit to the $\overline{GZ}$ curve in calm water.

$$\overline{GZ}(t,\phi) = \overline{GM}(t)\phi + K_3\phi^3 + K_5\phi^5 + ... \tag{3.35}$$

$$\begin{aligned}\overline{GM}(t) =& \overline{GM}_0 + \frac{1}{2}\sum_{m=1}^{N} a_m \left[f(\omega_m)e^{i(\omega_m t+\epsilon_m)} + \bar{f}(\omega_m)e^{-i(\omega_m t+\epsilon_m)}\right] \\ &+ \frac{1}{4}\sum_{m=1}^{N}\sum_{n=1}^{N} a_m a_n \left[g_1(\omega_m,\omega_n)e^{i\{(\omega_m+\omega_n)t+\epsilon_m+\epsilon_n\}}\right. \\ &+\bar{g}_2(\omega_m,\omega_n)e^{i\{(\omega_m-\omega_n)t+\epsilon_m-\epsilon_n\}} + g_2(\omega_m,\omega_n)e^{i\{(-\omega_m+\omega_n)t-\epsilon_m+\epsilon_n\}} \\ &\left.+\bar{g}_1(\omega_m,\omega_n)e^{i\{(-\omega_m-\omega_n)t-\epsilon_m-\epsilon_n\}}\right]\end{aligned} \tag{3.36}$$

The expression for $\overline{GZ}(t,\phi)$ is substituted into (3.4) to solve the differential equation for the roll motion time series. A comparison of the simulated roll motion using the Volterra $\overline{GM}$ model and SIMDYN is shown in Figure 3.7. It is clearly seen that the Volterra $\overline{GM}$ model is insufficient to model the reality as the simulated roll motion from Volterra $\overline{GM}$ model is significantly higher than the simulation from SIMDYN.

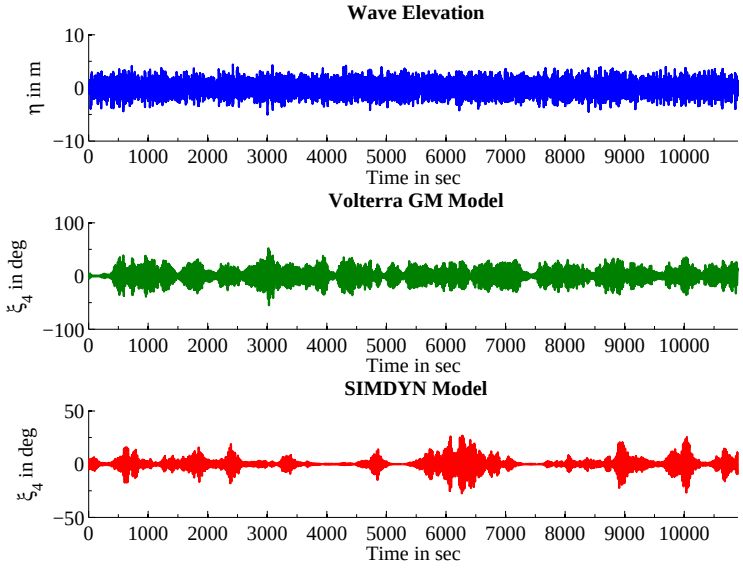

Figure 3.7: Comparison of roll motion between "SIMDYN" and "Volterra $\overline{GM}$ model" of Pram hull form in a 3-hour realization of Bretschneider spectrum with $H_s = 5\ m$ and $T_p = 13\ s$

3.5 Grim's Effective Wave Approach

This section describes a second approach to obtain the hydrostatic variation in waves. In this approach, instead of using the irregular wave profile across the ship, the problem is reduced to a ship in a regular wave. The original idea of representing the irregular wave profile by an equivalent regular wave was first proposed by Grim [101] in 1960s.

As before, the irregular head sea can be described by a linear superposition of linear regular components as shown in (3.5). It can also be expressed in an alternate form as (3.37).

$$\eta(t,x) = \sum_{m=1}^{N} a_m \cos(k_m x + \omega_m t + \epsilon_m) \tag{3.37}$$

Grim proposed replacing the irregular wave in space by a least squared fit regular

wave with a fixed wavelength equal to the length of the ship and whose amplitude varies with time. At every time instant the wave profile in space is represented by a regular wave whose length is equal to the length of the ship with either its crest or trough fixed at midship. At every time step, the amplitude of the considered regular wave is different and determined by least squares fit of the actual wave profile in space. The proposed equivalent wave profile η_g has the mathematical form shown in (3.38).

$$\eta_g(t,x) = a(t) + \eta_c(t)\cos\frac{2\pi x}{L} \tag{3.38}$$

Over the years, the Grim's effective wave has been modified to allow for the crest/trough of the equivalent wave to be at any point along the length of the hull [103, 105, 111]. This modified formulation is also sometimes referred to as the Improved Grim Effective Wave (IGEW) and is given by (3.39).

$$\eta_g(t,x) = a(t) + \eta_c(t)\cos\frac{2\pi x}{L} + \eta_s(t)\sin\frac{2\pi x}{L} \tag{3.39}$$

The additional sine term introduces a phase angle in space which now allows the crest or trough to be located at any point along the length of the ship. The coefficients $a(t)$, $\eta_c(t)$ and $\eta_s(t)$ can be found by solving the least square fit problem described in (3.41) and are shown in (3.42), (3.43) and (3.44) respectively.

$$L = \int_{-L/2}^{L/2} [\eta(t,x) - \eta_g(t,x)]^2\, dx \tag{3.40}$$

$$\frac{\partial L}{\partial a} = 0,\ \frac{\partial L}{\partial \eta_c} = 0,\ \frac{\partial L}{\partial \eta_s} = 0 \tag{3.41}$$

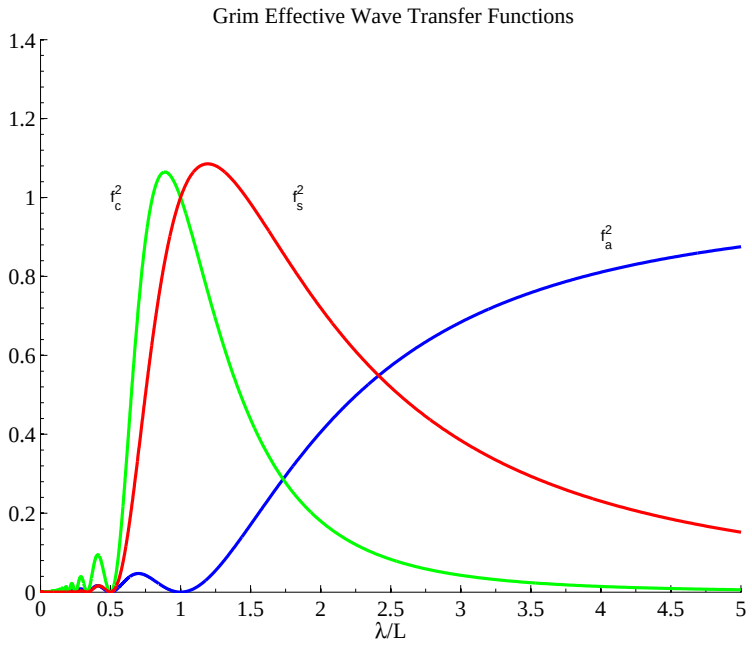

Figure 3.8: Square of IGEW transfer functions

$$a(t) = \sum_{m=1}^{N} a_m f_a(k_m) \cos(k_m x + \omega_m t + \epsilon_m) \tag{3.42}$$

$$\eta_c(t) = \sum_{m=1}^{N} a_m f_c(k_m) \cos(k_m x + \omega_m t + \epsilon_m) \tag{3.43}$$

$$\eta_s(t) = \sum_{m=1}^{N} a_m f_s(k_m) \sin(k_m x + \omega_m t + \epsilon_m) \tag{3.44}$$

where

$$f_a(k_m) = \frac{\sin Q}{Q} \qquad Q = \frac{-k_m L}{2}$$

$$f_c(k_m) = \frac{2Q \sin Q}{\pi^2 - Q^2}, \qquad f_s(k_m) = \frac{2\pi \sin Q}{\pi^2 - Q^2}$$

The square of the transfer functions $f_a(k_m)$, $f_c(k_m)$ and $f_s(k_m)$ are shown in Figure 3.8. Figure 3.9 shows the quality of fit of IGEW and Grim effective wave to

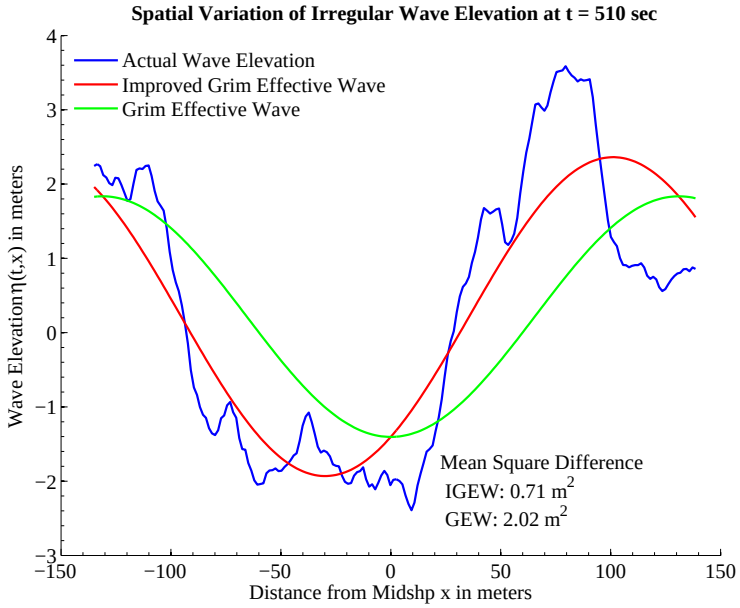

Figure 3.9: Comparison of IGEW and Grim effective wave with actual wave elevation from Bretschneider spectrum with $H_s = 5m$ and $T_p = 13s$

the actual wave elevation in space at a particular time instant. It can be seen that the flexibility of IGEW to move the crest along the length clearly results in a better fit than the original Grim effective wave.

With the improved Grim effective wave, the problem of calculating the hydrostatic stiffness of a ship on an irregular wave profile is reduced to that on an equivalent regular wave. Within this approach of using a regular wave approximation, there are two different approaches to model the hydrostatic stiffness.

3.5.1 No Effect of Dynamic Heave and Pitch

In this approach the hydrostatic stiffness is modeled using a time varying $\overline{GZ}$ in regular wave while disregarding the instantaneous heave and pitch of the vessel. The

roll equation of motion corresponding to this model is given by (3.45)

$$\ddot{\phi} + \int_{-\infty}^{t} k_{44}(t-\tau)\dot{\phi}(\tau)d\tau + b_1\dot{\phi} + b_2\dot{\phi}|\dot{\phi}| + \omega_0^2\left(\frac{\overline{GZ}(t,\phi)}{\overline{GM}_0}\right) = 0 \tag{3.45}$$

where ω_0 denotes the natural frequency corresponding to the linear stiffness given by (3.46) and $\overline{GM}_0$ denotes the calm water metacentric height.

$$\omega_0 = \sqrt{c_{44}\overline{GM}_0} = \sqrt{\frac{\rho g \nabla_0 \overline{GM}_0}{[I_{44} + A_{44}(\omega_0)]}} \tag{3.46}$$

At every time step the instantaneous wave profile across the ship is approximated by $\eta(t,x) \approx \eta_g(t,x)$. The instantaneous $\overline{GZ}$ at each time step is interpolated from a lookup table. The lookup table for $\overline{GZ}$ values are calculated prior to the simulation for various regular wave amplitudes, crest location along the length of the ship and different roll angles. This is similar to the approach used by Bulian [96], however, with an improvement of inclusion of convolution integral in the roll equation of motion. These $\overline{GZ}$ values for the interpolation table are usually obtained using a standard hydrostatic calculation software where the ship is statically balanced on the wave to match the calm water displacement. A sample $\overline{GZ}$ curve for a 4 m high regular wave for various crest positions is shown in Figure 3.10a.

It is important to note that this model does not include the effect of dynamic heave and pitch on the change in instantaneous waterline which implies that the $\overline{GZ}$ calculated in this case is the quasi-statically balanced hydrostatic restoring arm instead of the effective restoring arm as described in (3.3). While calculating the $\overline{GZ}$ lookup table, in each of the cases the model is allowed to trim freely. Thus a lookup table similar to a $\overline{GZ}$ can also be calculated for quasi-static trim angle as shown in Figure 3.10b which can then be used to compute the equilibrium trim angle time

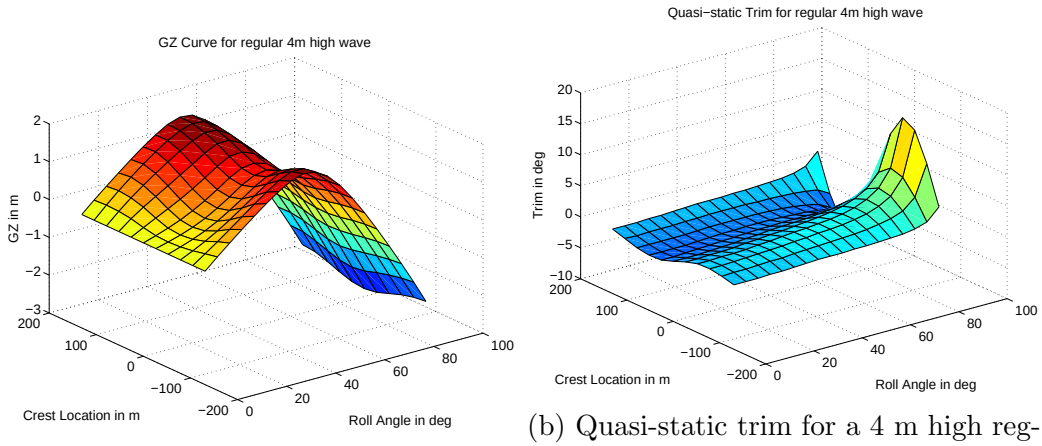

(a) GZ curve for a 4 m high regular wave

(b) Quasi-static trim for a 4 m high regular wave

Figure 3.10: GZ variation calculation using IGEW

series. It can be seen that the equilibrium trim time series differs considerably from the actual pitch time series as shown in Figure 3.11.

3.5.2 Including the Effect of Dynamic Heave and Pitch

Unlike the previous section where the dynamic effect of heave and pitch is neglected, the model described below includes the effect of dynamic heave and pitch in the calculation of $\overline{GZ}$ while assuming the improved Grim effective wave (IGEW) profile. In this model the exact effective $\overline{GZ}$ in waves is evaluated at every time step using the IGEW wave profile superimposed with the instantaneous dynamic heave and pitch motion. It can be seen that this model is not strictly analytical. However this analysis is implemented to make a fair comparison with the Volterra models described in section 3.4 and section 3.6 which include dynamic heave and pitch effect. The simulated roll motion using the IGEW model including the dynamic heave and pitch motions is compared against SIMDYN simulation in Figure 3.12.

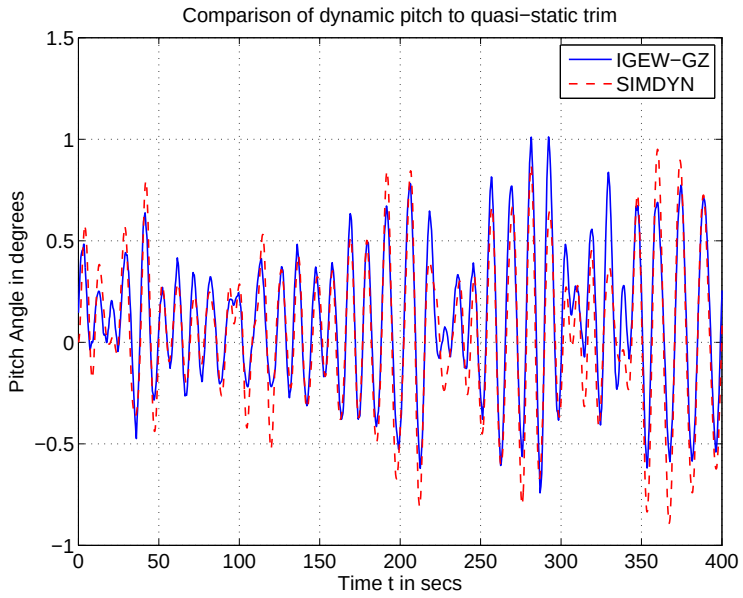

Figure 3.11: Comparison of quasi-static trim with dynamic pitch for Pram hull form in 5 knots forward speed subjected to an input wave realized from Bretschneider spectrum with significant wave height $H_s = 3m$ and modal period $T_p = 14.1s$

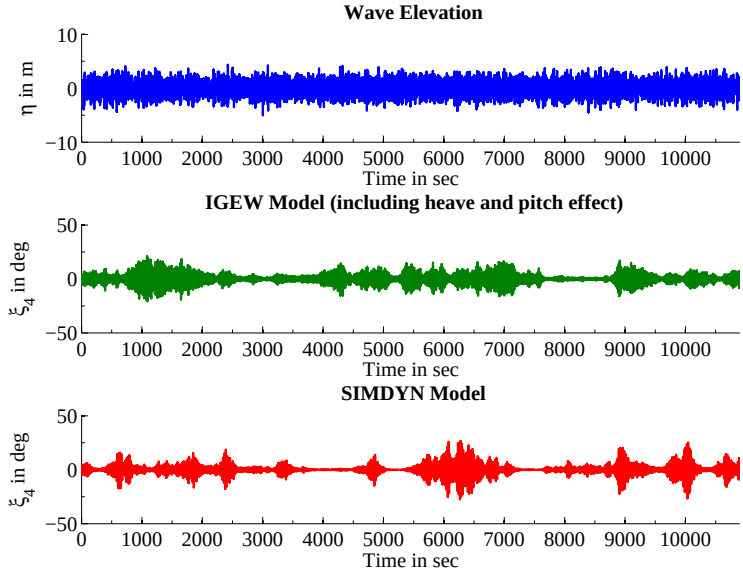

Figure 3.12: Comparison of roll motion between "SIMDYN" and "IGEW model" (including dynamic heave and pitch effect) of Pram hull form in a 3-hour realization of Bretschneider spectrum with $H_s = 5\ m$ and $T_p = 13\ s$

3.6 Volterra Series Method for GZ Variation

This section describes the method of obtaining the $\overline{GZ}$ variation in waves using a Volterra series approach. This is an extension of the method proposed in section 3.4 where the linear stiffness term was assumed to change in waves while the cubic and higher order terms were assumed to be invariant with time. Time varying $\overline{GZ}$ can be expressed as shown in (3.47) where the explicit dependence with respect to time t and instantaneous roll angle ϕ is shown.

$$\overline{GZ} = \overline{GZ}(t, \phi) \tag{3.47}$$

The ship is divided into a set of transverse sections as described in section 3.3 which allows expressing $\overline{GZ}(t, \phi)$ in terms of $\overline{GZ}^{2D}(t, x, \phi)$ as shown in (3.48) where ∇ is the displacement under the calm waterline in upright condition and $A(x)$ is the sectional area under the calm waterline at the section located x meters from midship in the upright condition.

$$\overline{GZ}(t, \phi) = \frac{1}{\nabla} \int_L \overline{GZ}^{2D}(t, x, \phi) A(x) dx \tag{3.48}$$

It can be seen from (3.48) that $\overline{GZ}^{2D}$ depends explicitly on time t. However, at the local section located at a distance x from midship, the time dependence of $\overline{GZ}^{2D}$ is due the change of instantaneous draft at the section with time. Thus without loss of generality the time dependence can be expressed in terms of the local draft as

$$\overline{GZ}(t, \phi) = \frac{1}{\nabla} \int_L \overline{GZ}^{2D}(T + r(t, x), x, \phi) A(x) dx \tag{3.49}$$

where T is the mean draft in calm water and $r(t, x)$ is the relative waterline as

defined in (3.6). Assuming a separation of variables, $\overline{GZ}^{2D}$ can be expressed as an odd polynomial of roll angle ϕ with coefficients which are functions x and $r(t,x)$ as shown in (3.50).

$$\begin{aligned}\overline{GZ}^{2D}(T+r(t,x),x,\phi) = k_1(T+r(t,x),x)\phi + k_3(T+r(t,x),x)\phi^3 \\ + k_5(T+r(t,x),x)\phi^5 + ...\end{aligned} \tag{3.50}$$

Substituting (3.50) into (3.49) results in polynomial approximation for $\overline{GZ}$

$$\overline{GZ}(t,\phi) = K_1(t)\phi + K_3(t)\phi^3 + K_5(t)\phi^5 + ... \tag{3.51}$$

where

$$K_1(t) = \left[\frac{1}{\nabla}\int_L k_1(T+r(t,x),x)A(x)dx\right] \tag{3.52}$$

$$K_3(t) = \left[\frac{1}{\nabla}\int_L k_3(T+r(t,x),x)A(x)dx\right] \tag{3.53}$$

$$K_5(t) = \left[\frac{1}{\nabla}\int_L k_5(T+r(t,x),x)A(x)dx\right] \tag{3.54}$$

and so on

Expanding $k_i(T+r(t,x),x)$ for $i = 1,3,5,...$ as Taylor series about the mean draft T, $K_i(t)$, the time varying coefficient of ϕ^i in (3.51), can be expressed as

$$\begin{aligned}K_i(t) = &\frac{1}{\nabla}\int_L k_i(T,x)A(x)dx + \frac{1}{\nabla}\int_L \frac{\partial k_i}{\partial z}(T,x)r(t,x)A(x)dx \\ &+ \frac{1}{\nabla}\int_L \frac{1}{2!}\frac{\partial^2 k_i}{\partial z^2}(T,x)r^2(t,x)A(x)dx + ...\end{aligned} \tag{3.55}$$

$$K_i(t) = K_i^{(0)} + K_i^{(1)}(t) + K_i^{(2)}(t) + ... \tag{3.56}$$

where

$$K_i^{(0)} = \frac{1}{\nabla}\int_L k_i(T,x)A(x)dx \tag{3.57}$$

$$K_i^{(1)}(t) = \frac{1}{\nabla}\int_L \frac{\partial k_i}{\partial z}(T,x)r(t,x)A(x)dx \tag{3.58}$$

$$K_i^{(2)}(t) = \frac{1}{\nabla}\int_L \frac{1}{2!}\frac{\partial^2 k_i}{\partial z^2}(T,x)r^2(t,x)A(x)dx \tag{3.59}$$

Substituting the relative wave elevation from (3.6) in (3.58) results in an expression for $K_i^{(1)}(t)$

$$\begin{aligned} K_i^{(1)}(t) &= \frac{1}{\nabla}\int_L \frac{\partial k_i}{\partial z}(T,x)r(t,x)A(x)dx \\ &= \frac{1}{2}\sum_{m=1}^{N} a_m \left[\left\{\frac{1}{\nabla}\int_L \frac{\partial k_i}{\partial z}(T,x)\nu(\omega_m,x)dx\right\}e^{i(\omega_m t+\epsilon_m)}\right. \\ &\quad \left.+\left\{\frac{1}{\nabla}\int_L \frac{\partial k_i}{\partial z}(T,x)\bar{\nu}(\omega_m,x)dx\right\}e^{-i(\omega_m t+\epsilon_m)}\right] \\ &= \frac{1}{2}\sum_{m=1}^{N} a_m \left[f_i(\omega_m)e^{i(\omega_m t+\epsilon_m)} + \bar{f}_i(\omega_m)e^{-i(\omega_m t+\epsilon_m)}\right] \end{aligned} \tag{3.60}$$

where $f_i(\omega_e)$ is the first order transfer function given by

$$f_i(\omega_e) = \frac{1}{\nabla}\int_L \frac{\partial k_i}{\partial z}(T,x)\nu(\omega_e,x)dx \tag{3.61}$$

Figure 3.13 shows the first order transfer functions $f_i(\omega_i)$ for $i = 1, 3$ and 5. Substituting the relative wave elevation from (3.6) in (3.59) results in an expression for $K_i^{(2)}(t)$

$$K_i^{(2)}(t) = \frac{1}{\nabla}\int_L \frac{1}{2!}\frac{\partial^2 k_i}{\partial z^2}(T,x)r^2(t,x)A(x)dx \tag{3.62}$$

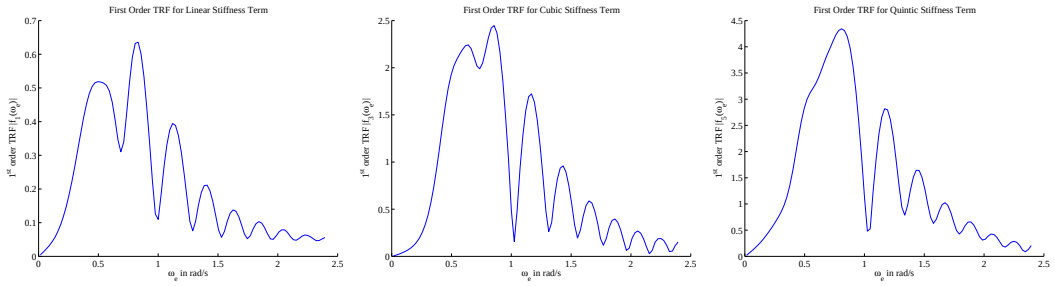

(a) Linear Stiffness (b) Cubic Stiffness (c) Quintic Stiffness

Figure 3.13: First Order Transfer Functions $f_i(\omega_e)$

$$K_i^{(2)}(t) = \frac{1}{4}\sum_{m=1}^{N}\sum_{n=1}^{N} a_m a_n \left[\left\{ \int_L \frac{1}{2!}\frac{\partial^2 k_i}{\partial z^2}(T,x)\nu(\omega_m,x)\nu(\omega_n,x)dx \right\} e^{i\{(\omega_m+\omega_n)t+\epsilon_m+\epsilon_n\}} \right.$$
$$+ \left\{ \int_L \frac{1}{2!}\frac{\partial^2 k_i}{\partial z^2}(T,x)\nu(\omega_m,x)\bar{\nu}(\omega_n,x)dx \right\} e^{i\{(\omega_m-\omega_n)t+\epsilon_m-\epsilon_n\}}$$
$$+ \left\{ \int_L \frac{1}{2!}\frac{\partial^2 k_i}{\partial z^2}(T,x)\bar{\nu}(\omega_m,x)\nu(\omega_n,x)dx \right\} e^{i\{(-\omega_m+\omega_n)t-\epsilon_m+\epsilon_n\}}$$
$$\left. + \left\{ \int_L \frac{1}{2!}\frac{\partial^2 k_i}{\partial z^2}(T,x)\bar{\nu}(\omega_m,x)\bar{\nu}(\omega_n,x)dx \right\} e^{i\{(-\omega_m-\omega_n)t-\epsilon_m-\epsilon_n\}} \right] \tag{3.63}$$

$$K_i^{(2)}(t) = \frac{1}{4}\sum_{m=1}^{N}\sum_{n=1}^{N} a_m a_n \left[u_i(\omega_m,\omega_n)e^{i\{(\omega_m+\omega_n)t+\epsilon_m+\epsilon_n\}} + \bar{v}_i(\omega_m,\omega_n)e^{i\{(\omega_m-\omega_n)t+\epsilon_m-\epsilon_n\}} \right.$$
$$\left. + v_i(\omega_m,\omega_n)e^{i\{(-\omega_m+\omega_n)t-\epsilon_m+\epsilon_n\}} + \bar{u}_i(\omega_m,\omega_n)e^{i\{(-\omega_m-\omega_n)t-\epsilon_m-\epsilon_n\}} \right] \tag{3.64}$$

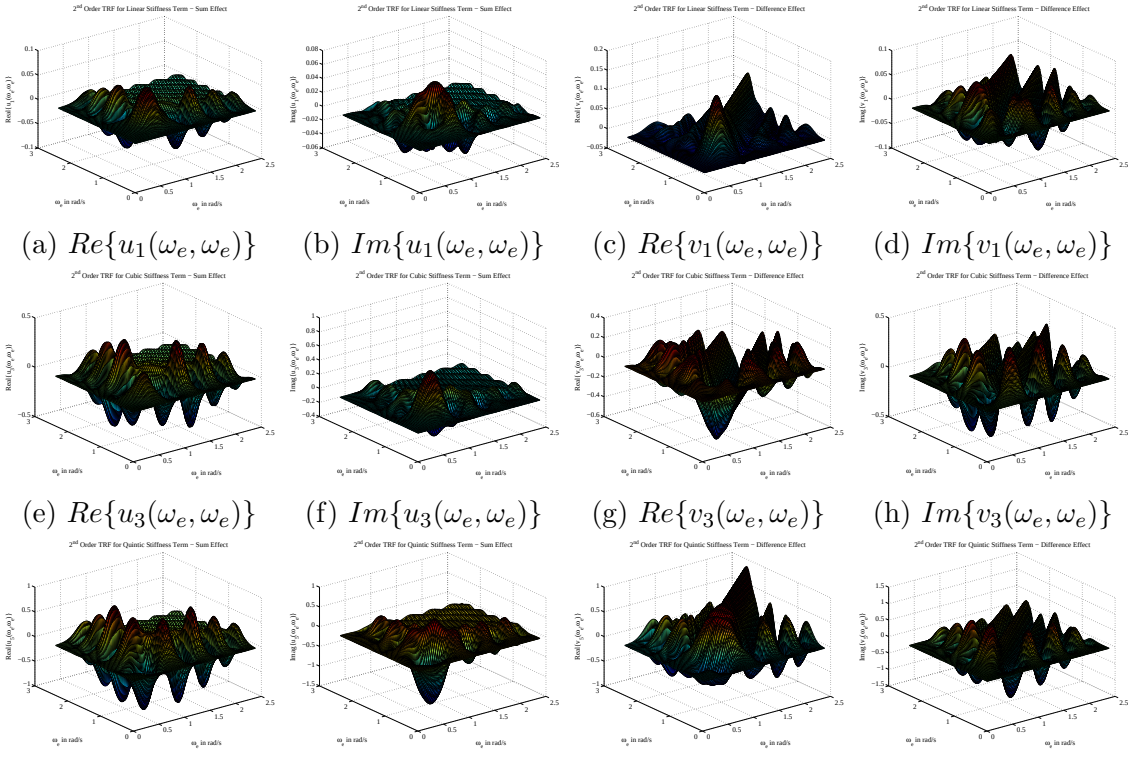

(a) $Re\{u_1(\omega_e, \omega_e)\}$ (b) $Im\{u_1(\omega_e, \omega_e)\}$ (c) $Re\{v_1(\omega_e, \omega_e)\}$ (d) $Im\{v_1(\omega_e, \omega_e)\}$

(e) $Re\{u_3(\omega_e, \omega_e)\}$ (f) $Im\{u_3(\omega_e, \omega_e)\}$ (g) $Re\{v_3(\omega_e, \omega_e)\}$ (h) $Im\{v_3(\omega_e, \omega_e)\}$

(i) $Re\{u_5(\omega_e, \omega_e)\}$ (j) $Im\{u_5(\omega_e, \omega_e)\}$ (k) $Re\{v_5(\omega_e, \omega_e)\}$ (l) $Im\{v_5(\omega_e, \omega_e)\}$

Figure 3.14: Second order transfer functions $u_i(\omega_e, \omega_e)$ and $v_i(\omega_e, \omega_e)$ for Linear ($i = 1$), Cubic ($i = 3$) and Quintic ($i = 5$) Stiffness Coefficients

where $u_i(\omega_e, \omega_e)$ and $v_i(\omega_e, \omega_e)$ are second order transfer functions given by

$$u_i(\omega_m, \omega_n) = \int_L \frac{1}{2!} \frac{\partial^2 k_i}{\partial z^2}(T, x)\nu(\omega_m, x)\nu(\omega_n, x)dx \tag{3.65}$$

$$\bar{v}_i(\omega_m, \omega_n) = \int_L \frac{1}{2!} \frac{\partial^2 k_i}{\partial z^2}(T, x)\nu(\omega_m, x)\bar{\nu}(\omega_n, x)dx \tag{3.66}$$

$$v_i(\omega_m, \omega_n) = \int_L \frac{1}{2!} \frac{\partial^2 k_i}{\partial z^2}(T, x)\bar{\nu}(\omega_m, x)\nu(\omega_n, x)dx \tag{3.67}$$

$$\bar{u}_i(\omega_m, \omega_n) = \int_L \frac{1}{2!} \frac{\partial^2 k_i}{\partial z^2}(T, x)\bar{\nu}(\omega_m, x)\bar{\nu}(\omega_n, x)dx \tag{3.68}$$

The second order transfer functions $u_i(\omega_e, \omega_e)$ and $v_i(\omega_e, \omega_e)$ for $i = 1, 3$ and 5

are shown in Figure 3.14. Thus the effective restoring arm in waves $\overline{GZ}(t,\phi)$ is given by (3.69)

$$\overline{GZ}(t,\phi) = K_1(t)\phi + K_3(t)\phi^3 + K_5(t)\phi^5 + ... \tag{3.69}$$

$$K_i(t) = K_i^{(0)} + K_i^{(1)}(t) + K_i^{(2)}(t) \tag{3.70}$$

where $K_i^{(0)}$ represent the time invariant coefficients of i^{th} power of ϕ for the calm water $\overline{GZ}$ curve, $K_i^{(1)}(t)$ and $K_i^{(2)}(t)$ represent the time varying change of the coefficients of i^{th} power of ϕ for the effective restoring arm $\overline{GZ}$ in waves and are given by (3.71) and (3.72) respectively.

$$K_i^{(1)}(t) = \frac{1}{2}\sum_{m=1}^{N} a_m \left[f_i(\omega_m) e^{i(\omega_m t + \epsilon_m)} + \bar{f}_i(\omega_m) e^{-i(\omega_m t + \epsilon_m)} \right] \tag{3.71}$$

$$\begin{aligned} K_i^{(2)}(t) = \frac{1}{4}\sum_{m=1}^{N}\sum_{n=1}^{N} a_m a_n \Big[& u_i(\omega_m,\omega_n) e^{i\{(\omega_m+\omega_n)t+\epsilon_m+\epsilon_n\}} + \bar{v}_i(\omega_m,\omega_n) e^{i\{(\omega_m-\omega_n)t+\epsilon_m-\epsilon_n\}} \\ & + v_i(\omega_m,\omega_n) e^{i\{(-\omega_m+\omega_n)t-\epsilon_m+\epsilon_n\}} + \bar{u}_i(\omega_m,\omega_n) e^{i\{(-\omega_m-\omega_n)t-\epsilon_m-\epsilon_n\}} \Big] \end{aligned} \tag{3.72}$$

Figure 3.15a shows a comparison of the $\overline{GZ}$ curves in irregular waves predicted by Volterra $\overline{GZ}$ and exact $\overline{GZ}$ methods. The corresponding $\overline{GM}$ values are shown in Figure 3.15b. Although the Volterra $\overline{GZ}$ and exact $\overline{GZ}$ curves look similar, the corresponding $\overline{GM}$ values are significantly different. This means that the resulting dynamics from the Volterra $\overline{GZ}$ and exact $\overline{GZ}$ models will have considerable differences. This is further discussed in section 3.7.

The effective restoring arm in waves $\overline{GZ}(t,\phi)$ is substituted into (3.4) and resulting differential equation is solved for the roll motion. A comparison of the simulated roll motion using the Volterra $\overline{GZ}$ model and SIMDYN is shown in Figure 3.16.

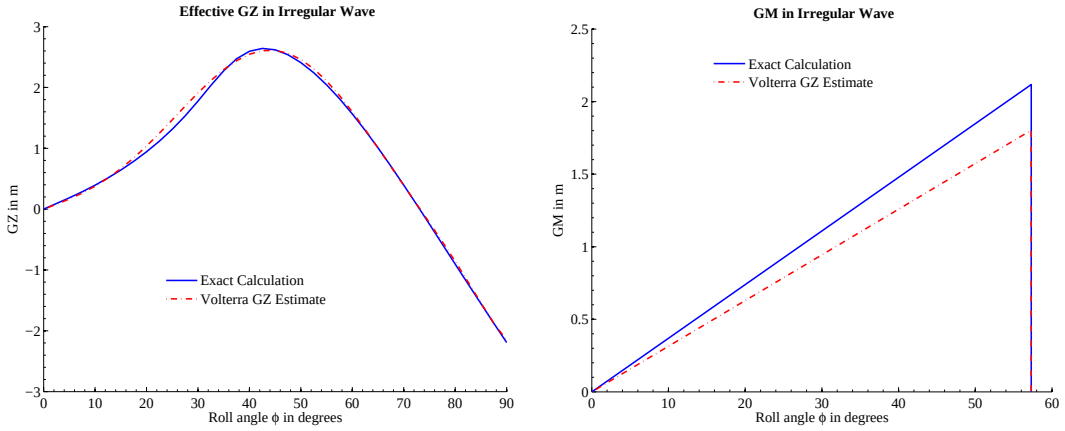

(a) $\overline{GZ}$ curve (b) Corresponding $\overline{GM}$

Figure 3.15: Comparison of $\overline{GZ}$ curve prediction in irregular waves from Volterra $\overline{GZ}$ and exact $\overline{GZ}$ methods at time $t = 350\ s$ for a wave elevation from Bretschneider spectrum with $H_s = 5.0\ m$ and $T_p = 13.0\ s$

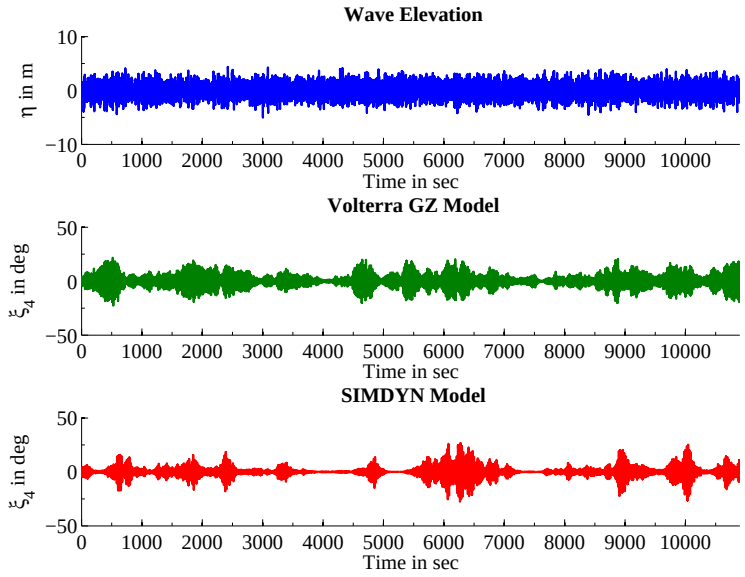

Figure 3.16: Comparison of roll motion between "SIMDYN" and "Volterra $\overline{GZ}$ model" of Pram hull form in a 3-hour realization of Bretschneider spectrum with $H_s = 5.0$ meters and $T_p = 13.0$ seconds

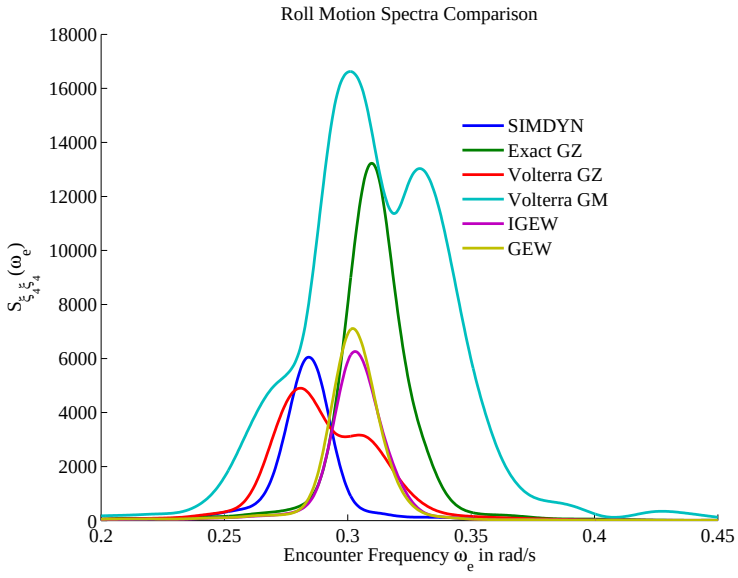

Figure 3.17: Comparison of roll spectra using different modeling techniques

3.7 Comparison of Single Degree of Freedom Models

Five different models have been discussed in this chapter for evaluating $\overline{GZ}(t,\phi)$ for the proposed single degree of freedom model:

1. Exact $\overline{GZ}$ model
2. Volterra $\overline{GM}$ model with time invariant higher order stiffness terms
3. Improved Grim effective wave (IGEW) model incorporating dynamic heave and pitch effects
4. Grim effective wave (GEW) model incorporating dynamic heave and pitch effects
5. Volterra $\overline{GZ}$ model

In order to compare the performance of these models, the simulated roll motion from each of these models is compared against SIMDYN simulations. Figure 3.17

shows the comparison of spectra of roll motion obtained by different models on a single plot. It can be seen that the Volterra $\overline{GM}$ method significantly over-predicts the roll response. The exact $\overline{GZ}$ method and the IGEW $\overline{GZ}$ method (including dynamic heave and pitch effects) lead to a roll spectrum peak shifted away from the roll spectrum peak obtained from SIMDYN simulation. Volterra $\overline{GZ}$ method has a peak matching with SIMDYN simulations but also shows a larger bandwidth.

An interesting observation is that although the $\overline{GZ}$ curve in irregular waves predicted by Volterra $\overline{GZ}$ method is relatively close to exact $\overline{GZ}$ method (as seen in Figure 3.15a), the resulting roll spectrum is significantly different. This illustrates the high sensitivity of parametric roll phenomenon to the nonlinear stiffness in addition to the sensitivity to damping (as discussed in chapter 2). Specifically it can be seen that the slope of the two righting arm curves at zero heel in Figure 3.15b are different which leads significantly different response to the same excitation for the two models.

Each of the single degree of freedom models differ from SIMDYN in terms of the physics involved in them. SIMDYN, described in chapter 2, uses Wheeler [53] stretching to capture the dynamic pressure above the mean water line. However, the single degree of freedom models assume the purely hydrostatic pressure over the instantaneous underwater hull form to calculate the effective restoring arm. As the single degree of freedom models do not include the effect of dynamic pressure in calculation of $\overline{GZ}(t, \phi)$, the resulting roll amplitudes are expected to differ. However, it can also be seen that of the suggested four single degree of freedom models, the Volterra $\overline{GZ}$ model is the closest to SIMDYN simulations and is chosen as the candidate for further analytical analysis. The Volterra $\overline{GZ}$ method will be utilized in chapter 4 and chapter 5 to evaluate the stochastic roll response of the ship in irregular waves.

4. MELNIKOV PROCESS AND PHASE SPACE FLUX EVALUATION

Continuing on the development of SDOF roll models for parametric roll in irregular head seas, this chapter discusses the application of analytical techniques to obtain statistical characteristics of the response. In this chapter, the roll equation of motion is analyzed using the nonlinear dynamical systems approach where more emphasis is placed on the geometrical characteristics of the solution in order to understand the global behavior of multiple solutions.

The nonlinear roll response of a ship in irregular waves has been studied extensively in the past century. Beginning with Froude [22] and Moseley [112] many researchers have investigated this problem to varying degrees of complexity. For a general floating vessel, all the degrees of freedom are coupled to each other. However, using certain simplifying assumptions (Webster [109]) the roll motion can be shown to be decoupled from the other modes of motion. This has led to the analytical description of roll using a single degree of freedom equation of motion [14, 113].

Various different methods have been developed to solve the nonlinear roll equation of motion. The most intuitive approach is to obtain a numerical solution to the system assuming different initial conditions. Testing many initial conditions gives an idea of the nature of nonlinearity and its effect on the response. Thompson et al. [114] used this approach to study the nonlinear roll motion in detail. Other investigators adopting this approach include Spyrou [115] and Virgin [116]. Although this method helps understand the system behavior, it is not practical to determine the effect of various parameters on the system response using this approach. Also due to the need to perform time consuming simulations for several initial conditions, this method is not practically applicable to analyze a set of designs in a short period

of time.

Some analytical approaches applied by researchers to overcome this limitation include the multiple scale method (e.g. Neyfeh and Khdeir [117]), collocation approach and the harmonic balance method (HBM) (e.g. Lou and Xie [118]). However, multiple scale method suffers from the limitation of being applicable to weakly nonlinear systems and cannot be effectively applied to analyze large angle roll motion. Similarly, HBM suffers from a drawback that as the nonlinearity of the problem increases it requires solving the coefficients of a large number of secular terms which make the problem untenable [16].

In contrast to the above approaches, Guckenheimer and Holmes [12] (also Greenspan and Holmes [119] and Wiggins [120]) discussed the application of the Melnikov method (originally due to Melnikov [121]) to analyze complex dynamics exhibited by a nonlinear oscillator. Instead of obtaining the numerical response of the system, this approach focuses on the geometric behavior of the solution in the phase space (defined in section 4.2). Due to its simple approach, generic nature and its capability to analyze strongly nonlinear systems it quickly became the popular approach to analyze strongly nonlinear oscillators exhibiting complex chaotic dynamics. Falzarano [14] was one of the first researchers to apply this technique to investigate capsizing of a ship being excited by regular beam seas.

The Melnikov approach and many of the nonlinear dynamical system approaches were limited to systems which could be expressed as autonomous systems (no external time varying forcing). Since only non-autonomous systems with a periodic excitation could be recast as an autonomous system with higher dimension [13], for a long time this method was limited to regular wave excitation. However, Frey and Simiu [122] in 1993 extended the Melnikov method for application to a nonlinear system being excited by a random forcing by introducing the concept of the Melnikov process

and the rate of phase space flux. They showed that the rate of phase space flux defined as the rate at which the area of safe basin (initial conditions leading to bounded solutions) was being transported out could be related to the area under the Melnikov function when it is non-negative. Hsieh et al. [123] used this approach to analyze the capsizing of a vessel in random beam seas. However, Hsieh et al. [123] still approximated the frequency dependent radiation moment by considering the added mass and radiation damping at the roll natural frequency. Jiang et al. [16] improved upon this model to consider the effect of frequency dependent radiation damping through a convolution integral. Around the same time Vishnubhotla et. al. [124] applied an innovative technique to analyze the complicated dynamics of a vessel in random seas. This method incorporated the use of closed form analytical solutions to be accurate up to the first order of randomness allowing the method to be more accurate than the general Melnikov analysis.

While the Melnikov approach was extensively used to analyze roll motion in beam sea, there is only limited literature discussing its application to parametric roll in head seas. Falzarano [14] briefly discussed the parametrically excited roll motion in regular waves. A further detailed analysis of the behavior of manifolds for a parametrically excited roll motion for both biased and unbiased ships in regular waves was undertaken by Esparza and Falzarano [125]. Falzarano et al. [126] also looked at the problem of saturation induced roll motion in regular waves, where the heave/pitch motion causes a time varying restoring force resulting in a parametrically excited roll motion. Unlike for the directly excited roll motion, there is very limited literature which discusses the application of the Melnikov approach to the problem of parametric roll in irregular waves. This chapter provides a detailed description of the Melnikov method and discusses the extension of the approach for parametrically excited systems and is one of the unique contributions of this dissertation.

4.1 State Space Formulation

We begin with the roll equation of motion given by (4.1) which is the same as described in chapter 3.

$$[I_{44} + A_{44}(\infty)]\phi' + \int_{-\infty}^{u} K_{44}(u-v)\phi'(v)dv + B_1\dot{\phi} + B_2\phi'|\phi'| + \rho g \nabla_0 \overline{GZ}(u,\phi) = 0 \tag{4.1}$$

$\overline{GZ}(u,\phi)$ is approximated by a odd polynomial as described in section 3.6. In case of parametrically excited roll motion it is well known that the response is narrow banded around the linear roll natural frequency of the vessel ω_n. Therefore, it is reasonable to approximate the roll radiation moment using the added mass and radiation damping at the roll natural frequency. This leads to the simplification shown in (4.2).

$$\ddot{x} + \epsilon\delta_1\dot{x} + \epsilon\delta_2\dot{x}|\dot{x}| + \left[\alpha_1 x + \alpha_3 x^3 + \alpha_5 x^5 + ...\right] + \left[\epsilon p_1(t)x + \epsilon p_3(t)x^3 + \epsilon p_5(t)x^5 + ...\right] = 0 \tag{4.2}$$

where

$$x = \phi \qquad t = \omega_n u \qquad \dot{(\ )} = \frac{d}{dt}(\ ) = \frac{1}{\omega_n}\frac{d}{du}(\ ) \tag{4.3}$$

$$\epsilon\delta_1 = \frac{B_1 + A_{44}(\omega_n)}{[I_{44} + A_{44}(\omega_n)]\omega_n} = b_1 \tag{4.4}$$

$$\epsilon\delta_2 = \frac{B_2}{[I_{44} + A_{44}(\omega_n)]} = b_2 \tag{4.5}$$

$$\epsilon p_1(t) = k_1(t) - \alpha_1 \qquad \epsilon p_3(t) = k_3(t) - \alpha_3 \qquad \epsilon p_5(t) = k_5(t) - \alpha_5 \qquad ... \tag{4.6}$$

$$k_1(t) = \frac{K_1(\frac{t}{\omega_n})}{\overline{GM}_0} \qquad k_3(t) = \frac{K_3(\frac{t}{\omega_n})}{\overline{GM}_0} \qquad k_5(t) = \frac{K_5(\frac{t}{\omega_n})}{\overline{GM}_0} \qquad \text{and so on} \tag{4.7}$$

Note that $K_1(u), K_3(u), K_5(u), ...$ are the time varying stiffness terms and are defined in section 3.6. The odd polynomial in ϕ with coefficients $\alpha_1, \alpha_3, \alpha_5, ...$ represent the calm water $\overline{GZ}_0$. From the definition it can be seen that $\alpha_1 = 1$. The parameter ϵ is introduced to represent the relative order of the various terms in the equation of motion. The relative order indicates that the terms proportional to ϵ^0 govern the global geometrical characteristics of the system (in the phase space - defined in section 4.2) and the effect of excitation and damping on the change in global geometrical characteristics is of the order of ϵ. The excitation and damping being proportional to ϵ does not imply that system and developed methods are applicable to only small excitation or damping. However, it is assumed that the excitation and damping do not drastically alter the global geometry of the solutions.

The system can be expressed in the state space form as shown in (4.8) and (4.9) where $x = \phi$ and $y = \dot{\phi}$. It can be seen that the time varying perturbation is $O(\epsilon)$ and the system can be thought of as a Hamiltonian system with small perturbations.

$$\dot{x} = y \tag{4.8}$$

$$\begin{aligned} \dot{y} = &- \left[\alpha_1 x + \alpha_3 x^3 + \alpha_5 x^5 + ...\right] \\ &+ \epsilon \left\{ - \delta_1 \dot{x} - \delta_2 \dot{x}|\dot{x}| - \left[p_1(t)x + p_3(t)x^3 + p_5(t)x^5 + ...\right] \right\} \end{aligned} \tag{4.9}$$

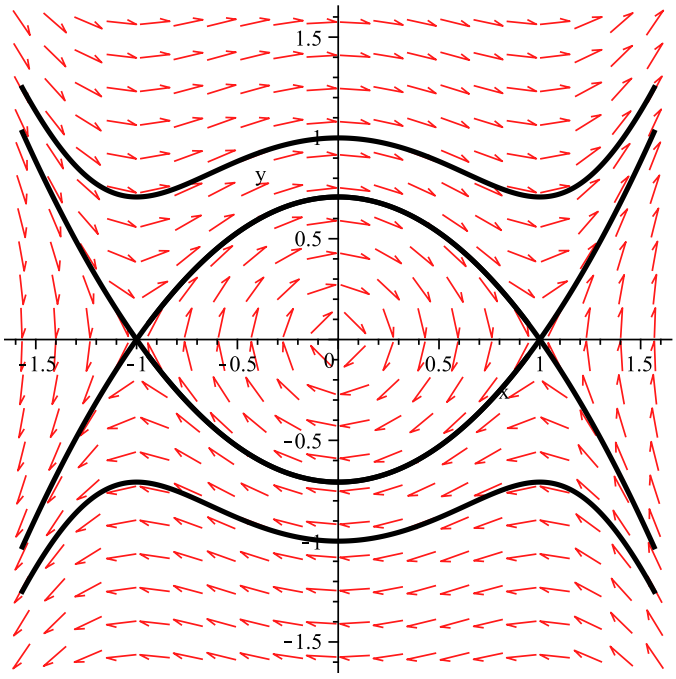

Figure 4.1: Phase portrait for $\ddot{x} + x - x^3 = 0$

4.2 Phase Plane and the Concept of Safe Basin

The unperturbed system ($\epsilon = 0$) is given by (4.10) and (4.11).

$$\dot{x} = y \tag{4.10}$$

$$\dot{y} = -\left[\alpha_1 x + \alpha_3 x^3 + \alpha_5 x^5 + ...\right] \tag{4.11}$$

The solution of the differential equations represented in (4.10) and (4.11) is understood in terms of a map of some interval $I \subset \mathbb{R}^1$ to $\mathbb{R}^n$ where $n = 2$ in this specific

example. The solution is represented as:

$$\begin{bmatrix} x(t) \\ y(t) \end{bmatrix} : I \to \mathbb{R}^2 \tag{4.12}$$

where $[x(t)\ y(t)]^T$ satisfies (4.10) and (4.11). The map $[x(t)\ y(t)]^T$ has the geometrical interpretation of a curve in the domain of the dynamical system $\mathbb{R}^2$. The domain of the dynamical system is also known as the phase space and since for $n = 2$ the phase space is a plane $\mathbb{R}^2$ it is also referred to as the phase plane. Eqns. (4.10) and (4.11) provide the tangent vector of the solution at any point in the phase plane. For this reason, the dynamical system is also referred to as the vector field [13]. The phase portrait of a solution starting at point (x_0, y_0) is defined as the geometric evolution of the solution $(x(t), y(t))$ starting from point $(x(0), y(0)) = (x_0, y_0)$ in the phase plane. Fixed or equilibrium points of the vector field are defined as the points in phase plane where the solution does not change in time and can be calculated using:

$$\dot{x} = y = 0 \tag{4.13}$$

$$\dot{y} = -\left[\alpha_1 x + \alpha_3 x^3 + \alpha_5 x^5 + ...\right] = 0 \tag{4.14}$$

Figure 4.1 shows the plot of the solutions on (x, y) plane (phase plane) for a particular example with $\alpha_1 = 1$, $\alpha_3 = -1$ and $\alpha_5 = \alpha_7 = ... = 0$. It can be seen from the phase portrait (Figure 4.1) that the system has 3 fixed points located at $(0, 0)$ and $(\pm 1, 0)$. The stability of these equilibrium points is found by evaluating the eigenvalues of the Jacobian matrix evaluated at the equilibrium point. For a

Table 4.1: Type of equilibrium point and its stability

Eigenvalues of Jacobian Matrix	Type	Stability
Both real positive	Source	Unstable
Both real negative	Sink	Stable
One real positive, one real negative	Saddle	-
Complex conjugates with positive real part	Unstable Spiral	Unstable
Complex conjugates with negative real part	Stable Spiral	Stable
Purely imaginary	Center	Neutrally stable

general system described by

$$\begin{Bmatrix} \dot{x} \\ \dot{y} \end{Bmatrix} = \begin{Bmatrix} f_1(x,y) \\ f_2(x,y) \end{Bmatrix} \tag{4.15}$$

the Jacobian matrix is given by

$$J = \begin{bmatrix} \frac{\partial f_1}{\partial x} & \frac{\partial f_1}{\partial y} \\ \frac{\partial f_2}{\partial x} & \frac{\partial f_2}{\partial y} \end{bmatrix} \tag{4.16}$$

The eigenvalues of the Jacobian matrix determine the type and stability of the equilibrium point in the phase plane. Table 4.1 lists the various possible values for the eigenvalues of the Jacobian matrix and their correspondence to the type and stability of the equilibrium point.

The equilibrium point at $(0,0)$ corresponds to a center characterized by purely imaginary eigenvalues ($\lambda_{1,2} = \pm i$) of the Jacobian matrix $J = \begin{bmatrix} 0 & 1 \\ 3x^2-1 & 0 \end{bmatrix}_{(0,0)} = \begin{bmatrix} 0 & 1 \\ -1 & 0 \end{bmatrix}$. The equilibrium points at $(\pm 1, 0)$ correspond to saddle points character-

ized by one eigenvalue $\lambda_1 = \sqrt{2} > 0$ and another $\lambda_2 = -\sqrt{2} < 0$ of the Jacobian matrix $J = \begin{bmatrix} 0 & 1 \\ 3x^2 - 1 & 0 \end{bmatrix}_{(\pm 1,0)} = \begin{bmatrix} 0 & 1 \\ 2 & 0 \end{bmatrix}$. The saddle point has both stable and unstable characteristics at the same time.

The flow of the solutions in time is demonstrated by the red arrows in Figure 4.1. In the region above the x-axis $\dot{x} = y > 0$ which implies that x must increase with time and hence the flow is towards the right. Similarly in the region below the x-axis $\dot{x} = y < 0$ which corresponds to decrease of x with time and hence the flow is towards the left. It can be seen from Figure 4.1 that the phase space flow approaches towards the saddle points along two directions and also moves away along two other directions. The limiting solutions along the curve (black curve in Figure 4.1) approaching the saddle point are called stable manifolds and the limiting solutions along the curve (black curve in Figure 4.1) moving away from the saddle point are called the unstable manifolds. It can be seen that the unstable manifold of saddle point $(-1, 0)$ coincides with the stable manifold of saddle point $(1, 0)$ and vice-versa for the unperturbed system.

The limiting solution joining the fixed points at $(\pm 1, 0)$ is also known as the separatrix or the heteroclinic manifold. The heteroclinic manifolds separate the solution space into two regions. The solutions in the region beyond the separatrix do not possess any oscillatory behavior and lead to capsize by escaping to $\pm\infty$. The solutions inside the eye-shaped region between $(\pm 1, 0)$ corresponds to bounded oscillatory solutions about the fixed point $(0, 0)$. For this reason, the area inside the eye-shaped region is also termed as the safe basin. The separatrices are also otherwise referred to as the invariant manifolds due to the property that if the system starts with an initial condition on any of the invariant manifolds, it will continue to stay on it for all future and past times [120].

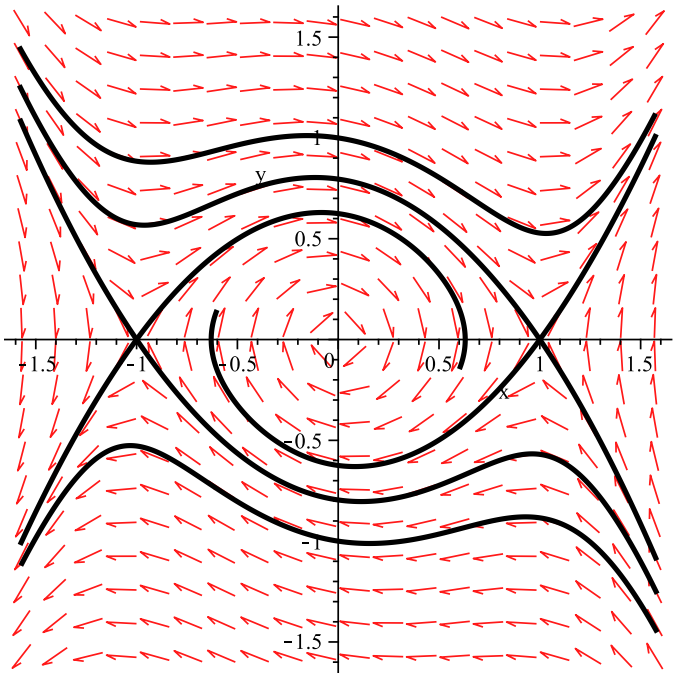

Figure 4.2: Phase portrait for $\ddot{x} + 0.1\dot{x} + 0.05\dot{x}|\dot{x}| + x - x^3 = 0$

Introducing damping or excitation (not necessarily harmonic or periodic) results in the separation of the heteroclinic manifolds as shown in Figure 4.2. A time varying excitation leads to a time varying position of the fixed points in the phase space. If the excitation is periodic, then the position of the fixed point and the vector field given by (4.8) and (4.9) will be exactly the same at any two times separated by the period of excitation. Thus, the fixed points are transformed into periodic orbits and the invariant manifolds oscillate periodically with time. However, sampling the phase space every period of excitation provides a unique insight into the dynamics of the system and was originally introduced by Poincaré and is hence termed a Poincaré map. A trajectory in the phase space when observed in Poincaré map is described by a discrete set of points on the trajectory sampled every period of the excitation. Thus a periodic orbit resulting due to a periodic excitation still appears as a fixed point

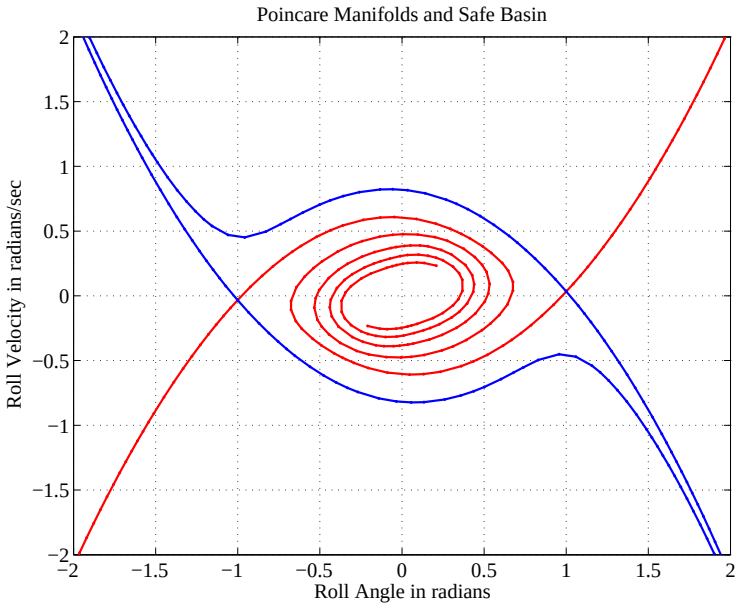

Figure 4.3: Numerically computed Poincaré manifolds for $\ddot{x} + 0.1\dot{x} + 0.05\dot{x}|\dot{x}| + (1 + 0.1\sin(2t))x - x^3 = 0$

on a Poincaré map. Similarly, the oscillating invariant manifolds appear as a fixed curves on a Poincaré map. Numerically computed Poincaré manifolds for system with damping and excitation are shown in Figure 4.3. The numerical computation of Poincaré manifolds is performed by implementing the algorithm described by Parker and Chua [127] in MATLAB. The blue curves denote the stable manifolds and the red curves denote the unstable manifolds. The bounded region between the blue stable manifolds are the set of initial conditions which when iterated in time will converge to the fixed point at $(0, 0)$.

When the excitation is increased beyond a critical level, the separated heteroclinic manifolds can intersect with each other. However the heteroclinic manifolds are themselves invariant implying that if a system starts with an initial condition on a manifold, all its forward and backward iterations under Poincaré map will also lie on the same manifold. Now if the manifolds intersect each other once, this implies

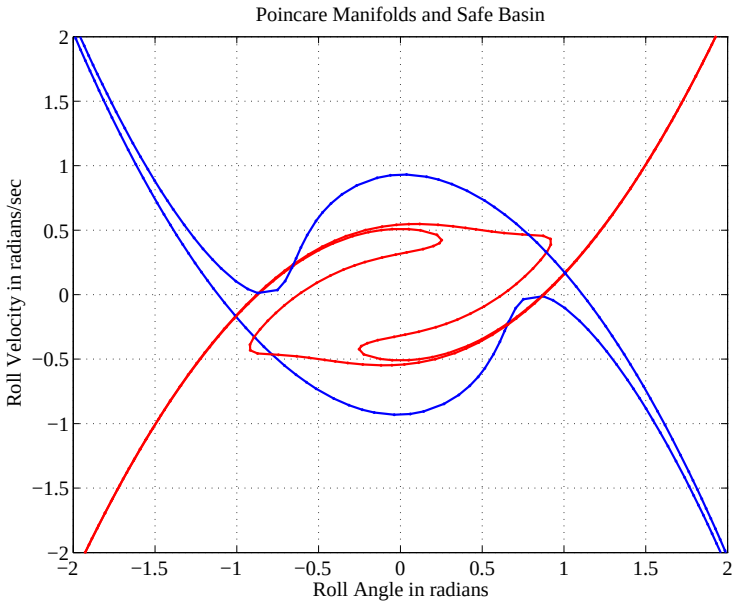

Figure 4.4: Numerically computed Poincaré manifolds for $\ddot{x} + 0.1\dot{x} + 0.05\dot{x}|\dot{x}| + (1 + 0.5\sin(2t))x - x^3 = 0$

that if the system had an initial condition corresponding to this intersection, then the further iterations of the Poincaré map will also have to be points of intersection of the manifolds. Thus there will be infinitely many intersection between the stable and unstable manifolds. These infinite intersections lead to the formation of lobes of phase space entrapped between the two manifolds. The lobes of initial conditions exhibit complicated dynamics which creates a possibility for the solutions near the separatrices to be transported out of the safe basin. Such transitions usually may lead to the occurrence of chaotic responses and even capsizing situations [128, 114, 116]. Numerically computed Poincaré manifolds for the same system as shown in Figure 4.3 with higher forcing are shown in Figure 4.4. Figure 4.4 only shows a few intersection points between the stable and unstable manifolds due to the finite length computation of the numerical scheme. In theory if the manifolds are fully computed then they will intersect over and over infinite number of times.

Wiggins [120, 13] discusses chaotic responses to harmonically excited systems using Poincaré maps in detail. However, if the excitation (direct or parametric) is random then eventually at some time the excitation will be large enough to cause the intersection of stable and unstable manifolds and transport from the safe to unsafe region will occur eventually. It is also important to note that in case of random excitation, the periodicity of vector field does not exist which means that the invariant manifolds can no longer be visualized.

However, as discussed above it is the intersections between the stable and unstable manifolds which allow for the possibility of transport from safe to unsafe region. Melnikov [121] came up with a clever idea to analytically calculate the transverse distance between the manifolds. This distance given by the Melnikov function can be calculated even when the manifolds themselves cannot be visualized. This opened the door for further study of dynamics of nonlinear dynamical systems excited by random excitation. Hsieh et al. [15] applied this approach to study the roll motion of a vessel in beam seas and suggested that the transport between the safe and unsafe regions becomes significant at certain critical levels of excitation which can be quantified by the Melnikov function.

4.3 Melnikov Function

As previously seen in Figure 4.2, perturbation of the unforced and undamped system by excitation and damping leads to the separation of the stable and unstable manifolds of the heteroclinic separatrix. The separation $d(t_0)$ between them to $O(\epsilon)$ is defined as the Melnikov function and can be shown to be equal to the expression

in (4.18)

$$d(t_0) = \epsilon M(t_0) + O(\epsilon^2) \tag{4.17}$$

$$M(t_0) = \int_{-\infty}^{\infty} y_0(t) \Bigg\{ -\delta_1 y_0(t) - \delta_2 y_0(t)|y_0(t)| - \left[p_1(t+t_0)x_0(t) + p_3(t+t_0)x_0^3(t) + p_5(t+t_0)x_0^5(t) + ...\right] \Bigg\} dt \tag{4.18}$$

where $x_0(t)$ and $y_0(t)$) are solutions representing the separatrices of the unperturbed system (Eqns. (4.10) and (4.11)). The theoretical proof that the Melnikov function represents the separation distance to $O(\epsilon)$ can be found in classical texts on nonlinear dynamical systems [12, 120]. An alternate approach to derive the distance between the manifolds was investigated by Vishnubhotla [124] with an accuracy up to the first order of randomness. It was also shown from this method that considering up to $O(\epsilon)$ the expressions for the distance between the manifolds was equivalent to the Melnikov function.

The Melnikov function can be separated into two parts - the time invariant mean component $\overline{M}$ which depends on the damping and the time varying oscillatory part $\tilde{M}(t_0)$ which depends on the excitation.

$$M(t_0) = \overline{M} + \tilde{M}(t_0) \tag{4.19}$$

where

$$\overline{M} = \int_{-\infty}^{\infty} y_0(t) \Bigg\{ -\delta_1 y_0(t) - \delta_2 y_0(t)|y_0(t)| \Bigg\} dt \tag{4.20}$$

$$\tilde{M}(t_0) = \int_{-\infty}^{\infty} y_0(t)\Big\{ - \big[p_1(t+t_0)x_0(t) + p_3(t+t_0)x_0^3(t) + p_5(t+t_0)x_0^5(t) + ...\big] \Big\} dt \tag{4.21}$$

It can further be expressed as

$$\tilde{M}(t_0) = \tilde{M}_{p_1}(t_0) + \tilde{M}_{p_3}(t_0) + \tilde{M}_{p_5}(t_0) + ... \tag{4.22}$$

where

$$\tilde{M}_{p_1}(t_0) = - \int_{-\infty}^{\infty} y_0(t)x_0(t)p_1(t+t_0)dt \tag{4.23}$$

$$\tilde{M}_{p_3}(t_0) = - \int_{-\infty}^{\infty} y_0(t)x_0^3(t)p_3(t+t_0)dt \tag{4.24}$$

$$\tilde{M}_{p_5}(t_0) = - \int_{-\infty}^{\infty} y_0(t)x_0^5(t)p_5(t+t_0)dt \tag{4.25}$$

In the case of systems excited by only direct excitation the oscillatory component of the Melnikov function is a linear function of only a single component - roll excitation moment [14, 123, 16, 21]. However, for the case of parametric excitation, $\tilde{M}(t_0)$ is a sum of stochastic processes as shown in (4.22). Note that the evaluation of the Melnikov function requires only the knowledge of the closed form solution of the unperturbed system $(x_0(t), y_0(t))$. As the degree of odd polynomial used to represent the stiffness is increased, it becomes harder to obtain the unperturbed solutions $(x_0(t), y_0(t))$ in closed form [129]. A cubic restoring model is the most commonly used model for representing the stiffness in directly excited systems and has been applied and investigated well by Falzarano et al. [128] and Hsieh et al. [15] for the problem of ship rolling. However, only a few researchers have investigated the fifth and higher order restoring models [14, 130, 131]. Although up to 5^{th} order stiffness

it is still possible to get analytical expression for $(x_0(t), y_0(t))$, for higher orders of stiffness $(x_0(t), y_0(t))$ can only be evaluated numerically [14].

Ideally one would like to use a 9^{th} or 11^{th} order polynomial to represent the nonlinear roll stiffness. However, due to the lack of closed form expressions much of the literature is limited to 3^{rd} or at most 5^{th} order representations. While the 3^{rd} order polynomial approximation enables capturing a softening stiffness, a 5^{th} order representation is required to capture the initial hardening and eventual softening of a typical righting arm curve for wall sided ships. This effect of initial hardening and eventual softening is more enhanced when the righting arm is calculated for the condition of wave crest at midship and is shown in Figure 4.5 for the Pram hull form. The variation in $\overline{GZ}$ due to the location of wave crest relative to the ship hull is shown in Figure 4.6. As the wave crest moves away from the midship leading to the situation of trough at midship, the initial hardening effect is less pronounced. However to accurately capture both cases one must use at least a 5^{th} order representation. For this reason, in this investigation of Melnikov methods for the problem of parametric rolling, a 11^{th} order restoring term will be used to represent the nonlinear roll stiffness. Since no closed form solutions are available, the unperturbed solutions in this study are evaluated numerically.

Each of the components of the oscillatory part of Melnikov function $\tilde{M}_{p_i}(t_0)$ for $i = 1, 3, 5, ...$ are linear functions of the parametric excitations $p_i(t)$ for $i = 1, 3, 5, ...$ respectively. From chapter 3, it is known that the parametric excitations $p_i(t)$ for $i = 1, 3, 5, ...$ are related to the wave elevation through various orders of Volterra transfer functions. A comparison of the first and second order of $\overline{GM}$ variation obtained using the Volterra $\overline{GZ}$ formulation for irregular sea state characterized by Bretschneider spectrum with $H_s = 4\ m$ and $T_p = 13\ s$ is shown in Figure 4.7. It can be seen that the second order of variation of $\overline{GM}$ is significantly smaller in magnitude than the

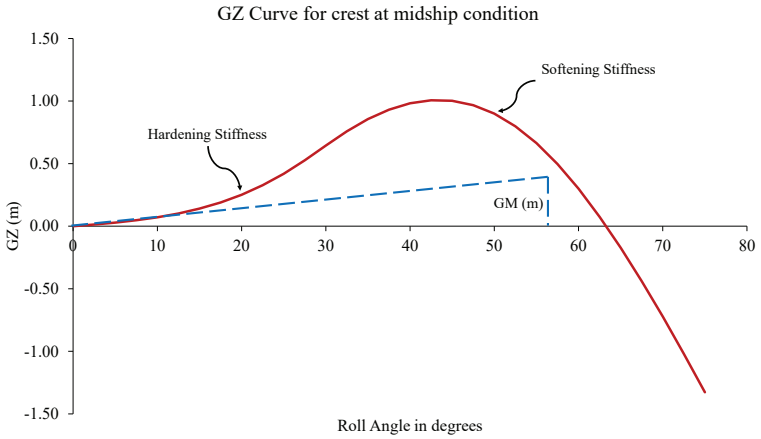

Figure 4.5: $\overline{GZ}$ curve of Pram hull in case of wave crest at midship

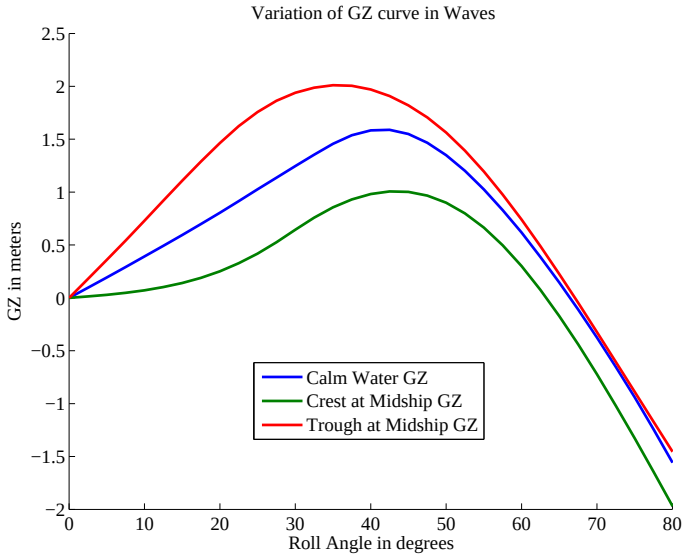

Figure 4.6: $\overline{GZ}$ curve variation in waves

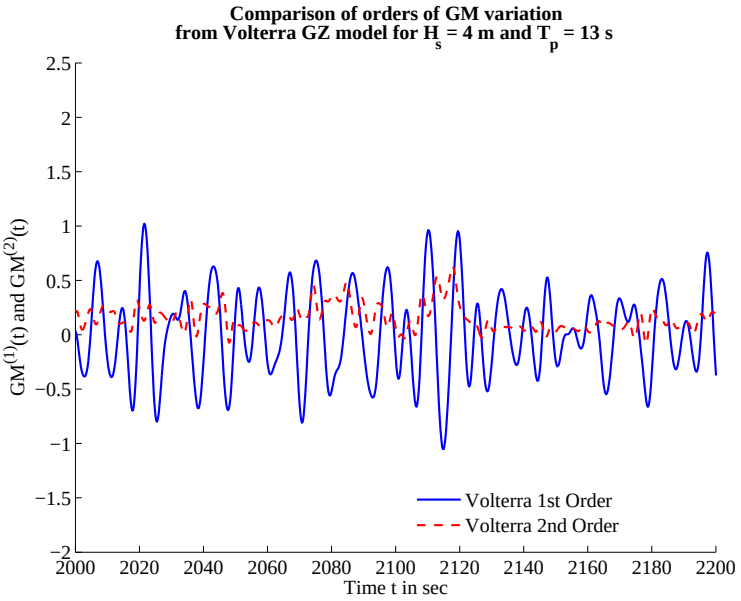

Figure 4.7: Comparison of first and second order of $\overline{GM}$ variation from Volterra $\overline{GZ}$ model for $H_s = 4\ m$ and $T_p = 13\ s$

first order variation.

If the parametric excitations $p_i(t)$ for $i = 1, 3, 5, ...$ are evaluated using only the first order transfer functions, then by definition $p_i(t)$ for $i = 1, 3, 5, ...$ are all zero mean random processes. Under the assumption that wave elevation is an ergodic Gaussian process, it follows that $p_i(t)$ for $i = 1, 3, 5, ...$ evaluated using only the first order Volterra transfer functions will also be ergodic Gaussian processes. Since $\tilde{M}_{p_i}(t_0)$ for $i = 1, 3, 5, ...$ are linear functions of the parametric excitations $p_i(t)$ for $i = 1, 3, 5, ...$, it also follows that $\tilde{M}_{p_i}(t_0)$ for $i = 1, 3, 5, ...$ are ergodic Gaussian processes. From (4.22), $\tilde{M}(t_0)$ is a sum of Gaussian random variables $\tilde{M}_{p_i}(t_0)$ for $i = 1, 3, 5, ...$ and hence has a Gaussian distribution as well. The spec-

trum of $\tilde{M}(t_0)$ expressed as $S_{\tilde{M}\tilde{M}}(\omega)$ is given by

$$S_{\tilde{M}\tilde{M}}(\Omega) = \sum_{j=1,3,5,\ldots}^{N_q} \sum_{k=1,3,5,\ldots}^{N_q} S_{\tilde{M}_{p_j}\tilde{M}_{p_k}}(\Omega) \tag{4.26}$$

where N_q is the order of stiffness considered in the Volterra Model (in this work a 11^{th} order stiffness is used) and the cross spectra $S_{\tilde{M}_{p_j}\tilde{M}_{p_k}}(\Omega)$ are given by

$$S_{\tilde{M}_{p_j}\tilde{M}_{p_k}}(\Omega) = (2\pi)^2 \bar{T}_j(\Omega) T_k(\Omega) S_{p_j p_k}(\Omega) \tag{4.27}$$

$$= \epsilon^2 (2\pi)^2 \bar{T}_j(\Omega) T_k(\Omega) \bar{f}_j(\Omega) f_k(\Omega) S_{\eta\eta}(\Omega) \tag{4.28}$$

Note that $\bar{(\,)}$ represents complex conjugate, $\Omega = \frac{\omega_e}{\omega_n}$ is the scaled encounter frequency and $S_{\eta\eta}(\Omega)$ is the wave encounter spectrum. f_j represents the first order Volterra transfer function and is given by (3.61). The transfer function T_j is the Fourier transform of $-y_0(t)x_0^j(t)$ and is given by

$$T_j(\Omega) = \frac{1}{2\pi} \int_{-\infty}^{\infty} -y_0(t) x_0^j(t) e^{-i\Omega t} dt \tag{4.29}$$

Since each of the components of the oscillatory part of the Melnikov function have zero mean, $\tilde{M}$ is also a zero mean ergodic Gaussian process. The mean square value of $\tilde{M}$ is given by

$$\begin{aligned} \sigma_{\tilde{M}}^2 &= E[\tilde{M}^2(t_0)] \\ &= \int_0^{\infty} S_{\tilde{M}\tilde{M}}(\Omega) d\Omega \\ &= \epsilon^2 (2\pi)^2 \sum_{j=1,3,5,\ldots}^{N_q} \sum_{k=1,3,5,\ldots}^{N_q} \int_0^{\infty} \bar{T}_j(\Omega) T_k(\Omega) \bar{f}_j(\Omega) f_k(\Omega) S_{\eta\eta}(\Omega) d\Omega \end{aligned} \tag{4.30}$$

Since a Gaussian distribution of a process is characterized by its mean and stan-

dard deviation, the probability density function of $\tilde{M}$ is given by

$$p_{\tilde{M}}(x) = \frac{1}{\sqrt{2\pi}\sigma_{\tilde{M}}} \exp\left(-\frac{x^2}{2\sigma_{\tilde{M}}^2}\right) \tag{4.31}$$

4.4 Phase Space Flux

By its definition, for a system with small excitation and damping, a negative value of the Melnikov function $M(t_0) < 0$ indicates that the stable manifold lies outside of the unstable manifold as depicted in Figure 4.2. If for a system the unstable manifold lies outside of the stable manifold for all times, then all the solutions with initial conditions outside the boundary will be unstable and lead to capsize and the Melnikov function $M(t_0) > 0$ for all times. A unforced system with negative damping coefficient is an example where the Melnikov function will always be greater than zero.

However, the more commonly encountered case is the multiple intersections of the stable and unstable manifolds caused by higher levels of excitation leading to continual switching of the relative orientations of the stable and unstable manifolds. This leads to the possibility of stable initial conditions near the boundary to be transported into the unsafe regions at some future time. The dynamics of these lobes of phase space with switching boundaries is described in more detail by Wiggins [120] and Falzarano [14]. In this case, the Melnikov function switches sign depending on whether the stable or unstable manifold is on the outside at that particular time. The amount of phase space transported out of the safe region is related to the area of the lobes formed where the unstable manifold lies outside the stable manifold. Since the Melnikov function is representative of the distance between the manifolds, the area of the lobes where the unstable manifold lies outside of the stable manifold can

be quantified in terms of the area under the Melnikov function where it is positive [122, 15, 132]. The rate at which the solutions escape from the safe basin can then be calculated by taking a long term average of the positive part of the Melnikov function. This quantity is known as the rate of phase-space flux Φ and is defined mathematically as shown in (4.32) [133]

$$\Phi = \lim_{T\to\infty} \frac{1}{2T} \int_{-T}^{T} M^{+}(t_0) dt_0 \tag{4.32}$$

where $M^{+}(t_0)$ represents the positive part of the Melnikov function and is given by

$$M^{+}(t_0) = \begin{cases} M(t_0) & \text{if } M(t_0) \geq 0 \\ 0 & \text{otherwise} \end{cases} \tag{4.33}$$

Since $\tilde{M}(t_0)$ is an ergodic Gaussian process, it follows that the Melnikov process $M(t_0)$ is also an ergodic Gaussian process with a mean value of $\overline{M}$. Thus, the long term time average in (4.32) can be equated to the ensemble average as shown in (4.34).

$$\begin{aligned} \lim_{T\to\infty} \frac{1}{2T} \int_{-T}^{T} M^{+}(t_0) dt_0 &= E\left[M^{+}(t_0)\right] \\ &= E\left[(\overline{M} + \tilde{M}(t_0))^{+}\right] \end{aligned} \tag{4.34}$$

Using the probability density function for $\tilde{M}$ shown in (4.31), the rate of phase-

space flux is given by

$$\begin{aligned}
\Phi &= E\left[(\overline{M}+\tilde{M}(t_0))^+\right] \\
&= \int_{-\overline{M}}^{\infty}(x+\overline{M})p_{\tilde{M}}(x)dx \\
&= \int_{-\overline{M}}^{\infty}(x+\overline{M})\frac{1}{\sqrt{2\pi}\sigma_{\tilde{M}}}\exp\left(-\frac{x^2}{2\sigma_{\tilde{M}}^2}\right)dx \\
&= \sigma_{\tilde{M}}\int_{-\frac{\overline{M}}{\sigma_{\tilde{M}}}}^{\infty}(z+\frac{\overline{M}}{\sigma_{\tilde{M}}})\frac{1}{\sqrt{2\pi}\sigma_{\tilde{M}}}\exp\left(-\frac{z^2}{2}\right)dz \\
&= \left[\sigma_{\tilde{M}}p\left(\frac{-\overline{M}}{\sigma_{\tilde{M}}}\right)+\overline{M}\left(1-P\left(\frac{-\overline{M}}{\sigma_{\tilde{M}}}\right)\right)\right] \qquad (4.35)
\end{aligned}$$

The variation of rate of phase space flux Φ with significant wave height for various peak periods is shown in Figure 4.8. The rate of phase space flux is non-zero for all non-zero wave heights which means that the system has a finite probability of capsize as soon as excitation is applied. However, the probability of capsize will be extremely low for small wave heights and will assume significant values only for higher wave heights. The corresponding variation of rate of phase space flux Φ with peak period of spectrum for various significant wave heights is shown in Figure 4.9. The rate of phase space flux increases with an increase in peak period until $T_p \approx 15\ s$ and then decreases with further increase in period. This is consistent with the highly tuned nature of parametric roll where the system stops to demonstrate a parametric response as the excitation period moves away from the $2:1$ subharmonic resonant period (see appendix D). For the Pram hull form the $2:1$ excitation period corresponds to $T \approx 13\ s$.

If $\sigma_{\tilde{M}}^{(1)}$ is denoted as the RMS value of the oscillatory part of the Melnikov function when the system is excited by a unit significant wave height, the rate of phase space

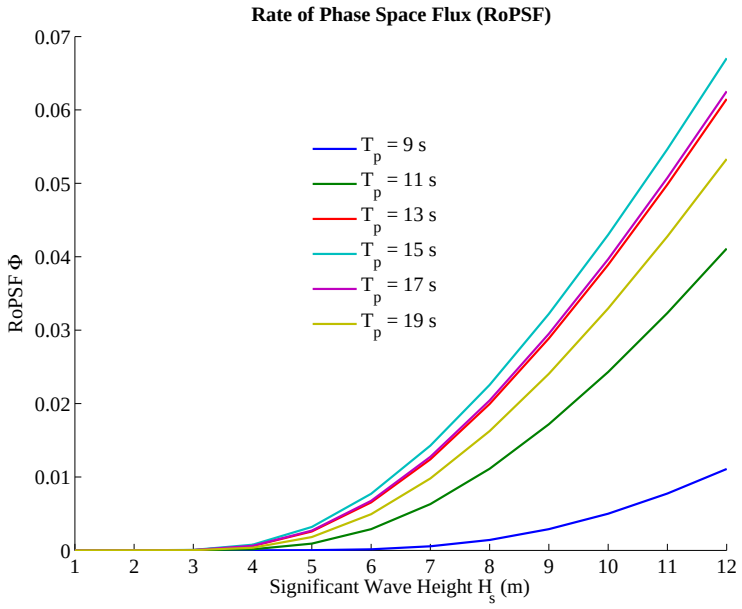

Figure 4.8: Variation of the rate of phase space flux with significant wave height H_s for various peak periods T_p

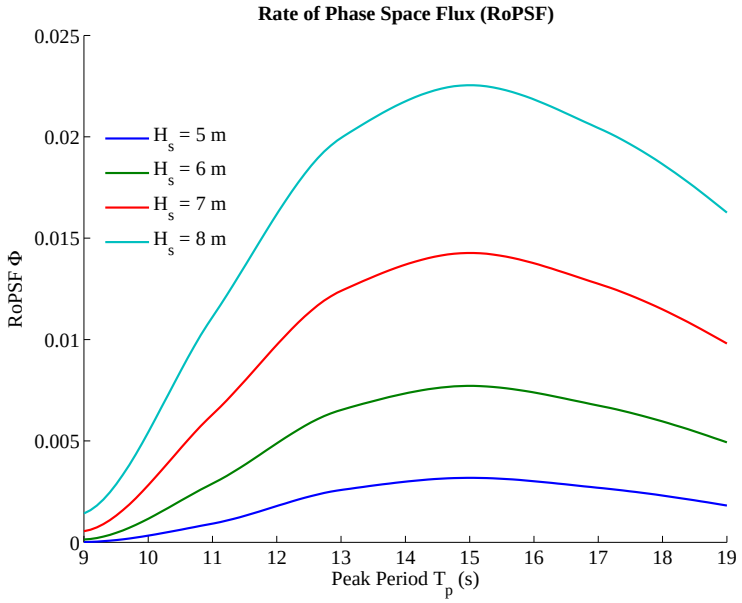

Figure 4.9: Variation of the rate of phase space flux with peak periods T_p for various significant wave heights H_s

flux can be expressed as

$$\Phi = \left[\sigma_{\tilde{M}}^{(1)} H_s p\left(\frac{-\overline{M}}{\sigma_{\tilde{M}}^{(1)} H_s}\right) + \overline{M}\left(1 - P\left(\frac{-\overline{M}}{\sigma_{\tilde{M}}^{(1)} H_s}\right)\right)\right] \tag{4.36}$$

As the significant wave height is increased, the rate of phase space flux also increases steadily until it reaches a linear asymptote. This limiting behavior can also be derived mathematically from (4.36) by taking the limit $H_s \to \infty$. The rate of phase space flux approaches a linear asymptote given by (4.37).

$$\Phi = \left[\frac{1}{\sqrt{2\pi}}\sigma_{\tilde{M}}^{(1)} H_s + \frac{1}{2}\overline{M}\right] \tag{4.37}$$

The linear asymptote has an intercept of H_s^* on the H_s axis corresponding to zero phase space flux. This value is defined as the critical wave height and corresponds to the significant wave height at which substantial phase space flux is initiated. The mathematical expression for H_s^* is given by

$$H_s^* = -\sqrt{\frac{\pi}{2}}\frac{\overline{M}}{\sigma_{\tilde{M}}^{(1)}} \tag{4.38}$$

Since the rate of phase space flux increases almost linearly with significant wave height beyond $H_s = H_s^*$, the critical significant wave height H_s^* can be thought of as providing a limiting value of significant wave height H_s for a given peak period beyond which the vessel has a higher probability of capsizing. Although an exact mathematical dependence between critical significant wave height and the probability of capsize is unknown at present, there are several researchers including Hsieh et. al. [15] and Jiang et. al. [132, 16] who have demonstrated that the critical significant wave height H_s^* predicted using the Melnikov analysis does agree well with the estimated H_s boundary (calculated using Monte Carlo simulations) beyond which

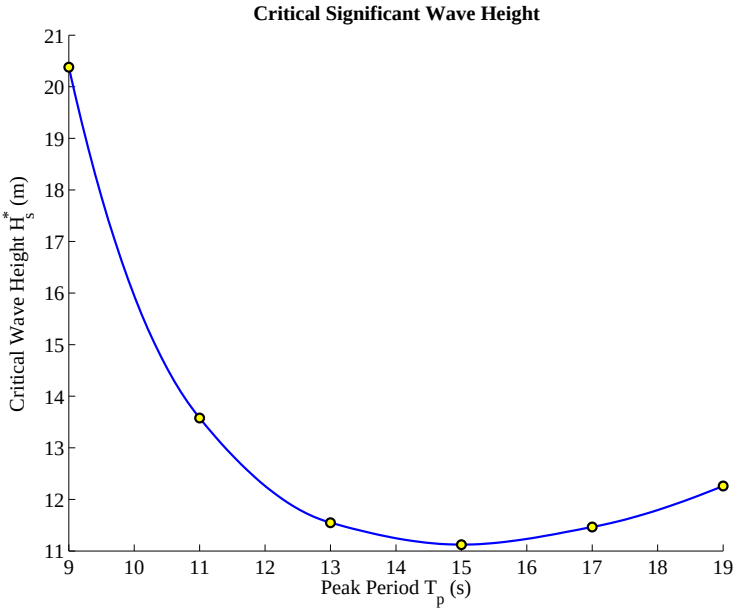

Figure 4.10: Variation of critical significant wave height with the peak period of the spectrum

capsize probability increases rapidly.

The variation of critical significant wave height with peak period of the spectrum is shown in Figure 4.10. Due to the highly tuned nature of parametric excitation and observed variation of rate of phase space flux with peak period (see Figure 4.9), the critical significant wave height is expected to be lowest when the peak period is close to the $2:1$ subharmonic resonance period (see appendix D). It is also expected to increase quickly as the peak period shifts away from the subharmonic resonance period. Figure 4.10 displays this expected behavior of the critical significant wave height.

However, if a designer deems the capsize probability corresponding to the critical significant wave height H_s^* to be either too high or too low, an alternate criterion can be used to estimate the limiting significant wave height based on specified values of rate of phase space flux. In this case, the limiting value of H_s is obtained by solving

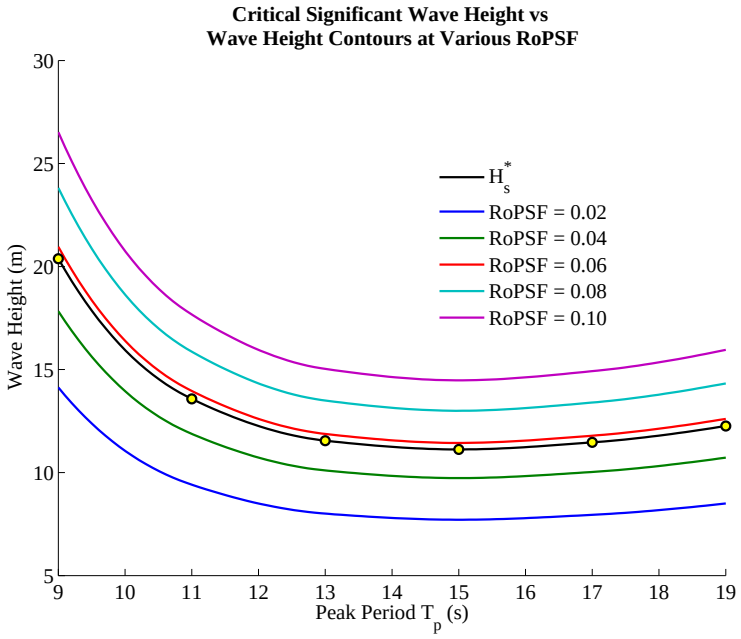

Figure 4.11: Variation of critical significant wave height with the peak period of the spectrum

(4.36) after setting the rate of phase space flux to a prescribed value chosen by the designer. A comparison of the limiting values of H_s using this approach for various specified values of rate of phase space flux and the critical significant wave height H_s^* is shown in Figure 4.11. Although H_s^* seems to have a trend similar to the limiting H_s obtained by equating phase space flux to a constant value, it is important to remember that the rate of phase space flux Φ is not constant as the peak period varies along the H_s^* curve.

It can be seen from (4.36) and (4.38) that both the rate of phase space flux Φ and the critical significant wave height H_s^* depend on the mean value of the Melnikov function $\overline{M}$ and the root mean square (RMS) value of the oscillatory component of the Melnikov function when the system is excited by a unit significant wave height $\sigma_{\tilde{M}}^{(1)}$. While $\overline{M}$ depends on the damping in the system, $\sigma_{\tilde{M}}^{(1)}$ is a function of the

input wave elevation. While the calculation of $\overline{M}$ and $\sigma^{(1)}_{\tilde{M}}$ are not based off of analytical expressions (due to the use of 11^{th} order stiffness instead of a 3^{rd} or 5^{th} order approximation with closed form expressions for $[x_0(t)y_0(t)]^T$), the computation involved is minuscule. Thus, the rate of phase space flux Φ and the critical significant wave height H_s^* can be effectively used as design criteria for assessment of stability of parametric response of a vessel in head seas.

Simiu [133] compared the rate of phase space flux of a Duffing-Holmes oscillator with the mean escape rate $\frac{1}{\tau_e}$ (defined as the inverse of mean first passage time τ_e) estimated from Monte Carlo simulations and demonstrated that the two quantities are proportional to each other. Based on this observed proportionality Simiu further suggested the possible use of rate of phase space flux as a measure of the escape rate. A similar comparison of the mean escape rate and the rate of phase space flux for directly excited roll motion was investigated by Su and Falzarano [17]. In this study too a comparison between the rate of phase space flux and the mean escape rate for the parametrically excited roll motion is discussed in chapter 6.

5. STOCHASTIC AVERAGING OF ENERGY ENVELOPE

In contrast to the nonlinear dynamical systems approach utilized in chapter 4, this chapter explores a different technique known as stochastic averaging which is based on the principles of stochastic dynamics. As the stochastic averaging technique builds upon the concepts of stochastic dynamics, it is important to first describe the basic concepts and terminology of stochastic dynamics. However, in the interest of brevity, this material is described in detail in appendix E and will be referred to as and when needed.

It is well known that for a linear system excited by a Gaussian excitation, the response also follows a Gaussian distribution. However, when the equations of motion are nonlinear, such as for the problem of parametric roll (as described in chapter 3), the probability distribution of the response can deviate significantly from a Gaussian distribution (as was shown in chapter 2). Obtaining a probabilistic description of the response for such systems is often a challenge. A few of the analytical methods available to solve the problem of nonlinear random vibration include Markov methods, equivalent linearization [134], equivalent non-linearization[135, 136], moment and cumulant closure techniques [137, 138, 87], perturbation methods, stochastic averaging and numerical simulations.

Markov methods refer to the approximation of the excitation in the equations of motion by a white noise process (see appendix E for definition). A system excited by colored noise (see appendix E for definition) can also be recast as a higher dimensional system with white noise input by using a filter to transform the white noise into the colored noise. Modeling the excitations using white noise processes comes at the cost of introducing more state variables (corresponding to the filter) in

the system. For a system whose excitations are modeled as white noise processes, the equation of motion can be expressed in the vector form as an Itô stochastic differential equation (SDE). See appendix E for mathematical description of SDEs. The probability distribution of the response is obtained by solving the corresponding Fokker-Planck-Kolmogorov (FPK) equation (see appendix E), alternatively also known as Kolmogorov's forward equation [84]. If the system is stable and achieves stationarity eventually, the time derivative can be set to zero and the corresponding equation can be solved to obtain a stationary probability distribution of the response. However, exact analytical expressions exist only for very few special cases (see for example Caughey [139]). For higher order systems (with many state variables) very few exact solutions are available.

In cases where exact solutions are unavailable, many researchers have investigated the numerical approach to solve the FPK equation. Some of the methods in this approach include iterative methods [140], series expansion methods [137, 138], random walk analogies and path integral methods [141, 142, 143]. However, obtaining exact solutions to the FPK equation is generally a time consuming procedure and is impractical for assessing various design iterations in the basic design phase.

However, in the recent years, the stochastic averaging technique has received a lot of attention due its ability to reduce the dimension of the stochastic system and thus reduce the complexity of the problem. One of the other advantages of stochastic averaging is its applicability to systems excited by not only white but also colored noise. The method of stochastic averaging is originally credited to Stratonovich [137, 138]. It aims at approximating an actual process by a representative Markov process when the excitation process has a larger bandwidth (broad-banded) as compared to the response. Since its proposition by Stratonovich [137], this technique has been examined in detail by many researchers to provide mathematical rigor to the ap-

proach [144, 145] and is now formalized as the well known Stratonovich-Khas'minskii theorem. According to Roberts [146] and Lin and Cai [18] the approach can be regarded as the generalization of the deterministic averaging due to Bogoliubov and Mitropolsky [147].

5.1 Energy-Phase Transformation

We begin with the dimensional roll equation of motion as derived in chapter 3.

$$[I_{44} + A_{44}(\infty)]\ddot{\phi} + \int_{-\infty}^{u} K_{44}(u-v)\dot{\phi}(v)dv + B_1\dot{\phi} + B_2\dot{\phi}|\dot{\phi}| + \rho g \nabla_0 \overline{GZ}(t,\phi) = 0 \tag{5.1}$$

Since the stochastic averaging relies on considering the response as a Markov process (see appendix E for the definition of Markov process), the convolution term poses a mathematical problem as it includes the dependence of the current state of response over all of the previous history. However, in case of parametrically excited roll motion, it is well known that the response is narrow banded around the linear natural frequency of the vessel ω_n. Thus for the case of a parametrically excited system it is a reasonable approximation to use the roll added mass moment of inertia and radiation damping at the natural frequency ω_n instead of the convolution integral. Under this assumption, the roll equation of motion is given by

$$[I_{44} + A_{44}(\omega_n)]\ddot{\phi} + B_{44}(\omega_n)\dot{\phi} + B_1\dot{\phi} + B_2\dot{\phi}|\dot{\phi}| + \rho g \nabla_0 \overline{GM}_0 \frac{\overline{GZ}(u,\phi)}{\overline{GM}_0} = 0 \tag{5.2}$$

The roll equation shown in (5.2) can further be simplified and expressed in its

non-dimensional form as shown in (5.3)

$$\ddot{x} + \varepsilon^2\delta_1\dot{x} + \varepsilon^2\delta_2\dot{x}|\dot{x}| + \left[\alpha_1 x + \alpha_3 x^3 + \alpha_5 x^5 + ...\right] + \left[\varepsilon p_1(t)x + \varepsilon p_3(t)x^3 + \varepsilon p_5(t)x^5 + ...\right] = 0 \tag{5.3}$$

where

$$x = \phi \qquad t = \omega_n u \qquad (\dot{\ }) = \frac{d}{dt}(\ ) = \frac{1}{\omega_n}\frac{d}{du}(\ ) \tag{5.4}$$

$$\varepsilon^2\delta_1 = \frac{B_{44}(\omega_n) + B_1}{[I_{44} + A_{44}(\omega_n)]\omega_n} = b_1^{(v)} \tag{5.5}$$

$$\varepsilon^2\delta_2 = \frac{B_2}{[I_{44} + A_{44}(\omega_n)]} = b_2^{(v)} \tag{5.6}$$

$$\varepsilon p_1(t) = k_1(t) - \alpha_1 \qquad \varepsilon p_3(t) = k_3(t) - \alpha_3 \qquad \varepsilon p_5(t) = k_5(t) - \alpha_5 \qquad ... \tag{5.7}$$

$$k_1(t) = \frac{K_1(\frac{t}{\omega_n})}{\overline{GM}_0} \qquad k_3(t) = \frac{K_3(\frac{t}{\omega_n})}{\overline{GM}_0} \qquad k_5(t) = \frac{K_5(\frac{t}{\omega_n})}{\overline{GM}_0} \qquad ... \tag{5.8}$$

The odd polynomial in ϕ with coefficients $\alpha_1, \alpha_3, \alpha_5, ...$ in (5.3) represents the non-dimensional calm water $\overline{GZ}_0$. Again as seen in the previous chapters, $\alpha_1 = 1$. $K_1(u),\ K_3(u),\ K_5(u),\ ...$ represent the time varying coefficients for the polynomial expression of $\overline{GZ}$ developed in chapter 3. The parameter ε is introduced to represent the relative order of various terms in the equation of motion. However, note that ε is different from the scaling parameter ϵ used in chapter 4. The current scaling ensures that the standard deviation of the response is $O(\varepsilon)$ as $\varepsilon \to 0$ and does not

imply that the excitation is weak [148].

Assuming a more general form, the non-dimensional roll equation can be represented as

$$\ddot{x} + \varepsilon^2 F(\dot{x}) + G(x) + \varepsilon G_1(t, x) = 0 \tag{5.9}$$

where $F(\dot{x})$ is a nonlinear damping function, $G(x)$ is the time invariant nonlinear stiffness and $G_1(t, x)$ is the time varying stiffness in waves. For our specific example $F(\dot{x})$, $G(x)$ and $G_1(t, x)$ are given by

$$\varepsilon^2 F(\dot{x}) = b_1^{(v)}\dot{x} + b_2^{(v)}\dot{x}|\dot{x}| \tag{5.10}$$

$$\overline{GZ}(t, x) = \overline{GZ}_0(x) + \varepsilon\overline{GZ}_1(t, x) \tag{5.11}$$

$$G(x) = \frac{\overline{GZ}_0(x)}{\overline{GM}_0} = \sum_{j=1,3,5,\ldots}^{2n_q-1} \alpha_j x^j \tag{5.12}$$

$$G_1(t, x) = \frac{\overline{GZ}_1(t, x)}{\overline{GM}_0} = \sum_{j=1,3,5,\ldots}^{2n_q-1} p_j(t) x^j \tag{5.13}$$

where $p_k(t)$ represents the parametric time varying coefficients of $\overline{GZ}$ curve and are calculated using Volterra $\overline{GZ}$ formulation detailed in chapter 3. The degree of the restoring arm is given by $2n_q - 1$. In this work $n_q = 6$ is used to result in a 11^{th} order restoring curve. The total energy $E(t)$ is defined as the sum of kinetic and potential energy as shown in

$$E = \frac{\dot{x}^2}{2} + U(x) \tag{5.14}$$

where $U(x)$ is the potential energy associated with the nonlinear stiffness $G(x)$

and is given by

$$U(x) = \int_0^x G(\xi) d\xi \tag{5.15}$$

The equation of motion can be recast in terms of energy $E(t)$ and a related phase angle $\theta(t)$ defined such that the following transformations hold and also satisfy (5.14).

$$\mathrm{sgn}(x)\sqrt{U(x)} = \sqrt{E}\cos(\theta) \tag{5.16}$$

$$\frac{\dot{x}}{\sqrt{2}} = -\sqrt{E}\sin(\theta) \tag{5.17}$$

where

$$\mathrm{sgn}(x) = \begin{cases} 1 & \text{if } x \geq 0 \\ 0 & \text{if } x < 0 \end{cases} \tag{5.18}$$

The differential equation governing $E(t)$ is obtained by differentiating (5.14) with respect to time and is given by

$$\begin{aligned} \dot{E} &= \ddot{x}\dot{x} + G(x)\dot{x} \\ &= \dot{x}\left[-\varepsilon^2 F(\dot{x}) - \varepsilon G_1(t,x)\right] \\ &= \varepsilon^2\left(f(E,\theta)\sqrt{2E}\sin(\right) + \varepsilon\left(g_1(t,E,\theta)\sqrt{2E}\sin(\theta)\right) \end{aligned} \tag{5.19}$$

where

$$f(E,\theta) = F(\dot{x}) \tag{5.20}$$

$$g_1(t,E,\theta) = G_1(t,x) \tag{5.21}$$

Similarly the differential equation governing the phase angle $\theta(t)$ is obtained using (5.16) and (5.17) and is given by

$$\begin{aligned}
\dot{\theta} &= \frac{d}{dt}\left[\tan^{-1}\left(-\frac{\dot{x}}{\sqrt{2U(x)}}\right)\right] \\
&= \frac{1}{1+\left(\frac{\dot{x}^2}{2U(x)}\right)}\frac{-1}{\sqrt{2}}\frac{\ddot{x}\sqrt{U(x)}-\frac{\dot{x}^2 G(x)}{2\sqrt{U(x)}}}{U(x)} \\
&= \frac{-\cos^2\theta}{\sqrt{2}}\left[\frac{-\varepsilon^2 f(E,\theta)-\varepsilon g_1(t,E,\theta)-g(E,\theta)}{\sqrt{E}\cos(\theta)}-\frac{\tan^2(\theta)g(E,\theta)}{\sqrt{E}\cos(\theta)}\right] \\
&= \varepsilon^2\frac{f(E,\theta)\cos\theta}{\sqrt{2E}}+\varepsilon\frac{g_1(t,E,\theta)\cos\theta}{\sqrt{2E}}+\frac{g(E,\theta)}{\sqrt{2E}\cos\theta}
\end{aligned} \tag{5.22}$$

It can be seen from (5.19) that for the unperturbed system ($\varepsilon = 0$), energy E is independent of time. With the introduction of damping and parametric excitation, energy now varies slowly with time. This property of $E(t)$ enables the application of stochastic averaging which allows the energy to be approximated as a Markov process.

Introducing the phase angle $\theta_0(t)$ for the unperturbed case defined by

$$\theta_0 = \int \frac{g(E,\theta)}{\sqrt{2E}\cos(\theta)}dt \tag{5.23}$$

and defining a new phase process $\lambda(t)$ defined by

$$\lambda = \theta - \theta_0 \tag{5.24}$$

it can be seen that the governing equation for $\lambda(t)$ is given by

$$\dot{\lambda} = \varepsilon^2\frac{f(E,\theta_0+\lambda)\cos(\theta_0+\lambda)}{\sqrt{2E}}+\varepsilon\frac{g_1(t,E,\theta_0+\lambda)\cos(\theta_0+\lambda)}{\sqrt{2E}} \tag{5.25}$$

This transformation is required to obtain a new phase process $\lambda(t)$ to achieve a vector process $\boldsymbol{Z}(t) = \begin{Bmatrix} E(t) \\ \lambda(t) \end{Bmatrix}$ which is slowly varying with time. The equation of motion for $\boldsymbol{Z}(t)$ is given by

$$\dot{\boldsymbol{Z}}(t) = \begin{bmatrix} \dot{E} \\ \dot{\lambda} \end{bmatrix} = \varepsilon^2 \boldsymbol{a}(\boldsymbol{Z}) + \varepsilon \boldsymbol{b}(t, \boldsymbol{Z}) \tag{5.26}$$

where

$$\boldsymbol{a}(\boldsymbol{Z}) = \begin{bmatrix} a_1(E,\theta) \\ a_2(E,\theta) \end{bmatrix} = \begin{bmatrix} f(E,\theta)\sqrt{2E}\sin(\theta) \\ \frac{f(E,\theta)\cos(\theta)}{\sqrt{2E}} \end{bmatrix} \tag{5.27}$$

$$\boldsymbol{b}(t, \boldsymbol{Z}) = \begin{bmatrix} b_1(t,E,\theta) \\ b_2(t,E,\theta) \end{bmatrix} = \begin{bmatrix} g_1(t,E,\theta)\sqrt{2E}\sin(\theta) \\ \frac{g_1(t,E,\theta)\cos(\theta)}{\sqrt{2E}} \end{bmatrix} \tag{5.28}$$

Since $g_1(t,E,\theta) = \sum_{j=1,3,5,\ldots}^{2n_q-1} p_j(t)\,[x(E,\theta)]^j$, the expression for $\boldsymbol{b}(t,\boldsymbol{Z})$ can be expanded as

$$\boldsymbol{b}(t, \boldsymbol{Z}) = \sum_{r=1,3,5,\ldots}^{2n_q-1} \boldsymbol{d}_r(\boldsymbol{Z}) p_r(t) \tag{5.29}$$

where

$$\boldsymbol{d}_r(\boldsymbol{Z}) = \begin{bmatrix} d_{r1}(E,\theta) \\ d_{r2}(E,\theta) \end{bmatrix} = \begin{bmatrix} x^r(E,\theta)\sqrt{2E}\sin(\theta) \\ \frac{x^r(E,\theta)\cos(\theta)}{\sqrt{2E}} \end{bmatrix} \tag{5.30}$$

Thus the equation of motion for $\boldsymbol{Z}(t)$ is given by

$$\dot{\boldsymbol{Z}}(t) = \varepsilon^2 \boldsymbol{a}(\boldsymbol{Z}) + \varepsilon \sum_{r=1,3,5,\ldots}^{2n_q-1} \boldsymbol{d}_r(\boldsymbol{Z}) p_r(t) \tag{5.31}$$

5.2 Approximation of a Real Process by Markov Process

In general both the excitation $p_r(t)$ for $r = 1, 3, 5, ..., (2n_q - 1)$ and response $\boldsymbol{Z}(t)$ are not Markov processes. However, if the response $\boldsymbol{Z}(t)$ is approximated as a Markov process, it allows for further analysis using stochastic methods which are primarily applicable to Markov processes. With this motivation, we explore the conditions under which a real process can be approximated by a Markov process. Here we limit our discussions to heuristic arguments to better appreciate the physical significance behind the stochastic averaging technique and do not dwell too much into mathematical proofs. For a rigorous mathematical proof of stochastic averaging, readers are referred to the works of Khas'minskii [145] and Papanicolau and Kohler [144].

Since the Markov process is a mathematical idealization and it is hard to find a physical process with similar properties. It is well known that for a Markov process, its increments in non-overlapping time increments are independent. Approximation of a real process by a Markov process is usually justified on the basis of how the close increments of the process in non-overlapping time intervals are nearly independent.

Let's assume that a continuous time process $\boldsymbol{Z}(t)$ is being observed at discrete time instants starting from t with intervals of $\Delta t_1, \Delta t_2, ...$ and the respective increments in the process over these time intervals be given by $\Delta \boldsymbol{Z}_1, \Delta \boldsymbol{Z}_2, ...$ If $\Delta \boldsymbol{Z}_1, \Delta \boldsymbol{Z}_2, ...$ be independent of each other regardless of how short $\Delta t_1, \Delta t_2, ...$ are (even as they approach zero which implies continuous time observation), then $\boldsymbol{Z}(t)$

satisfies the sufficient condition to be a Markov process. However, real processes rarely possess this property.

On the other hand, if the system response varies much more slowly than the excitation, then it is easy to appropriately choose these time gaps $\Delta t_1, \Delta t_2, ...$ such that they are much larger than the correlation time of excitation τ_{corr}. The correlation time τ_{corr} is a measure of the "memory" of the excitation of its earlier state. Lin and Cai [18] define the correlation time as

$$\tau_{rs} = \frac{1}{\sqrt{w_{rr}(0)w_{ss}(0)}} \int_{-\infty}^{0} |w_{rs}(\tau)| d\tau \tag{5.32}$$

where covariance stationarity is assumed between zero mean processes $p_r(u)$ and $p_s(v)$ and the stationary covariance function is given by

$$w_{rs}(u - v) = E\left[p_r(u)p_s(v)\right] \tag{5.33}$$

If the time gaps $\Delta t_1, \Delta t_2, ...$ are chosen to be much larger than correlation time ($\Delta t_i >> \tau_{corr}$), the increments of the process $\Delta \boldsymbol{Z}_1, \Delta \boldsymbol{Z}_2, ...$ will appear independent. In such a scenario, if we choose to observe the process $\boldsymbol{Z}(t)$ at times which are separated by at least one correlation time τ_{corr} then the process will appear to have independent increments over non-overlapping time increments and may be approximated as a Markov process.

However, care must be taken that the time gaps are significantly smaller than the *relaxation time* of the system τ_{rel}, which is a measure of the "memory" of the system of its earlier state, without taking into account the effect of excitation [18]. If $\Delta t_i > \tau_{rel}$ then too much detail of the process is lost in the approximation. For oscillatory systems, Lin and Cai [18] define this as the time required for the amplitude

of the process to decrease by a factor of e^{-1}.

In our example of interest, roll x and roll velocity $\dot{x}$ fluctuate rapidly. However, the transformed coordinates - energy E and phase difference from unperturbed solution λ vary slowly on a much larger time scale as is evident from (5.31). Applying similar arguments as discussed above, $\boldsymbol{Z}(t)$ can be approximated as a diffusion (a Markov process whose sample functions are continuous with probability 1).

Mathematically, the Itô SDE governing the diffusion process can be expressed as (5.34)

$$d\boldsymbol{Z} = \boldsymbol{m}(\boldsymbol{Z})dt + \boldsymbol{\sigma}(\boldsymbol{Z})d\boldsymbol{B}_t \tag{5.34}$$

where $\boldsymbol{m}(\boldsymbol{Z})$ and $\boldsymbol{\sigma}(\boldsymbol{Z})$ are the drift and diffusion coefficients respectively and $\boldsymbol{B}_t$ represents the vector Brownian motion. The transition probability density of $\boldsymbol{Z}(t)$, given by $p(\boldsymbol{z}, t|\boldsymbol{z}_0, t_0)$, is governed by the FPK equation given by

$$\begin{aligned}\frac{\partial p}{\partial t} = &-\sum_{i=1}^{2} \frac{\partial}{\partial z_i}\left[m_i(\boldsymbol{Z})p(\boldsymbol{z}, t|\boldsymbol{z}_0, t_0)\right] \\ &+ \frac{1}{2}\sum_{i=1}^{2}\sum_{j=1}^{2} \frac{\partial^2}{\partial z_i \partial z_j}\left[D_{ij}(\boldsymbol{Z})p(\boldsymbol{z}, t|\boldsymbol{z}_0, t_0)\right]\end{aligned} \tag{5.35}$$

where $\boldsymbol{D} = \boldsymbol{\sigma}\boldsymbol{\sigma}^T$.

The drift $\boldsymbol{m}(\boldsymbol{Z})$ and diffusion $\boldsymbol{D}(\boldsymbol{Z})$ coefficients of the approximated Markov process $\boldsymbol{Z}(t)$ are obtained from the equation governing the physical process (5.26) by the application of Stratonovich-Khas'minskii limit theorem. The Stratonovich-Khas'minskii theorem embodies the mathematical rigor involved with the heuristic argument developed above. The proof of this theorem can be found in the works of Khas'minskii [145] and Papanicolau and Kohler [144]. The resulting expressions for

the drift and diffusion coefficients from the application of this theorem are given by (5.36) and (5.37) respectively.

$$\boldsymbol{m} = \boldsymbol{A}(E) + \int_{-\infty}^{0} \left\langle E\left[\left(\frac{\partial \boldsymbol{b}}{\partial \boldsymbol{Z}}\right)_t (\boldsymbol{b})_{t+\tau}\right]\right\rangle d\tau \tag{5.36}$$

$$\boldsymbol{D} = \boldsymbol{\sigma}\boldsymbol{\sigma}^T = \int_{-\infty}^{\infty} \left\langle E\left[(\boldsymbol{b})_t (\boldsymbol{b})_{t+\tau}^T\right]\right\rangle d\tau \tag{5.37}$$

where

$$\frac{\partial \boldsymbol{b}}{\partial \boldsymbol{Z}} = \begin{bmatrix} \frac{\partial b_1}{\partial E} & \frac{\partial b_1}{\partial \lambda} \\ \frac{\partial b_2}{\partial E} & \frac{\partial b_2}{\partial \lambda} \end{bmatrix} \tag{5.38}$$

$$\boldsymbol{A}(E) = \begin{bmatrix} A_1(E) \\ A_2(E) \end{bmatrix} = \langle \boldsymbol{a}(E, \theta_0) \rangle = \frac{1}{T(E)} \int_0^{T(E)} \boldsymbol{a}(E, \theta_0) dt \tag{5.39}$$

Note that $\langle [.] \rangle$ denotes the time average over the unperturbed system period $T(E)$ and is given by

$$\langle [\ .\ ] \rangle = \frac{1}{T(E)} \int_0^{T(E)} [\ .\ ] dt \tag{5.40}$$

where the unperturbed system period $T(E)$ is given by

$$T(E) = \oint \left|\frac{dx}{\dot{x}}\right| = 4\int_0^b \frac{dx}{\sqrt{2E}\sin(\theta)} = 2\sqrt{2}\int_0^b \frac{dx}{\sqrt{E - U(x)}} \tag{5.41}$$

Substitution of (5.27) and (5.28) into (5.36) and (5.37) results in the following expressions for the drift and diffusion coefficients. The details of the derivation of

expressions for the drift and diffusion coefficients is provided in appendix F.

$$m_1 = A_1(E) + \sum_{n=1}^{\infty} \sum_{j=1,3,5,\ldots}^{2n_q-1} \sum_{k=1,3,5,\ldots}^{2n_q-1} \left[\left(\int_{-\infty}^{0} w_{jk}(\tau) \cos\left(\frac{2\pi n}{T(E)} \tau \right) d\tau \right) \times \left\{ \frac{b_n^{(1j)} b_n^{(1k)}}{2} + \frac{a_n^{(1j)} a_n^{(1k)}}{2} + (j) \frac{b_n^{(2j)} b_n^{(1k)}}{2} + (j) \frac{a_n^{(2j)} a_n^{(1k)}}{2} \right\} \right] \tag{5.42}$$

$$m_2 = A_2(E) + \sum_{n=1}^{\infty} \sum_{j=1,3,5,\ldots}^{2n_q-1} \sum_{k=1,3,5,\ldots}^{2n_q-1} \left[\left(\int_{-\infty}^{0} w_{jk}(\tau) \sin\left(\frac{2\pi n}{T(E)} \tau \right) d\tau \right) \times \left\{ -\frac{a_n^{(1j)} b_n^{(1k)}}{4E} + \frac{b_n^{(1j)} a_n^{(1k)}}{4E} + (j) \frac{d_n^{(2j)} b_n^{(1k)}}{2} + (j) \frac{b_n^{(2j)} a_n^{(1k)}}{4E} \right\} \right] \tag{5.43}$$

$$D_{11} = \sum_{n=1}^{\infty} \sum_{j=1,3,5,\ldots}^{2n_q-1} \sum_{k=1,3,5,\ldots}^{2n_q-1} \left[(2\pi E) \left\{ b_n^{(1j)} b_n^{(1k)} \right\} S_{jk}^{(c)} \left(\frac{2\pi n}{T(E)} \right) \right] \tag{5.44}$$

$$D_{12} = \sum_{n=1}^{\infty} \sum_{j=1,3,5,\ldots}^{2n_q-1} \sum_{k=1,3,5,\ldots}^{2n_q-1} \left[-\pi b_n^{(1j)} a_n^{(1k)} S_{jk}^{(s)} \left(\frac{2\pi n}{T(E)} \right) \right] \tag{5.45}$$

$$D_{21} = \sum_{n=1}^{\infty} \sum_{j=1,3,5,\ldots}^{2n_q-1} \sum_{k=1,3,5,\ldots}^{2n_q-1} \left[\pi a_n^{(1j)} b_n^{(1k)} S_{jk}^{(s)} \left(\frac{2\pi n}{T(E)} \right) \right] \tag{5.46}$$

$$D_{22} = \sum_{n=1}^{\infty} \sum_{j=1,3,5,\ldots}^{2n_q-1} \sum_{k=1,3,5,\ldots}^{2n_q-1} \left[\frac{\pi}{2E} \left\{ a_n^{(1j)} a_n^{(1k)} \right\} S_{jk}^{(c)} \left(\frac{2\pi n}{T(E)} \right) \right] \tag{5.47}$$

where $a_n^{(1k)}$, $b_n^{(1k)}$, $a_n^{(2k)}$, $b_n^{(2k)}$ and $d_n^{(2k)}$ are functions of energy E and are defined

as follows:

$$\sin(\theta_0(t))x_0^k(t) = \sum_{n=1}^{\infty} b_n^{(1k)} \sin\left(\frac{2\pi n}{T(E)}t\right) \tag{5.48}$$

$$\cos(\theta_0(t))x_0^k(t) = \sum_{n=1}^{\infty} a_n^{(1k)} \cos\left(\frac{2\pi n}{T(E)}t\right) \tag{5.49}$$

$$\frac{2E}{g(E,\theta_0(t))} \sin(\theta_0(t)) \cos^2(\theta_0(t))x_0^{k-1}(t) = \sum_{n=1}^{\infty} b_n^{(2k)} \sin\left(\frac{2\pi n}{T(E)}t\right) \tag{5.50}$$

$$\frac{2E}{g(E,\theta_0(t))} \sin^2(\theta_0(t)) \cos(\theta_0(t))x_0^{k-1}(t) = \sum_{n=1}^{\infty} a_n^{(2k)} \cos\left(\frac{2\pi n}{T(E)}t\right) \tag{5.51}$$

$$\frac{\cos^3\theta_0(t)}{g(E,\theta_0(t))}x_0^{k-1}(t) = \sum_{n=1}^{\infty} d_n^{(2k)} \cos\left(\frac{2\pi n}{T(E)}t\right) \tag{5.52}$$

where $\theta_0(t)$ and $x_0(t)$ are the unperturbed system solutions. The cosine and sine cross spectra $S_{jk}^{(c)}(\omega)$ and $S_{jk}^{(s)}(\omega)$ are defined as

$$S_{jk}^{(c)}(\omega) = \frac{1}{2\pi}\int_{-\infty}^{\infty} w_{jk}(\tau)\cos(\omega\tau)\,d\tau \tag{5.53}$$

$$S_{jk}^{(s)}(\omega) = \frac{1}{2\pi}\int_{-\infty}^{\infty} w_{jk}(\tau)\sin(\omega\tau)\,d\tau \tag{5.54}$$

The drift and the diffusion coefficients of the energy equation computed using (5.42), (5.44) and (5.45) are shown in Figure 5.1 and Figure 5.2 respectively.

So far we have proved that $\boldsymbol{Z}(t)$ can be approximated as a two dimensional Markov process. However, it can be seen from Figure 5.2 that D_{12} is zero which implies that the Itô equation governing energy E is decoupled from the phase λ. Thus, the energy E can approximated as a Markov process and the dimension of the system is reduced.

From (5.45) and (5.46) it is clear that the cross diffusion coefficients depend on the product $a_n^{(1j)}b_n^{(1k)}$. Figure 5.3 and Figure 5.4 show the plot of $a_n^{(1j)}(E)$ and $b_n^{(1j)}(E)$ for

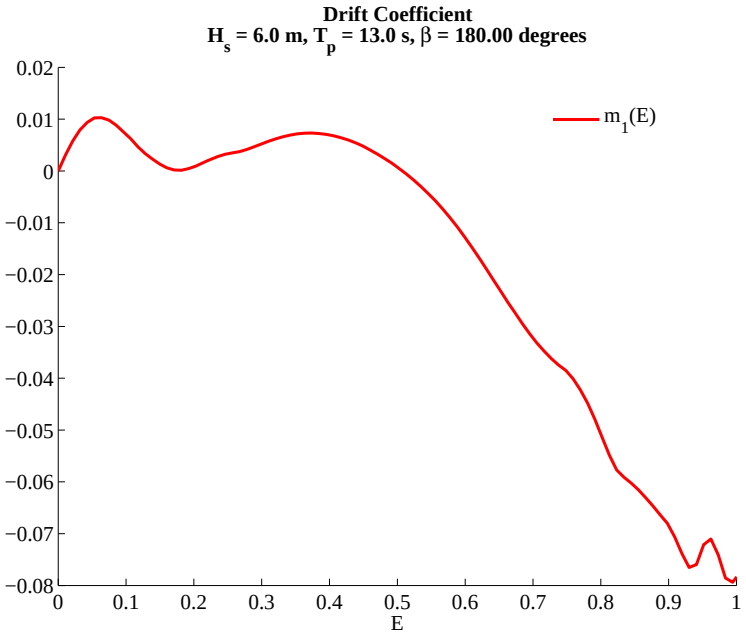

Figure 5.1: Drift coefficient $m_1(E)$ for $H_s = 6.0\ m$ and $T_p = 13.0\ s$

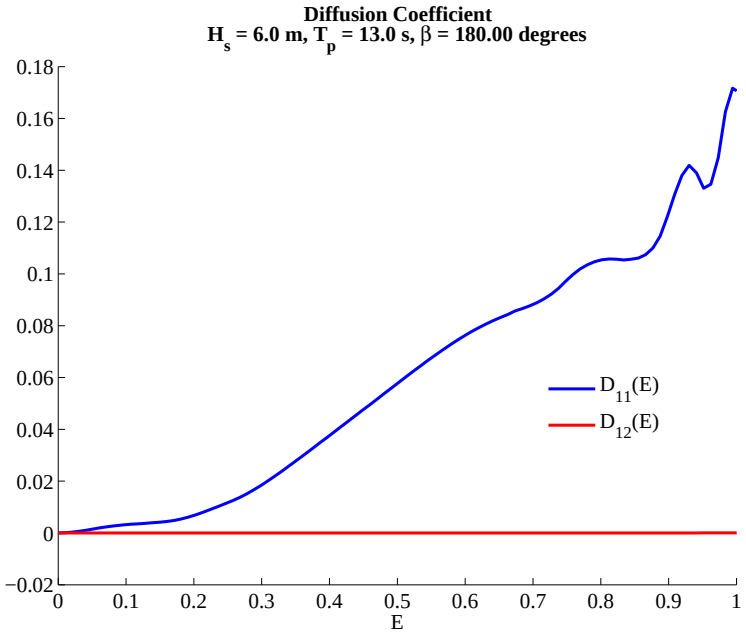

Figure 5.2: Diffusion coefficients $D_{11}(E)$ and $D_{12}(E)$ for $H_s = 6.0\ m$ and $T_p = 13.0\ s$

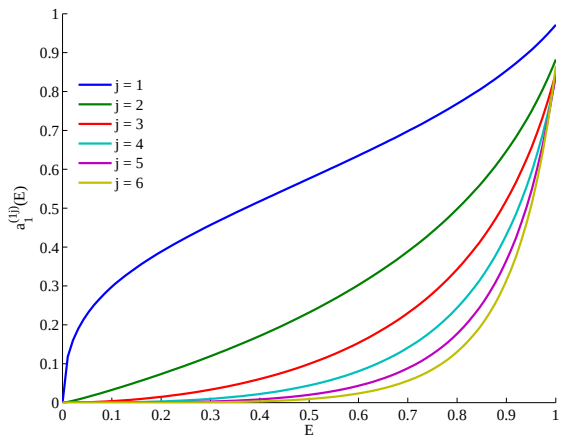

(a) $a_1^{(1j)}(E)$

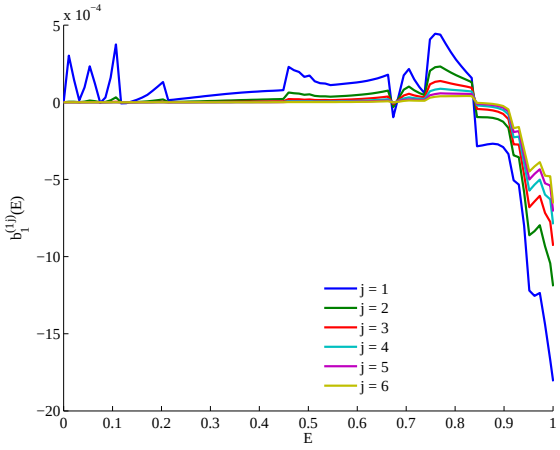

(b) $b_1^{(1j)}(E)$

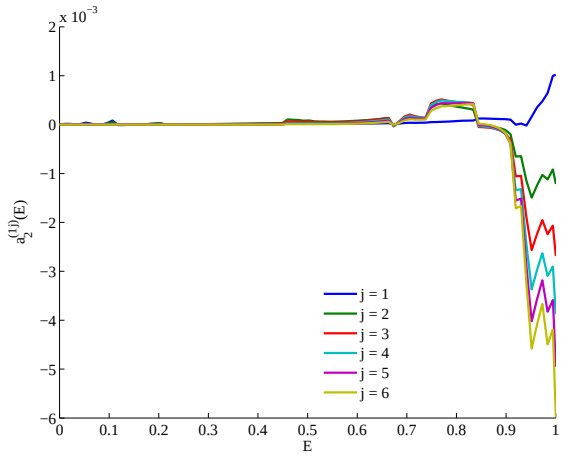

(c) $a_2^{(1j)}(E)$

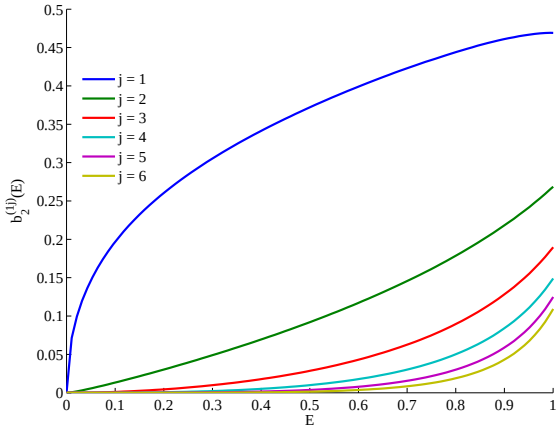

(d) $b_2^{(1j)}(E)$

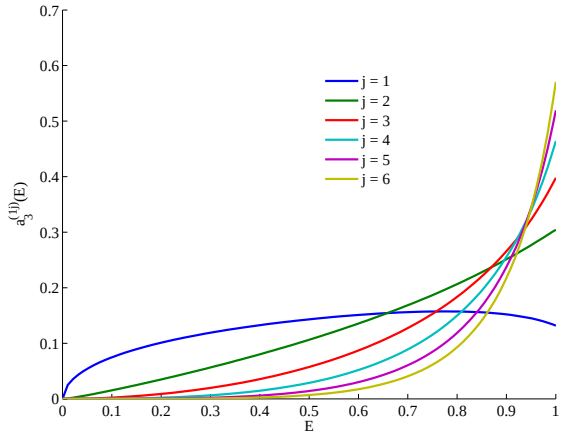

(e) $a_3^{(1j)}(E)$

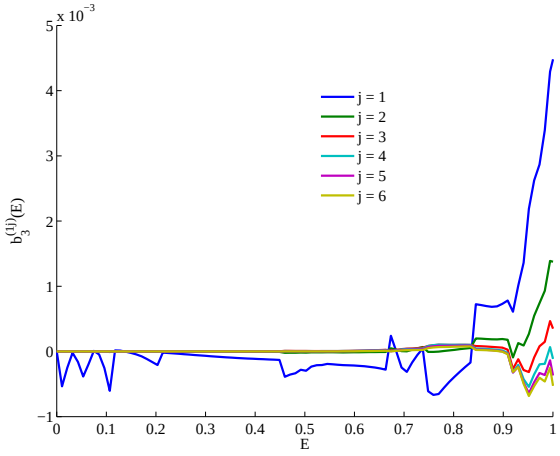

(f) $b_3^{(1j)}(E)$

Figure 5.3: Plot of $a_n^{(1j)}(E)$ and $b_n^{(1j)}(E)$ for $n = 1, 2$ and 3 for $H_s = 5.0\ m$ and $T_p = 13.0\ s$

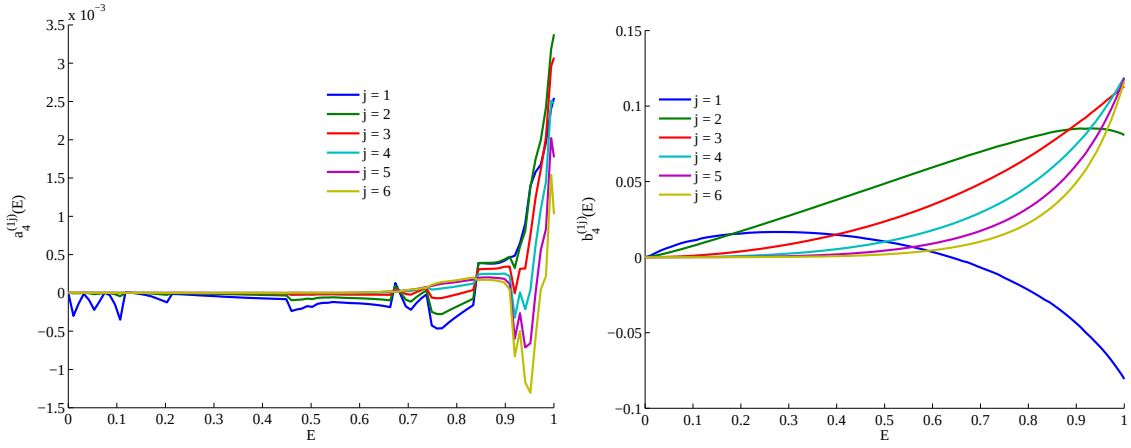

(a) $a_4^{(1j)}(E)$ (b) $b_4^{(1j)}(E)$

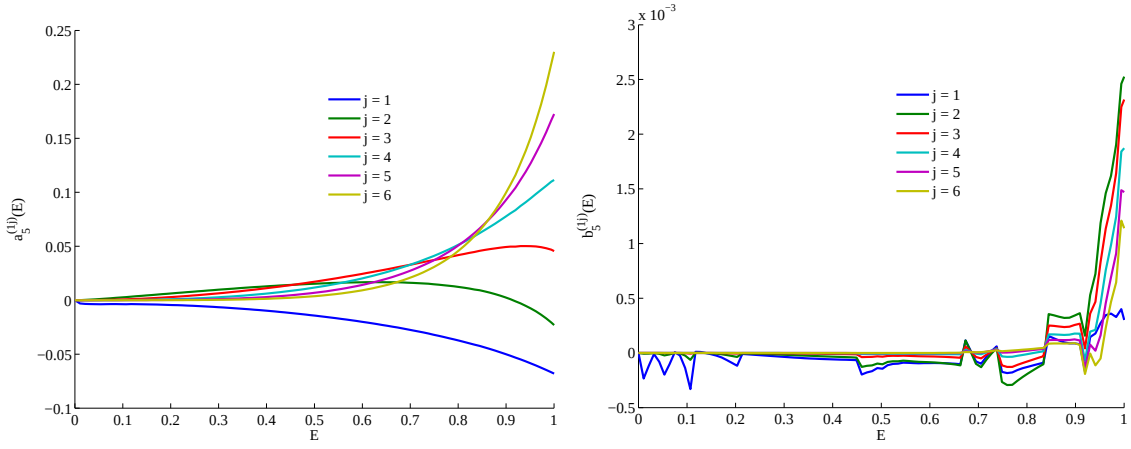

(c) $a_5^{(1j)}(E)$ (d) $b_5^{(1j)}(E)$

Figure 5.4: Plot of $a_n^{(1j)}(E)$ and $b_n^{(1j)}(E)$ for $n = 4$ and 5 for $H_s = 5.0\ m$ and $T_p = 13.0\ s$

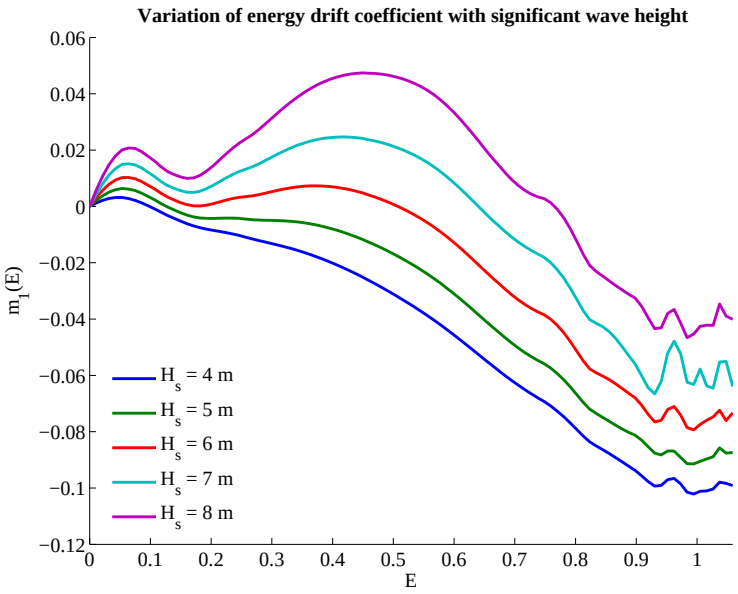

Figure 5.5: Energy drift coefficient for various H_s and a fixed chosen $T_p = 13.0\ s$

$n = 1, 2, 3, 4$ and 5. It can be seen that $a_n^{(1j)} \approx 0$ for an even value of n and $b_n^{(1j)} \approx 0$ for an odd value of n.

It can be argued that $x_0(t)$ has a periodicity similar to $\cos(\theta_0(t))$ and hence when substituted into (5.49) results in a non-zero value for $a_n^{(1j)}(E)$ only when n is odd. A similar argument can be made that substitution of $x_0(t)$ into (5.48) results in a non-zero value for $b_n^{(1j)}(E)$ only when n is even. This type of heuristic approach has also been adopted by Cai [149] who investigated a Duffing oscillator excited by both direct and parametric non-white excitations. This assumption is further validated by Figure 5.2 which shows that the numerically computed cross diffusion coefficient of the energy equation is close to zero. However, a mathematically rigorous proof of this result is still currently unavailable.

Figure 5.5 and Figure 5.6 show the variation of drift and diffusion coefficients of the energy equation for different Bretschneider spectra with varying significant wave heights and constant peak period $T_p = 13.0\ s$. It can be seen that the drift

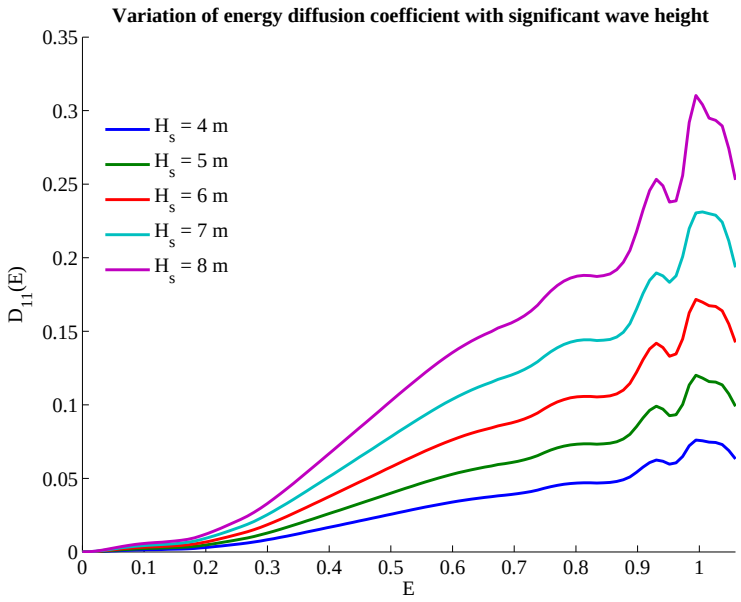

Figure 5.6: Energy diffusion coefficient for various H_s and a fixed chosen $T_p = 13.0\ s$

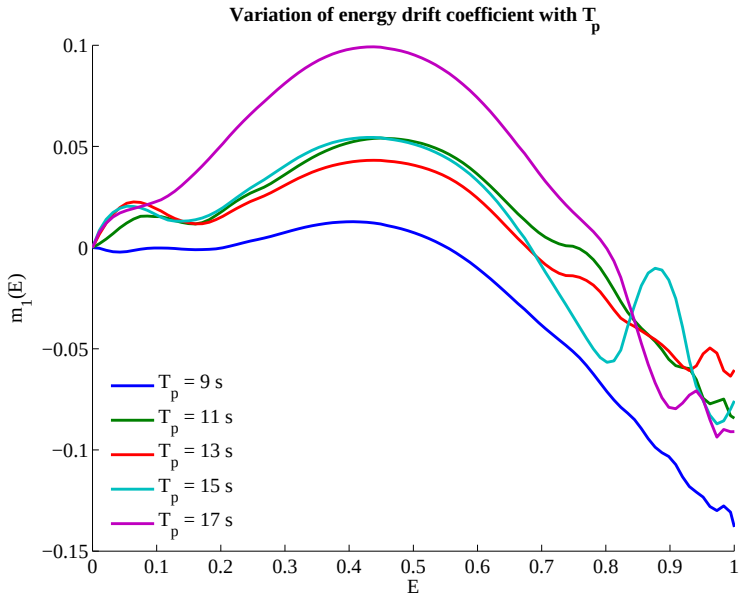

Figure 5.7: Energy drift coefficient for various T_p and a fixed chosen $H_s = 8.0\ m$

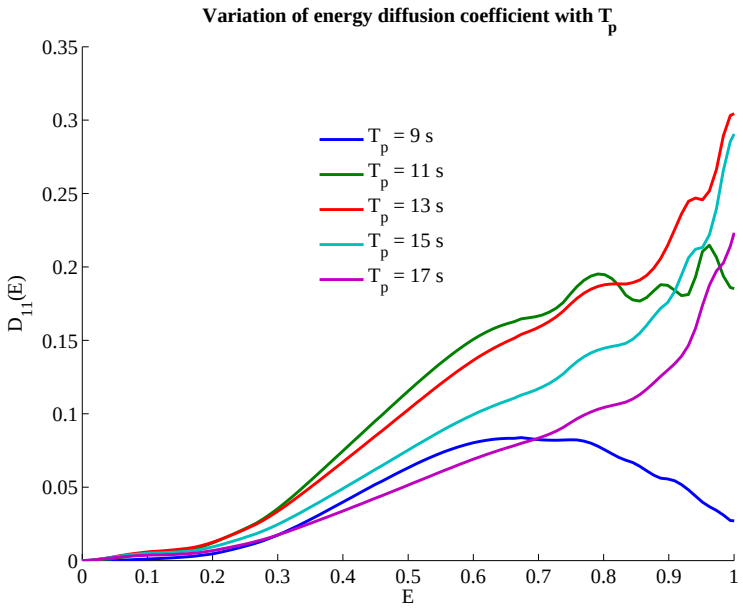

Figure 5.8: Energy diffusion coefficient for various T_p and a fixed chosen $H_s = 8.0\ m$

and diffusion coefficients vary monotonically with significant wave height. Figure 5.7 and Figure 5.8 show the variation of drift and diffusion coefficients of the energy equation for different Bretschneider spectra with varying peak periods and constant significant wave height $H_s = 8.0\ m$.

5.3 Stationary Probability Density Function

Once the drift and diffusion coefficients for the energy equation are known, the transition probability density function can be obtained by solving the corresponding FPK equation given by

$$\frac{\partial p}{\partial t} = -\frac{\partial}{\partial E}\left[m_1(E)p(E,t|E_0,t_0)\right] + \frac{1}{2}\frac{\partial^2}{\partial E^2}\left[D_{11}(E)p(E,t|E_0,t_0)\right] \tag{5.55}$$

If further stationarity is assumed, the FPK equation reduces to an ordinary dif-

ferential equation given by

$$\frac{dp}{dE} + \frac{1}{D_{11}} \left[\frac{dD_{11}}{dE} - 2m_1 \right] p = 0 \tag{5.56}$$

whose solution is given by (5.57)

$$p(E) = K_1 \exp \left\{ - \int_0^E \frac{1}{D_{11}(s)} \left[\frac{dD_{11}}{ds}(s) - 2m_1(s) \right] ds \right\} \tag{5.57}$$

where K_1 is a normalization constant chosen such that

$$\int_0^\infty p(E) dE = 1 \tag{5.58}$$

Figure 5.9 and Figure 5.10 show the stationary probability density function and cumulative distribution function of the energy for the case of incident wave environment with $H_s = 5.0\ m$ and $T_p = 13.0\ s$ incident at angle $\beta = 180^0$.

5.4 First Passage Failure Analysis

While solving the FPK equation assuming stationarity helps obtain the probability density function of energy, it is of more interest to estimate the probability that the energy of the system will exceed a critical value within some specified period of time. This problem is classically referred to as the first passage failure analysis. The mean first passage time is indicative of the stability of the system and hence can be used as a design assessment metric to compare different systems. However, according to Lin and Cai [18], the first passage problem is among the most difficult problems in the theory of probabilistic structural dynamics.

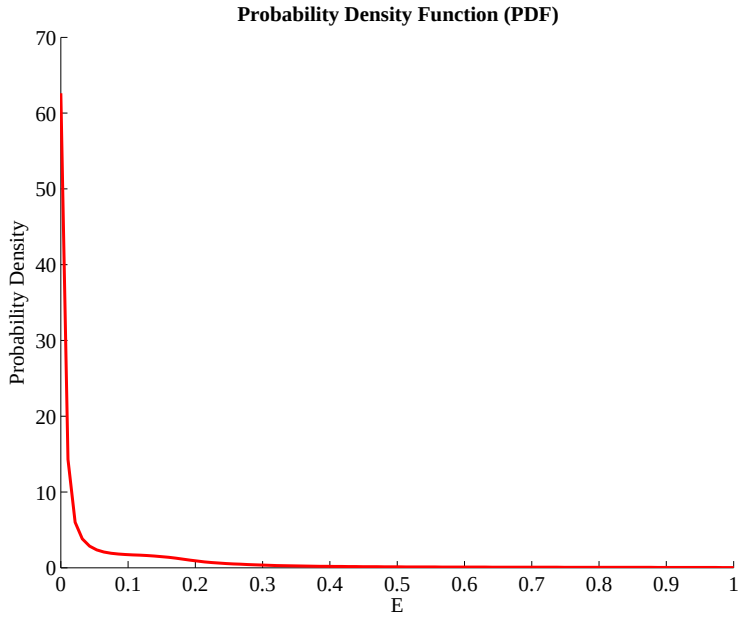

Figure 5.9: Stationary probability density function of energy E for $H_s = 6.0\ m$ and $T_p = 13.0\ s$

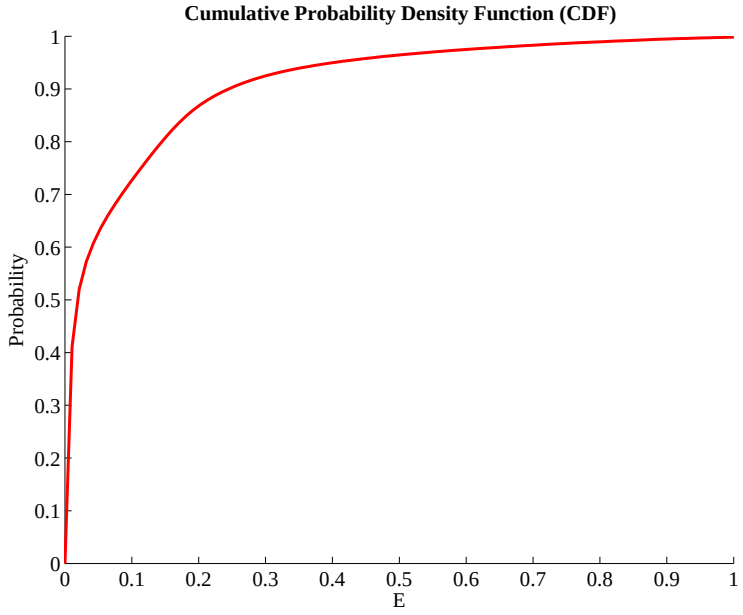

Figure 5.10: Stationary cumulative distribution function of energy E for $H_s = 6.0\ m$ and $T_p = 13.0\ s$

Consider the decoupled Itô equation for the energy process given by

$$dE = m_1(E)dt + \sigma_{11}(E)dB_t \tag{5.59}$$

where $\sigma_{11}(E) = \sqrt{D_{11}(E)}$. Specifically, we are interested in the random time τ_{FP} when the scalar energy process $E(t)$ exceeds a critical value E_c given that the system starts from an initial energy level of E_0 at time t_0. Assuming that the transition probability density function for the energy process is given by $p(E, t|E_0, t_0)$, it is possible to define a reliability function $R(E_c, t|E_0, t_0)$ which denotes the probability of $0 \leq E(t) < E_c$. The reliability function $R(E_c, t|E_0, t_0)$ is mathematically defined as

$$R(E_c, t|E_0, t_0) = \int_0^{E_c} p(E, t|E_0, t_0)dE \tag{5.60}$$

It is further assumed that the boundary at $E = E_c$ is an absorbing boundary. This implies that a sample path is removed from the population of sample paths once it reaches the boundary $E = E_c$. Without this assumption of absorbing boundary condition, the population of sample paths can include a sample path which exceeds E_c and at a later time goes below E_c. In such a scenario, it is particularly hard to calculate the mean first passage time as it needs to be ensured that the process has never exceeded the boundary before the considered first passage time. However, in the problem of parametric roll, the boundary $E = E_c$ corresponds to the energy level at the tipping point beyond which capsize results. Considering $E = E_c$ as an absorbing boundary is equivalent to saying that the energy process $E(t)$ can never achieve a value of E_c without resulting in capsize. Since the population of sample paths at time t only include those paths which have not crossed E_c even once, the

reliability function defined above is also equal to the probability that the first passage time $\tau_{FP} > t - t_0$.

$$R(E_c, t|E_0, t_0) = \int_0^{E_c} p(E, t|E_0, t_0)dE = \text{Prob}\left[\tau_{FP} > t - t_0 | E(t_0) = E_0\right] \tag{5.61}$$

With an absorbing boundary condition, the process can never attain stationarity. This also implies that the probability in the region $0 \leq E \leq E_c$ is not conserved as otherwise the reliability function would be unity. Since $p(E, t|E_0, t_0)$ satisfies the Kolmogorov backward equation (see appendix E), the reliability function R will also satisfy the same.

$$\frac{\partial R}{\partial t_0} + m_1(E_0)\frac{\partial R}{\partial E_0} + \frac{1}{2}D_{11}(E_0)\frac{\partial^2 R}{\partial E_0^2} = 0 \tag{5.62}$$

Defining a change of variable $\tau = t - t_0$, (5.62) can be expressed as

$$-\frac{\partial R}{\partial \tau} + m_1(E_0)\frac{\partial R}{\partial E_0} + \frac{1}{2}D_{11}(E_0)\frac{\partial^2 R}{\partial E_0^2} = 0 \tag{5.63}$$

The probability distribution function of the first passage time τ_{FP} is given by

$$F_{\tau_{FP}}(\tau, E_c, E_0) = \text{Prob}\left[\tau_{FP} \leq \tau | E(t_0) = E_0\right] \tag{5.64}$$

$$= 1 - R(\tau, E_c, E_0) \tag{5.65}$$

The probability density function of τ_{FP} is given by

$$p_{\tau_{FP}}(\tau, E_c, E_0) = \frac{\partial F_{\tau_{FP}}}{\partial \tau}(\tau, E_c, E_0) = -\frac{\partial R}{\partial \tau}(\tau, E_c, E_0) \tag{5.66}$$

Thus, the n^{th} moment of τ_{FP} is given by

$$\mu_n(E_c, E_0) = E\left[\tau_{FP}^n\right] = -\int_0^\infty \tau^n \frac{\partial R}{\partial \tau}(\tau, E_c, E_0) d\tau \tag{5.67}$$

Assuming $\tau^n R(\tau, E_c, E_0)$ tends to zero as $\tau \to 0$, $\mu_n(E_c, E_0)$ can be expressed as

$$\mu_n(E_c, E_0) = n \int_0^\infty \tau^{n-1} R(\tau, E_c, E_0) d\tau \tag{5.68}$$

Multiplying (5.63) by τ^n and integrating with respect to τ from 0 to ∞ results in a recursive set of ordinary differential equations for the moments of τ_{FP}.

$$n\mu_{n-1} + m_1(E_0)\frac{d}{dE_0}\mu_n + \frac{1}{2}D_{11}(E_0)\frac{d^2}{dE_0^2}\mu_n = 0 \tag{5.69}$$

These set of equations shown in (5.69) are known as generalized Pontryagin equations and can be solved recursively. Substituting $n = 1$ and $\mu_0 = 1$ leads to Pontryagin equation governing the mean first passage time $\mu_1 = E\left[\tau_{FP}\right]$ given by (5.70).

$$1 + m_1(E_0)\frac{d\mu_1}{dE_0} + \frac{1}{2}D_{11}(E_0)\frac{d^2\mu_1}{dE_0^2} = 0 \tag{5.70}$$

The boundary conditions for (5.70) are given by

$$\mu_1(E_c, E_0)|_{E_0=E_c} = 0 \tag{5.71}$$

$$\mu_1(E_c, E_0)|_{E_0=0} < \infty \tag{5.72}$$

Much of the steps of the derivation of the Pontryagin equation provided above follows the works of Lin and Cai [18] and have been summarized here for completeness.

5.5 Boundary Condition at $E = 0$

The second boundary condition shown in (5.72) physically signifies that given enough time, the system will eventually reach the critical boundary. This condition is "qualitative" rather than "quantitative", and is only useful when closed form solutions exist. In many of the practical cases where close form solutions do not exist, (5.70) is solved numerically to obtain estimates of $\mu_1(E_c, E_0)$. In such cases, it is necessary to convert the boundary condition shown in (5.72) into a quantitative condition which can be applied numerically. Lin and Cai [18] provide a discussion of the various types of boundary conditions applicable to different scenarios.

Specifically, when $D_{11}(0) = 0$ as in our example of parametric roll (see Figure 5.6 and Figure 5.8), the boundary at $E = 0$ is known as a singular boundary of the first kind. If further $m_1(0) = 0$ (as seen in Figure 5.5 and Figure 5.7), then the boundary is further classified as of type *trap*. Since the Pontryagin equation is based on the assumption that given enough time, the system will eventually reach the critical boundary, only those boundary conditions which allow for this possibility can yield meaningful results. Specifically, a solution of the Pontryagin equation is possible only for a regular, entry or repulsively natural types of trap (see appendix G for description) and the corresponding boundary condition applicable for a numerical implementation is given by (5.73) [150].

$$m_1(E_0)\mu_1'(E_0) < \infty \text{ as } E_0 \to 0 \tag{5.73}$$

As $E \to 0$ the nonlinear oscillator can be approximated using only the linear damping and linear restoring terms. The drift and diffusion coefficients for this linear oscillator can easily be obtained using stochastic averaging. The corresponding Pontryagin equation for the linear oscillator can be solved to obtain an analytical

expression for $\mu_1'(E_0)$ near $E_c = 0$. Applying this technique to the Volterra $\overline{GZ}$ model, leads to boundary condition given by (5.74). Detailed derivation of the drift and diffusion coefficients for the linear system and the boundary condition for the singular boundary at $E = 0$ are provided in appendix G.

$$E_0\mu_1'(E_0) = \frac{-2}{\pi S_{11}^c(2) - 2\delta_1} < \infty \tag{5.74}$$

Note that although (5.74) provides a quantitative condition, it cannot be applied exactly at $E = 0$ when attempting a direct numerical solution of the Pontryagin equation. Instead this boundary condition is applied at a point slightly away from $E = 0$.

5.6 Comparison with Monte Carlo Simulations

In order to check the validity of the developed theory, the obtained mean first passage times are compared against estimates from Monte Carlo simulations of the averaged system. The averaged system refers to the Itô SDE obtained after the application of stochastic averaging. Since the excitation process is white noise for the Itô SDE every realization will eventually reach the boundary E_c. For each significant wave height case, five energy levels are chosen and for each energy level 1000 Monte Carlo simulations are performed. The times to reach the basin boundary E_c from each of these simulations are averaged to get the mean first passage time for that energy level. The governing Itô SDE shown in (5.59) is used to simulate the energy process. The Milstein scheme described by Higham [151] is used to simulate the Itô SDE.

Figure 5.11 shows the comparison of the mean first passage times obtained from solving the Pontryagin equation against the estimates from Monte Carlo simulations of Itô SDE. It can be seen that the mean first passage time estimates from solving

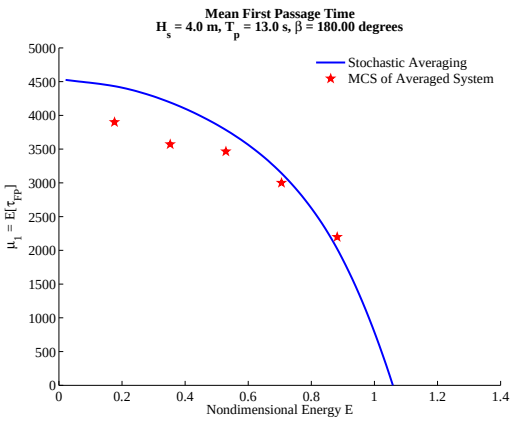

(a) $H_s = 4.0m$

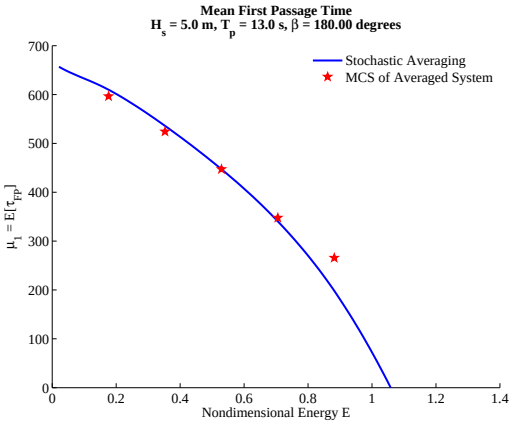

(b) $H_s = 5.0m$

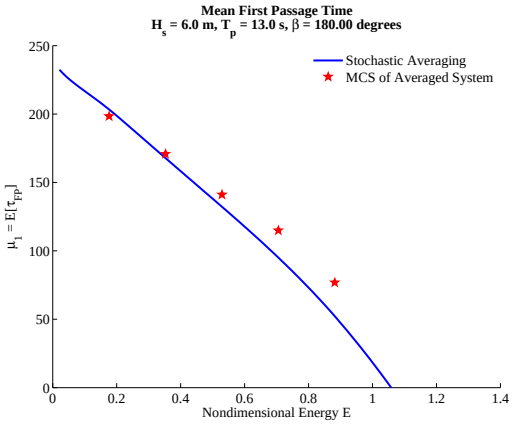

(c) $H_s = 6.0m$

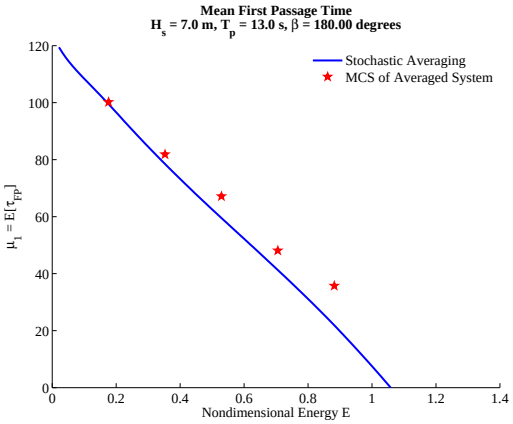

(d) $H_s = 7.0m$

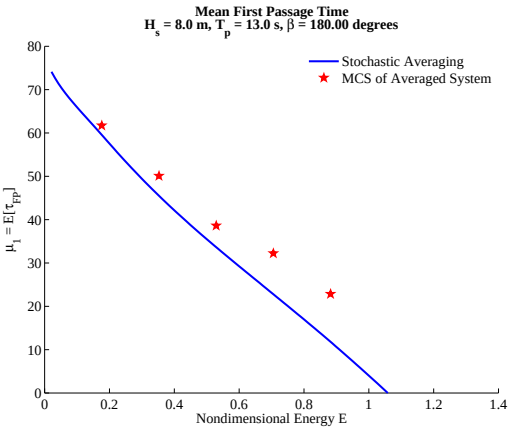

(e) $H_s = 8.0m$

Figure 5.11: Comparison of mean first passage times calculated from stochastic averaging and Monte Carlo simulations for different significant wave heights and fixed peak period $T_p = 13.0\ s$

the Pontryagin equations agree well with the estimates from simulations. The slight deviation between the theory and the Monte Carlo simulations at higher energy levels indicate that the stochastic averaging is more conservative in the estimation of mean first passage time. This implies that if a designer utilizes this approach, the designed system will be at least as stable or even more stable than if the designer had utilized the simulation approach to estimate the mean first passage time.

After application of stochastic averaging, the resulting averaged Itô system is excited by a white noise process. Thus, every realization of the averaged system will eventually capsize due to the unbounded variation of the excitation. Hence for the Monte Carlo simulations of the averaged system it is practically possible to choose a large maximum simulation time T_{max} such that all of the 1000 simulations will reach the basin boundary before this T_{max}. For the simulations in Figure 5.11, the maximum simulation time is chosen as $T_{max} \approx 10(\mu_1)_{E_0=0}$.

However, the original system excited by a narrow banded spectrum does not demonstrate a similar trend. Given a maximum simulation time, not every realization will capsize within a practically specified maximum simulation time. Therefore for estimating of the mean first passage times from the Monte Carlo simulations of the original system, only those simulations are chosen which capsize within the specified maximum simulation time. Figure 5.12 shows the comparison of mean first passage time obtained from Pontryagin equation with the estimates from both Monte Carlo simulations of the original and the averaged system. It can be seen that the trend of the Monte Carlo simulations of the original as well as the averaged system are in reasonable agreement with the solution of the Pontryagin equation.

Note that the when choosing the initial conditions for the Monte Carlo simulations of the original system, the energy level is specified prior to the simulation. However the phase angle θ is chosen from a uniformly distributed random variable varying

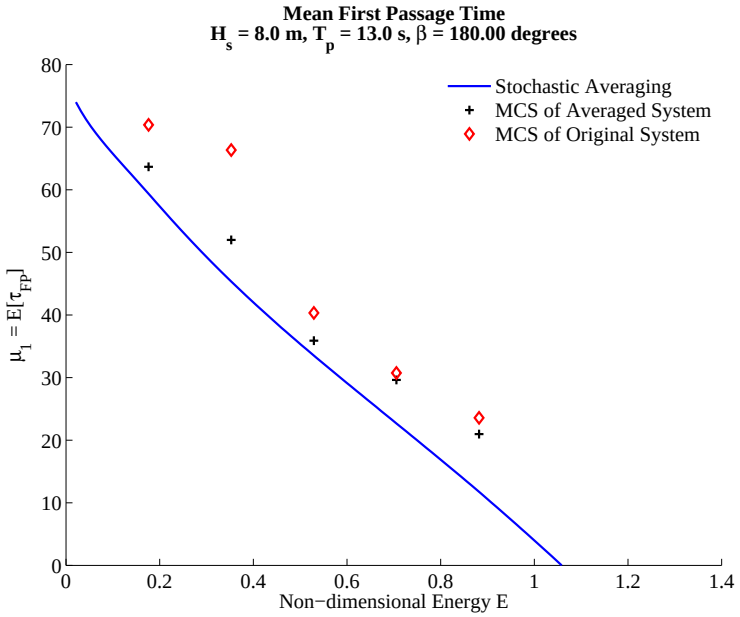

Figure 5.12: Comparison of mean first passage time calculated from stochastic averaging and Monte Carlo simulations of both original and the averaged system for the case with $H_s = 8.0\ m$ and $T_p = 13.0\ s$

between 0 and 2π. The corresponding pair of (E, θ) are transformed to obtain the initial roll angle and angular velocity which are then used as the initial conditions for simulation of the original system. It is also important to note that the estimates for higher initial energy levels result in more realizations which capsize and hence have more data points in the estimation of mean first passage times. This is also the reason for the deviation of the mean first passage time estimates from Monte Carlo simulations of the original system from the other two methods at lower initial energy levels.

The relative ease of computation of the mean first passage times from solving Pontryagin equations compared to the corresponding estimates from Monte Carlo simulations, suggests the use of this technique as design assessment tool which can be used to compare the stability of various designs quickly. The use of this technique

to assess the stability is further discussed in chapter 6.

6. COMPARISON OF THE MARKOV AND THE MELNIKOV APPROACHES

So far chapter 4 and chapter 5 have detailed the Melnikov and the stochastic averaging approaches to assess the stability of a vessel susceptible to parametric roll in irregular head seas. While the rate of phase space flux is the quantitative measure of stability from the Melnikov approach, the corresponding stability measure from stochastic averaging is the mean first passage time. The Melnikov approach is based on the theory of nonlinear dynamical systems and the stochastic averaging stems from the theory of stochastic dynamics. As these two methods are completely independent of each other, they provide the designer with the option to cross check the results from one method with the other to gain confidence. In this chapter, these two methods are compared against each other to highlight the similarities between them. Particular emphasis is laid on the sensitivity analysis where the influence of various parameters on the stability of the system are investigated.

While the Melnikov function introduced in chapter 4 was used primarily to calculate the rate of phase space flux, it is also well known from the theory of chaotic dynamics that the Melnikov function being positive is a necessary condition for the system to demonstrate chaos [92]. Since it is evident from the examples observed in chapter 4 that the Melnikov function attains positive values, it leads to the question of whether the response observed is chaotic or not. In order to determine definitively if chaos is occurring or not, we investigate the Lyapunov exponents of the system which is discussed in the following section.

6.1 Lyapunov Exponent

It is known from the theory of chaotic dynamics [152] that one of the necessary conditions for a system to exhibit chaotic response is its sensitive dependence to

initial conditions. Sensitive dependence on initial conditions means that two orbits arbitrarily close to each other in the phase space at a particular time will eventually diverge from each other at an exponential rate. One of the ways to ascertain whether a system possesses sensitive dependence to initial conditions is to evaluate the Lyapunov exponents of the system. Lyapunov exponents are defined as the average exponential rates of convergence or divergence of nearby orbits in the phase plane [153].

Thus from the definition it is clear that for a motion converging to a fixed point, like a node, all the Lyapunov exponents must be negative. Similarly, for a periodic motion at least one Lyapunov exponent must be zero and finally for chaotic motion, at least one Lyapunov exponent must be positive. While the sign of the Lyapunov exponent ascertains if a system is chaotic or not, its value quantifies the chaos in a system. For certain simple systems it is possible to evaluate the largest Lyapunov exponent analytically. However, for most of the real world cases this is not possible. When an analytical expression cannot be derived, the exponent is estimated numerically from a time history of the process obtained either from experiments or simulations. One such algorithm to calculate the largest Lyapunov exponent from a simulated or experimentally measured time history has been developed by Wolf et. al. [153]. This algorithm encoded as a MATLAB program is also freely available on the web and has been utilized in evaluating the largest Lyapunov exponent from simulated roll motion time series data in this dissertation.

While calculating the largest Lyapunov exponent from time series data is fairly accurate, an approximate estimate of the Lyapunov exponent in the vicinity of the equilibrium point can also be obtained in analytical form using the stochastically averaged system described in chapter 5 [154, 155, 156]. Consider a n-dimensional stochastic process $\boldsymbol{X}(t)$ whose stability is of interest. Let $||\boldsymbol{X}(t)||$ denote the Eu-

clidean norm of the vector $\boldsymbol{X}(t)$ defined by Equation 6.1.

$$||\boldsymbol{X}(t)|| = \sqrt{\boldsymbol{X}^T(t)\boldsymbol{X}(t)} = \sqrt{\left[\sum_{i=1}^{n} X_i^2(t)\right]} \tag{6.1}$$

Then the Lyapunov exponent λ defined as the average exponential rate of convergence or divergence can be mathematically defined as shown in Equation 6.2.

$$\lambda = \lim_{t\to\infty} \frac{1}{t} \ln(||\boldsymbol{X}(t)||) \tag{6.2}$$

For a one dimensional system $V(t)$ this expression reduces to Equation 6.3.

$$\lambda = \lim_{t\to\infty} \frac{1}{t} \ln(V(t)) \tag{6.3}$$

From chapter 5 we know that the energy E in the roll system can be approximated as a one dimensional Markov process and is governed by the Itô SDE shown in Equation 6.4

$$dE = m_1(E)dt + \sigma_{11}(E)dB_t \tag{6.4}$$

where the drift $m_1(E)$ and diffusion $\sigma_{11}(E) = \sqrt{D_{11}(E)}$ coefficient are given by Equation 5.42 and Equation 5.44 respectively. Linearizing this system about the equilibrium point $E = 0$, the SDE governing the dynamics in the vicinity of the trivial solution $E = 0$ can be expressed as

$$dE = m_1'(0)Edt + \sigma_{11}'(0)EdB_t \tag{6.5}$$

where $m_1'(E)$ and $\sigma_{11}'(E)$ represent the derivative of the drift $m_1(E)$ and diffusion

$\sigma_{11}(E)$ coefficients with respect to E. The Itô equation governing $\ln(E(t))$ can be obtained by applying the Itô formula (see appendix E) and is given by

$$d(\ln(E)) = \left\{ m_1'(0) - \frac{1}{2}\left[\sigma_{11}'(0)\right]^2 \right\} dt + \sigma_{11}'(0) dB_t \tag{6.6}$$

The solution of this SDE is given by

$$\ln(E) = \ln(E_0) + \int_0^t \left\{ m_1'(0) - \frac{1}{2}\left[\sigma_{11}'(0)\right]^2 \right\} dt + \int_0^t \sigma_{11}'(0) dB_t \tag{6.7}$$

Now, the Lyapunov exponent near the trivial solution $E = 0$ can be obtained by applying the definition shown in Equation 6.3. Thus, the estimate of the Lyapunov exponent in the vicinity of the equilibrium point $E = 0$ is given by

$$\begin{aligned} \lambda &= \lim_{t\to\infty} \frac{1}{t} \ln(E) \\ &= \lim_{t\to\infty} \frac{1}{t} \int_0^t \left\{ m_1'(0) - \frac{1}{2}\left[\sigma_{11}'(0)\right]^2 \right\} dt \\ &= \left\{ m_1'(0) - \frac{1}{2}\left[\sigma_{11}'(0)\right]^2 \right\} \end{aligned} \tag{6.8}$$

6.2 Sensitivity Analysis

In this section the sensitivity of the stability measures from the stochastic averaging technique and the Melnikov approach are compared for various cases to gain an understanding of the relationship between the two methods. The sensitivity parameters include the significant wave height, peak period, bilge keel width and the calm water $\overline{GM}_0$.

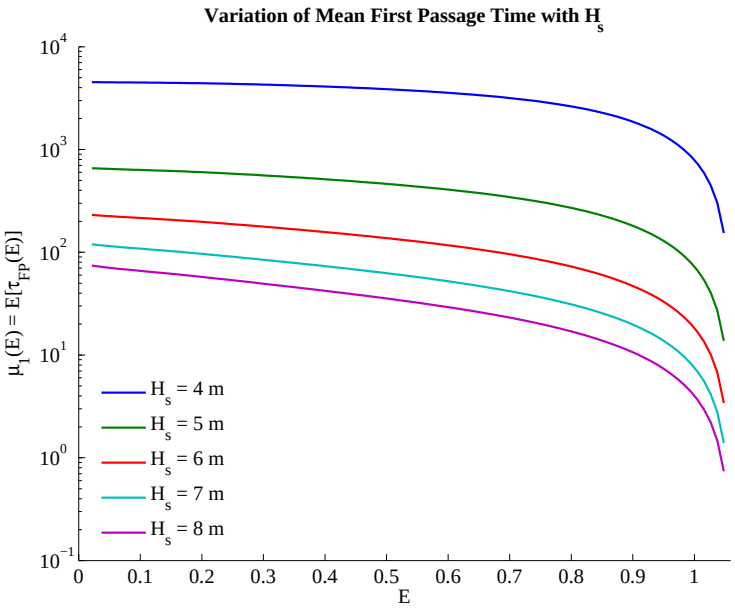

Figure 6.1: Sensitivity of mean first passage time to significant wave height ($T_p = 13.0\ s$)

6.2.1 Sensitivity to Significant Wave Height

The two methods of analysis are applied to a range of cases where the peak period is kept constant at $T_p = 13.0\ s$ and the significant wave height is varied from 4.0 m to 8.0 m. The variation of drift and diffusion coefficients for various significant wave heights are shown in Figure 5.5 and Figure 5.6 respectively. The corresponding mean first passage times are compared in Figure 6.1. It can be seen from Figure 6.1 that the mean first passage time decreases with increase in significant wave height. This trend is expected since higher significant wave heights lead to more energy being input to the system resulting in larger responses and hence lower mean first passage times.

Figure 6.2 shows the comparison of rate of phase space flux with the mean first escape rate (defined as the inverse of mean first passage time evaluated for the initial

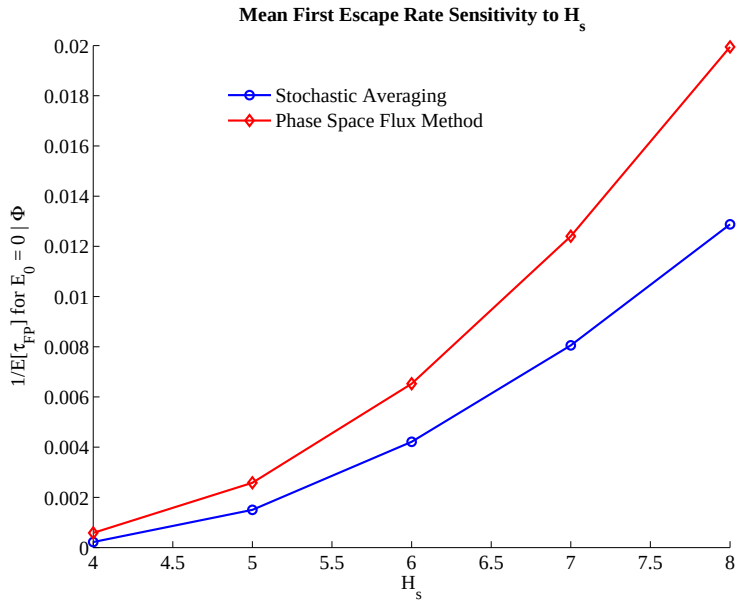

Figure 6.2: Sensitivity of mean first escape rate to significant wave height ($T_p = 13.0\ s$)

condition $E_0 = 0$). It can be seen that both mean first escape rate $\frac{1}{\mu_1(0)}$ and rate of phase space flux Φ vary monotonically with H_s. Plotting the rate of phase space flux against the mean first escape rate (Figure 6.3) demonstrates an almost linear relationship between the two measures.

The comparison of the approximate estimate of the Lyapunov exponent from stochastic averaging against the Lyapunov exponent calculated from simulated roll motion is shown in Figure 6.4. It can be seen that the estimate from stochastic averaging is always greater than the value calculated from the time series. Since the estimate from stochastic averaging is an approximation of the Lyapunov exponent at $E = 0$, it is only representative of the local behavior and is not as accurate as the value calculated from the time series. It can be seen that the Lyapunov exponent assumes only a small positive value suggesting that the trivial solution $E = 0$ is asymptotically unstable. However a value close to zero also signifies that the system

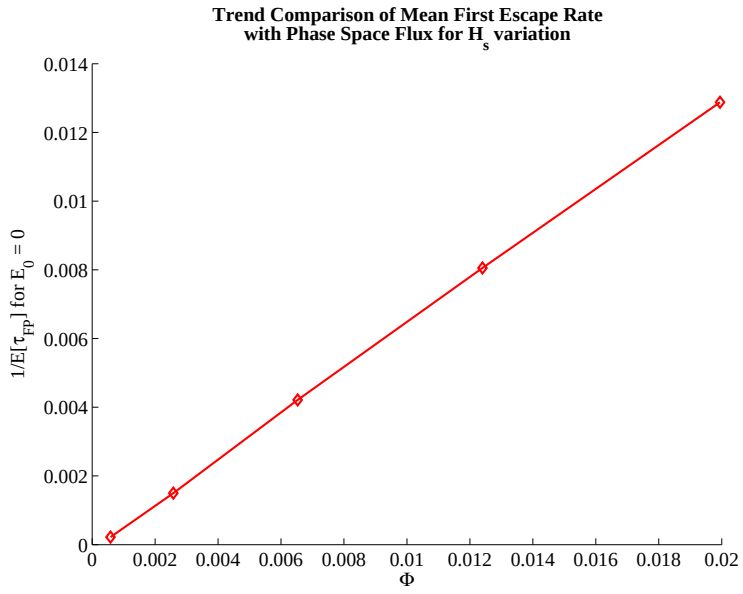

Figure 6.3: Relationship between mean first escape rate and rate of phase space flux for increasing significant wave heights ($T_p = 13.0\ s$)

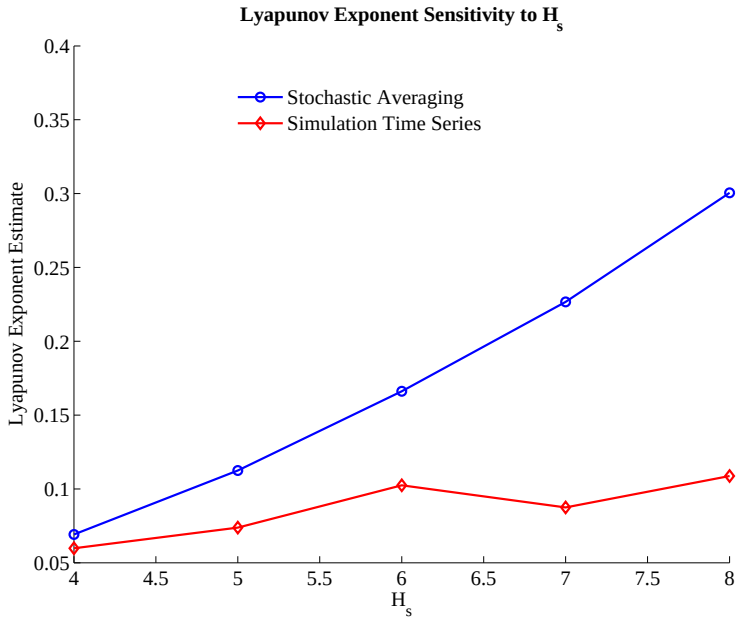

Figure 6.4: Variation of the Lyapunov exponent with significant wave height ($T_p = 13.0\ s$)

does not display a sensitivity to initial conditions (necessary to demonstrate chaos) and has a nearly periodic response. This is consistent with the parametric roll response which is a subharmonic response of the system and exhibits a strong $2:1$ periodicity (see appendix D).

6.2.2 Sensitivity to Peak Period

Figure 6.5 shows the variation of mean first passage time with initial energy level for various peak periods of the excitation spectra. In all these cases, the significant wave height is fixed at $H_s = 6.0\ m$. As the peak period is increased, the mean first passage time decreases due to the modal frequency of the encounter wave spectrum being closer to twice the roll natural frequency. Figure 6.6 shows the variation of the rate of phase space flux and the mean first escape with peak period of the spectrum. Both the rate of phase space flux and the mean first escape rate demonstrate similar trends and an almost linear relationship is observed between them as seen in Figure 6.7.

The variation of Lyapunov exponent with peak period is shown in Figure 6.8. Similar to the previous case, the estimate of Lyapunov exponent from stochastic averaging is higher than the estimate from time series. However, it can be seen that at $T_p = 9.0\ s$ both methods estimate a negative Lyapunov exponent. This means that for $T_p = 9.0\ s$ and $H_s = 6.0\ m$ no parametric roll is observed and the trivial solution $E = 0$ is asymptotically stable. This is also seen from the time history shown in Figure 6.9. Note that for this case the Pontryagin equation is not applicable and hence excluded in Figure 6.5.

6.2.3 Sensitivity to Damping

Figure 6.10 shows the variation of mean first passage time with initial energy for three different damping scenarios. As expected, the mean first passage time increases

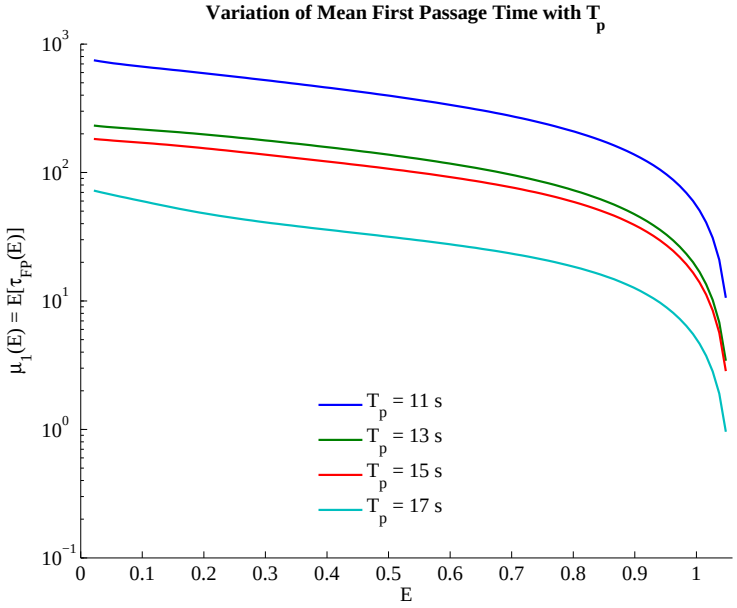

Figure 6.5: Sensitivity of mean first passage time to peak period ($H_s = 6.0\ m$)

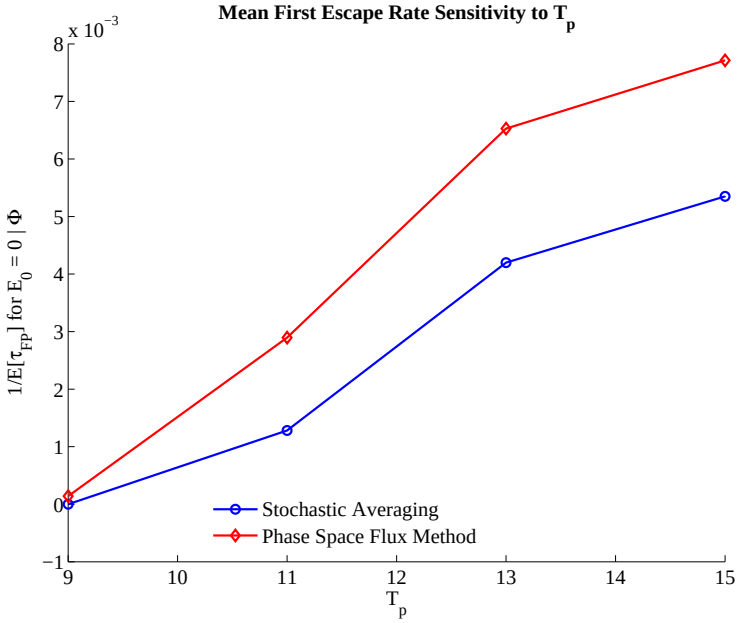

Figure 6.6: Sensitivity of mean first escape rate to peak period ($H_s = 6.0\ m$)

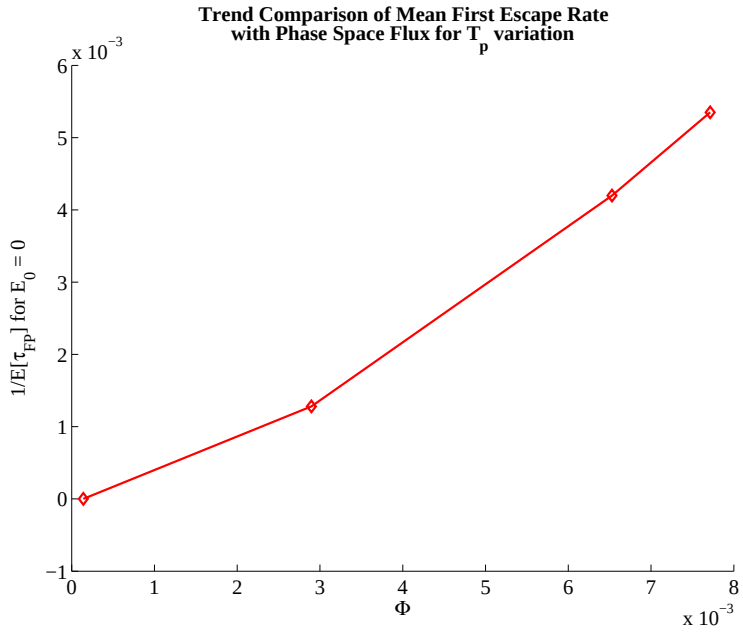

Figure 6.7: Relationship between mean first escape rate and rate of phase space flux for increasing peak period ($H_s = 6.0\ m$)

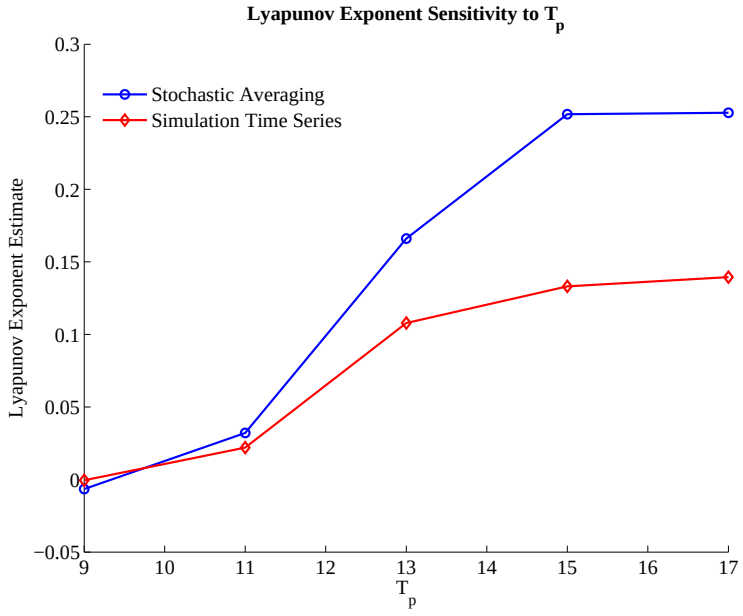

Figure 6.8: Variation of the Lyapunov exponent with peak period ($H_s = 6.0\ m$)

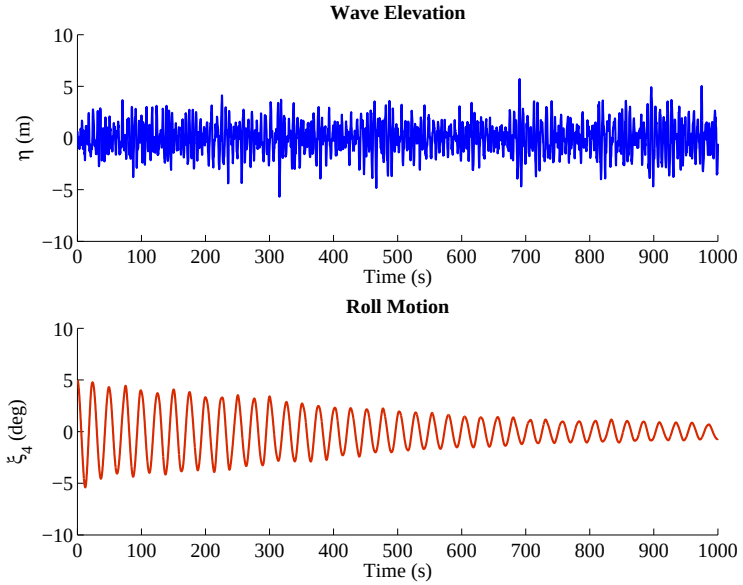

Figure 6.9: Wave elevation and roll motion time history ($H_s = 6.0\ m, T_p = 9.0\ s$)

as the bilge keel width is increased. The damping in three cases is estimated using the Ikeda approach [10] summarized in chapter 2. The corresponding variation of drift and diffusion coefficients is shown in Figure 6.11 and Figure 6.12 respectively. Since the diffusion coefficient only depends on the external excitation (see Equation 5.44), no variation is observed in the diffusion coefficient with increase of damping. However, the drift coefficient is significantly dependent on the damping in the system as seen in Equation 5.42.

The variation of mean first escape rate and rate of phase space flux with bilge keel width is shown in Figure 6.13. It can be seen that although the trend of rate of phase space flux is similar to that of the mean first escape rate, the magnitudes are different.

Figure 6.14 shows the variation of estimated largest Lyapunov exponent from both stochastic averaging and the simulated time series with the bilge keel width. From Figure 6.11 it can be seen that the slope of the drift coefficient at $E = 0$ is

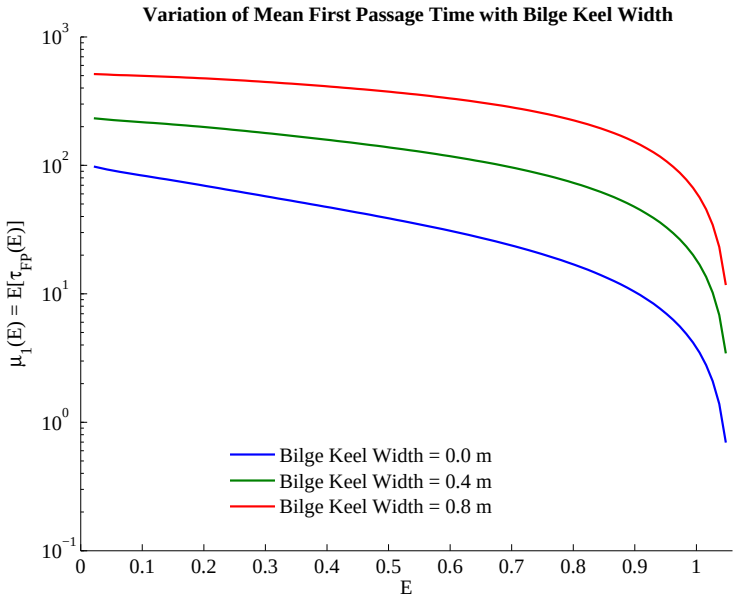

Figure 6.10: Sensitivity of mean first passage time to bilge keel width ($H_s = 6.0\ m,\ T_p = 13.0\ s$)

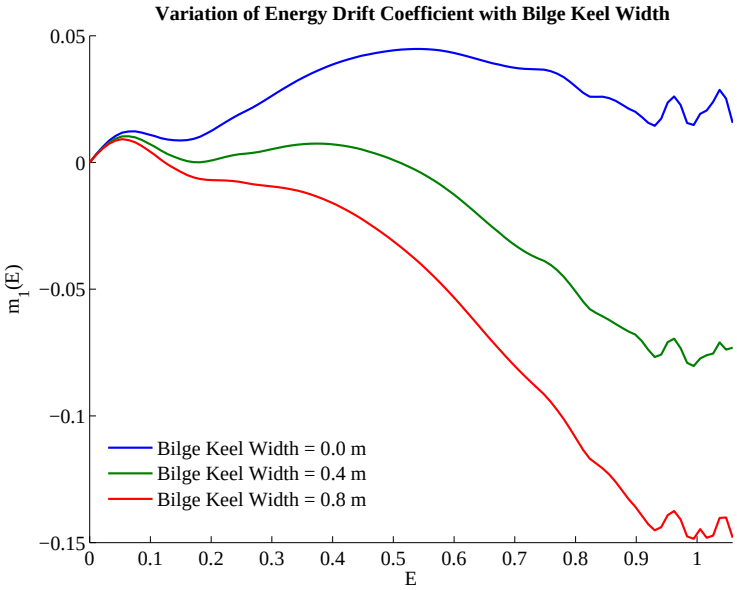

Figure 6.11: Sensitivity of drift coefficient to bilge keel width ($H_s = 6.0\ m,\ T_p = 13.0\ s$)

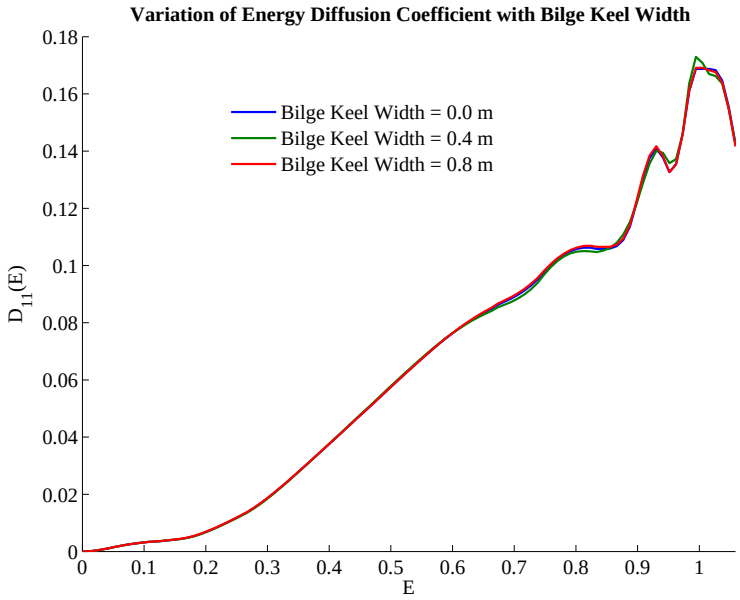

Figure 6.12: Sensitivity of diffusion coefficient to bilge keel width ($H_s = 6.0\ m,\ T_p = 13.0\ s$)

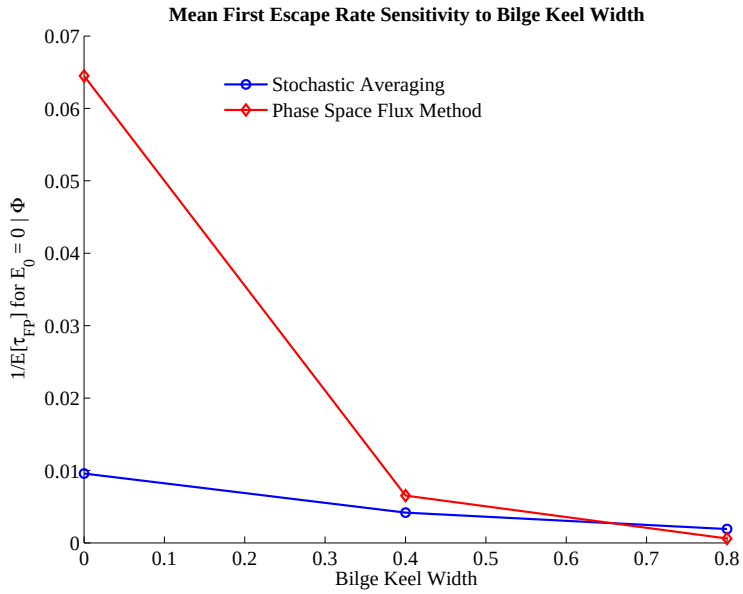

Figure 6.13: Sensitivity of mean first escape rate to bilge keel width ($H_s = 6.0\ m,\ T_p = 13.0\ s$)

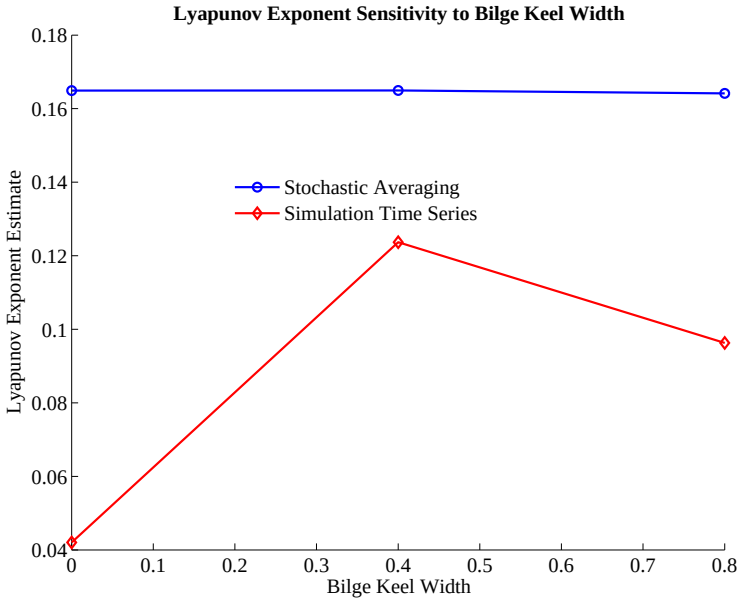

Figure 6.14: Variation of the Lyapunov exponent with bilge keel width ($H_s = 6.0\ m,\ T_p = 13.0\ s$)

almost the same for all three damping cases. From Equation 6.8 we know that the Lyapunov exponent estimate from stochastic averaging depends only on the slope of the drift and diffusion coefficient at $E = 0$. Thus, no considerable variation in the estimate of Lyapunov exponent is seen in Figure 6.14. Although the estimate from simulated time series shows some variation, these values are close to zero indicating that the motion is almost periodic. This can also be seen from the simulated time series shown in Figure 6.15.

6.2.4 Sensitivity to Calm Water Metacentric Height

Figure 6.16 shows the comparison of the mean first passage time for three different values of $\overline{GM}_0$. However, unlike the previous sensitivity studies, a change in metacentric height changes the natural frequency of the vessel. To enable a consistent comparison, the peak period has also been changed for the three cases such that

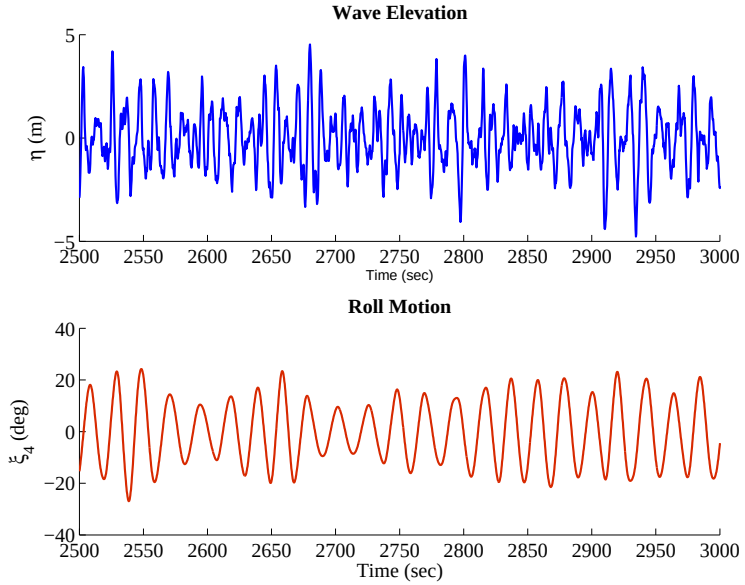

Figure 6.15: Wave elevation and roll motion time history ($H_s = 6.0\ m,\ T_p = 13.0\ s$) for bilge keel width of 0.4 m

the modal frequency of the spectrum is aligned with twice the roll natural frequency. It can be seen that the mean first passage time increases with an increase in the calm water metacentric height $\overline{GM}_0$.

The comparison of the mean first escape rate and the rate of phase space flux is shown in Figure 6.17. The rate of phase space flux varies linearly with calm water metacentric height $\overline{GM}_0$. While, the mean first escape rate also decreases with increase in $\overline{GM}_0$, it is clearly not a linear relation.

Figure 6.18 shows the variation of Lyapunov exponent with calm water $\overline{GM}_0$. Both estimates from stochastic averaging and simulations show a similar decreasing trend with increase in $\overline{GM}_0$.

From the sensitivity studies it can be seen that both the mean first escape rate (calculated using stochastic averaging) and the rate of phase space flux (calculated using the Melnikov analysis) agree well in trend. Although a rigorous mathematical

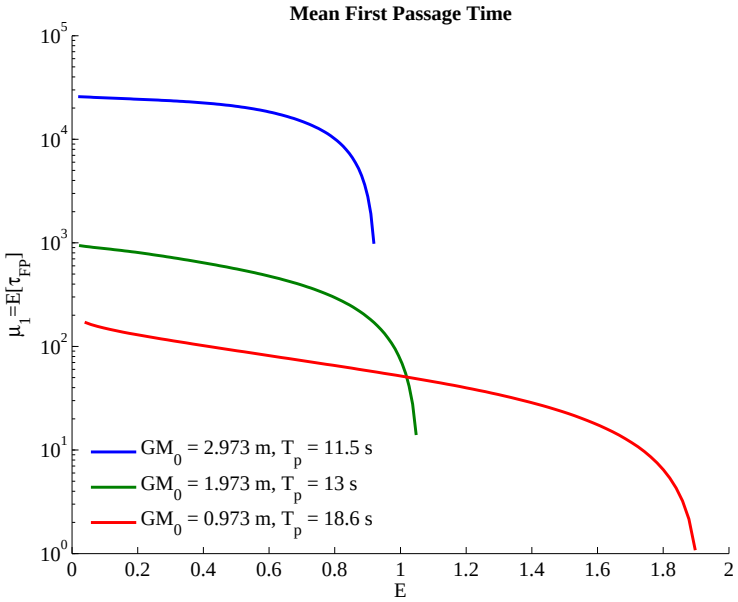

Figure 6.16: Sensitivity of mean first passage time to calm water $\overline{GM}_0$ ($H_s = 6.0\ m$)

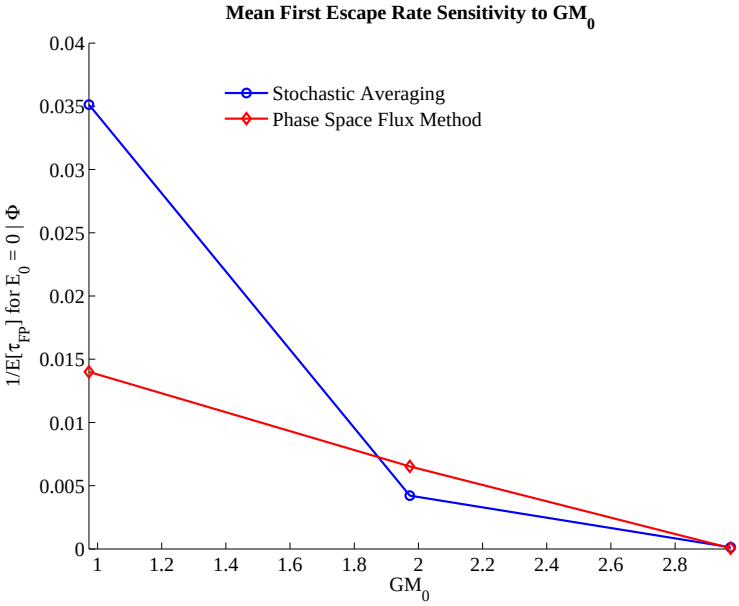

Figure 6.17: Sensitivity of mean first escape rate to calm water $\overline{GM}_0$ ($H_s = 6.0\ m$)

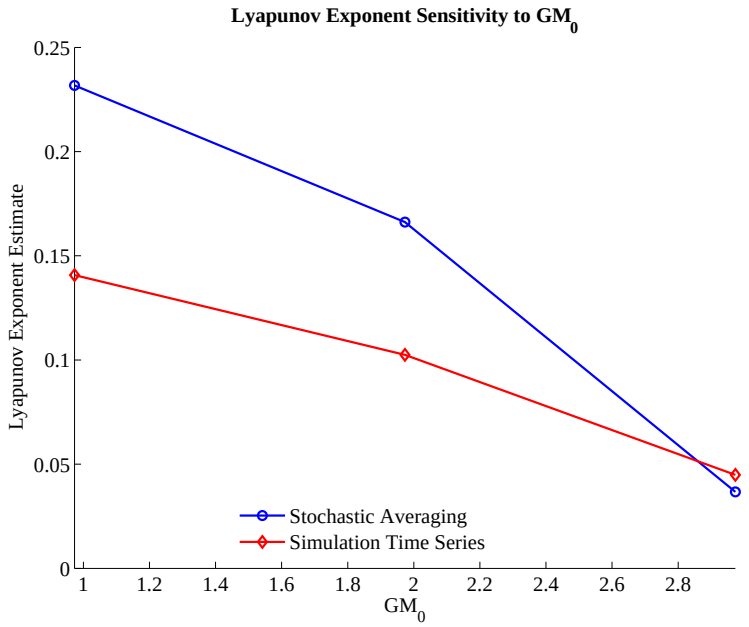

Figure 6.18: Variation of the Lyapunov exponent with calm water $\overline{GM}_0$ ($H_s = 6.0\ m$)

relationship between the two methods does not exist, they both show similar sensitivity trends. Thus these results indicate that both methods are equally robust in the assessment of stability of parametric roll motion in irregular seas. Since these methods are independent of each other they also allow the designer to cross check the two methods and gain confidence on the stability assessment.

7. CONCLUSION AND FUTURE DIRECTIONS

In this dissertation the stability assessment of vessels susceptible to parametric roll in irregular seas has been studied in detail and two independent analytical methods were developed to help a designer quickly quantify the dynamic roll response in irregular head seas. This work provides possible solutions for the ongoing discussions at the International Maritime Organization (IMO) about the development of a second generation of intact stability code with a focus on dynamic stability.

Due to the lack of existing commercial software capable of simulating parametric roll, an early part of the investigation is focused on the development of a generic nonlinear time domain simulation tool SIMDYN capable of simulating the complicated nonlinear dynamics of a vessel at sea. The Euler angle formulation is implemented in the tool to account for large amplitudes of rotation. The nonlinear force vector is computed taking into account both nonlinear restoring and damping forces. The nonlinear restoring forces and moments are computed by integrating the nonlinear Froude-Krylov and hydrostatic pressures over the instantaneous wetted surface under the incident waterline. The nonlinear roll damping is calculated by the program using the empirical formulation as described by Ikeda [63] and Himeno [62].

The developed program is validated extensively with available parametric roll experiments to gain confidence and to ascertain that the simulations accurately capture the relevant dynamics. Further, a statistical study is performed to demonstrate the practical non-ergodicity of parametric roll in irregular seas. The developed program is also applied to simulate the parametric response of a classic spar platform and the results are compared against an available experimental time history to verify that the nonlinear simulation program can capture the dynamics of parametric response

for both ship shaped and non-ship shaped structures.

Although time domain simulations are accurate, they are time consuming and hence unsuitable for stability assessment in the basic design phase. Thus for a stability assessment technique to be applicable in the basic design phase, the criterion must be either analytic or at least semi-analytic in nature for quick assessment. With this in mind, further investigation is centered around developing an analytical model for the roll motion which captures the relevant dynamics of the problem. On comparison with the time domain simulation tool, it is found that the existing models in the literature like the Volterra $\overline{GM}$ model and the Grim's effective wave model are not sufficiently accurate in capturing the dynamics of the parametric roll. Particularly it is found that the Grim's approximation of irregular wave profile in space by a regular wave does not agree well with the nonlinear time domain simulations. Thus, a new analytical model for roll motion is proposed and developed (known as the Volterra $\overline{GZ}$ model) to accurately capture the restoring moment in head seas. Through comparisons with SIMDYN it is shown that the Volterra $\overline{GZ}$ model captures the roll dynamics much better than the existing models. The development of the Volterra $\overline{GZ}$ model is one of the unique contributions of this dissertation.

The Volterra $\overline{GZ}$ model is used as a basis for applying further analytical techniques to quantify the stability of a vessel in irregular head seas. Two independent methods have been developed in this dissertation to assess the stability of a vessel subjected to indirect excitation in irregular seas.

The first technique known as the Melnikov approach is based on the theory of nonlinear dynamical systems. In this approach the Melnikov function for the parametrically excited roll motion is derived based on the analytical Volterra $\overline{GZ}$ model. Stability is assessed in terms of the rate of phase space flux which physically signifies the rate at which the safe basin characterizing the originally safe (bounded) set of

initial conditions is eroded under the effect of the excitation. Closed form expressions for the rate of phase space flux are derived and an associated critical significant wave height is derived. These expressions allow for a quick evaluation of rate of phase space flux without the need to simulate a time history of the process.

The second technique is known as the stochastic averaging approach or alternatively as the Markov approach and is based on the theory of stochastic dynamics. In this approach, the Volterra $\overline{GZ}$ roll model is averaged to yield that the energy of the system can be approximated as a Markov process. Further the coefficients of the governing Itô SDE for the energy process can be related back to the Volterra $\overline{GZ}$ transfer functions and the input wave elevation spectrum. This approximation of energy as a Markov process allows the application of the Pontryagin equation to solve for the mean first passage time. The mean first passage time represents the expected time for the process to reach the capsize boundary given that the system starts with zero energy. The mean first passage time acts as a measure of the stability of the system when subjected to indirect excitation. The mean first passage times obtained from the theory are compared with estimates from Monte Carlo simulations of the roll equation and are found to agree well with each other. The application of stochastic averaging yields analytical expressions for the drift and diffusion coefficients in the Itô equation. The next step of getting the mean first passage time involves solving a boundary value problem given by the Pontryagin equation which makes this method semi-analytical. However, solving this boundary value problem is not at all computationally intense and yields solutions almost instantaneously which enables the use of this approach for quick design assessment.

These two methods are compared for a series of cases and it is found that the stability assessments from both methods are in agreement with each other. Both the Melnikov approach and the Markov approach developed here are original contri-

butions of this dissertation as they have not been previously used to analyze parametrically excited systems which are significantly more challenging than the directly excited systems. Due to the analytical and semi-analytical nature of these methods, they provide for a quick and easy assessment of stability of vessels subjected to parametric excitation which can be easily implemented into either stability guidelines or a regulatory framework.

7.1 Reliability Analysis

So far the discussion of quantifying the susceptibility of a ship to parametric roll has been limited to one sea state defined by the significant wave height H_s and peak period T_p. However, often when designing marine or offshore structures designers are interested in quantifying the maximum response the structure is likely to experience in its lifetime. A ship or offshore structure encounters several sea states over the course of its life. Therefore the environment can no longer be considered to be stationary with one chosen value of significant wave height H_s and peak period T_p. For a long term analysis, the environment is usually specified in the form of a wave scatter diagram indicating the frequency of occurrence of various combinations of significant wave height and peak period.

For estimating the response likely to occur over large intervals of time, recourse is usually taken to long term extreme value prediction theory and reliability analysis. These research areas have been studied extensively in the past and their application to marine and offshore structures are well documented too [157, 158, 159, 160, 161, 162, 163]. However, most of these studies involve expressing the long term probability distribution of the extreme value in terms of long term crossing rates or the probability distribution of peaks or short term extremes [164]. However a common theme in these approaches is that the probability density function of the response

for a given value of significant wave height and peak period is usually known either from simulations or by obtaining the solution of FPK equation.

The Melnikov and Markov approaches lead to the calculation of rate of phase space flux and mean first passage time which are indicative of how much time the system takes before reaching a critical boundary. This is significantly different from the probability distribution of the response. Therefore the traditional reliability analysis methods quantifying the probability of exceedance are not directly applicable to this problem herein.

However, an attempt can still be made to estimate the system reliability by combining some of the ideas of the long term extreme value analysis. One possible approach includes calculating the mean first passage time estimate from either the Melnikov or stochastic dynamics approach for several combinations of significant wave height and peak period and then calculating the long term mean first passage estimate by taking a weighted sum based on the frequency of occurrence listed in the wave scatter diagram. Mathematically, the long term mean first passage time $\mu_1^{(l)}$ can be expressed as shown in (7.1).

$$\mu_1^{(l)} = \iint \mu_1(h_s, t_p) f_{H_s T_p}(h_s, t_p) dh_s dt_p \tag{7.1}$$

$f_{H_s T_p}(h_s, t_p)$ represents the joint probability density function of significant wave height and peak period which can be empirically determined from the wave scatter diagram. However if the wave scatter diagram is too coarse, leading to poor resolution in tail regions, Naess and Moan [164] suggest the use of smooth joint probability density function of the parameters characterizing the short term sea states as shown

below.

$$f_{H_sT_p}(h_s, t_p) = f_{H_s}(h_s) f_{T_p|H_s}(t_p|h_s) \tag{7.2}$$

where

$$f_{H_s}(h_s) = \begin{cases} \frac{1}{\sqrt{2\pi}\alpha h_s} \exp\{-\frac{(\ln(h_s)-\theta)^2}{2\alpha^2}\} & h_s \leq \eta \\ \frac{\beta}{\rho}\left(\frac{h_s}{\rho}\right)^{\beta-1} \exp\{-\left(\frac{h_s}{\rho}\right)^{\beta}\} & h_s > \eta \end{cases} \tag{7.3}$$

$$f_{T_p|H_s}(t_p|h_s) = \frac{1}{\sqrt{2\pi}\sigma t_p} \exp\{-\frac{(\ln(t_p)-\mu)^2}{2\sigma^2}\} \tag{7.4}$$

The parameters μ and σ are given by

$$\mu = a_1 + a_2 h_s^{a_3} \tag{7.5}$$

$$\sigma = b_1 + b_2 \exp(-b_3 h_s) \tag{7.6}$$

The parameters α, θ, β, η, ρ, a_1, a_2, a_3, b_1, b_2, b_3 depend on the geographical location. For the North sea these values are given as $\alpha = 0.6565$, $\theta = 0.77$, $\beta = 2.691$, $\eta = 2.90$, $\rho = 1.503$, $a_1 = 1.134$, $a_2 = 0.892$, $a_3 = 0.225$, $b_1 = 0.005$, $b_2 = 0.120$, $b_3 = 0.455$ [164]. The parameter η is the transition parameter separating the log-normal distribution for smaller significant wave heights and the Weibull distribution for the large wave heights. The use of a different distribution focusing on the tail region is a commonly employed approach to achieve a better prediction of the extreme values of a process [86, 85].

Note that the short term mean first passage time $\mu_1(h_s, t_p)$ can be estimated using either the stochastic dynamics approach or the Melnikov approach (inverse of the

rate of phase space flux). The calculated long term mean first passage time can then used as a measure for reliability of the structure. In particular it can be compared against the design life of the structure to effectively understand the risk associated with each design. Due to the use of analytical techniques, this method of estimating reliability of the structure will not be computationally intensive and can be managed in a reasonable amount of time.

As is evident from above, demonstration of method will require knowing the environmental conditions in significant detail which are not always readily available and also significantly depend on the geographical location under consideration. Hence this approach is deemed out of the scope of this dissertation and is included as future work continuing on the developments described here.

REFERENCES

[1] Haslum H. Simplified methods applied to nonlinear motion of spar platforms [PhD Dissertation]. Norwegian University of Science and Technology. Trondheim; 2000.

[2] France W, Levadou M, Treakle TW, Paulling JR, Michel RK, Moore C. An investigation of head-sea parametric rolling and its influence on container lashing systems. Marine Technology. 2003;40(1):1–19.

[3] Haslum H. Various applications of spar platforms. In: 70 Years Anniversary Seminar for Professors Odd M. Faltinsen and Torgeir Moan. Trondheim: Norwegian University of Science and Technology; 2004. p. 1–16.

[4] Guha A, Somayajula A, Falzarano J. Time domain simulation of large amplitude motions in shallow water. In: 21st SNAME Offshore Symposium. Houston, TX: Society of Naval Architects and Marine Engineers; 2016. p. 1–20.

[5] Guide for the assessment of parametric roll resonance in the design of container carriers. Houston, TX, USA: American Bureau of Shipping (ABS); 2004.

[6] Francescutto A. Intact stability criteria of ships - Past, present and future. Ocean Engineering. 2016;120(2016):312–317.

[7] Haslum HA, Faltinsen OM. Alternative shape of spar platforms for use in hostile areas. In: Offshore Technology Conference. Houston, TX: Society of Petroleum Engineers; 1999. p. 1–12.

[8] Koo BJ, Kim MH, Randall RE. Mathieu instability of a spar platform with mooring and risers. Ocean Engineering. 2004;31(17-18):2175–2208.

[9] Somayajula A, Falzarano J. Large-amplitude time-domain simulation tool for marine and offshore motion prediction. Marine Systems & Ocean Technology. 2015 apr;10(1):1–17.

[10] Falzarano J, Somayajula A, Seah R. An overview of the prediction methods for roll damping of ships. Ocean Systems Engineering. 2015;5(2):55–76.

[11] Somayajula AS, Falzarano J. A comparative assessment of simplified models for simulating parametric roll. Journal of Offshore Mechanics and Arctic Engineering. 2017 jan;139(2):021103.

[12] Guckenheimer J, Holmes P. Nonlinear Oscillations, Dynamical Systems, and Bifurcations of Vector Fields. vol. 42 of Applied Mathematical Sciences. 1st ed. Marsden JE, Sirovich L, editors. New York: Springer New York; 1983.

[13] Wiggins S. Introduction to Applied Nonlinear Dynamical Systems and Chaos. vol. 2 of Texts in Applied Mathematics. 2nd ed. Marsden JE, Sirovich L, Antman SS, editors. New York: Springer-Verlag; 2003.

[14] Falzarano JM. Predicting complicated dynamics leading to vessel capsizing [PhD Dissertation]. University of Michigan. Ann Arbor; 1990.

[15] Hsieh SR, Troesch AW, Shaw SW. A nonlinear probabilistic method for predicting vessel capsizing in random beam seas. Proceedings of the Royal Society A: Mathematical, Physical and Engineering Sciences. 1994 jul;446(1926):195–211.

[16] Jiang C, Troesch AW, Shaw SW. Capsize criteria for ship models with memory-dependent hydrodynamics and random excitation. Philosophical Transactions of the Royal Society A: Mathematical, Physical and Engineering Sciences. 2000;358(1771):1761–1791.

[17] Su Z, Falzarano JM. Markov and Melnikov based methods for vessel capsizing criteria. Ocean Engineering. 2013;64:146–152.

[18] Lin Y, Cai G. Probabilistic Structural Dynamics: Advanced Theory and Applications. 1st ed. New York: McGraw-Hill; 2004.

[19] Roberts J. A stochastic theory for nonlinear ship rolling in irregular seas. Journal of Ship Research. 1982;26(4):229–245.

[20] Roberts J, Dacunha N. Roll motion of a ship in random beam waves: Comparison between theory and experiment. Journal of Ship Research. 1985;29(2):112–126.

[21] Su Z. Nonlinear response and stability analysis of vessel rolling motion in random waves using stochastic dynamical systems [PhD Dissertation]. Texas A&M University. College Station; 2012.

[22] Froude W. On the rolling of ships. London: Institution of Naval Architects; 1861.

[23] Salvesen N, Tuck E, Faltinsen O. Ship motions and sea loads. Transactions of Society of Naval Architects and Marine Engineers. 1970;78(8):250–287.

[24] Newman J. The theory of ship motions. In: Advances in Applied Mechanics. vol. 18. New York: Academic Press; 1979. p. 221–283.

[25] Ogilvie T, Tuck E. A rational strip theory of ship motions: part I. Ann Arbor, MI, USA: University of Michigan; 1969.

[26] Journée J. Theoretical manual of SEAWAY. Delft, Netherlands: Delft University of Technology; 2001.

[27] Beck R, Troesch A. Documentation and user's manual for the computer program SHIPMO. Ann Arbor, MI, USA: University of Michigan; 1989.

[28] Nakos D, Sclavounos P. Ship motions by a three-dimensional Rankine panel method. In: 18th Symposium on Naval Hydrodynamcis. Ann Arbor, MI: The National Academies Press; 1991. p. 21–40.

[29] Lee CH, Newman J. Computation of wave efects using the panel method. In: Chakrabarti SK, editor. Numerical Models in Fluid-Structure Interaction. vol. 42. Southampton: WIT Press; 2005. p. 211–251.

[30] Faltinsen OM. Wave loads on offshore structures. Annual Review of Fluid Mechanics. 1990 jan;22(1):35–56.

[31] Guha A, Falzarano J. Estimation of hydrodynamic forces and motion of ships with steady forward speed. International Shipbuilding Progress. 2016 apr;62(3-4):113–138.

[32] Liapis S. Time-domain analysis of ship motions [PhD Dissertation]. University of Michigan. Ann Arbor; 1986.

[33] King B. Time-domain analysis of wave exciting forces on ships and bodies [PhD Dissertation]. University of Michigan. Ann Arbor; 1987.

[34] Lin W, Yue D. Numerical solutions for large-amplitude ship motions in the time domain. In: 18th Symposium on Naval Hydrodynamcis. Ann Arbor, MI: The National Academies Press; 1991. p. 41–66.

[35] Magee AR. Large-amplitude ship motions in the time domain [PhD Dissertation]. University of Michigan. Ann Arbor; 1991.

[36] Bingham H. Simulating ship motions in the time domain [PhD Dissertation]. Massachusetts Institute of Technology. Cambridge; 1994.

[37] Beck RF. Time-domain computations for floating bodies. Applied Ocean Research. 1994 jan;16(5):267–282.

[38] Sen D. Time-domain computation of large amplitude 3D ship motions with forward speed. Ocean Engineering. 2002 jul;29(8):973–1002.

[39] Somayajula AS, Falzarano JM. Validation of Volterra series approach for modelling parametric rolling of ships. In: Proceedings of 34th International Conference on Ocean, Offshore and Arctic Engineering - Volume 11: Prof. Robert F. Beck Honoring Symposium on Marine Hydrodynamics. St. John's, NL, Canada: ASME; 2015. p. V011T12A043.

[40] Somayajula A. Time domain ship motion simulation using the transient time domain green function. College Station, TX, USA: Texas A&M University; 2014.

[41] Guha A, Falzarano J. Development of a computer program for three dimensional analysis of zero speed first order wave body interaction in frequency domain. In: Proceedings of the 32nd International Conference on Ocean, Offshore and Arctic Engineering - Volume 5: Ocean Engineering. Nantes, France: ASME; 2013. p. V005T06A094.

[42] Somayajula A, Guha A, Falzarano J, Chun HH, Jung KH. Added resistance and parametric roll prediction as a design criteria for energy efficient ships. Ocean Systems Engineering. 2014 jun;4(2):117–136.

[43] Vugts JH. The hydrodynamic forces and ship motions in waves [PhD Dissertation]. Delft University of Technology. Delft; 1970.

[44] Abkowitz M. Stability and Motion Control of Ocean Vehicles. Cambridge: MIT Press; 1969.

[45] Lewandowski EM. The Dynamics of Marine Craft. vol. 22 of Advanced Series on Ocean Engineering. Singapore: World Scientific; 2004.

[46] Ogilvie T. Second-order hydrodynamic effects on ocean platforms. In: Yeung RW, editor. International Workshop on Ship and Platform Motions. Berkley, CA: University of California, Berkley; 1983. p. 205–265.

[47] Somayajula A, Falzarano J. A comparative assessment of approximate methods to simulate second order roll motion of FPSOs. Ocean Systems Engineering. 2017;7(1):53–74.

[48] Paulling JR. MultiSim - Time domain platform motion simulation. Geyserville, CA, USA: J. Randolph Paulling Inc; 1995.

[49] Magee AR. RATANA - Rotations et translations à amplitude finie d ' un navire. Val-de-Reuil, France: Bassin D'essais des Carènes; 1997.

[50] Shin YS, Belenky V, Lin WM, Weems KM, Engle AH. Nonlinear time domain simulation technology for seakeeping and wave-load analysis for modern ship design. Transactions of Society of Naval Architects and Marine Engineers. 2003;111:557–583.

[51] Singh SP, Sen D. A comparative linear and nonlinear ship motion study using 3-D time domain methods. Ocean Engineering. 2007;34(13):1863–1881.

[52] Guha A. Development of a computer program for three dimensional frequency domain analysis of zero speed first order wave body interaction [Masters Thesis]. Texas A&M University. College Station; 2012.

[53] Wheeler JD. Method for calculating forces produced by irregular waves. Journal of Petroleum Technology. 1970;22(3):359–367.

[54] Cummins W. The impulse response function and ship motions. Washington D.C., USA: David Taylor Model Basin; 1962.

[55] Ogilvie T. Recent progress toward the understanding and prediction of ship motions. In: 5th Symposium on Naval Hydrodynamics. Bergen, Norway: The National Academies Press; 1964. p. 3–80.

[56] Greenhow M. High-and low-frequency asymptotic consequences of the Kramers-Kronig relations. Journal of Engineering Mathematics. 1986;20(4):293–306.

[57] Perez T, Fossen T. A derivation of high-frequency asymptotic values of 3D added mass and damping based on properties of the cummins' equation. Journal of Maritime Research. 2008;5(1):65–78.

[58] Tanaka N, Hishida T. A study on the bilge keels : Part 2 - Full sized model experiment. Journal of Zosen Kiokai. 1957;103:69–73.

[59] Tanaka N, Hishida T. A study on the bilge keels : Part 1 - Two dimensional model experiments. Journal of Zosen Kiokai. 1957;101:99–105.

[60] Tanaka N, Hishida T. A study on the bilge keels : Part 3 - The effect of the ship form and the bilge keel size on the action of the bilge keel. Journal of Zosen Kiokai. 1959;105:27–32.

[61] Tanaka N, Hishida T. A study on the bilge keels : Part 4 - On the eddy-making resistance to the rolling of a ship hull. Journal of Zosen Kiokai. 1960;109:205–212.

[62] Himeno Y. Prediction of ship roll damping - A state of the art. Ann Arbor, MI, USA: University of Michigan; 1981.

[63] Ikeda Y, Himeno Y, Tanaka N. A prediction method for ship roll damping. Osaka, Japan: University of Osaka Prefecture; 1978.

[64] Dalzell J. A note on the form of ship roll damping. Bathesda, MD, USA: David Taylor Naval Ship Research; 1976.

[65] Kaplan P. Lecture notes on nonlinear theory of ship roll motion in a random seaway. Glen Cove, NY, USA: Webb Institue of Naval Architecture; 1966.

[66] Ikeda Y, Himeno Y, Tanaka N. Components of roll damping of ship at forward speed. Journal of Society of Naval Architecture of Japan. 1978;143:113–125.

[67] Kato H. On the frictional resistance to the rolling ships. Journal of Society of Naval Architecture of Japan. 1958;102:115–122.

[68] Schmitke R. Ship sway, roll, and yaw motions in oblique seas. Transactions of Society of Naval Architects and Marine Engineers. 1978;86:26–46.

[69] Ikeda Y, Himeno Y, Tanaka N. On eddy making component of roll damping force on naked hull. Journal of Japan Society of Naval Architects. 1977;142:54–64.

[70] Standing R. Prediction of viscous roll damping and response of transportation barges in waves. In: 1st International Offshore and Polar Engineering Conference. vol. 3. Edinburgh, UK: International Society of Offshore and Polar Engineers (ISOPE); 1991. p. 409–419.

[71] Patel MH, Brown DT. On predictions of resonant roll motions for flat-bottomed barges. Transactions of Royal Institution of Naval Architects. 1986;128:235–245.

[72] Braathen A, Faltinsen OM. Application of a vortex tracking method to roll damping. Advances in Underwater Technology, Ocean Science and Offshore Engineering. 1988;15:177–193.

[73] Lewis FM. The inertia of water surrounding a vibrating ship. Transactions of Society of Naval Architects and Marine Engineers. 1929;37:1–20.

[74] McCormick M. Ocean Engineering Mechanics: With Applications. New York: Cambridge University Press; 2009.

[75] Rice SO. Mathematical analysis of random noise. Bell System Technical Journal. 1944 jul;23(3):282–332.

[76] Tucker MJ, Challenor PG, Carter DJT. Numerical simulation of a random sea: a common error and its effect upon wave group statistics. Applied Ocean Research. 1984 apr;6(2):118–122.

[77] Medina JR, Aguilar J. Comments on "Numerical simulation of a random sea: a common error and its effect upon wave group statistics by M.J. Tucker, T.G. Challenor and D.J.T. Carter". Applied Ocean Research. 1985 apr;7(2):113.

[78] Elgar S, Guza RT, Seymour RJ. Wave group statistics from numerical simulations of a random sea. Applied Ocean Research. 1985 apr;7(2):93–96.

[79] Belenky VL, Weems KM, Lin WM, Paulling JR. Probabilistic analysis of roll parametric resonance in head seas. In: Santos A, Neves M, Belenky VL, Kat JO, Spyrou K, Umeda N, editors. Contemporary Ideas on Ship Stability and Capsizing in Waves. vol. 97 of Fluid Mechanics and Its Applications. Dordrecht: Springer Netherlands; 2011. p. 555–569.

[80] Silva SRE, Soares CG, Turk A, Prpic-Orsic J, Uzunoglu E. Experimental assessment of the parametric rolling on a C11 class containership. In: HYDRALAB III Joint User Meeting. Hannover: HYDRALAB; 2010. .

[81] Somayajula A, Falzarano J. Critical assessment of reverse-MISO techniques for system identification of coupled roll motion of ships. Journal of Marine

Science and Technology. 2016 aug;p. 1–19.

[82] Somayajula A, Falzarano J. Estimation of roll motion parameters using R-MISO system identification technique. In: Chung JS, Muskulus M, Kokkinis T, Wang AM, editors. 26th International Offshore and Polar Engineering (ISOPE 2016) Conference. vol. 3. Rhodes (Rodos), Greece: International Society of Offshore and Polar Engineers (ISOPE); 2016. p. 568–574.

[83] Bulian G, Francescutto A, Lugni C. Theoretical, numerical and experimental study on the problem of ergodicity and 'practical ergodicity' with an application to parametric roll in longitudinal long crested irregular sea. Ocean Engineering. 2006 jun;33(8-9):1007–1043.

[84] Lutes LD, Sarkani S. Random Vibrations: Analysis of Structural and Mechanical Systems. 1st ed. Boston: Elsevier Butterworth-Heinemann; 2004.

[85] Somayajula A, Falzarano JM. Non-Gaussian analysis methods for planing craft motion. Ocean Systems Engineering. 2014 dec;4(4):293–308.

[86] Guha A, Somayajula A, Falzarano JM. Analysis of causeway ferry dynamics for safe operation of improved navy lighterage system. In: Proceedings of the 13th International Ship Stability Workshop. Brest, France: STAB International Standing Committee; 2013. p. 1–8.

[87] Su Z, Falzarano JM. Gaussian and non-Gaussian cumulant neglect application to large amplitude rolling in random waves. International Shipbuilding Progress. 2011;58:97–113.

[88] Liu Y, Yan H, Yung TW. Nonlinear resonant response of deep draft platforms in surface waves. In: 29th International Conference on Ocean, Offshore and Arctic Engineering: Volume 3. Shanghai, China: ASME; 2010. p. 773–780.

[89] Dahl LJCH. Octabuoy concept and spar buoys : Non-linear effects and analysis [Masters Thesis]. Norwegian University of Science and Technology. Trondheim; 2012.

[90] Huang E, Bhat S, Luo Y, Zou J. Evaluation of dry tree platform concepts. In: Offshore Technology Conference. Houston, TX: Society of Petroleum Engineers; 2000. p. 1–13.

[91] Chou F, Chianis J, Zhang X. Self-installed single column floater. In: 23rd International Conference on Offshore Mechanics and Arctic Engineering, Volume 1, Parts A and B. Vancouver, British Columbia, Canada: ASME; 2004. p. 803–815.

[92] Jordan DW, Smith P. Nonlinear Ordinary Differential Equations : An Introduction to Dynamical Systems. 4th ed. New York: Oxford University Press; 1999.

[93] Paulling JR. The transverse stability of a ship in a longitudinal seaway. Journal of Ship Research. 1961;4(4):37–49.

[94] Neves MAS, Rodriguez C. A coupled third order model of roll parametric resonance. In: Soares CG, Garbatov Y, Fonseca N, editors. Maritime Transportation and Exploitation of Ocean and Coastal Resources - Volume 1: Vessels for Maritime Transportation. London, UK: Taylor and Francis Group Plc; 2005. p. 243–253.

[95] Neves MAS, Rodríguez CA. Influence of non-linearities on the limits of stability of ships rolling in head seas. Ocean Engineering. 2007 aug;34(11-12):1618–1630.

[96] Bulian G. Development of analytical nonlinear models for parametric roll and hydrostatic restoring variations in regular and irregular waves [PhD Disserta-

tion]. Università degli studi di Trieste. Trieste; 2006.

[97] Spyrou KJ, Tigkas I, Scanferla G, Gavriilidis N. Problems and capabilities in the assessment of parametric rolling. In: Proceedings of the 10th International Ship Stability Workshop. vol. 4. Daejeon, South Korea: STAB International Standing Committee; 2005. p. 47–55.

[98] Spyrou KJ, Tigkas I, Scanferla G, Pallikaropoulos N, Themelis N. Prediction potential of the parametric rolling behaviour of a post-panamax containership. Ocean Engineering. 2008 aug;35(11-12):1235–1244.

[99] Moideen H, Falzarano JM, Sharma SA. Parametric roll of container ships in head waves. Ocean Systems Engineering. 2012 dec;2(4):239–255.

[100] Moideen H, Somayajula A, Falzarano JM. Parametric roll of high speed ships in regular waves. In: Proceedings of 32nd International Conference on Ocean, Offshore and Arctic Engineering - Volume 5: Ocean Engineering. Nantes, France: ASME; 2013. p. V005T06A095.

[101] Grim O. Beitrag zu dem Problem der Sicherheit des Schiffes im Seegang. Hamburg: Schiffbau-Versuchsanstalt; 1961.

[102] Umeda N, Hashimoto H, Vassalos D. Nonlinear dynamics on parametric roll resonance with realistic numerical modelling. International Shipbuilding Progress. 2004;51(2):205–220.

[103] Hashimoto H, Umeda N, Matsuda A, Nakamura S. Experimental and numerical studies on parametric roll of a post-panamax container ship in irregular waves. In: Proceedings of the 9th International Conference on Stability of Ships and Ocean Vehicles (STAB'06). vol. 1. Rio de Janerio, Brazil: STAB International Standing Committee; 2006. p. 181–190.

[104] Bulian G, Francescutto A, Umeda N, Hashimoto H. Qualitative and quantitative characteristics of parametric ship rolling in random waves in the light of physical model experiments. Ocean Engineering. 2008 dec;35(17-18):1661–1675.

[105] Hashimoto H, Umeda N, Ogawa Y, Taguchi H, Iseki T, Bulian G, et al. Prediction methods for parametric rolling with forward velocity and their validation - Final report of SCAPE committee (part 2). In: The 6th Osaka Colloquium on Seakeeping and Stability of Ships. Osaka, Japan: SCAPE Committee; 2008. .

[106] Hua J, Wang W, Chang J. A representation of GM-variation in waves by the Volterra system. Journal of Marine Science and Technology. 1999;7(2):94–100.

[107] Moideen H, Somayajula A, Falzarano JM. Application of Volterra series analysis for parametric rolling in irregular seas. Journal of Ship Research. 2014;58(2):97–105.

[108] Somayajula AS, Falzarano JM. Non-linear dynamics of parametric roll of container ship in irregular seas. In: Proceedings of 33rd International Conference on Ocean, Offshore and Arctic Engineering - Volume 7: Ocean Space Utilization; Professor Emeritus J. Randolph Paulling Honoring Symposium on Ocean Technology. San Francisco, CA: ASME; 2014. p. V007T12A018.

[109] Webster W. Motion in regular waves - Transverse motions. In: Lewis E, editor. Principles of Naval Architecture Vol III. Jersey City: SNAME; 1989. .

[110] Moideen H. Prediction of parametric roll of ships in regular and irregular sea [Masters Thesis]. Texas A&M University. College Station; 2010.

[111] Bulian G. On an improved Grim effective wave. Ocean Engineering. 2008;35(17):1811–1825.

[112] Moseley H. On the dynamical stability and on the oscillations of floating bodies. Philosophical Transactions of the Royal Society of London. 1850;140:609–643.

[113] Spyrou KJ, Thompson JMT. The nonlinear dynamics of ship motions: a field overview and some recent developments. Philosophical Transactions of the Royal Society of London Series A: Mathematical, Physical and Engineering Sciences. 2000;358(1771):1735–1760.

[114] Thompson JMT, Rainey RCT, Soliman MS. Mechanics of ship capsize under direct and parametric wave excitation. Philosophical Transactions of the Royal Society A: Mathematical, Physical and Engineering Sciences. 1992;338:471–490.

[115] Spyrou KJ. Dynamic instability in quartering seas: The behavior of a ship during broaching. Journal of Ship Research. 1996;40(1):46–59.

[116] Virgin LN. The nonlinear rolling response of a vessel including chaotic motions leading to capsize in regular seas. Applied Ocean Research. 1987;9(2):89–95.

[117] Nayfeh AH, Khdeir AA. Nonlinear rolling of ships in regular beam seas. International Shipbuilding Progress. 1986;33(379):40–49.

[118] Lou JYK, Xie G. Solution methods of complex nonlinear dynamic systems in offshore engineering. College Station, TX, USA: Offshore Technology Research Center, Texas A&M University; 1993.

[119] Greenspan B, Holmes P. Repeated resonance and homoclinic bifurcation in a periodically forced family of oscillators. SIAM Journal on Mathematical Analysis. 1984 jan;15(1):69–97.

[120] Wiggins S. Introduction to Applied Nonlinear Dynamical Systems and Chaos. 1st ed. John F, Marsden J, Sirovich L, Golubitsky M, Äger WJ, editors. New

York: Springer-Verlag; 1990.

[121] Melnikov VK. On the stability of the center for time-periodic perturbations. Transactions of Moscow Mathematical Society. 1963;12:1–57.

[122] Frey M, Simiu E. Noise-induced chaos and phase space flux. Physica D: Nonlinear Phenomena. 1993;63:321–340.

[123] Hsieh SR, Shaw SW, Troesch AW. A predictive method for vessel capsize in random seas. In: Falzarano JM, Papoulias F, editors. Proceedings of the 1993 ASME Winter Annual Meeting: Nonlinear Dynamics of Marine Vehicles. vol. 51. New Orleans, LA: ASME; 1993. p. 103–123.

[124] Vishnubhotla S, Falzarano J, Vakakis A. A new method to predict vessel/platform critical dynamics in a realistic seaway. Philosophical Transactions of the Royal Society A: Mathematical, Physical and Engineering Sciences. 2000 jun;358(1771):1967–1981.

[125] Esparza I, Falzarano J. Nonlinear rolling motion of a statically biased ship under the effect of external and parametric excitation. In: Sinha SC, Evan-Iwanowski RM, editors. Proceedings of the 14th Biennial Conference on Mechanical Vibration and Noise: Dynamics and Vibration of Time-Varying Systems and Structures. vol. 56. Albuquerque, NM: ASME; 1993. p. 111–122.

[126] Falzarano JM, Holappa K, Taz-Ul-Mulk M. A generalized analysis of saturation induced ship rolling motion. In: Falzarano JM, Papoulias F, editors. Proceedings of the 1993 ASME Winter Annual Meeting: Nonlinear Dynamics of Marine Vehicles. vol. 51. New Orleans, LA: ASME; 1993. p. 73–92.

[127] Parker TS, Chua LO. Practical Numerical Algorithms for Chaotic Systems. 1st ed. New York: Springer; 1989.

[128] Falzarano JM, Shaw SW, Troesch AW. Application of global methods for analyzing dynamical systems to ship rolling motion and capsizing. International Journal of Bifurcation and Chaos. 1992 mar;2(1):101–115.

[129] Spyrou KJ, Cotton B, Gurd B. Analytical expressions of capsize boundary for a ship with roll bias in beam waves. Journal of Ship Research. 2002;46(3):167–174.

[130] Huang X, Gu X, Bao W. The probability distribution of rolling amplitude of a ship in high waves. In: Proceedings of 5th International Conference on Stability of Shipsand Oean Vehicles (STAB94). vol. 4. Melbourne, FL: STAB International Standing Committee; 1994. p. 77–100.

[131] Scolan YM. Application de la méthode de Melnikov pour l'étude du roulis non linéaire des navires dans la houle. Comptes Rendus de l'Académie des Sciences - Series IIB - Mechanics-Physics-Astronomy. 1999 jan;327(1):1–6.

[132] Jiang C. Highly nonlinear rolling motion leading to capsize [PhD Dissertation]. University of Michigan. Ann Arbor; 1995.

[133] Simiu E. Chaotic Transitions in Deterministic and Stochastic Dynamical Systems: Applications of Melnikov Processes in Engineering, Physics, and Neuroscience. 1st ed. New Jersey: Princeton University Press; 2002.

[134] Roberts JB, Spanos PD. Random Vibration and Statistical Linearization. Mineola: Dover Publications; 2003.

[135] Caughey TK. On the response of non-linear oscillators to stochastic excitation. Probabilistic Engineering Mechanics. 1986 mar;1(1):2–4.

[136] Lutes LD. Approximate technique for treating random vibration of hysteretic systems. Journal of the Acoustical Society of America. 1970 jul;48(1B):299–

306.

[137] Stratonovich RL. Topics in the Theory of Random Noise: Volume I. Silverman RA, editor. New York: Gordon and Breach, Science Publishers, Inc.; 1963.

[138] Stratonovich RL. Topics in the Theory of Random Noise: Volume II. Silverman RA, editor. New York: Gordon and Breach, Science Publishers, Inc.; 1967.

[139] Caughey TK. Nonlinear theory of random vibrations. In: Yih CS, editor. Advances in Applied Mechanics (Volume 11). New York: Academic Press; 1971. p. 209–253.

[140] Mayfield W. A sequence solution to the Fokker-Planck equation. IEEE Transactions on Information Theory. 1973 mar;19(2):165–176.

[141] Wehner MF, Wolfer WG. Numerical evaluation of path-integral solutions to Fokker-Planck equations. Physical Review A. 1983 may;27(5):2663–2670.

[142] Jamnongpipatkul A. Ship rolling motion subjected to colored noise excitation [Masters Thesis]. Texas A&M University. College Station; 2010.

[143] Chai W, Naess A, Leira BJ, Carlo M. Stochastic dynamic analysis and reliability of a vessel rolling in random beam seas. Journal of Ship Research. 2015;59(2):113–131.

[144] Papanicolaou GC, Kohler W. Asymptotic theory of mixing stochastic ordinary differential equations. Communications on Pure and Applied Mathematics. 1974 sep;27(5):641–668.

[145] Khas'minskii R. A limit theorem for the solutions of differential equations with random right-hand sides. Theory of Probability & Its Applications. 1966;11(3):390–406.

[146] Roberts JB. Averaging methods in random vibration. Lyngby, Denmark: Technical University Denmark; 1989.

[147] Bogoliubov NN, Mitropolski YA. Asymptotic Methods in the Theory of Nonlinear Oscillations. 1st ed. New York: Gordon and Breach; 1961.

[148] Roberts JB, Vasta M. Energy-based stochastic estimation for nonlinear oscillators with random excitation. Journal of Applied Mechanics. 2000;67(4):763–771.

[149] Cai GQ. Random vibration of nonlinear system under nonwhite excitations. Journal of Engineering Mechanics. 1995 may;121(5):633–639.

[150] Cai GQ, Lin YK. On statistics of first-passage failure. Journal of Applied Mechanics. 1994;61(1):93.

[151] Higham DJ. An algorithmic introduction to numerical simulation of stochastic differential equations. SIAM Review. 2001 jan;43(3):525–546.

[152] Devaney R. An Introduction to Chaotic Dynamical Systems. 1st ed. Redwood City: Addison Wesley Publishing Company; 1989.

[153] Wolf A, Swift JB, Swinney HL, Vastano JA. Determining Lyapunov exponents from a time series. Physica D: Nonlinear Phenomena. 1985;16(3):285–317.

[154] Zhu WQ. Lyapunov exponent and stochastic stability of quasi-non-integrable Hamiltonian systems. International Journal of Non-Linear Mechanics. 2004;39(4):569–579.

[155] Zhu WQ. Nonlinear stochastic dynamics and control in Hamiltonian formulation. Applied Mechanics Reviews. 2006;59(4):230.

[156] Zhu WQ. Recent developments and applications of the stochastic averaging method in random vibration. Applied Mechanics Reviews. 1996;49(10S):S72–S80.

[157] Ochi MK. Extreme behaviour of a ship in rough seas - Slamming and shipping of green water. Transactions of Society of Naval Architects and Marine Engineers. 1964;2:143–202.

[158] Ochi MK. On prediction of extreme values. Journal of Ship Research. 1973;17(1):29–37.

[159] Ochi M. Wave statistics for the design of ships and ocean structures. Transactions of Society of Naval Architects and Marine Engineers. 1978;86:47–76.

[160] Ochi M. Principles of extreme value statistics and their application. In: Extreme Loads Response Symposium. Arlington, VA: Society of Naval Architects and Marine Engineers; 1981. p. 15–30.

[161] Ochi M. Ocean Waves: The Stochastic Approach. Cambridge, UK: Cambridge University Press; 2005.

[162] Naess A. Technical note: On the long-term statistics of extremes. Applied Ocean Research. 1984 oct;6(4):227–228.

[163] Naess A, Gaidai O. Estimation of extreme values from sampled time series. Structural Safety. 2009 jul;31(4):325–334.

[164] Naess A, Moan T. Probabilistic design of offshore structures. In: Chakrabarti SK, editor. Handbook of Offshore Engineering. London, UK: Elsevier; 2005. p. 197–277.

[165] Duan J. An Introduction to Stochastic Dynamics. vol. 51. 1st ed. New York: Cambridge University Press; 2015.

[166] Dynkin EB. Markov Processes. Berlin and Heidelberg: Springer Berlin Heidelberg; 1965.

[167] Karlin S, Taylor HM. A Second Course in Stochastic Processes. New York: Academic Press; 1981.

[168] Itô K. On stochastic differential equations. Memoirs of the American Mathematical Society. 1951;4:1–51.

[169] Feller W. Diffusion processes in one dimension. Transactions of the American Mathematical Society. 1954 jan;77(1):1–31.

APPENDIX A

RELATION BETWEEN TIME AND FREQUENCY DOMAIN DESCRIPTION

The radiation force vector as described in subsection 2.3.2 is shown in (A.1). For simplicity in notation the subscript in $\{F_{Rad}\}$ has been dropped.

$$\{F\} = -[A(\infty)]\{\ddot{\xi}\} - [B(\infty)]\{\dot{\xi}\} - \int_{-\infty}^{t} [K(t-\tau)]\{\dot{\xi}(\tau)\}\ d\tau \tag{A.1}$$

Expanding the matrix form and using a change of variables in the integral, (A.1) can be expressed in the summation form as shown below.

$$\begin{aligned} F_j = &- \sum_{k=1}^{6} A_{jk}(\infty)\ddot{\xi}_k - \sum_{k=1}^{6} B_{jk}(\infty)\dot{\xi}_k \\ &- \sum_{k=1}^{6} \int_{0}^{\infty} K_{jk}(\tau)\dot{\xi}_k(t-\tau)\ d\tau \quad \text{for } j = 1, 2, ..., 6 \end{aligned} \tag{A.2}$$

Taking a Fourier transform of (A.2) yields

$$\mathscr{F}[F_j] = \sum_{k=1}^{6} \omega^2 A_{jk}(\infty)\mathscr{F}[\xi_k] - \sum_{k=1}^{6} i\omega B_{jk}(\infty)\mathscr{F}[\xi_k] - \sum_{k=1}^{6} \mathscr{F}\left[\int_{0}^{\infty} K_{jk}(\tau)\dot{\xi}_k(t-\tau)\ d\tau\right] \tag{A.3}$$

where

$$\mathscr{F}[f(t)] = \int_{-\infty}^{\infty} e^{-i\omega t} f(t)\ dt \tag{A.4}$$

$$\mathscr{F}^{-1}[F(\omega)] = \frac{1}{2\pi} \int_{-\infty}^{\infty} e^{i\omega t} F(\omega)\ d\omega \tag{A.5}$$

If $f(t) = 0$ for $t < 0$

$$\mathscr{F}[f] = \mathscr{F}_c[f] - i\mathscr{F}_s[f] \tag{A.6}$$

where

$$\mathscr{F}_c[f(t)] = \int_0^\infty f(t)\cos(\omega t)\ dt \tag{A.7}$$

$$\mathscr{F}_s[f(t)] = \int_0^\infty f(t)\sin(\omega t)\ dt \tag{A.8}$$

The Fourier transform of the convolution integral can be expanded as shown below.

$$\mathscr{F}\left[\int_0^\infty K_{jk}(\tau)\dot{\xi}_k(t-\tau)d\tau\right] = \int_{-\infty}^\infty e^{-i\omega t}\int_0^\infty K_{jk}(\tau)\dot{\xi}_k(t-\tau)\ d\tau\ dt \tag{A.9}$$

$$= \int_0^\infty K_{jk}(\tau)\int_{-\infty}^\infty e^{-i\omega t}\dot{\xi}_k(t-\tau)\ dt\ d\tau \tag{A.10}$$

$$= \int_0^\infty K_{jk}(\tau)e^{-i\omega\tau}\int_{-\infty}^\infty e^{-i\omega(t-\tau)}\dot{\xi}_k(t-\tau)\ dt\ d\tau \tag{A.11}$$

$$= i\omega\mathscr{F}[\xi_k(t)]\int_0^\infty K_{jk}(\tau)e^{-i\omega\tau}\ d\tau \tag{A.12}$$

$$= i\omega\mathscr{F}[\xi_k(t)]\left(\mathscr{F}_c[K_{jk}(\tau)] - i\mathscr{F}_s[K_{jk}(\tau)]\right) \tag{A.13}$$

Substituting (A.13) into (A.3)

$$\mathscr{F}[F_j] = \sum_{k=1}^{6}\left[\omega^2 A_{jk}(\infty) - \omega\mathscr{F}_s[K_{jk}(\tau)] - i\omega\{B_{jk}(\infty) + \mathscr{F}_c[K_{jk}(\tau)]\}\right]\mathscr{F}[\xi_k] \tag{A.14}$$

However, it is known from frequency domain formulation that

$$\mathscr{F}[F_j] = \sum_{k=1}^{6} \left[\omega^2 A_{jk}(\omega) - i\omega B_{jk}(\omega)\right] \mathscr{F}[\xi_k] \tag{A.15}$$

Comparing the real and imaginary parts of (A.14) and (A.15) yields the following equations relating the frequency domain quantities to the time domain impulse response functions.

$$A_{jk}(\omega) = A_{jk}(\infty) - \frac{1}{\omega}\int_0^\infty K_{jk}(\tau)\sin(\omega\tau)\ d\tau \tag{A.16}$$

$$B_{jk}(\omega) = B_{jk}(\infty) + \int_0^\infty K_{jk}(\tau)\cos(\omega\tau)\ d\tau \tag{A.17}$$

Taking a inverse transform yields

$$K_{jk}(\tau) = \frac{2}{\pi}\int_0^\infty \omega\left[A_{jk}(\infty) - A_{jk}(\omega)\right]\sin(\omega\tau)\ d\omega \tag{A.18}$$

$$K_{jk}(\tau) = \frac{2}{\pi}\int_0^\infty \left[B_{jk}(\omega) - B_{jk}(\infty)\right]\cos(\omega\tau)\ d\omega \tag{A.19}$$

APPENDIX B

RECASTING EQUATIONS OF MOTION FOR NUMERICAL INTEGRATION *

The complete nonlinear equations of motion are given by (B.1) and (B.2).

$$m[\ddot{\boldsymbol{\xi}} + \dot{\boldsymbol{\omega}} \times (\boldsymbol{x_G} - \boldsymbol{\xi}) + \boldsymbol{\omega} \times [\boldsymbol{\omega} \times (\boldsymbol{x_G} - \boldsymbol{\xi})]] = \boldsymbol{F} \tag{B.1}$$

$$I\dot{\boldsymbol{\omega}}' + \boldsymbol{\omega}' \times I\boldsymbol{\omega}' = R\,[\boldsymbol{M} - \boldsymbol{x_G} \times \boldsymbol{F}] \tag{B.2}$$

Let $\boldsymbol{\alpha} = \{\xi_4\ \xi_5\ \xi_6\}^T$. Then $\boldsymbol{\omega}'$ and $\boldsymbol{\omega}$ from (2.12) and (2.14) can expressed as shown in (B.4) and (B.6) respectively.

$$\boldsymbol{\omega}' = \begin{Bmatrix} c_5c_6\dot{\xi_4} + s_6\dot{\xi_5} \\ -c_5s_6\dot{\xi_4} + c_6\dot{\xi_5} \\ s_5\dot{\xi_4} + \dot{\xi_6} \end{Bmatrix} = \begin{bmatrix} c_5c_6 & s_6 & 0 \\ -c_5s_6 & c_6 & 0 \\ s_5 & 0 & 1 \end{bmatrix} \begin{Bmatrix} \dot{\xi_4} \\ \dot{\xi_5} \\ \dot{\xi_6} \end{Bmatrix} \tag{B.3}$$

$$= P\dot{\boldsymbol{\alpha}} \tag{B.4}$$

$$\boldsymbol{\omega} = \begin{Bmatrix} \dot{\xi_4} + \dot{\xi_6}s_5 \\ \dot{\xi_5}c_4 + \dot{\xi_6}s_4c_5 \\ \dot{\xi_5}s_4 + \dot{\xi_6}c_4c_5 \end{Bmatrix} = \begin{bmatrix} 1 & 0 & s_5 \\ 0 & c_4 & s_4c_5 \\ 0 & s_4 & c_4c_5 \end{bmatrix} \begin{Bmatrix} \dot{\xi_4} \\ \dot{\xi_5} \\ \dot{\xi_6} \end{Bmatrix} \tag{B.5}$$

$$= Q\dot{\boldsymbol{\alpha}} \tag{B.6}$$

Let $\boldsymbol{a} = a_1\hat{i} + a_2\hat{j} + a_3\hat{k}$ and $\boldsymbol{b} = b_1\hat{i} + b_2\hat{j} + b_3\hat{k}$ be two vectors. The cross product

*This appendix is reprinted with permission from "Large-amplitude time-domain simulation tool for marine and offshore motion prediction", 2015. Marine Systems and Ocean Technology, 10(1), pp 1-17, Copyright 2015 by Sociedade Brasileira de Engenharia Naval

of the two vectors can be expressed as a multiplication of a matrix and a vector as shown in (B.7) and (B.8).

$$\begin{aligned}
\boldsymbol{a} \times \boldsymbol{b} &= (a_2b_3 - b_2a_3)\hat{i} + (a_3b_1 - b_3a_1)\hat{j} + (a_1b_2 - b_1a_2)\hat{k} \\
&= \begin{Bmatrix} (a_2b_3 - b_2a_3) \\ (a_3b_1 - b_3a_1) \\ (a_1b_2 - b_1a_2) \end{Bmatrix} \\
&= \begin{bmatrix} 0 & -a_3 & a_2 \\ a_3 & 0 & -a_1 \\ -a_2 & a_1 & 0 \end{bmatrix} \begin{Bmatrix} b_1 \\ b_2 \\ b_3 \end{Bmatrix} \\
&= C_1(\boldsymbol{a})\boldsymbol{b}
\end{aligned} \tag{B.7}$$

$$\begin{aligned}
\boldsymbol{a} \times \boldsymbol{b} &= (a_2b_3 - b_2a_3)\hat{i} + (a_3b_1 - b_3a_1)\hat{j} + (a_1b_2 - b_1a_2)\hat{k} \\
&= \begin{Bmatrix} (a_2b_3 - b_2a_3) \\ (a_3b_1 - b_3a_1) \\ (a_1b_2 - b_1a_2) \end{Bmatrix} \\
&= \begin{bmatrix} 0 & b_3 & -b_2 \\ -b_3 & 0 & b_1 \\ b_2 & -b_1 & 0 \end{bmatrix} \begin{Bmatrix} a_1 \\ a_2 \\ a_3 \end{Bmatrix} \\
&= C_2(\boldsymbol{b})\boldsymbol{a}
\end{aligned} \tag{B.8}$$

C_1 and C_2 for any general vector $\boldsymbol{a} = a_1\hat{i} + a_2\hat{j} + a_3\hat{k}$ are given by

$$C_1(\boldsymbol{a}) = \begin{bmatrix} 0 & -a_3 & a_2 \\ a_3 & 0 & -a_1 \\ -a_2 & a_1 & 0 \end{bmatrix} \tag{B.9}$$

$$C_2(\boldsymbol{a}) = -C_1(\boldsymbol{a}) = \begin{bmatrix} 0 & a_3 & -a_2 \\ -a_3 & 0 & a_1 \\ a_2 & -a_1 & 0 \end{bmatrix} \tag{B.10}$$

Substituting expression for F from (B.1) into (B.2) gives

$$\begin{aligned} I\dot{\boldsymbol{\omega}}' + \boldsymbol{\omega}' \times I\boldsymbol{\omega}' =& R[\boldsymbol{M} - \boldsymbol{x_G} \times m[\ddot{\boldsymbol{\xi}} + \dot{\boldsymbol{\omega}} \times (\boldsymbol{x_G} - \boldsymbol{\xi}) \\ & + \boldsymbol{\omega} \times [\boldsymbol{\omega} \times (\boldsymbol{x_G} - \boldsymbol{\xi})]]] \end{aligned} \tag{B.11}$$

$$\begin{aligned} & I\dot{\boldsymbol{\omega}}' + R[\boldsymbol{x_G} \times m[\ddot{\boldsymbol{\xi}} + \dot{\boldsymbol{\omega}} \times (\boldsymbol{x_G} - \boldsymbol{\xi})]] \\ & \quad = R[\boldsymbol{M} - \boldsymbol{x_G} \times m[\boldsymbol{\omega} \times [\boldsymbol{\omega} \times (\boldsymbol{x_G} - \boldsymbol{\xi})]]] - \boldsymbol{\omega}' \times I\boldsymbol{\omega}' \end{aligned} \tag{B.12}$$

$$\begin{aligned} & IP\ddot{\boldsymbol{\alpha}} + mRC_1(\boldsymbol{x_G})\ddot{\boldsymbol{\xi}} + mRC_1(\boldsymbol{x_G})C_2(\boldsymbol{x_G} - \boldsymbol{\xi})\dot{\boldsymbol{\omega}} \\ & \quad = R[\boldsymbol{M} - \boldsymbol{x_G} \times m[\boldsymbol{\omega} \times [\boldsymbol{\omega} \times (\boldsymbol{x_G} - \boldsymbol{\xi})]]] \\ & \quad - \boldsymbol{\omega}' \times I\boldsymbol{\omega}' - I\dot{P}\dot{\boldsymbol{\alpha}} \end{aligned} \tag{B.13}$$

$$
\begin{aligned}
&mRC_1(\boldsymbol{x_G})\ddot{\boldsymbol{\xi}} + IP\ddot{\boldsymbol{\alpha}} + mRC_1(\boldsymbol{x_G})C_2(\boldsymbol{x_G}-\boldsymbol{\xi})Q\ddot{\boldsymbol{\alpha}} \\
&\quad = R[\boldsymbol{M} - mC_1(\boldsymbol{x_G})[Q\dot{\boldsymbol{\alpha}} \times [Q\dot{\boldsymbol{\alpha}} \times (\boldsymbol{x_G}-\boldsymbol{\xi})]]] \\
&\quad - P\dot{\boldsymbol{\alpha}} \times IP\dot{\boldsymbol{\alpha}} - [I\dot{P} + mRC_1(\boldsymbol{x_G})C_2(\boldsymbol{x_G}-\boldsymbol{\xi})\dot{Q}]\dot{\boldsymbol{\alpha}}
\end{aligned} \tag{B.14}
$$

Similarly, the translational equation (B.1) can be rearranged to obtain

$$
\begin{aligned}
&m\ddot{\boldsymbol{\xi}} + mC_2(\boldsymbol{x_G}-\boldsymbol{\xi})Q\ddot{\boldsymbol{\alpha}} \\
&\quad = \boldsymbol{F} - m[\boldsymbol{\omega} \times [\boldsymbol{\omega} \times (\boldsymbol{x_G}-\boldsymbol{\xi})]] - mC_2(\boldsymbol{x_G}-\boldsymbol{\xi})\dot{Q}\dot{\boldsymbol{\alpha}}
\end{aligned} \tag{B.15}
$$

Combining (B.15) and (B.14)

$$
\begin{aligned}
&\begin{bmatrix} mI_d^{3\times3} & mC_2(\boldsymbol{x_G}-\boldsymbol{\xi})Q \\ RC_1(\boldsymbol{x_G}) & IP + mRC_1(\boldsymbol{x_G})C_2(\boldsymbol{x_G}-\boldsymbol{\xi})Q \end{bmatrix} \begin{Bmatrix} \ddot{\boldsymbol{\xi}} \\ \ddot{\boldsymbol{\alpha}} \end{Bmatrix} \\
&= \begin{Bmatrix} \boldsymbol{F} - m[\boldsymbol{\omega} \times [\boldsymbol{\omega} \times (\boldsymbol{x_G}-\boldsymbol{\xi})]] - mC_2(\boldsymbol{x_G}-\boldsymbol{\xi})\dot{Q}\dot{\boldsymbol{\alpha}} \\ \begin{pmatrix} R[\boldsymbol{M} - mC_1(\boldsymbol{x_G})[Q\dot{\boldsymbol{\alpha}} \times [Q\dot{\boldsymbol{\alpha}} \times (\boldsymbol{x_G}-\boldsymbol{\xi})]]] \\ -P\dot{\boldsymbol{\alpha}} \times IP\dot{\boldsymbol{\alpha}} - [I\dot{P} + mRC_1(\boldsymbol{x_G})C_2(\boldsymbol{x_G}-\boldsymbol{\xi})\dot{Q}]\dot{\boldsymbol{\alpha}} \end{pmatrix} \end{Bmatrix}
\end{aligned} \tag{B.16}
$$

where $I_d^{3\times3}$ is 3×3 identity matrix. Now the force and moment vector still contain the infinite added mass terms which are proportional to the acceleration.

$$
\begin{Bmatrix} \boldsymbol{F} \\ \boldsymbol{M} \end{Bmatrix} = \begin{Bmatrix} \boldsymbol{F_1} \\ \boldsymbol{M_1} \end{Bmatrix} - \begin{bmatrix} A_{11}^{3\times3} & A_{12}^{3\times3} \\ A_{21}^{3\times3} & A_{22}^{3\times3} \end{bmatrix}_{6\times6} \begin{Bmatrix} \ddot{\boldsymbol{\xi}} \\ \ddot{\boldsymbol{\alpha}} \end{Bmatrix} \tag{B.17}
$$

$$\begin{bmatrix} mI_d^{3\times3} + A_{11}^{3\times3} & mC_2(\boldsymbol{x_G} - \boldsymbol{\xi})Q + A_{12}^{3\times3} \\ RC_1(\boldsymbol{x_G}) + A_{21}^{3\times3} & IP + mRC_1(\boldsymbol{x_G})C_2(\boldsymbol{x_G} - \boldsymbol{\xi})Q + A_{22}^{3\times3} \end{bmatrix} \begin{Bmatrix} \ddot{\boldsymbol{\xi}} \\ \ddot{\boldsymbol{\alpha}} \end{Bmatrix}$$
$$= \begin{Bmatrix} \boldsymbol{F_1} - m[\boldsymbol{\omega} \times [\boldsymbol{\omega} \times (\boldsymbol{x_G} - \boldsymbol{\xi})]] - mC_2(\boldsymbol{x_G} - \boldsymbol{\xi})\dot{Q}\dot{\boldsymbol{\alpha}} \\ \begin{pmatrix} R[\boldsymbol{M_1} - mC_1(\boldsymbol{x_G})[Q\dot{\boldsymbol{\alpha}} \times [Q\dot{\boldsymbol{\alpha}} \times (\boldsymbol{x_G} - \boldsymbol{\xi})]]] \\ -P\dot{\boldsymbol{\alpha}} \times IP\dot{\boldsymbol{\alpha}} - [I\dot{P} + mRC_1(\boldsymbol{x_G})C_2(\boldsymbol{x_G} - \boldsymbol{\xi})\dot{Q}]\dot{\boldsymbol{\alpha}} \end{pmatrix} \end{Bmatrix} \tag{B.18}$$

which in simplified notation might be written as

$$[\boldsymbol{M_a}]\{\dot{\boldsymbol{v}}\} = \{\boldsymbol{f}\} \tag{B.19}$$

where $\boldsymbol{v} = \begin{Bmatrix} \dot{\boldsymbol{\xi}} \\ \dot{\boldsymbol{\alpha}} \end{Bmatrix} = \{\dot{\xi}_1\ \dot{\xi}_2\ \dot{\xi}_3\ \dot{\xi}_4\ \dot{\xi}_5\ \dot{\xi}_6\}^T$

APPENDIX C

CALCULATION OF $\overline{GZ}^{2D}$ FOR EXACT $\overline{GZ}$ CALCULATION IN IRREGULAR WAVE

The calculation of the 2-D GZ for each section in irregular waves is described in this appendix. As seen from chapter 3, $\overline{GZ}^{2D}$ varies over the length of the ship due to the variation in geometry and the wave elevation with length.

The first step in evaluating the $\overline{GZ}^{2D}(x)$ is to evaluate the instantaneous underwater hull form at every section and estimate the location of center of gravity and center of buoyancy in the heeled position.

For illustration purposes a specific example is considered here. The wave elevation is obtained from a Bretschneider spectrum with significant wave height $H_S = 5m$ and modal period $T_z = 13s$ and is shown in Figure C.1a. The corresponding heave and pitch motions from linear theory are shown in Figure C.1b and Figure C.1d respectively. The roll motion is simulated using an exact $\overline{GZ}$ formulation and is shown in Figure C.1c. The hull form is divided into 200 sections placed evenly along the length of the model. The relative wave elevation across the ship at each section at time $t = 4417s$ is shown in Figure C.1e.

The sections are numbered from 1 to 200 with section 1 and 200 being the aft most and forward most sections respectively. The instantaneous position of three sections - 20, 100 and 180 corresponding to aft, midship and forward regions of the ship are shown with respect to the position of the relative water line are shown in Figure C.2.

The green line represents the relative water at that particular section. The initial position of the section is shown as a blue curve. The rotated position of the section

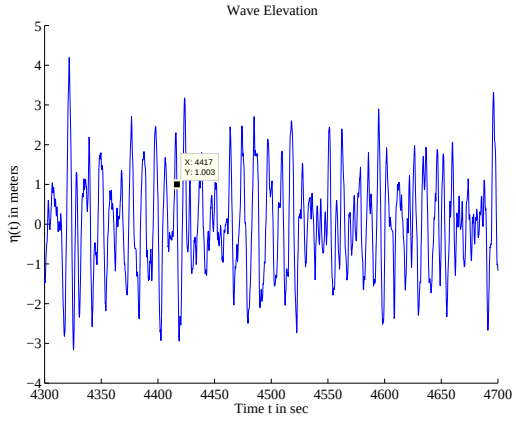

(a) Bretschneider Wave Elevation $H_s = 5m$ and $T_z = 13s$

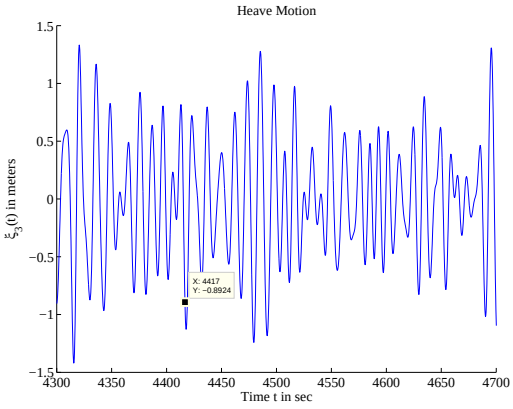

(b) Heave Motion - Linear Theory

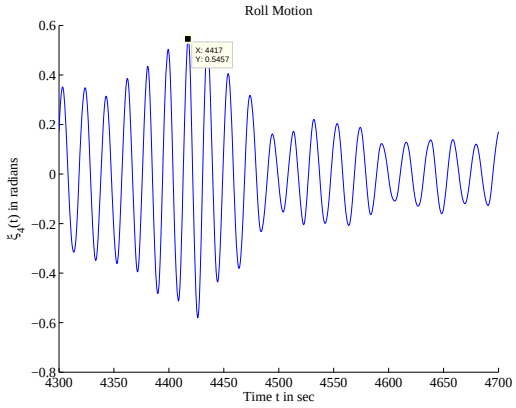

(c) Roll Motion - Simulated using Exact $\overline{GZ}$

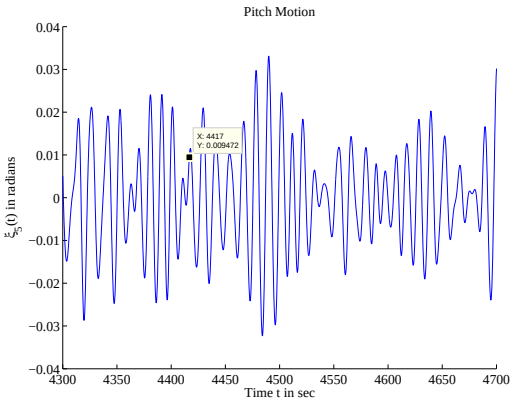

(d) Pitch Motion - Linear Theory

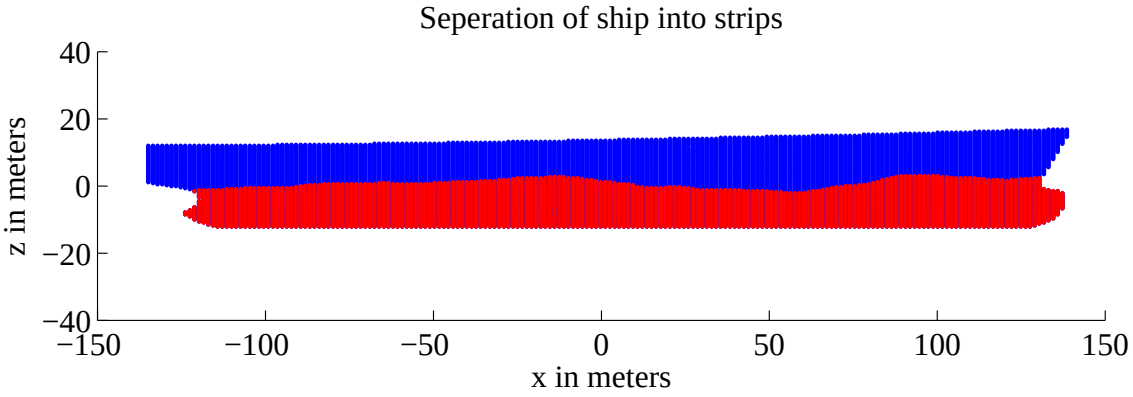

(e) Relative wave elevation at $t = 4417s$

Figure C.1: Wave elevation and motions in a 3-hour irregular sea

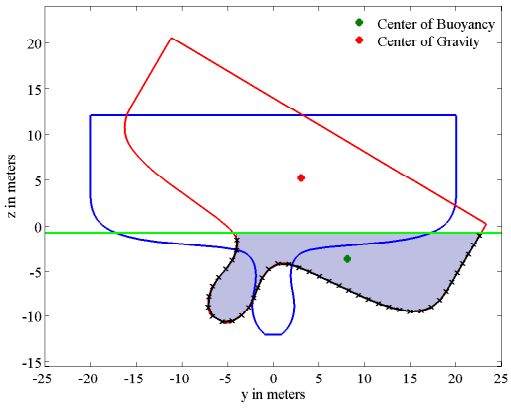

(a) Section 20: $x = -108.79m$ from midship

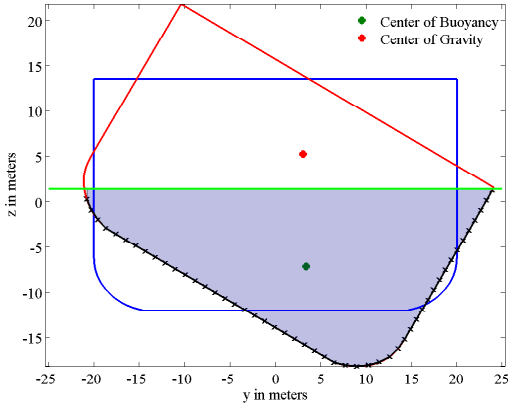

(b) Section 100: $x = 1.173m$ from midship

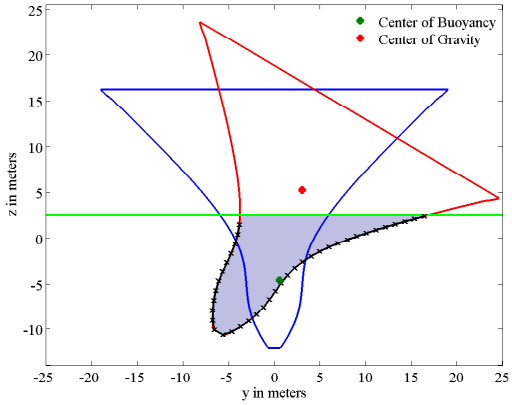

(c) Section 180: $x = 111.135m$ from midship

Figure C.2: Instantaneous position of hull form with respect to relative water line at $t = 4417s$

is obtained by a rotational transformation and is represented by the red curve. The intersection of the relative waterline (green line) with the rotated section (red curve) defines the instantaneous waterline on the hull.

The sectional area A is obtained by numerical integration of the section under the relative water line which is represented by the shaded area in Figure C.2. The new position of center of buoyancy for the section under consideration is the centroid of shaded area and is represented by the green dot in Figure C.2. Let the new position of center of buoyancy of the section in the rolled orientation be given by (y_B^r, z_B^r). Note that both sectional area and center of buoyancy are given by functions of the longitudinal position of section x.

$$A = A(x) \tag{C.1}$$

$$(y_B^r, z_B^r) = (y_B^r(x), z_B^r(x)) \tag{C.2}$$

Similarly the new position of center of gravity due to roll motion is calculated at each section and is represented by a red dot in Figure C.2. Let the old position of center of gravity in upright condition be given by (y_G, z_G) and its new position in the rolled orientation be given by (y_G^r, z_G^r). The two coordinates are related by the relation

$$y_G^r = y_G \cos\phi - z_G \sin\phi \tag{C.3}$$

$$z_G^r = y_G \sin\phi + z_G \cos\phi \tag{C.4}$$

where ϕ is the instantaneous roll angle. Note that while center of buoyancy (y_B^r, z_B^r) varies with length, the center of gravity (y_G^r, z_G^r) is invariant along the length of the ship. The sectional $\overline{GZ}^{2D}(x)$ now follows from a similar approach as shown in

(3.3), but applied to 2D case and is given by

$$\overline{GZ}^{2D}(x) = \frac{y_B^r(x)A(x) - y_G^r A_0(x)}{A_0(x)} = y_B^r(x)\frac{A(x)}{A_0(x)} - y_G^r \tag{C.5}$$

where $A_0(x)$ is the sectional area under the calm waterline in the upright ($\phi = 0$) condition.

APPENDIX D

SUBHARMONIC PARAMETRIC RESPONSE

This appendix discusses the $2:1$ subharmonic nature of the response of systems excited parametrically. For the ease of explanation the simple example of Mathieu equation is chosen. The Mathieu equation is given by (D.1).

$$\ddot{x} + \mu_1 \dot{x} + (\alpha + \gamma \cos(t))x = 0 \tag{D.1}$$

It can be thought of as a simplified version of the model described in chapter 3 where the roll restoring arm is approximated by a linear stiffness with a sinusoidally varying metacentric height, the frequency dependent added mass and radiation damping are assumed to be equal to their value at the roll natural frequency and the system is assumed to have only linear roll damping. This equation can be expressed in the state space form as shown in (D.2).

$$\begin{Bmatrix} \dot{x} \\ \dot{y} \end{Bmatrix} = \begin{bmatrix} 0 & 1 \\ -(\alpha + \gamma \cos(t)) & -\mu_1 \end{bmatrix} \begin{Bmatrix} x \\ y \end{Bmatrix} \tag{D.2}$$

In a general form this can be represented as (D.3)

$$\dot{\boldsymbol{x}} = P(t)\boldsymbol{x} \tag{D.3}$$

where $\boldsymbol{x}$ represents a $n \times 1$ vector and $P(t)$ represents a $n \times n$ time varying matrix with a minimal period of T ($P(t+T) = P(t)$ for the smallest possible T). Let $\Phi(t)$ be a fundamental matrix for the system shown in (D.3) which satisfies $\dot{\Phi}(t) = P(t)\Phi(t)$.

Due to the periodicity of $P(t)$, $\Phi(t+T)$ also satisfies the same equation and hence must be a fundamental matrix too. This implies that the columns of $\Phi(t+T)$ are some linear combinations of the columns of $\Phi(t)$. Mathematically, $\Phi(t)$ and $\Phi(t+T)$ are related by a constant matrix Q as shown in (D.4).

$$\Phi(t+T) = \Phi(t)Q \tag{D.4}$$

$$Q = \Phi(t)^{-1}\Phi(t+T) \tag{D.5}$$

Let λ be an eigenvalue of the constant matrix Q and $\boldsymbol{v}$ be the corresponding eigenvector. Consider a solution $\boldsymbol{\chi}(t) = \Phi(t)\boldsymbol{v}$, then $\boldsymbol{\chi}(t+T)$ is given by

$$\boldsymbol{\chi}(t+T) = \Phi(t+T)\boldsymbol{v} = \Phi(t)Q\boldsymbol{v} = \Phi(t)\lambda\boldsymbol{v} = \lambda\boldsymbol{\chi}(t) \tag{D.6}$$

This result that the system described by (D.7) where $P(t)$ is periodic with minimal period T has at least one non-trivial solution $\boldsymbol{\chi}(t)$ such that (D.6) holds is known as Floquet's theory [92].

$$\boldsymbol{\chi}(t+T) = \lambda\boldsymbol{\chi}(t) \tag{D.7}$$

Periodic solutions exist when the eigenvalue of the *monodromy matrix* Q is a m^{th} root of unity for any integer m as shown in (D.8).

$$\boldsymbol{\chi}(t+mT) = \lambda\boldsymbol{\chi}(t+(m-1)T) = ... = \lambda^m\boldsymbol{\chi}(t) = \boldsymbol{\chi}(t) \tag{D.8}$$

It is also clear from (D.7) that when $|\lambda| > 1$ the solutions are unstable and vice versa. Thus in order to determine the stability of a system it is important to determine when the absolute value of the eigenvalues of the monodromy matrix

exceed unity.

The product of all the eigenvalues of a system is given by (D.9) where $tr\{P(s)\}$ represents the trace of $P(s)$ [92].

$$\lambda_1\lambda_2...\lambda_n = exp\left(\int_0^T tr\{P(s)\}ds\right) \tag{D.9}$$

For the Mathieu equation shown in (D.2), the product of the two eigenvalues λ_1 and λ_2 is given by

$$\lambda_1\lambda_2 = e^{-\int_0^{2\pi}\mu_1 ds} = e^{-2\pi\mu_1} \tag{D.10}$$

When the system is damped ($\mu_1 > 0$), the product of the eigenvalues will always be less than unity ($\lambda_1\lambda_2 < 1$). If the two eigenvalues are complex conjugates ($\lambda_{1,2} = a \pm ib$), then the absolute value of each eigenvalue is less than unity. Thus the solution is asymptotically stable and converges to the trivial solution.

$$|\lambda_{1,2}| = \sqrt{a^2+b^2} = \sqrt{\lambda_1\lambda_2} = \sqrt{e^{-2\pi\mu_1}} < 1 \tag{D.11}$$

However, if the eigenvalues are real it means that at least one eigenvalue must have an absolute value greater than unity leading to unstable solutions. Particularly, there are two possibilities - $\lambda \geq 1$ and $\lambda \leq -1$ which both result in unstable solutions. $\lambda = 1$ corresponds to solution with minimal period 2π. However, $\lambda = -1$ corresponds to a solution with minimal period of 4π as shown below.

$$\boldsymbol{x}(t+4\pi) = -\boldsymbol{x}(t+2\pi) = \boldsymbol{x}(t) \tag{D.12}$$

Let $x_{2\pi}(t)$ and $x_{4\pi}(t)$ represent the 2π and 4π periodic solutions of the Mathieu

equation given in (D.2). These solutions can be expressed as Fourier series as shown below.

$$x_{2\pi}(t) = a_0 + \sum_{n=1}^{\infty} a_n \cos(nt) + b_n \sin(nt) \tag{D.13}$$

$$x_{4\pi}(t) = c_0 + \sum_{n=1,3,5,\ldots}^{\infty} c_n \cos\left(\frac{nt}{2}\right) + d_n \sin\left(\frac{nt}{2}\right) \tag{D.14}$$

Substituting the 2π periodic solution $x_{2\pi}(t)$ into the (D.1) and equating the coefficients of $\cos(nt)$ and $\sin(nt)$ to zero gives an infinite set of equations represented by

$$\begin{bmatrix} \alpha & \frac{\gamma}{2} & 0 & 0 & 0 & 0 & \cdots \\ \gamma & \alpha-1 & \mu_1 & \frac{\gamma}{2} & 0 & 0 & \cdots \\ 0 & \mu_1 & \alpha-1 & 0 & \frac{\gamma}{2} & 0 & \cdots \\ 0 & \frac{\gamma}{2} & 0 & \alpha-4 & 2\mu_1 & \frac{\gamma}{2} & \cdots \\ 0 & 0 & \frac{\gamma}{2} & 2\mu_1 & \alpha-4 & 0 & \cdots \\ \vdots & \vdots & \vdots & \vdots & \vdots & \vdots & \ddots \end{bmatrix} \begin{Bmatrix} a_0 \\ a_1 \\ b_1 \\ a_2 \\ b_2 \\ \vdots \end{Bmatrix} = \begin{Bmatrix} 0 \\ 0 \\ 0 \\ 0 \\ 0 \\ \vdots \end{Bmatrix} \tag{D.15}$$

Similarly substituting the 4π periodic solution $x_{4\pi}(t)$ into (D.1) and equating the coefficients of $\cos\left(\frac{nt}{2}\right)$ and $\sin\left(\frac{nt}{2}\right)$ to zero gives another infinite set of equations represented by

$$\begin{bmatrix} \alpha-\frac{1}{4}+\frac{\gamma}{2} & \frac{\mu_1}{2} & \frac{\gamma}{2} & 0 & 0 & \cdots \\ -\frac{\mu_1}{2} & \alpha-\frac{1}{4}-\frac{\gamma}{2} & \mu_1 & \frac{\gamma}{2} & 0 & \cdots \\ \frac{\gamma}{2} & 0 & \alpha-\frac{9}{4} & \frac{3\mu_1}{2} & \frac{\gamma}{2} & \cdots \\ 0 & \frac{\gamma}{2} & -\frac{3\mu_1}{2} & \alpha-\frac{9}{4} & 0 & \cdots \\ \vdots & \vdots & \vdots & \vdots & \vdots & \ddots \end{bmatrix} \begin{Bmatrix} c_1 \\ d_1 \\ c_2 \\ d_2 \\ \vdots \end{Bmatrix} = \begin{Bmatrix} 0 \\ 0 \\ 0 \\ 0 \\ \vdots \end{Bmatrix} \tag{D.16}$$

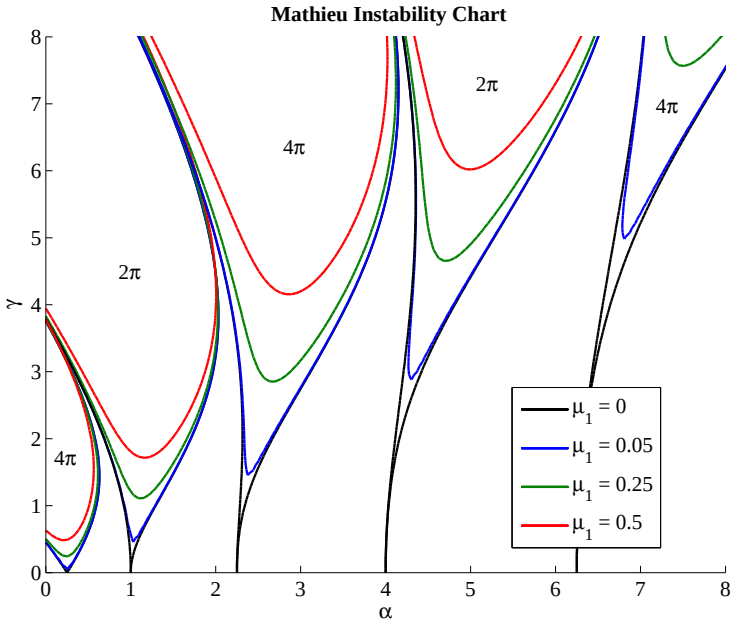

Figure D.1: Mathieu instability chart

Both (D.15) and (D.16) are infinite set of linear homogeneous equations and for a unique solution to exist, the determinant of the matrices must be zero. Although theoretically infinite determinants need to be computed, practically computing the determinant of the truncated infinite matrix provides implicit relations between α and γ. A plot of the boundaries on the $\alpha - \gamma$ plane is shown in Figure D.1.

Figure D.2 shows six points on the Mathieu instability chart which are chosen to be numerically simulated. Points A, B and C are in the unstable region of the instability chart while points D, E and F are in the stable region. The simulated time histories are shown in Figure D.3 and Figure D.4. It can be seen from Figure D.3 that the solution increases exponentially to reach extremely large values. However, the same cases when simulated with additional quadratic damping results in limiting the amplitude of response as shown in Figure D.5.

Simulated time history with quadratic damping also clearly shows period of re-

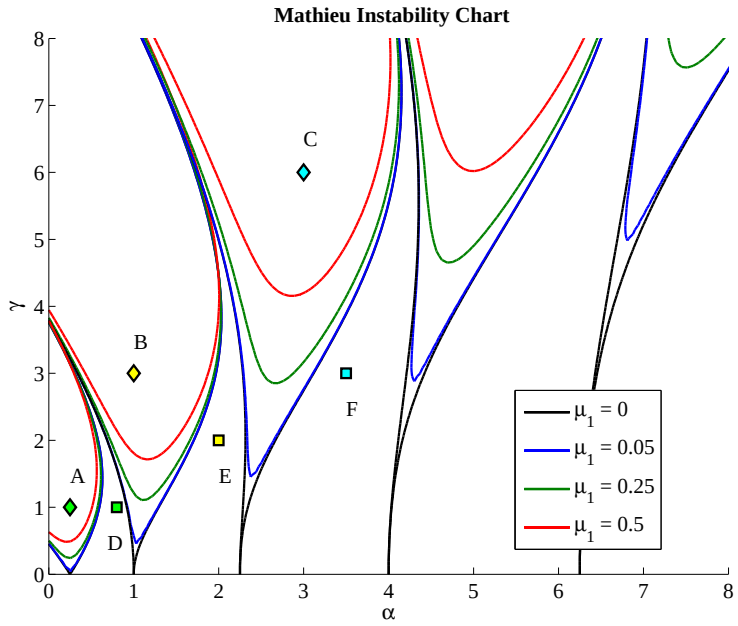

Figure D.2: Behavior of different positions on Mathieu instability chart

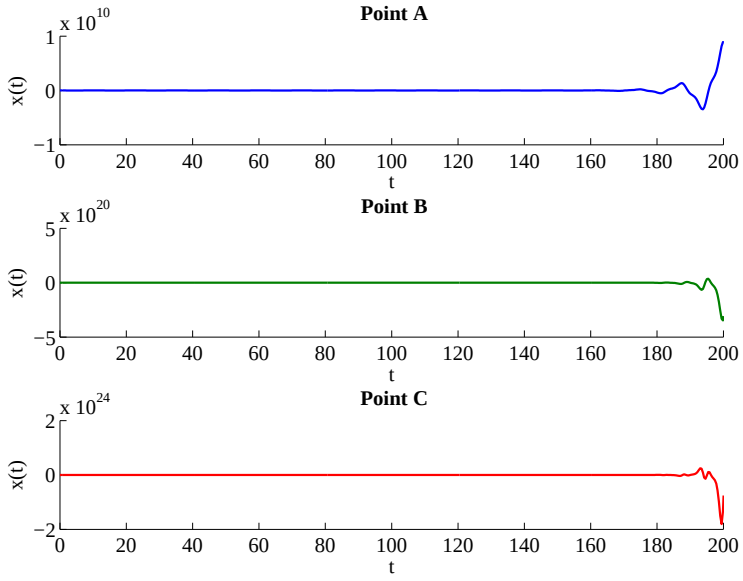

Figure D.3: Unstable solutions at points A, B and C simulated with no quadratic damping

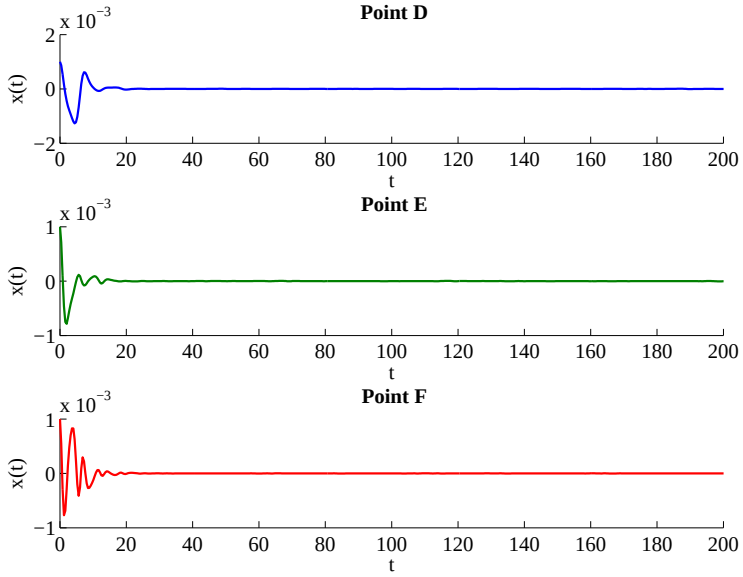

Figure D.4: Stable solutions at points D, E and F simulated with no quadratic damping

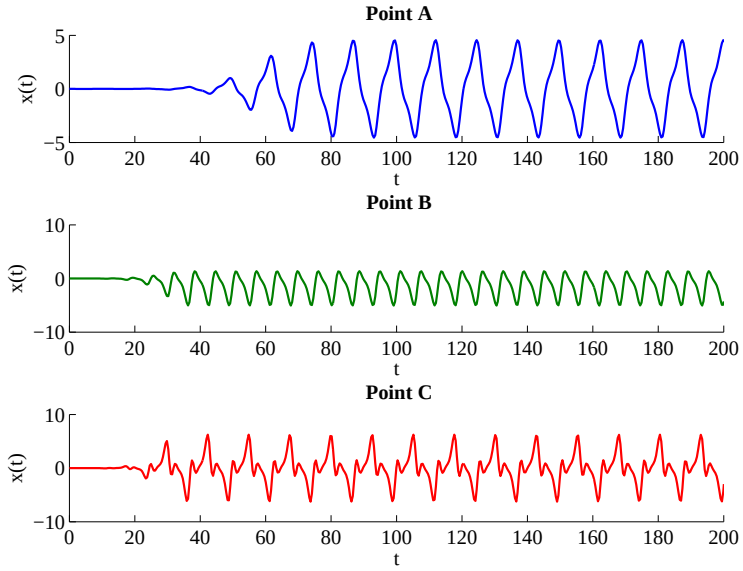

Figure D.5: Unstable solutions at points A, B and C simulated with quadratic damping

sponse. Points A and C which correspond to the 4π periodic solution tongues in Figure D.2 clearly show a similar period in the simulated time history too. Point B on the other hand lies in the tongue due to the 2π periodic solution and hence displays a period of 2π.

It is important to note that the first tongue on the Mathieu instability chart corresponds to the 4π solution. This means that the response in this region will have twice the period of the excitation. The Mathieu equation described in (D.1) shows that the excitation is 2π periodic and hence the response corresponding to point A in Figure D.5 shows a 4π periodic subharmonic response.

The parametric roll of a ship falls under this fundamental resonance region and hence displays a $2:1$ subharmonic response. On the other hand, parametric excitation of classic spar platforms usually falls in the higher harmonic tongues of the Mathieu instability chart. It can be seen from Figure D.1 that with the addition of linear damping, the higher tongues are pushed higher up, meaning that a significant excitation is needed to excite the system into instability corresponding to non-fundamental tongues. Therefore the problem for parametric excitation for spars is not as much of concern when compared to the problem of parametric roll for ships.

APPENDIX E

INTRODUCTION TO STOCHASTIC DYNAMICS

This appendix provides an introduction to the concepts of stochastic dynamics which are used in chapter 5 in the application of stochastic averaging technique. Since chapter 5 only uses the concepts of stochastic dynamics for one dimensional processes, the description in this appendix is restricted to scalar stochastic processes. For a more general description of vector stochastic processes please refer to standard textbooks such as Lutes and Sarkani [84] or Lin and Cai [18]. A more mathematically rigorous introduction to the subject can be found in the textbook by Duan [165].

In case of a linear system excited by Gaussian excitation, the response is also a Gaussian process and its probabilistic characteristics can be quantified exactly. However, such exact solutions do not exist for a general nonlinear system. In some special cases where the response can be characterized as a Markov process, it is possible to obtain exact solutions.

E.1 Markov Process and Chapman-Kolmogorov Equation

A stochastic process $X(t)$ is said to be a scalar *Markov process* if it satisfies the property shown in (E.1)

$$\begin{aligned} &P[X(t_n) \leq x_n | X(t_{n-1}) = x_{n-1}, X(t_{n-2}) = x_{n-2}, ..., X(t_0) = x_0] \\ &\qquad = P\left[X(t_n) \leq x_n | X(t_{n-1}) = x_{n-1}\right] \text{ for all } t_n > t_{n-1} > ... > t_0 \end{aligned} \quad \text{(E.1)}$$

where $P[B|A]$ represents the conditional probability of event B given that event A has occurred. It can further be shown [18] that a sufficient condition for a process

$X(t)$ to be Markov is that the increments of the process in non-overlapping time increments are independent i.e. $[X(t_4) - X(t_3)]$ and $[X(t_2) - X(t_1)]$ are independent for all possible values of $t_4 > t_3 \geq t_2 > t_1$.

The probability $P\left[X(t) \leq x | X(t_0) = x_0\right]$ is known as the *transition probability distribution function*. If the transition probability distribution function is differentiable, the corresponding *transition probability density function* is defined by (E.2).

$$p(x, t|x_0, t_0) \equiv p_{X(t)}(x|X(t_0) = x_0) = \frac{\partial}{\partial x} P\left[X(t) \leq x | X(t_0) = x_0\right] \tag{E.2}$$

A Markov process is completely characterized by its transition probability density function $p(x, t|x_0, t_0)$ and the probability density of the initial condition $p_{X(t_0)}(x)$. In case of a deterministic initial condition $X(t_0) = x_0$, the probability density function of the initial condition is given by a Dirac delta function as shown below.

$$p_{X(t_0)}(x) = \delta(x - x_0) \tag{E.3}$$

Using the Markov property shown in (E.1), the joint probability density function of $[X(t_n), X(t_{n-1}), ..., X(t_0)]$ expressed as $p(x_n, t_n; x_{n-1}, t_{n-1}; ...; x_0, t_0)$ is given by

$$\begin{aligned}
&p(x_n, t_n; x_{n-1}, t_{n-1}; ...; x_0, t_0) \\
&\qquad = p(x_n, t_n | x_{n-1}, t_{n-1}; ...; x_0, t_0) \times p(x_{n-1}, t_{n-1}; ...; x_0, t_0) \\
&\qquad = p(x_n, t_n | x_{n-1}, t_{n-1}) \times p(x_{n-1}, t_{n-1}; ...; x_0, t_0) \\
&\qquad = p(x_n, t_n | x_{n-1}, t_{n-1}) \times p(x_{n-1}, t_{n-1} | x_{n-2}, t_{n-2}) \times \\
&\qquad\qquad ... \times p(x_1, t_1 | x_0, t_0) \times p_{X(t_0)}(x_0)
\end{aligned} \tag{E.4}$$

This implies that for $t_0 < t < t_1$,

$$\begin{aligned} p(x_1, t_1; y, t|x_0, t_0) &= p(x_1, t_1|y, t; x_0, t_0) \times p(y, t|x_0, t_0) \\ &= p(x_1, t_1|y, t) \times p(y, t|x_0, t_0) \end{aligned} \tag{E.5}$$

Integrating (E.5) with respect to y leads to an expression for the transition probability density function $p(x_1, t_1|x_0, t_0)$ given by (E.6) and is known as the *Chapman-Kolmogorov equation*.

$$p(x_1, t_1|x_0, t_0) = \int_{-\infty}^{\infty} p(x_1, t_1|y, t) \times p(y, t|x_0, t_0) dy \tag{E.6}$$

E.2 Fokker Planck Kolmogorov (FPK) Equation

In this section the governing differential equation for the transition probability density function of a Markov process $X(t)$ is derived using a general approach adopted in Lutes and Sarkani [84]. The time derivative of the transition probability density function is given by

$$\begin{aligned} &\frac{\partial}{\partial t} p_{X(t)}(x|X(0) = x_0) \\ &\qquad = \lim_{\Delta t \to 0} \frac{1}{\Delta t} \left[p_{X(t+\Delta t)}(x|X(0) = x_0) - p_{X(t)}(x|X(0) = x_0) \right] \end{aligned} \tag{E.7}$$

The basic idea in deriving the governing differential equation involves rewriting (E.7) in terms of the conditional moments of the increment $\Delta X = X(t + \Delta t) - X(t)$. In many cases the conditional moments of the increments can be obtained using the equations of motion of the system which lead to the governing differential equation for the transition probability density function of the response of the system. As a

first step we rewrite the probability density function of $X(t+\Delta t)$ in terms of the joint probability density function of $X(t)$ and ΔX as shown in (E.8).

$$\begin{aligned} p_{X(t+\Delta t)}(y|X(0)=x_0) &= \int_{-\infty}^{\infty} p_{X(t),X(t+\Delta t)}(x,y|X(0)=x_0)dx \\ &= \int_{-\infty}^{\infty} p_{X(t)}(x|X(0)=x_0) \times p_{\Delta X}(y-x|X(t)=x, X(0)=x_0)dx \\ &= \int_{-\infty}^{\infty} p_{X(t)}(x|X(0)=x_0) \times p_{\Delta X}(y-x|X(t)=x)dx \end{aligned} \tag{E.8}$$

The conditional probability density function of the increment can be rewritten as (E.9) in order to obtain a range of values of ΔX which is later used to obtain the conditional moments.

$$p_{\Delta X}(y-x|X(t)=x) = \int_{-\infty}^{\infty} p_{\Delta X}(z|X(t)=x)\delta(z-y+x)dz \tag{E.9}$$

The Dirac delta function in (E.9) can be expressed as an inverse Fourier transform as shown below

$$\begin{aligned} \delta(z-y+x) &= \frac{1}{2\pi}\int_{-\infty}^{\infty} e^{i\theta(z-y+x)}d\theta \\ &= \frac{1}{2\pi}\int_{-\infty}^{\infty}\left[\sum_{n=0}^{\infty}\frac{(i\theta z)^n}{n!}\right]e^{-i\theta(y-x)}d\theta \end{aligned} \tag{E.10}$$

The conditional probability density function of ΔX is now given by

$$
\begin{aligned}
&p_{\Delta X}(y-x|X(t)=x) \\
&\quad = \int_{-\infty}^{\infty} p_{\Delta X}(z|X(t)=x)\left\{\frac{1}{2\pi}\int_{-\infty}^{\infty}\left[\sum_{n=0}^{\infty}\frac{(i\theta z)^n}{n!}\right]e^{-i\theta(y-x)}d\theta\right\}dz \\
&\quad = \frac{1}{2\pi}\int_{-\infty}^{\infty}\left[\sum_{n=0}^{\infty}\frac{(i\theta)^n}{n!}\left\{\int_{-\infty}^{\infty} z^n p_{\Delta X}(z|X(t)=x)dz\right\}\right]e^{-i\theta(y-x)}d\theta \\
&\quad = \frac{1}{2\pi}\int_{-\infty}^{\infty}\left[\sum_{n=0}^{\infty}\frac{(i\theta)^n}{n!}E\left[(\Delta X)^n|X(t)=x\right]\right]e^{-i\theta(y-x)}d\theta
\end{aligned}
\tag{E.11}
$$

Substituting (E.11) into (E.8) gives

$$
\begin{aligned}
&p_{X(t+\Delta t)}(y|X(0)=x_0) \\
&\quad = \int_{-\infty}^{\infty} p_{X(t)}(x|X(0)=x_0) \\
&\qquad \times\left\{\frac{1}{2\pi}\int_{-\infty}^{\infty}\left[\sum_{n=0}^{\infty}\frac{(i\theta)^n}{n!}E\left[(\Delta X)^n|X(t)=x\right]\right]e^{-i\theta(y-x)}d\theta\right\}dx \\
&\quad = p_{X(t)}(y|X(0)=x_0) + \int_{-\infty}^{\infty} p_{X(t)}(x|X(0)=x_0) \\
&\qquad \times\left\{\frac{1}{2\pi}\int_{-\infty}^{\infty}\left[\sum_{n=1}^{\infty}\frac{(i\theta)^n}{n!}E\left[(\Delta X)^n|X(t)=x\right]\right]e^{-i\theta(y-x)}d\theta\right\}dx
\end{aligned}
\tag{E.12}
$$

Substituting (E.12) into (E.7) and taking the limit results in

$$
\begin{aligned}
\frac{\partial p_{X(t)}}{\partial t}(y|X(0)=x_0) = \frac{1}{2\pi}\sum_{n=1}^{\infty}\Bigg[\int_{-\infty}^{\infty}\frac{(i\theta)^n}{n!} \\
\times\left\{\int_{-\infty}^{\infty}\left[C^{(j)}(x,t)p_{X(t)}(x|X(0)=x_0)\right]e^{-i\theta(y-x)}dx\right\}d\theta\Bigg]
\end{aligned}
\tag{E.13}
$$

where $C^{(n)}(x,t)$ known as the derivate moments [18] or intensity functions [137,

138] and are given by

$$\begin{aligned} C^{(n)}(x,t) &= \lim_{\Delta t \to 0} \frac{1}{\Delta t} E\left[(\Delta X)^n | X(t) = x\right] \\ &= \lim_{\Delta t \to 0} \frac{1}{\Delta t} \int_{-\infty}^{\infty} (y-x)^n p(y, t+\Delta t | x, t) dy \end{aligned} \tag{E.14}$$

Applying repeated integration by parts to the inner integral in (E.13) leads to the following simplification

$$\begin{aligned} &\frac{\partial p_{X(t)}}{\partial t}(y|X(0)=x_0) \\ &= \frac{1}{2\pi} \sum_{n=1}^{\infty} \left[\int_{-\infty}^{\infty} \frac{(-1)^n}{n!} \times \left\{ \int_{-\infty}^{\infty} \frac{\partial^n}{\partial x^n} \left[C^{(j)}(x,t) p_{X(t)}(x|X(0)=x_0) \right] e^{-i\theta(y-x)} dx \right\} d\theta \right] \\ &= \sum_{n=1}^{\infty} \left[\int_{-\infty}^{\infty} \frac{(-1)^n}{n!} \frac{\partial^n}{\partial x^n} \left[C^{(j)}(x,t) p_{X(t)}(x|X(0)=x_0) \right] \times \left\{ \frac{1}{2\pi} \int_{-\infty}^{\infty} e^{-i\theta(y-x)} d\theta \right\} dx \right] \\ &= \sum_{n=1}^{\infty} \left[\int_{-\infty}^{\infty} \frac{(-1)^n}{n!} \frac{\partial^n}{\partial x^n} \left[C^{(j)}(x,t) p_{X(t)}(x|X(0)=x_0) \right] \times \delta(x-y) dx \right] \end{aligned} \tag{E.15}$$

Finally the simplified expression is given by (E.16). This equation is known as the *Fokker Planck Kolmogorov (FPK) equation.* It is also sometimes referred to as the *Kolmogorov forward equation.*

$$\frac{\partial p_{X(t)}}{\partial t}(y|X(0)=x_0) = \sum_{n=1}^{\infty} \left[\frac{(-1)^n}{n!} \frac{\partial^n}{\partial y^n} \left[C^{(n)}(y,t) p_{X(t)}(y|X(0)=x_0) \right] \right] \tag{E.16}$$

When this theory is applied to a dynamical system, the derivate moments are evaluated using the equations of motion and the formulated FPK equation is solved with appropriate boundary conditions and the initial condition shown in (E.17). A detailed discussion of the different types of boundary conditions for the FPK

equations are discussed in Lin and Cai [18].

$$p_{X(t)}(y|X(0)=x_0) \equiv p(y,t|x_0,t_0) = \delta(y-x_0) \tag{E.17}$$

If in addition to being a Markov process, $X(t)$ is also a Gaussian process, then using the Gaussian property it can be shown that the derivate moments are zero $C^{(n)}(y,t)=0$ for $n>2$. Thus in this case the FPK equation reduces to (E.18).

$$\frac{\partial p}{\partial t} + \frac{\partial}{\partial y}\left[C^{(1)}p\right] - \frac{1}{2}\frac{\partial^2}{\partial y^2}\left[C^{(2)}p\right] = 0 \tag{E.18}$$

A *diffusion process* is a Markov process for which sample paths are continuous with probability 1 [18]. A sufficient condition for a Markov process to be a diffusion is given by Dynkin's condition [166] given by

$$\lim_{\Delta t\to 0}\frac{1}{\Delta t}P\left[||X(t+\Delta t)-X(t)|| > \epsilon | X(t)=x\right] = 0 \qquad \epsilon > 0 \tag{E.19}$$

However, a sufficient condition for the Dynkin's condition [167] is given by

$$\lim_{\Delta t\to 0}\frac{1}{\Delta t}E\left[||X(t+\Delta t)-X(t)||^{2+\delta} | X(t)=x\right] = 0 \qquad \delta > 0 \tag{E.20}$$

which again means that the derivate moments of order $n>2$ are zero. Thus, the simplified version of FPK equation shown in (E.18) holds for diffusion processes as well. Note that a general diffusion process need not be a Gaussian process, but the simpler form of FPK equation is still applicable.

E.3 Kolmogorov Backward Equation

In the derivation of the FPK equation the derivatives of the transition probability density function $p(x,t|x_0,t_0)$ have been considered with respect to t and x. However,

considering that $p(x,t|x_0,t_0)$ is a function of t_0 and x_0 and using a similar approach as above leads to the well known *Kolmogorov backward equation*.

In order to derive the Kolmogorov backward equation, we again consider the time derivative of the transition probability density function. However, unlike in (E.7) we consider the derivative with respect to t_0.

$$\frac{\partial p}{\partial t_0} = \lim_{\Delta t_0 \to 0} \frac{1}{\Delta t_0} \left[p(x,t|x_0,t_0) - p(x,t|x_0,t_0 - \Delta t_0) \right] \tag{E.21}$$

From Chapman Kolmogorov equation (E.6),

$$p(x,t|x_0,t_0 - \Delta t_0) = \int_{-\infty}^{\infty} p(x,t|y,t_0) p(y,t_0|x_0,t_0 - \Delta t_0) dy \tag{E.22}$$

Similarly,

$$p(x,t|x_0,t_0) = \int_{-\infty}^{\infty} p(x,t|x_0,t_0) p(y,t_0|x_0,t_0 - \Delta t_0) dy \tag{E.23}$$

where

$$\int_{-\infty}^{\infty} p(y,t_0|x_0,t_0 - \Delta t_0) dy = 1 \tag{E.24}$$

Substituting (E.22) and (E.23) into (E.21) leads to

$$\frac{\partial p}{\partial t_0} = \lim_{\Delta t_0 \to 0} \frac{1}{\Delta t_0} \int_{-\infty}^{\infty} \left[p(x,t|x_0,t_0) - p(x,t|y,t_0) \right] p(y,t_0|x_0,t_0 - \Delta t_0) dy \tag{E.25}$$

$p(x,t|y,t_0)$ can be expanded as a Taylor series as shown in (E.26).

$$p(x,t|y,t_0) = p(x,t|x_0,t_0) + (y-x_0)\frac{\partial}{\partial x_0}p(x,t|x_0,t_0) + (y-x_0)^2\frac{1}{2}\frac{\partial^2}{\partial x_0^2}p(x,t|x_0,t_0) + ... \tag{E.26}$$

Substituting (E.26) into (E.25) leads to

$$\frac{\partial p}{\partial t_0} = \lim_{\Delta t_0 \to 0}\frac{1}{\Delta t_0}\int_{-\infty}^{\infty}\left\{ -(y-x_0)\frac{\partial}{\partial x_0}p(x,t|x_0,t_0) - (y-x_0)^2\frac{1}{2}\frac{\partial^2}{\partial x_0^2}p(x,t|x_0,t_0) + ...\right\} \times p(y,t_0|x_0,t_0-\Delta t_0)dy \tag{E.27}$$

Rewriting the derivate moments shown in (E.14) as

$$C^{(n)}(x_0,t_0) = \lim_{\Delta t_0 \to 0}\frac{1}{\Delta t_0}\int_{-\infty}^{\infty}(y-x_0)^n p(y,t_0|x_0,t_0-\Delta t_0)dy \tag{E.28}$$

the partial differential equation is given by (E.29).

$$\frac{\partial p}{\partial t_0} + \sum_{n=1}^{\infty}\left[\frac{C^{(n)}}{n!}\frac{\partial^n p}{\partial x_0^n}\right] = 0 \tag{E.29}$$

For a Gaussian Markov process or a diffusion process, this further reduces to (E.30).

$$\frac{\partial p}{\partial t_0} + C^{(1)}\frac{\partial p}{\partial x_0} + \frac{1}{2}C^{(2)}\frac{\partial^2 p}{\partial x_0^2} = 0 \tag{E.30}$$

Similar to the Kolmogorov forward equation, the backward equation also requires two spatial boundary conditions and one initial condition. The initial condition is the same as that for the forward equation and is given by (E.17). The various types

of boundaries and the associated boundary conditions for the backward equation are discussed by Lin and Cai [18].

E.4 Brownian Motion

The simplest example of Markov process is the *Brownian motion* (also known as *Wiener process*), named after the English botanist Robert Brown who first observed such a random motion. Formally, Brownian motion $B(t)$ is defined as a stochastic process which satisfies the following properties:

1. $B(0) = 0$
2. $B(t)$ has continuous sample paths
3. $B(t)$ has independent increments i.e. for $t_1 < t_2 < ... < t_n$, the increments of the process given by $(B(t_n) - B(t_{n-1}))$, $(B(t_{n-1}) - B(t_{n-2}))$, ..., $(B(t_2) - B(t_1))$ are independent
4. $B(t)$ has stationary increments which are Gaussian distributed i.e. $(B(t) - B(s)) \sim N(0, t-s)$ for any $0 \leq s < t$

One of the prominent properties of Brownian motion is that almost every path has infinite variation on finite time interval. Consider the Brownian motion $B(t)$ over the interval $[a, b]$. Let the interval be divided uniformly into sub-intervals of length Δt given by $[t_i, t_{i+1}]$. Let the number of intervals be given by $N = \frac{b-a}{\Delta t}$. Now consider the sum $\sum_{i=1}^{N} |B(t_{i+1}) - B(t_i)|$. The expected value of this sum in the limit

$\Delta t \to 0$ is given by

$$\begin{aligned}
\lim_{\Delta t \to 0} E\left[\sum_{i=1}^{N} |B(t_{i+1}) - B(t_i)|\right] &= \lim_{\Delta t \to 0} \sum_{i=1}^{N} E\left[|B(t_{i+1}) - B(t_i)|\right] \\
&= \lim_{\Delta t \to 0} \sum_{i=1}^{N} E\left[|B(\Delta t)|\right] \\
&= \lim_{\Delta t \to 0} \sum_{i=1}^{N} \sqrt{\frac{2\Delta t}{\pi}} \\
&= \lim_{\Delta t \to 0} \sqrt{\frac{2}{\pi}} \frac{b-a}{\sqrt{\Delta t}} \to \infty
\end{aligned} \tag{E.31}$$

Although the first variation is infinite on every finite interval of time, the quadratic variation of Brownian motion is equal to the length of the interval itself.

$$\begin{aligned}
\lim_{\Delta t \to 0} E\left[\sum_{i=1}^{N} |B(t_{i+1}) - B(t_i)|^2\right] &= \lim_{\Delta t \to 0} \sum_{i=1}^{N} E\left[|B(t_{i+1}) - B(t_i)|^2\right] \\
&= \lim_{\Delta t \to 0} \sum_{i=1}^{N} (t_{i+1} - t_i) \\
&= b - a
\end{aligned} \tag{E.32}$$

For more details on the properties of the Brownian motion please refer to standard texts such as Duan [165].

E.5 Stochastic Differential Equations

While Brownian motion is the simplest example of a diffusion process, it can also be used as a building block to construct other Markov processes. Itô [168] suggested that an arbitrary Markov process can be generated using the Brownian motion $B(t)$

as shown in the stochastic differential equation (E.33).

$$dX_t = m(t, X_t)dt + \sigma(t, X_t)dB_t \tag{E.33}$$

The coefficients $m(t, X_t)$ and $\sigma(t, X_t)$ are called the *drift* and *diffusion* coefficients respectively. The stochastic differential equation can also be expressed in the integral form as shown below.

$$X(t) - X(0) = \int_0^t m(u, X(u))du + \int_0^t \sigma(u, X(u))dB_u \tag{E.34}$$

The first integral in (E.34) can be evaluated as a standard Riemann sum. However, the second integral requires a special treatment. Consider a general Riemann-Stieltjes integral of the form $\int_0^t f(u)dg(u)$. Let the interval $[0, t]$ be partitioned into smaller subintervals of maximal length δ defined by $0 = u_0 < u_1 < u_2 < ... < u_n = t$. Then the integral is evaluated by

$$\int_0^t f(u)dg(u) = \lim_{\delta \to 0} \sum_{i=0}^{n-1} f(v_i)[g(u_{i+1}) - g(u_i)] \tag{E.35}$$

where $v_i \in [u_i, u_{i+1}]$. A sufficient condition for this integral to exist is that $g(u)$ be of finite variation [165], or in other words,

$$\lim_{\delta \to 0} \sum_{i=0}^{n-1} |g(u_{i+1}) - g(u_i)| < \infty \tag{E.36}$$

Clearly, from (E.31) it is seen that $B(t)$ is not of finite variation and hence the second integral in (E.34) cannot be evaluated as a Riemann-Stieltjes integral. For stochastic integrals like the second term in (E.34) two specific approaches are available:

1. Itô integral approach

2. Stratonovich integral approach

Based on the Itô approach, the stochastic integral $\int_0^t \sigma(u, X(u))dB_u$ can be evaluated as follows. The interval $[0, t]$ is partitioned into subintervals of equal length $\delta_n = \frac{t-0}{n}$ and end points of the subintervals are sequenced as $0 = u_0^n < u_1^n < ... < u_n^n = t$. As $n \to 0$, δ_n converges to 0.

$$\begin{aligned}
&\int_0^t \sigma(u, X(u))dB_u \\
&\qquad = \lim_{n\to\infty} \text{ in m.s. } \int_0^t \sigma(u, X(u))dB_u \\
&\qquad = \lim_{n\to\infty} \text{ in m.s. } \sum_{i=0}^{n-1} \sigma(u_i^n, X(u_i^n)) \left[B(u_{i+1}^n) - B(u_i^n)\right]
\end{aligned} \tag{E.37}$$

Note that a sequence X_n is said to converges to X in mean square if $E\left[|X_n - X|^2\right] \to 0$ as $n \to \infty$. Similarly, based on the Stratonovich approach, the stochastic integral $\int_0^t \sigma(u, X(u)) \; o \; dB_u$ can be evaluated as follows. Assume a similar partitioning into subintervals as before. However, the evaluation of the Stratonovich integral is given by

$$\begin{aligned}
&\int_0^t \sigma(u, X(u)) \; o \; dB_u \\
&\qquad = \lim_{n\to\infty} \text{ in m.s. } \int_0^t \sigma(u, X(u)) \; o \; dB_u \\
&\qquad = \lim_{n\to\infty} \text{ in m.s. } \sum_{i=0}^{n-1} \left\{\frac{1}{2}\sigma(u_i^n, X(u_i^n)) + \frac{1}{2}\sigma(u_{i+1}^n, X(u_{i+1}^n))\right\} \left[B(u_{i+1}^n) - B(u_i^n)\right]
\end{aligned} \tag{E.38}$$

Both Itô and Stratonovich type of integrals can be converted from one to the other. Using Taylor series expansion and the mean value theorem it can be shown

[165] that

$$\int_0^t \sigma(u, X(u)) \; o \; dB_u = \int_0^t \sigma(u, X(u)) dB_u + \frac{1}{2} \int_0^t \sigma(u, X(u)) \frac{\partial \sigma}{\partial x}(u, X(u)) du \tag{E.39}$$

Equivalently in the differential form

$$\sigma(u, X(u)) \; o \; dB_u = \sigma(u, X(u)) dB_u + \frac{1}{2} \sigma(u, X(u)) \frac{\partial \sigma}{\partial x}(u, X(u)) du \tag{E.40}$$

This further implies that the Stratonovich SDE given by (E.41) when converted into an Itô SDE is given by (E.42).

$$dX_t = m(t, X_t)dt + \sigma(t, X_t) \; o \; dB_t \tag{E.41}$$

$$dX_t = \left\{ m(t, X_t) + \frac{1}{2} \sigma(t, X_t) \frac{\partial \sigma}{\partial x}(t, X_t) \right\} dt + \sigma(t, X_t) dB_t \tag{E.42}$$

Similarly, the Itô SDE given by (E.43) when converted into Stratonovich SDE is given by (E.44).

$$dX_t = m(t, X_t)dt + \sigma(t, X_t) dB_t \tag{E.43}$$

$$dX_t = \left\{ m(t, X_t) - \frac{1}{2} \sigma(t, X_t) \frac{\partial \sigma}{\partial x}(t, X_t) \right\} dt + \sigma(t, X_t) \; o \; dB_t \tag{E.44}$$

The correction term introduced in the transformation of Itô SDE into Stratonovich SDE is called the Wong-Zakai correction term. In case of directly excited systems, the diffusion coefficient σ is independent of the state of the response X_t in which case the correction term becomes zero. However, for parametrically excited systems, this term is non-zero and must be included in the analysis.

E.6 Itô's Formula

Consider an Itô SDE given by (E.45) where $m(X_t)$ and $\sigma(X_t)$ are the drift and diffusion coefficients respectively and B_t is a scalar Brownian motion.

$$dX_t = m(X_t)dt + \sigma(X_t)dB_t \tag{E.45}$$

The Itô SDE governing a scalar deterministic function $g(t, X_t)$ is given by (E.46) and is known at the *Itô's formula* and is equivalent to the chain rule of differentiation for stochastic SDEs. The term $\frac{1}{2}\sigma^2(X_t)\frac{\partial^2 g}{\partial x^2}(t, X_t)$ is called the Itô correction term and originates due to the unbounded variation of the Brownian motion in a finite interval of time.

$$\begin{aligned} dg(t, X_t) = &\left[\frac{\partial g}{\partial t}(t, X_t) + m(X_t)\frac{\partial g}{\partial x}(t, X_t) + \frac{1}{2}\sigma^2(X_t)\frac{\partial^2 g}{\partial x^2}(t, X_t)\right] dt \\ &+ \frac{\partial g}{\partial x}(t, X_t)\sigma(X_t)dB_t \end{aligned} \tag{E.46}$$

E.7 White Noise

There are various physical processes where the excitation $W(t)$ is caused due to noise. Typically for such systems it is assumed that the zero mean noise is so erratic that $W(t)$ and $W(s)$ are almost independent unless t and s are very close. A limiting process which is completely uncorrelated with itself at a different time will have a zero covariance for every time lag τ except at $\tau = 0$. Such limiting processes are called delta-correlated processes as the covariance function is characterized by a Dirac delta function. These class of processes are also known as *white noise*. However, when the covariance function is not a Dirac delta function, it is known as *colored noise*.

White noise can be modeled in terms of a time derivative of the Brownian motion

$B(t)$. Brownian motion, although continuous, is nowhere differentiable. Thus a specific interpretation of derivative is required to express white noise as a time derivative of Brownian motion. This is provided in terms of generalized derivatives which are discussed in detail by Duan [165]. The covariance function of the derivative of the Brownian motion can be obtained as follows.

$$\begin{aligned} E[\dot{B}(t)\dot{B}(s)] &= \frac{\partial^2}{\partial t \partial s} E[B(t)B(s)] = \frac{\partial^2}{\partial t \partial s} min(t,s) \\ &= \frac{\partial^2}{\partial t \partial s} \begin{cases} t, & t-s<0 \\ s, & t-s \geq 0 \end{cases} \\ &= \frac{\partial}{\partial t} \begin{cases} 0, & t-s<0 \\ 1, & t-s \geq 0 \end{cases} \\ &= \delta(t-s) \end{aligned} \tag{E.47}$$

It can be seen from (E.47) that the process $\dot{B}(t)$ is uncorrelated at different times. Therefore, the spectral density of white noise must have a constant absolute value. This is seen from (E.48) where the spectral density is obtained by taking a Fourier transform of the covariance function $E[\dot{B}(t)\dot{B}(s)]$ derived in (E.47).

$$\left| \mathscr{F}\left[E[\dot{B}(t)\dot{B}(s)] \right] \right| = \left| \mathscr{F}\left[\delta(t-s) \right] \right| = \left| e^{-i\theta s} \right| = 1 \tag{E.48}$$

APPENDIX F

DRIFT AND DIFFUSION COEFFICIENT EXPRESSIONS

F.1 Drift Coefficient Calculation

The drift vector $\boldsymbol{m}$ for the Markov process $\boldsymbol{Z}(t)$ is given by (5.36). The components of the drift vector $\boldsymbol{m}$ are given by

$$m_1 = A_1(E) + \int_{-\infty}^{0} \left\langle E\left[\left(\frac{\partial b_1}{\partial E}\right)_t (b_1)_{t+\tau} + \left(\frac{\partial b_1}{\partial \lambda}\right)_t (b_2)_{t+\tau}\right]\right\rangle d\tau \tag{F.1}$$

$$m_2 = A_2(E) + \int_{-\infty}^{0} \left\langle E\left[\left(\frac{\partial b_2}{\partial E}\right)_t (b_1)_{t+\tau} + \left(\frac{\partial b_2}{\partial \lambda}\right)_t (b_2)_{t+\tau}\right]\right\rangle d\tau \tag{F.2}$$

F.1.1 Energy Drift Coefficient

$$m_1 = A_1(E) + \int_{-\infty}^{0} \left\langle E\left[\left(\frac{\partial b_1}{\partial E}\right)_t (b_1)_{t+\tau} + \left(\frac{\partial b_1}{\partial \lambda}\right)_t (b_2)_{t+\tau}\right]\right\rangle d\tau \tag{F.3}$$

where

$$(b_1)_t = g_1(t, E, \theta)\sqrt{2E}\sin(\theta) = \sqrt{2E}\sin(\theta) \sum_{j=1,3,5,\ldots}^{2n_q-1} p_j(t)x^j \tag{F.4}$$

$$(b_2)_t = \frac{g_1(t, E, \theta_0)\cos(\theta)}{\sqrt{2E}} = \frac{\cos(\theta)}{\sqrt{2E}} \sum_{j=1,3,5,\ldots}^{2n_q-1} p_j(t)x^j \tag{F.5}$$

F.1.1.1 Evaluation of 1^{st} Term in (F.3)

$$\left(\frac{\partial b_1}{\partial E}\right)_t = \frac{\sin(\theta)}{\sqrt{2E}} \sum_{j=1,3,5,\ldots}^{2n_q-1} p_j(t)x^j + \sqrt{2E}\sin(\theta) \sum_{j=1,3,5,\ldots}^{2n_q-1} (j)p_j(t)x^{j-1} \left(\frac{\partial x}{\partial E}\right) \quad \text{(F.6)}$$

$$\begin{aligned} E = \frac{\dot{x}^2}{2} + U(x) &= \frac{\dot{x}^2}{2} + \int_0^x \sum_{k=1,3,5,\ldots}^{2n_q-1} \alpha_k \xi^k d\xi \\ &= \frac{\dot{x}^2}{2} + \sum_{k=1,3,5,\ldots}^{2n_q-1} \frac{\alpha_k x^{k+1}}{k+1} \end{aligned} \quad \text{(F.7)}$$

Taking partial derivative with respect to E

$$1 = \dot{x}\frac{\partial \dot{x}}{\partial E} + \sum_{k=1,3,5,\ldots}^{2n_q-1} \alpha_k x^k \frac{\partial x}{\partial E} \quad \text{(F.8)}$$

Substituting $\dot{x} = -\sqrt{2E}\sin(\theta)$ from (5.17) into the above equation leads to

$$\frac{\partial x}{\partial E} = \frac{\cos^2(\theta)}{g(E,\theta)} \quad \text{(F.9)}$$

Substituting back into (F.6) gives

$$\left(\frac{\partial b_1}{\partial E}\right)_t = \frac{\sin(\theta)}{\sqrt{2E}} \sum_{j=1,3,5,\ldots}^{2n_q-1} p_j(t)x^j + \frac{\sqrt{2E}\sin(\theta)\cos^2(\theta)}{g(E,\theta)} \sum_{j=1,3,5,\ldots}^{2n_q-1} (j)p_j(t)x^{j-1} \quad \text{(F.10)}$$

$$E\left[\left(\frac{\partial b_1}{\partial E}\right)_t (b_1)_{t+\tau}\right] = \sin(\theta(t))\sin(\theta(t+\tau)) \times \sum_{j=1,3,5,\ldots}^{2n_q-1}\sum_{k=1,3,5,\ldots}^{2n_q-1} E\left[p_j(t)p_k(t+\tau)\right]x^j(t)x^k(t+\tau) + \frac{2E}{g(E,\theta(t))}\sin(\theta(t))\cos^2(\theta(t))\sin(\theta(t+\tau)) \times \sum_{j=1,3,5,\ldots}^{2n_q-1}\sum_{k=1,3,5,\ldots}^{2n_q-1}(j)E\left[p_j(t)p_k(t+\tau)\right]x^{j-1}(t)x^k(t+\tau) \tag{F.11}$$

Assuming a covariance stationarity between $p_j(t)$ and $p_k(t)$ leads to the following simplification

$$E\left[\left(\frac{\partial b_1}{\partial E}\right)_t (b_1)_{t+\tau}\right] = \sin(\theta(t))\sin(\theta(t+\tau))\sum_{j=1,3,5,\ldots}^{2n_q-1}\sum_{k=1,3,5,\ldots}^{2n_q-1} w_{jk}(\tau)x^j(t)x^k(t+\tau) + \frac{2E}{g(E,\theta(t))}\sin(\theta(t))\cos^2(\theta(t))\sin(\theta(t+\tau)) \times \sum_{j=1,3,5,\ldots}^{2n_q-1}\sum_{k=1,3,5,\ldots}^{2n_q-1}(j)w_{jk}(\tau)x^{j-1}(t)x^k(t+\tau) \tag{F.12}$$

where $w_{jk}(\tau) = E\left[p_j(t)p_k(t+\tau)\right]$.

F.1.1.2 Evaluation of 2^{nd} Term in (F.3)

$$\left(\frac{\partial b_1}{\partial \lambda}\right)_t = \sqrt{2E}\cos(\theta)\sum_{j=1,3,5,\ldots}^{2n_q-1} p_j(t)x^j + \sqrt{2E}\sin(\theta)\sum_{j=1,3,5,\ldots}^{2n_q-1}(j)p_j(t)x^{j-1}\left(\frac{\partial x}{\partial \lambda}\right) \tag{F.13}$$

$$\lambda = \tan^{-1}\left[-\frac{\dot{x}}{\sqrt{2U(x)}}\right] - \theta_0 \tag{F.14}$$

Taking partial derivative with respect to λ

$$1 = \frac{1}{1+\frac{\dot{x}^2}{2U(x)}}\left[\dot{x}\frac{G(x)}{[2U(x)]^{\frac{3}{2}}}\frac{\partial x}{\partial \lambda} - \frac{1}{\sqrt{2U(x)}}\frac{\partial \dot{x}}{\partial \lambda}\right] \tag{F.15}$$

Substituting $\dot{x} = -\sqrt{2E}\sin(\theta)$ from (5.17) into the above equation leads to

$$\frac{\partial x}{\partial \lambda} = \frac{-2E\sin(\theta)\cos(\theta)}{g(E,\theta)} \tag{F.16}$$

Substituting back into (F.13) gives

$$\left(\frac{\partial b_1}{\partial \lambda}\right)_t = \sqrt{2E}\cos(\theta)\sum_{j=1,3,5,\ldots}^{2n_q-1} p_j(t)x^j - \frac{(2E)^{\frac{3}{2}}\sin^2(\theta)\cos(\theta)}{g(E,\theta)}\sum_{j=1,3,5,\ldots}^{2n_q-1}(j)p_j(t)x^{j-1} \tag{F.17}$$

$$\begin{aligned} E\left[\left(\frac{\partial b_1}{\partial \lambda}\right)_t (b_2)_{t+\tau}\right] &= \cos(\theta(t))\cos(\theta(t+\tau)) \\ &\quad \times \sum_{j=1,3,5,\ldots}^{2n_q-1}\sum_{k=1,3,5,\ldots}^{2n_q-1} E\left[p_j(t)p_k(t+\tau)\right]x^j(t)x^k(t+\tau) \\ &\quad + \frac{2E}{g(E,\theta(t))}\sin^2(\theta(t))\cos(\theta(t))\cos(\theta(t+\tau)) \\ &\quad \times \sum_{j=1,3,5,\ldots}^{2n_q-1}\sum_{k=1,3,5,\ldots}^{2n_q-1}(j)E\left[p_j(t)p_k(t+\tau)\right]x^{j-1}(t)x^k(t+\tau) \end{aligned} \tag{F.18}$$

Assuming a covariance stationarity between $p_j(t)$ and $p_k(t)$ leads to the following

simplification

$$E\left[\left(\frac{\partial b_1}{\partial \lambda}\right)_t (b_2)_{t+\tau}\right] = \cos(\theta(t))\cos(\theta(t+\tau)) \sum_{j=1,3,5,\ldots}^{2n_q-1} \sum_{k=1,3,5,\ldots}^{2n_q-1} w_{jk}(\tau) x^j(t) x^k(t+\tau)$$
$$+ \frac{2E}{g(E,\theta(t))} \sin^2(\theta(t))\cos(\theta(t))\cos(\theta(t+\tau))$$
$$\times \sum_{j=1,3,5,\ldots}^{2n_q-1} \sum_{k=1,3,5,\ldots}^{2n_q-1} (j) w_{jk}(\tau) x^{j-1}(t) x^k(t+\tau) \qquad \text{(F.19)}$$

where $w_{jk}(\tau) = E\left[p_j(t)p_k(t+\tau)\right]$. Substituting (F.12) and (F.19) into (F.3) results in

$$m_1 = A_1(E) + \sum_{j=1,3,5,\ldots}^{2n_q-1} \sum_{k=1,3,5,\ldots}^{2n_q-1}$$
$$\left[\int_{-\infty}^{0} w_{jk}(\tau) \left\langle \sin(\theta(t)) x^j(t) \sin(\theta(t+\tau)) x^k(t+\tau) \right\rangle d\tau \right.$$
$$+(j) \int_{-\infty}^{0} w_{jk}(\tau) \left\langle \frac{2E}{g(E,\theta(t))} \sin(\theta(t)) \cos^2(\theta(t)) x^{j-1}(t) \sin\theta(t+\tau) x^k(t+\tau) \right\rangle d\tau$$
$$+ \int_{-\infty}^{0} w_{jk}(\tau) \left\langle \cos(\theta(t)) x^j(t) \cos(\theta(t+\tau)) x^k(t+\tau) \right\rangle d\tau$$
$$-(j) \int_{-\infty}^{0} w_{jk}(\tau)$$
$$\left. \times \left\langle \frac{2E}{g(E,\theta(t))} \sin^2(\theta(t)) \cos(\theta(t)) x^{j-1}(t) \cos(\theta(t+\tau)) x^k(t+\tau) \right\rangle d\tau \right] \qquad \text{(F.20)}$$

F.1.1.3 Fourier Expansions for Energy Drift Calculation

To evaluate the time average of the quantities inside $\langle\ .\ \rangle$ in (F.20), it is convenient to expand the various terms as Fourier series as shown below.

$$\sin(\theta(t))x^k(t) = \sum_{n=1}^{\infty} b_n^{(1k)} \sin\left(\frac{2\pi n}{T}t\right) \tag{F.21}$$

$$\cos(\theta(t))x^k(t) = \sum_{n=1}^{\infty} a_n^{(1k)} \cos\left(\frac{2\pi n}{T}t\right) \tag{F.22}$$

$$\frac{2E}{g(E,\theta(t))} \sin(\theta(t)) \cos^2(\theta(t))x^{k-1}(t) = \sum_{n=1}^{\infty} b_n^{(2k)} \sin\left(\frac{2\pi n}{T}t\right) \tag{F.23}$$

$$\frac{2E}{g(E,\theta(t))} \sin^2(\theta(t)) \cos(\theta(t))x^{k-1}(t) = \sum_{n=1}^{\infty} a_n^{(2k)} \cos\left(\frac{2\pi n}{T}t\right) \tag{F.24}$$

Note that these coefficients $b_n^{(1k)}$, $a_n^{(1k)}$, $b_n^{(2k)}$ and $a_n^{(2k)}$ are functions of energy level E. Since λ is assumed to be fixed, the Fourier coefficients actually relate to the unperturbed solutions $\theta_0(t)$ and $x_0(t)$. Substituting these Fourier series expressions simplifies the time averages as follows

$$\left\langle \sin(\theta(t))x^j(t) \sin(\theta(t+\tau))x^k(t+\tau) \right\rangle = \sum_{n=1}^{\infty} \frac{b_n^{(1j)} b_n^{(1k)}}{2} \cos\left(\frac{2\pi n}{T}\tau\right) \tag{F.25}$$

$$\left\langle \cos(\theta(t))x^j(t) \cos(\theta(t+\tau))x^k(t+\tau) \right\rangle = \sum_{n=1}^{\infty} \frac{a_n^{(1j)} a_n^{(1k)}}{2} \cos\left(\frac{2\pi n}{T}\tau\right) \tag{F.26}$$

$$\left\langle \frac{2E}{g(E,\theta(t))} \sin(\theta(t)) \cos^2(\theta(t))x^{j-1}(t) \sin(\theta(t+\tau))x^k(t+\tau) \right\rangle = \sum_{n=1}^{\infty} \frac{b_n^{(2j)} b_n^{(1k)}}{2} \cos\left(\frac{2\pi n}{T}\tau\right) \tag{F.27}$$

$$\left\langle \frac{2E}{g(E,\theta(t))} \sin^2(\theta(t)) \cos(\theta(t))x^{j-1}(t) \cos(\theta(t+\tau))x^k(t+\tau) \right\rangle = \sum_{n=1}^{\infty} \frac{a_n^{(2j)} a_n^{(1k)}}{2} \cos\left(\frac{2\pi n}{T}\tau\right) \tag{F.28}$$

Substituting into (F.20) leads to

$$m_1 = A_1(E) + \sum_{n=1}^{\infty} \sum_{j=1,3,5,\ldots}^{2n_q-1} \sum_{k=1,3,5,\ldots}^{2n_q-1} \left[\left(\int_{-\infty}^{0} w_{jk}(\tau) \cos\left(\frac{2\pi n}{T} \tau \right) d\tau \right) \times \left\{ \frac{b_n^{(1j)} b_n^{(1k)}}{2} + \frac{a_n^{(1j)} a_n^{(1k)}}{2} + (j) \frac{b_n^{(2j)} b_n^{(1k)}}{2} + (j) \frac{a_n^{(2j)} a_n^{(1k)}}{2} \right\} \right] \tag{F.29}$$

F.1.2 Phase Drift Coefficient

$$m_2 = A_2(E) + \int_{-\infty}^{0} \left\langle E \left[\left(\frac{\partial b_2}{\partial E} \right)_t (b_1)_{t+\tau} + \left(\frac{\partial b_2}{\partial \lambda} \right)_t (b_2)_{t+\tau} \right] \right\rangle d\tau \tag{F.30}$$

where

$$(b_1)_t = g_1(t, E, \theta) \sqrt{2E} \sin(\theta) = \sqrt{2E} \sin(\theta) \sum_{j=1,3,5,\ldots}^{2n_q-1} p_j(t) x^j \tag{F.31}$$

$$(b_2)_t = \frac{g_1(t, E, \theta_0) \cos(\theta)}{\sqrt{2E}} = \frac{\cos(\theta)}{\sqrt{2E}} \sum_{j=1,3,5,\ldots}^{2n_q-1} p_j(t) x^j \tag{F.32}$$

F.1.2.1 Evaluation of 1^{st} *Term in* (F.30)

$$\left(\frac{\partial b_2}{\partial E} \right)_t = \frac{-\cos(\theta)}{(2E)^{\frac{3}{2}}} \sum_{j=1,3,5,\ldots}^{2n_q-1} p_j(t) x^j + \frac{\cos(\theta)}{\sqrt{2E}} \sum_{j=1,3,5,\ldots}^{2n_q-1} (j) p_j(t) x^{j-1} \left(\frac{\partial x}{\partial E} \right) \tag{F.33}$$

Substituting (F.9) into (F.33)

$$\left(\frac{\partial b_2}{\partial E} \right)_t = \frac{-\cos(\theta)}{(2E)^{\frac{3}{2}}} \sum_{j=1,3,5,\ldots}^{2n_q-1} p_j(t) x^j + \frac{\cos^3(\theta)}{g(E, \theta)\sqrt{2E}} \sum_{j=1,3,5,\ldots}^{2n_q-1} (j) p_j(t) x^{j-1} \tag{F.34}$$

$$E\left[\left(\frac{\partial b_2}{\partial E}\right)_t (b_1)_{t+\tau}\right] = \frac{-1}{2E}\cos(\theta(t))\sin(\theta(t+\tau)) \times \sum_{j=1,3,5,\ldots}^{2n_q-1}\sum_{k=1,3,5,\ldots}^{2n_q-1} E\left[p_j(t)p_k(t+\tau)\right]x^j(t)x^k(t+\tau) + \frac{\cos^3(\theta(t))}{g(E,\theta(t))}\sin(\theta(t+\tau)) \times \sum_{j=1,3,5,\ldots}^{2n_q-1}\sum_{k=1,3,5,\ldots}^{2n_q-1}(j)E\left[p_j(t)p_k(t+\tau)\right]x^{j-1}(t)x^k(t+\tau) \tag{F.35}$$

Assuming a covariance stationarity between $p_j(t)$ and $p_k(t)$ so that $E\left[p_j(t)p_k(t+\tau)\right] = w_{jk}(\tau)$ leads to the following simplification

$$E\left[\left(\frac{\partial b_2}{\partial E}\right)_t (b_1)_{t+\tau}\right] = \frac{-1}{2E}\cos(\theta(t))\sin(\theta(t+\tau))\sum_{j=1,3,5,\ldots}^{2n_q-1}\sum_{k=1,3,5,\ldots}^{2n_q-1} w_{jk}(\tau)x^j(t)x^k(t+\tau) + \frac{\cos^3(\theta(t))}{g(E,\theta(t))}\sin(\theta(t+\tau))\sum_{j=1,3,5,\ldots}^{2n_q-1}\sum_{k=1,3,5,\ldots}^{2n_q-1}(j)w_{jk}(\tau)x^{j-1}(t)x^k(t+\tau) \tag{F.36}$$

F.1.2.2 Evaluation of 2^{nd} Term in (F.30)

$$\left(\frac{\partial b_2}{\partial \lambda}\right)_t = \frac{-\sin(\theta)}{\sqrt{2E}}\sum_{j=1,3,5,\ldots}^{2n_q-1} p_j(t)x^j + \frac{\cos(\theta)}{\sqrt{2E}}\sum_{j=1,3,5,\ldots}^{2n_q-1}(j)p_j(t)x^{j-1}\left(\frac{\partial x}{\partial \lambda}\right) \tag{F.37}$$

Substituting (F.16) into (F.37)

$$\left(\frac{\partial b_2}{\partial \lambda}\right)_t = \frac{-\sin(\theta)}{\sqrt{2E}}\sum_{j=1,3,5,\ldots}^{2n_q-1} p_j(t)x^j + \frac{-\sqrt{2E}\sin(\theta)\cos^2(\theta)}{g(E,\theta)}\sum_{j=1,3,5,\ldots}^{2n_q-1}(j)p_j(t)x^{j-1} \tag{F.38}$$

$$
\begin{aligned}
E\left[\left(\frac{\partial b_2}{\partial \lambda}\right)_t (b_2)_{t+\tau}\right] =& \frac{-1}{2E}\sin(\theta(t))\cos(\theta(t+\tau)) \\
& \times \sum_{j=1,3,5,\ldots}^{2n_q-1} \sum_{k=1,3,5,\ldots}^{2n_q-1} E\left[p_j(t)p_k(t+\tau)\right] x^j(t)x^k(t+\tau) \\
& + \frac{-1}{g(E,\theta(t))}\sin(\theta(t))\cos^2(\theta(t))\cos(\theta(t+\tau)) \\
& \times \sum_{j=1,3,5,\ldots}^{2n_q-1} \sum_{k=1,3,5,\ldots}^{2n_q-1} (j) E\left[p_j(t)p_k(t+\tau)\right] x^{j-1}(t)x^k(t+\tau)
\end{aligned}
\tag{F.39}
$$

Assuming a covariance stationarity between $p_j(t)$ and $p_k(t)$ leads to the following simplification

$$
\begin{aligned}
E\left[\left(\frac{\partial b_2}{\partial \lambda}\right)_t (b_2)_{t+\tau}\right] =& \frac{-1}{2E}\sin\theta(t)\cos\theta(t+\tau) \\
& \times \sum_{j=1,3,5,\ldots}^{2n_q-1} \sum_{k=1,3,5,\ldots}^{2n_q-1} w_{jk}(\tau) x^j(t)x^k(t+\tau) \\
& - \frac{1}{g(E,\theta(t))}\sin\theta(t)\cos^2\theta(t)\cos\theta(t+\tau) \\
& \times \sum_{j=1,3,5,\ldots}^{2n_q-1} \sum_{k=1,3,5,\ldots}^{2n_q-1} (j) w_{jk}(\tau) x^{j-1}(t)x^k(t+\tau)
\end{aligned}
\tag{F.40}
$$

where $w_{jk}(\tau) = E\left[p_j(t)p_k(t+\tau)\right]$. Substituting (F.36) and (F.40) into (F.30)

results in

$$
\begin{aligned}
m_2 = A_2(E) + & \sum_{j=1,3,5,\ldots}^{2n_q-1} \sum_{k=1,3,5,\ldots}^{2n_q-1} \\
& \left[-\frac{1}{2E} \int_{-\infty}^{0} w_{jk}(\tau) \left\langle \cos(\theta(t)) x^j(t) \sin(\theta(t+\tau)) x^k(t+\tau) \right\rangle d\tau \right. \\
& + (j) \int_{-\infty}^{0} w_{jk}(\tau) \left\langle \frac{\cos^3(\theta(t))}{g(E,\theta(t))} x^{j-1}(t) \sin(\theta(t+\tau)) x^k(t+\tau) \right\rangle d\tau \\
& - \frac{1}{2E} \int_{-\infty}^{0} w_{jk}(\tau) \left\langle \sin(\theta(t)) x^j(t) \cos(\theta(t+\tau)) x^k(t+\tau) \right\rangle d\tau \\
& - \frac{1}{2E} (j) \int_{-\infty}^{0} w_{jk}(\tau) \\
& \left. \times \left\langle \frac{2E}{g(E,\theta(t))} \sin(\theta(t)) \cos^2(\theta(t)) x^{j-1}(t) \cos(\theta(t+\tau)) x^k(t+\tau) \right\rangle d\tau \right] \qquad \text{(F.41)}
\end{aligned}
$$

F.1.2.3 Fourier Expansions for Phase Drift Calculation

To evaluate the time average of the quantities inside $<\quad>$ in (F.41), it is convenient to expand the various terms as Fourier series as shown below.

$$\cos(\theta(t)) x^k(t) = \sum_{n=1}^{\infty} a_n^{(1k)} \cos\left(\frac{2\pi n}{T} t\right) \qquad \text{(F.42)}$$

$$\sin(\theta(t)) x^k(t) = \sum_{n=1}^{\infty} b_n^{(1k)} \sin\left(\frac{2\pi n}{T} t\right) \qquad \text{(F.43)}$$

$$\frac{2E}{g(E,\theta(t))} \sin(\theta(t)) \cos^2(\theta(t)) x^{k-1}(t) = \sum_{n=1}^{\infty} b_n^{(2k)} \sin\left(\frac{2\pi n}{T} t\right) \qquad \text{(F.44)}$$

$$\frac{\cos^3(\theta(t))}{g(E,\theta(t))} x^{k-1}(t) = \sum_{n=1}^{\infty} d_n^{(2k)} \cos\left(\frac{2\pi n}{T} t\right) \qquad \text{(F.45)}$$

Note that these coefficients $b_n^{(1k)}$, $a_n^{(1k)}$, $b_n^{(2k)}$ and $d_n^{(2k)}$ are functions of energy level E. Since λ is assumed to be fixed, the Fourier coefficients actually relate to the unperturbed solutions $\theta_0(t)$ and $x_0(t)$. Substituting these Fourier series expressions

simplifies the time averages as follows

$$\left\langle \cos(\theta(t))x^j(t)\sin(\theta(t+\tau))x^k(t+\tau)\right\rangle = \sum_{n=1}^{\infty}\frac{a_n^{(1j)}b_n^{(1k)}}{2}\sin\left(\frac{2\pi n}{T}\tau\right) \tag{F.46}$$

$$\left\langle \frac{\cos^3(\theta(t))}{g(E,\theta(t))}x^{j-1}(t)\sin(\theta(t+\tau))x^k(t+\tau)\right\rangle = \sum_{n=1}^{\infty}\frac{d_n^{(2j)}b_n^{(1k)}}{2}\sin\left(\frac{2\pi n}{T}\tau\right) \tag{F.47}$$

$$\left\langle \sin(\theta(t))x^j(t)\cos(\theta(t+\tau))x^k(t+\tau)\right\rangle = \sum_{n=1}^{\infty}-\frac{b_n^{(1j)}a_n^{(1k)}}{2}\sin\left(\frac{2\pi n}{T}\tau\right) \tag{F.48}$$

$$\left\langle \frac{2E}{g(E,\theta(t))}\sin^2(\theta(t))\cos(\theta(t))x^{j-1}(t)\cos(\theta(t+\tau))x^k(t+\tau)\right\rangle = \sum_{n=1}^{\infty}-\frac{b_n^{(2j)}a_n^{(1k)}}{2}\sin\left(\frac{2\pi n}{T}\tau\right) \tag{F.49}$$

Substituting into (F.41) leads to

$$\begin{aligned} m_2 =& A_2(E) + \sum_{n=1}^{\infty}\sum_{j=1,3,5,\ldots}^{2n_q-1}\sum_{k=1,3,5,\ldots}^{2n_q-1}\left[\left(\int_{-\infty}^{0} w_{jk}(\tau)\sin\left(\frac{2\pi n}{T}\tau\right)d\tau\right)\right. \\ &\left.\times\left\{-\frac{a_n^{(1j)}b_n^{(1k)}}{4E}+\frac{b_n^{(1j)}a_n^{(1k)}}{4E}+(j)\frac{d_n^{(2j)}b_n^{(1k)}}{2}+(j)\frac{b_n^{(2j)}a_n^{(1k)}}{4E}\right\}\right] \end{aligned} \tag{F.50}$$

F.2 Diffusion Coefficient Calculation

For a stationary covariance $w_{jk}(\tau)$, the cross spectrum is defined by

$$S_{jk}^{(c)}(\omega) = \frac{1}{2\pi}\int_{-\infty}^{\infty} w_{jk}(\tau)\cos(\omega\tau)\,d\tau \tag{F.51}$$

$$S_{jk}^{(s)}(\omega) = \frac{1}{2\pi}\int_{-\infty}^{\infty} w_{jk}(\tau)\sin(\omega\tau)\,d\tau \tag{F.52}$$

$$
\begin{aligned}
D_{11} &= \int_{-\infty}^{\infty} \left\langle E\left[(b_1)_t\,(b_1)_{t+\tau}^T\right]\right\rangle d\tau \\
&= \sum_{j=1,3,5,\ldots}^{2n_q-1}\sum_{k=1,3,5,\ldots}^{2n_q-1}\left[2E\int_{-\infty}^{\infty} w_{jk}(\tau)\left\langle \sin(\theta(t))x^j(t)\sin(\theta(t+\tau))x^k(t+\tau)\right\rangle d\tau\right] \\
&= \sum_{n=1}^{\infty}\sum_{j=1,3,5,\ldots}^{2n_q-1}\sum_{k=1,3,5,\ldots}^{2n_q-1}\left[2E\int_{-\infty}^{\infty} w_{jk}(\tau)\frac{b_n^{(1j)}b_n^{(1k)}}{2}\cos\left(\frac{2\pi n}{T}\tau\right)d\tau\right] \\
&= \sum_{n=1}^{\infty}\sum_{j=1,3,5,\ldots}^{2n_q-1}\sum_{k=1,3,5,\ldots}^{2n_q-1}\left[(2\pi E)\left\{b_n^{(1j)}b_n^{(1k)}\right\}S_{jk}^{(c)}\left(\frac{2\pi n}{T(E)}\right)\right]
\end{aligned}
\tag{F.53}
$$

$$
\begin{aligned}
D_{12} &= \int_{-\infty}^{\infty} \left\langle E\left[(b_1)_t\,(b_2)_{t+\tau}^T\right]\right\rangle d\tau \\
&= \sum_{j=1,3,5,\ldots}^{2n_q-1}\sum_{k=1,3,5,\ldots}^{2n_q-1}\left[\int_{-\infty}^{\infty} w_{jk}(\tau)\left\langle \sin(\theta(t))x^j(t)\cos(\theta(t+\tau))x^k(t+\tau)\right\rangle d\tau\right] \\
&= \sum_{n=1}^{\infty}\sum_{j=1,3,5,\ldots}^{2n_q-1}\sum_{k=1,3,5,\ldots}^{2n_q-1}\left[\int_{-\infty}^{\infty} w_{jk}(\tau)\left(-\frac{b_n^{(1j)}a_n^{(1k)}}{2}\right)\sin\left(\frac{2\pi n}{T}\tau\right)d\tau\right] \\
&= \sum_{n=1}^{\infty}\sum_{j=1,3,5,\ldots}^{2n_q-1}\sum_{k=1,3,5,\ldots}^{2n_q-1}\left[-\pi b_n^{(1j)}a_n^{(1k)}S_{jk}^{(s)}\left(\frac{2\pi n}{T(E)}\right)\right]
\end{aligned}
\tag{F.54}
$$

$$
\begin{aligned}
D_{21} &= \int_{-\infty}^{\infty} \left\langle E\left[(b_2)_t\,(b_1)_{t+\tau}^T\right]\right\rangle d\tau \\
&= \sum_{j=1,3,5,\ldots}^{2n_q-1}\sum_{k=1,3,5,\ldots}^{2n_q-1}\left[\int_{-\infty}^{\infty} w_{jk}(\tau)\left\langle \cos(\theta(t))x^j(t)\sin(\theta(t+\tau))x^k(t+\tau)\right\rangle d\tau\right] \\
&= \sum_{n=1}^{\infty}\sum_{j=1,3,5,\ldots}^{2n_q-1}\sum_{k=1,3,5,\ldots}^{2n_q-1}\left[\int_{-\infty}^{\infty} w_{jk}(\tau)\left(\frac{a_n^{(1j)}b_n^{(1k)}}{2}\right)\sin\left(\frac{2\pi n}{T}\tau\right)d\tau\right] \\
&= \sum_{n=1}^{\infty}\sum_{j=1,3,5,\ldots}^{2n_q-1}\sum_{k=1,3,5,\ldots}^{2n_q-1}\left[\pi a_n^{(1j)}b_n^{(1k)}S_{jk}^{(s)}\left(\frac{2\pi n}{T(E)}\right)\right]
\end{aligned}
\tag{F.55}
$$

$$
\begin{aligned}
D_{22} &= \int_{-\infty}^{\infty} \left\langle E\left[(b_2)_t \, (b_2)_{t+\tau}^T \right] \right\rangle d\tau \\
&= \sum_{j=1,3,5,\ldots}^{2n_q-1} \sum_{k=1,3,5,\ldots}^{2n_q-1} \left[\frac{1}{2E} \int_{-\infty}^{\infty} w_{jk}(\tau) \left\langle \cos(\theta(t)) x^j(t) \cos(\theta(t+\tau)) x^k(t+\tau) \right\rangle d\tau \right] \\
&= \sum_{n=1}^{\infty} \sum_{j=1,3,5,\ldots}^{2n_q-1} \sum_{k=1,3,5,\ldots}^{2n_q-1} \left[\frac{1}{2E} \int_{-\infty}^{\infty} w_{jk}(\tau) \frac{a_n^{(1j)} a_n^{(1k)}}{2} \cos\left(\frac{2\pi n}{T} \tau \right) d\tau \right] \\
&= \sum_{n=1}^{\infty} \sum_{j=1,3,5,\ldots}^{2n_q-1} \sum_{k=1,3,5,\ldots}^{2n_q-1} \left[\frac{\pi}{2E} \left\{ a_n^{(1j)} a_n^{(1k)} \right\} S_{jk}^{(c)} \left(\frac{2\pi n}{T(E)} \right) \right]
\end{aligned}
\tag{F.56}
$$

APPENDIX G

DERIVATION OF THE SINGULAR BOUNDARY CONDITION OF PONTRYAGIN EQUATION AT $E = 0$

According to Feller [169], the boundaries of a diffusion process can be classified as follows:

1. *Regular boundary*: The process can reach the boundary starting from an interior point and vice versa

2. *Absorbing/Exit boundary*: The process can reach the boundary starting from an interior point but cannot reach an interior point starting from the boundary

3. *Entrance boundary*: The process can reach an interior point beginning from the boundary but cannot reach the boundary starting from an interior point

4. *Natural boundary*: The process cannot reach the boundary starting from an interior point and vice versa. Lin and Cai [18] further specify a sub-classification of natural boundary into strictly natural, attractively natural and repulsively natural boundary types.

Often various conclusions about the existence of a stationary transition probability density function can be drawn based on the type of boundaries. In general, the type of boundary can be mathematically ascertained and is described in detail by Lin and Cai [18]. However, for certain special types of boundaries called the singular boundaries the above approach is not applicable and requires special consideration. A boundary at $E = E_b$ of a diffusion process $E(t)$ is defined to be singular if at the boundary either of the following hold:

1. The diffusion coefficient at the boundary is zero ($D_{11}(E_b) = \sigma_{11}^2(E_b) = 0$)

2. The drift coefficient at the boundary is unbounded ($m_1(E_b) \to \pm\infty$)

Further a singular boundary condition of the first kind is called a *trap* if the drift coefficient at the boundary is zero. When the drift coefficient at the boundary is non-zero, it is called a *shunt*.

To determine the Feller classification of a singular boundary of the first kind, the following definitions are introduced as $E \to E_b$ where $E = E_b$ is the singular boundary under consideration:

1. *Diffusion exponent* α_b where $\sigma_{11}^2(E) = O(|E - E_b|^{\alpha_b})$ as $E \to E_b$

2. *Drift exponent* β_b where $m_1(E) = O(|E - E_b|^{\beta_b})$ as $E \to E_b$

3. *Character value* c_b where $c_b = \frac{2m_1(E)(E-E_b)^{\alpha_b-\beta_b}}{\sigma_{11}^2(E)}$ as $E \to E_b$

A Feller classification of the singular boundaries is provided in the works of Lin and Cai [18] based on the values of the drift exponent, diffusion exponent and the character value.

From Figure 5.6 and Figure 5.8 it can be seen that the first condition holds for the Markov energy process $E(t)$ considered in (5.59). Thus the boundary $E = 0$ is a singular boundary of the first kind. From Figure 5.5 and Figure 5.7 it can further be seen that the boundary at $E = 0$ is a trap as the drift coefficient at $E = 0$ is zero.

Since we are interested in the boundary condition at $E = 0$, the nonlinear oscillator can be linearized in the vicinity of the boundary. Thus considering only the linear stiffness and linear damping to be dominant near $E = 0$, the original oscillator given by (5.3) can be approximated as

$$\ddot{x} + \varepsilon^2\delta_1\dot{x} + x + \varepsilon p_1(t)x = 0 \tag{G.1}$$

The energy and phase in this case are defined as

$$E = \frac{\dot{x}^2}{2} + \frac{x^2}{2} \tag{G.2}$$

$$\theta = \tan^{-1}\left(\frac{-\dot{x}}{x}\right) \tag{G.3}$$

The displacement x and velocity $\dot{x}$ in the linear case are given by

$$x = \sqrt{2E}\cos(\theta) \tag{G.4}$$

$$\dot{x} = -\sqrt{2E}\sin(\theta) \tag{G.5}$$

The differential equation governing $E(t)$ and $\theta(t)$ are obtained by differentiating (G.2) and (G.3) with respect to time t respectively.

$$\dot{E} = \varepsilon^2\left(-2E\delta_1\sin^2(\theta)\right) + \varepsilon p_1(t)E\sin(2\theta) \tag{G.6}$$

$$\dot{\theta} = 1 + \varepsilon^2\left(-\frac{\delta_1}{2}\sin(2\theta)\right) + \varepsilon p_1(t)\cos^2(\theta) \tag{G.7}$$

Defining a new phase process $\lambda(t) = \theta(t) - t$,

$$\dot{E} = \varepsilon^2\left(-2E\delta_1\sin^2(\theta)\right) + \varepsilon p_1(t)E\sin(2\theta) \tag{G.8}$$

$$\dot{\lambda} = \varepsilon^2\left(-\frac{\delta_1}{2}\sin(2\theta)\right) + \varepsilon p_1(t)\cos^2(\theta) \tag{G.9}$$

Thus the vector process $\boldsymbol{Z}(t) = \begin{Bmatrix} E(t) \\ \lambda(t) \end{Bmatrix}$ is a slowly varying with time and is

given by

$$\dot{\boldsymbol{Z}}(t) = \begin{bmatrix} \dot{E} \\ \dot{\lambda} \end{bmatrix} = \varepsilon^2 \boldsymbol{a}(\boldsymbol{Z}) + \varepsilon \boldsymbol{b}(t, \boldsymbol{Z}) \tag{G.10}$$

where

$$\boldsymbol{a}(\boldsymbol{Z}) = \begin{bmatrix} a_1(E, \theta) \\ a_2(E, \theta) \end{bmatrix} = \begin{bmatrix} -2E\delta_1 \sin^2(\theta) \\ -\frac{\delta_1}{2} \sin(2\theta) \end{bmatrix} \tag{G.11}$$

$$\boldsymbol{b}(t, \boldsymbol{Z}) = \begin{bmatrix} b_1(t, E, \theta) \\ b_2(t, E, \theta) \end{bmatrix} = \begin{bmatrix} p_1(t) E \sin(2\theta) \\ p_1(t) \cos^2(\theta) \end{bmatrix} \tag{G.12}$$

Applying the technique of stochastic averaging as described in chapter 5, the drift and diffusion coefficients of the linear system are given by

$$\boldsymbol{m} = \boldsymbol{A}(E) + \int_{-\infty}^{0} \left\langle E \left[\left(\frac{\partial \boldsymbol{b}}{\partial \boldsymbol{Z}} \right)_t (\boldsymbol{b})_{t+\tau} \right] \right\rangle d\tau \tag{G.13}$$

$$\boldsymbol{D} = \boldsymbol{\sigma}\boldsymbol{\sigma}^T = \int_{-\infty}^{\infty} \left\langle E \left[(\boldsymbol{b})_t (\boldsymbol{b})_{t+\tau}^T \right] \right\rangle d\tau \tag{G.14}$$

where

$$\frac{\partial \boldsymbol{b}}{\partial \boldsymbol{Z}} = \begin{bmatrix} \frac{\partial b_1}{\partial E} & \frac{\partial b_1}{\partial \lambda} \\ \frac{\partial b_2}{\partial E} & \frac{\partial b_2}{\partial \lambda} \end{bmatrix} \tag{G.15}$$

$$\boldsymbol{A}(E) = \begin{bmatrix} A_1(E) \\ A_2(E) \end{bmatrix} = \langle \boldsymbol{a}(E, \theta_0) \rangle = \frac{1}{T(E)} \int_0^{T(E)} \boldsymbol{a}(E, \theta_0) dt \tag{G.16}$$

Note that $\langle [.] \rangle$ denotes the time average over the unperturbed system period $T(E)$ and is given by

$$\langle [\ .\ ] \rangle = \frac{1}{T(E)} \int_0^{T(E)} [\ .\ ] dt \tag{G.17}$$

where the unperturbed system period $T(E)$ is given by

$$T(E) = \oint \left| \frac{dx}{\dot{x}} \right| = 4 \int_0^b \frac{dx}{\sqrt{2E}\sin(\theta)} = 4 \int_{-\frac{\pi}{2}}^0 \frac{\sqrt{2E}\sin(\theta) d\theta}{\sqrt{2E}\sin(\theta)} = 2\pi \tag{G.18}$$

$$A_1(E) = \frac{1}{2\pi} \int_0^{T(E)} -\delta_1 2E \sin^2(\theta_0) dt = \frac{1}{2\pi} \int_0^{2\pi} -\delta_1 2E \sin^2(t) dt = -\delta_1 E \tag{G.19}$$

$$A_2(E) = \frac{1}{2\pi} \int_0^{T(E)} -\frac{\delta_1}{2} \sin(2\theta_0) dt = \frac{1}{2\pi} \int_0^{2\pi} -\frac{\delta_1}{2} \sin(2t) dt = 0 \tag{G.20}$$

The drift and diffusion coefficients corresponding to the energy process are given by

$$\begin{aligned} m_1 &= A_1(E) + \int_{-\infty}^0 \left\langle E \left[\left(\frac{\partial b_1}{\partial E} \right)_t (b_1)_{t+\tau} + \left(\frac{\partial b_1}{\partial \lambda} \right)_t (b_2)_{t+\tau} \right] \right\rangle d\tau \\ &= \left(\pi S_{11}^{(c)}(2) - \delta_1 \right) E \end{aligned} \tag{G.21}$$

$$D_{11} = \int_{-\infty}^{\infty} \left\langle E \left[(b_1)_t (b_1)_{t+\tau}^T \right] \right\rangle d\tau = \pi S_{11}^{(c)}(2) E^2 \tag{G.22}$$

$$D_{12} = \int_{-\infty}^{\infty} \left\langle E \left[(b_1)_t (b_2)_{t+\tau}^T \right] \right\rangle d\tau = 0 \tag{G.23}$$

Note that since $D_{12} = 0$, the energy process is also a Markov process itself in the vicinity of $E = 0$. It can be seen from (G.21) that the drift exponent is $\alpha_0 = 2$. Similarly from (G.22) it can be seen that diffusion exponent $\beta_0 = 1$. The character value c_0 is given by

$$c_0 = \frac{2m_1(E)(E-0)^{\alpha_0-\beta_0}}{\sigma_{11}^2(E)} = 2\left(1 - \frac{\delta_1}{\pi S_{11}^{(c)}(2)}\right) \tag{G.24}$$

As described in section 5.4, the Pontryagin formulation assumes that every sample path will eventually reach the critical boundary $E = E_c$ (given by $\mu_1(E_c, E_0)|_{E_0=0} < \infty$). Thus only those boundary conditions which allow for this possibility are admissible. Thus, if the singular boundary at $E = 0$ is a regular or entrance or a repulsively natural trap then all sample paths will eventually reach the exit boundary at $E = E_c$. However, if the singular boundary at $E = 0$ is an exit, a strictly natural or attractively natural boundary then not every sample path starting at or near $E = 0$ will reach the critical boundary $E = E_c$. For more detailed discussion refer the works of Lin and Cai [18]. Since Pontryagin equation formulation assumes that for sample path will eventually reach the critical boundary $(\mu_1(E_c, E_0)|_{E_0=0} < \infty)$, an exit, a strictly natural or a attractively natural boundary condition is not admissible.

According to Lin and Cai [18], a drift exponent $\beta_0 = 1$ and a diffusion exponent $\alpha_0 = 2$ corresponds to a natural boundary at $E = 0$. The character value c_0 decides if the boundary is further strictly ($c_0 = 1$), attractively ($c_0 < 1$) or repulsively natural ($c_0 > 1$). Thus the Pontryagin equation is applicable only if $c_0 > 1$. In this case, the Pontryagin equation is given by

$$\frac{\pi S_{11}^{(c)}(2)}{2} E^2 \frac{d^2\mu_1}{dE^2} + (\pi S_{11}^{(c)}(2) - \delta_1) E \frac{d\mu_1}{dE} + 1 = 0 \tag{G.25}$$

Since the above equation is an Euler type differential equation, it can be integrated to yield

$$\frac{d\mu_1}{dE}(E) = C_1 E^{\left[\frac{2\delta_1}{\pi S_{11}^{(c)}(2)} - 2\right]} - \frac{2}{\left(\pi S_{11}^{(c)}(2) - 2\delta_1\right)} \tag{G.26}$$

Imposing the boundary condition of the form (5.73) gives $C_1 = 0$ and results in the boundary condition given in (5.74).

APPENDIX H

SUPPLEMENTARY FILES

A supplementary file named "`Pram_hull.igs`" is included which provides the geometry of the Pram hull analyzed in this dissertation. The origin is located at the intersection of midship, centerline and waterline. The roll and pitch radii of gyration about the coordinate system with origin as specified above are 13.61 m and 62.55 m respectively.